AD NUMBER
AD809557
NEW LIMITATION CHANGE
TO Approved for public release, distribution unlimited
FROM Distribution authorized to DoD only; Administrative/Operational Use; JAN 1967. Other requests shall be referred to U.S. Army Aviation Materiel Command, Fort Eustis, VA.
AUTHORITY
USAAML ltr, 16 Jun 1969

AC

USAAVLABS TECHNICAL REPORT 66-90

SMALL GAS TURBINE ENGINE COMPONENT TECHNOLOGY REGENERATOR RESEARCH

By

A. J. Wheeler

H. R. Dolf

V. J. Klein

J. Acurio

January 1967

U. S. ARMY AVIATION MATERIEL LABORATORIES
FORT EUSTIS, VIRGINIA

CONTRACT DA 44-177-AMC-173(T)

THE BOEING COMPANY
TURBINE DIVISION
SEATTLE, WASHINGTON

Disclaimers

Disposition Instructions

DEPARTMENT OF THE ARMY
U. S. ARMY AVIATION MATERIEL LABORATORIES
FORT EUSTIS. VIRGINIA 23604

Appropriate technical personnel have reviewed this
report and concur with the conclusions contained herein.

The findings and recommendations as outlined in this report
will be used in planning future heat exchanger system programs
for regenerative gas turbine engines.

Task 1M121401D14413

Contract DA 44-177-AMC-173(T)

USAAVLABS Technical Report 66-90

January 1967

SMALL GAS TURBINE ENGINE COMPONENT TECHNOLOGY
REGENERATOR RESEARCH

FINAL REPORT
D4-3371

by

A. J. Wheeler
H. R. Dolf
V. J. Klein
J. Acurio

Prepared by

THE BOEING COMPANY
TURBINE DIVISION
SEATTLE, WASHINGTON

for

U. S. ARMY AVIATION MATERIEL LABORATORIES

FORT EUSTIS, VIRGINIA

ABSTRACT

This report finalizes the research conducted on the regenerator section of Contract DA 44-177-AM ? :73'T) — Advancement of Small Gas Turbine Engine Component Technology. The program was authorized by Task No. IM121401D14413. Work conducted by The Boeing Company under this task also included research on high-temperature turbine materials and high-pressure-ratio centrifugal compressors.

The regenerator program covered by this report was started in May, 1964, and included (a) analytical studies of the heat transfer and pressure drop characteristics associated with small diameter, thin-walled tubes, (b) design of full-size modules for regenerators, and (c) development of these modules by testing.

CONTENTS

FOR OFFICIAL USE ONLY

CONTENTS (Continued)

vi

FOR OFFICIAL USE ONLY

FOR OFFICIAL USE ONLY

ILLUSTRATIONS

FOR OFFICIAL USE ONLY

ILLUSTRATIONS (Continued)

ILLUSTRATIONS (Continued)

FOR OFFICIAL USE ONLY

ILLUSTRATIONS (Continued)

x

FOR OFFICIAL USE ONLY

ILLUSTRATIONS (Continued)

xi

ILLUSTRATIONS (Continued)

ILLUSTRATIONS (Continued)

ILLUSTRATIONS (Continued)

TABLES

TABLES (Continued)

SYMBOLS

DIMENSIONAL VARIABLES

A   Heat exchanger surface area on one side, Ft^2 or $In.^2$

Ac   Heat exchanger free-flow area on one side, Ft^2 or $In.^2$

c_p Fluid, specific heat, Btu/Lb Mass - °F

D_H Hydraulic diameter, 4L Ac/A

D   Diameter, In.

g_c Gravitational constant, 32.2 $\dfrac{Ft\text{-}Lb\ Mass}{Lb\ Force\text{ - }Sec^2}$

h   Heat transfer convective conductance, Btu/Hr - Ft^2 - °F

ID   Inside diameter, In.

L   Length, Ft or In.

δ Thickness, In.

P   Pressure, Lb Force/Ft^2 or Lb Force/$In.^2$

R, r   Radius, In.

sfc   Specific fuel consumption, Lb Mass/Hp - Hr

T   Temperature, °F or °R

TIT   Turbine inlet temperature, °F

t   Wall thickness, In.

U   Overall convective conductance, Btu/Hr - Ft^2 - °F

u   Velocity, Ft/Sec

μ Viscosity, Lb Mass/Hr - Ft

v	Specific volume, air, Ft^3/Lb Mass
v	Core specific volume, Ft^3/Lb Airflow/Sec
W	Flow rate, Lb Mass/Hr or Lb Mass/Sec
ρ	Air density, Lb Mass/Ft^3
x, y	Distance, In.

DIMENSIONLESS VARIABLES

f	Friction factor
j	Colburn factor, $N_{St}N_{Pr}^{2/3}$
K_c	Loss coefficient at pipe entrance
K_T	Loss coefficient
N_D	Dean number
N_R	Reynolds number, $W D_H/A_c \mu$
N_{St}	Stanton number, hA_c/Wc_p
N_{Pr}	Prandtl number
Ntu	Number of heat transfer units, Ah/Wc_p, AU/Wc_p
Δ	Denotes difference
ϵ	Effectiveness
σ	Ratio of free flow to frontal area
η_c	Compressor efficiency
η_{pt}	Power turbine efficiency
η_{gpt}	Gas producer turbine efficiency
η_B	Burner efficiency

PR   Compressor pressure ratio

$\Delta P/P$ Pressure drop over inlet pressure

$\dfrac{C_{min}}{C_{max}}$ Flow stream capacity ratio (Wc_{p_A}/Wc_{p_G})

X_l Ratio of longitudinal pitch to tube diameter for flow across tubes

X_t Ratio of transverse pitch to tube diameter for flow across tubes

<u>SUBSCRIPTS</u>

A   Air side

B   Burner

C   Compressor

G   Gas side

gpt   Gas-producer turbine

i   Inner

NF   No flow

pt   Power turbine

o   Outer

T   Test condition

T-S   Total-to-static

T-T   Total-to-total

W   Condition at wall

X   Extrapolated value

1   Inlet

2   Outlet

SUMMARY

The gas turbine engine industry has long recognized the need for reducing engine fuel consumption and has considered regeneration to be one of the most promising solutions. Basically, the regenerated engine system uses a heat exchanger to recover much of the energy in the form of heat normally lost in the exhaust gases. The heat is transferred to compressor discharge air, thereby reducing the amount of fuel required by the combustor to raise gas temperatures to required levels.

A major consideration in the design of a successful regenerated engine is one of providing a regenerator of sufficiently small size, low weight, and low cost to be attractive to the user. Accordingly, the purpose of this program has been to develop a lightweight, compact heat exchanger unit of reasonable cost for gas turbine engines. In keeping with parallel advances anticipated in other fields of gas turbine component research, the design conditions selected for the regenerator were based on a turbine inlet temperature of 2300°F and a compressor pressure ratio of 10:1. Specific targets were established by Boeing as follows:

Effectiveness	70 Pct
Total Pressure Drop	6 Pct
Core Specific Volume	0.2 Ft^3/Lb Airflow/Sec
Core Specific Weight	10 Lb/Lb Airflow/Sec
Maximum Working Pressure	150 Psia
Maximum Temperature During Transient	1800°F
Maximum Steady-State Working Temperature	1350°F
Specific Regenerator Weight (cores plus manifolds, ducts, and structure)	20 Lb/Lb Airflow/Sec
Leakage	0 Pct
Compact Type Surface	420 Ft^2/Ft^3

To meet these conditions and targets, it was proposed that the core design incorporate small-diameter (0.060-inch), thin-walled tubing with ends expanded into a rectangular shape. The concept is based on stacking the tubes in such a manner that the formed ends would produce the proper alignment and spacing without requiring a perforated header sheet. The ends then could be brazed at the face to form a continuous leakproof joint. The core was divided into a number of small units or modules to allow for thermal growth, to facilitate manufacture, and to provide ease of handling. Analytical studies showed that the concept had the potential for achieving half the weight and volume of other designs available at the outset of the program. These advantages made the design particularly suited to aircraft applications, and it was with this in mind that work on the research program began in May 1964. For the cycle conditions under consideration, a configuration was designed that would reduce fuel consumption by 20 to 25 percent when compared with a simple cycle.

In a complete regenerator assembly, the modules were arranged in a two-pass, cross-counterflow design. Each module was supported independently by a flexible suspension to accommodate thermal growth of the core and to minimize forces associated with unequal thermal expansion between the manifolds and the core. To provide the necessary heat transfer surface in compact, lightweight units, tubes of 0.060-inch outside diameter with 0.003-inch walls were selected. The tubes were designed with expanded ends to eliminate the header sheets found in conventional heat exchangers; therefore, it was expected that this design would lend itself to economical mass production. In the core arrangement, hot gas flowed through tubes with cooler air outside; this resulted in a design with the least fouling tendency, the easiest cleaning characteristics, and the lowest tube wall temperatures.

Under the selected conditions described above, analytical studies of tube surfaces and shapes were conducted to establish design details for full-size modules to be tested. Tubes of various shapes and surface roughness were fabricated and subjected to laboratory tests to determine heat transfer versus pressure loss characteristics. From these studies, it was determined that the best balance of performance parameters was achieved with tubes of either straight or wavy form. With this knowledge, modules were designed, and two with straight tubes and one with wavy tubes were fabricated for test. All were made from AISI type 347 stainless steel, with a palladium-silver brazing alloy. Manufacturing difficulties caused some early delays in the program; however, these problems were solved with the assistance of experimental assembly and brazing specialists.

Testing was conducted in four areas of investigation: performance, fouling, vibration, and structural behavior (thermal shock).

Test data of the straight tube module, extrapolated to 2300°F TIT, 10:1 PR engine conditions and a two-pass arrangement, showed that a 70-percent effectiveness and a 6-percent pressure drop could be achieved with a core volume of 0.21 cubic foot per pound of airflow per second. At the same conditions, wavy tubes showed this performance with a core volume of 0.19 cubic foot per pound of airflow per second.

Vibration tests showed that no problems existed in the tube bundle; however, failure occurred in the flexible suspension during runs at the resonant frequency of the module suspension system. A modification of the suspension, consisting of enlarging the cross section at the corner of the module, overcame this problem.

In other tests, fouling did not occur at conditions corresponding to full-load engine operation. At 50-percent power fouling occurred but after a few hours tended to stabilize at a tolerable level. At idle, fouling increased with time, such that it would handicap the operation of an engine. When full-load power conditions were resumed on a fouled module, deposits were rapidly cleaned off by vaporizing the condensibles with increased gas stream temperatures, showing that a fouled regenerator need not be dismantled for cleaning.

During investigation of general structural behavior by thermal shock testing, cracks developed in the tube wall near the brazed end of the first straight-tube module. At first these cracks were attributed to locally high thermal stresses caused by new and imperfect brazing techniques in which a slight excess of brazing alloy resulted in larger than desired fillets at the tube joints. Although there was some evidence of intergranular oxidation and corrosion, it did not appear to be sufficient to cause the initially observed failures. The wavy-tube module, fabricated with refined brazing techniques, showed no evidence of similar failures during a comparable test period of about 50 hours; this indicated that thermal stress was within safe operating limits for the material. After an additional 45 hours of testing, tube failures in the form of crosswise cracks near the tube ends became apparent. Metallurgical examination showed that the material had suffered severe intergranular oxidation. Further studies indicated that chromium-carbide precipitation, sulfidation, and a high stress level may have been contributing factors. Continued material tests under supplementary company-sponsored research indicated that higher temperature resistant materials, such as Hastelloy X, should be used in future designs.

With the exception of the need for a higher temperature resistant material, it was demonstrated that the design targets, in terms of performance, size, weight, and structural requirements, could be met.

The results of this research program showed the following:

a) Performance

	Effectiveness	Total Pressure Drop
Target	70 Pct	6 Pct
Straight Tubes	70 Pct	6 Pct
Wavy Tubes	70 Pct	6 Pct

b) Size

	Volume	No-Flow Length
Target	0.2 Ft^3/Lb/Sec	-
Straight Tubes	0.21 Ft^3/Lb/Sec	20 In./Lb/Sec
Wavy Tubes	0.19 Ft^3/Lb/Sec	23 In./Lb/Sec

c) Core Weight

Target	10 Lb/Lb/Sec
Straight Tubes	11.3 Lb/Lb/Sec
Wavy Tubes	10.2 Lb/Lb/Sec

The most difficult aspect of the research proved to be in finding suitable methods for mass producing the modules. Specifically, the raw tubing was identified as the item with inherently high costs. Despite extensive surveys of manufacturing processes, no feasible way was found to manufacture the small-diameter tubing at the required low cost level. Conclusions on the inherent cost problem were reached as a result of studies conducted by Superior Tube Company and others in cooperation with Boeing.

4

INTRODUCTION

Gas turbine engine design has progressed to the point where improvements in simple cycle performance due to increased component efficiencies and to higher turbine inlet temperatures and pressure ratios are difficult to achieve and, at best, are modest in magnitude. However, the addition of a regenerator, a heat exchanger which recovers energy normally lost in the exhaust and uses it to preheat air between the compressor and burner, can produce a substantial decrease in engine fuel consumption. The schematic flow diagrams for a regenerated and non-regenerated engine are compared in Figure 1. In the illustration, the energy flowing in each stream is approximately proportional to its width. In effect, part of the exhaust gas energy stream supplements the fuel energy stream. Figure 2 shows how regeneration appears on a temperature-entropy diagram. If a regenerator is to effect a fuel saving, the turbine exhaust temperature (point B) must be higher than the compressor discharge temperature (point A). As pressure ratio is increased, the points approach the same temperature level. Increasing turbine inlet temperature, on the other hand, tends to move point B higher relative to A. Also, it can be concluded that there is a best design pressure ratio for each turbine inlet temperature and that this best pressure ratio increases with turbine inlet temperature.

Figure 3 shows an example of the improvement in specific fuel consumption that can be achieved with regeneration. It is significant that at the higher turbine inlet temperatures, the addition of a regenerator to a cycle at a pressure ratio of 6 produces a more substantial improvement in fuel consumption than does an increase in the pressure ratio from 6 to 10 in a simple cycle. Also apparent is the greater improvement achievable at the higher turbine inlet temperatures. It should be noted that although power and cycle efficiency improve as turbine inlet temperature is increased, the best specific power and best specific fuel consumption do not occur at the same design cycle conditions. In addition, because of its associated pressure losses, regeneration will produce a lower specific power than a simple cycle, all other parameters being held equal.

To determine the best balance of design cycle parameters for typical Army aviation applications, several prior mission studies were conducted. These earlier studies were based on a high-temperature, high-pressure-ratio, nonregenerative engine cycle with a design-point specific fuel consumption of 0.50 pound per horsepower-hour. To this cycle, a regeneration was added. The weight of the regenerated engine was determined as a function of the specific fuel consumption; i.e., low fuel consumption

5

COMPRESSOR

AIR IN   2300° F   EXHAUST

FUEL   POWER
                  OUT

ENERGY BALANCE

BURNER

COMPRESSOR   TURBINE   POWER
                                     OUT

AIR IN   EXHAUST

SCHEMATIC

SIMPLE CYCLE

COMPRESSOR

AIR IN   2300° F   EXHAUST

                  POWER
                  OUT

FUEL
       REGENERATOR

ENERGY BALANCE

BURNER

COMPRESSOR   TURBINE   POWER
                                     OUT

          REGEN-
          ERATOR
AIR IN   EXHAUST

SCHEMATIC
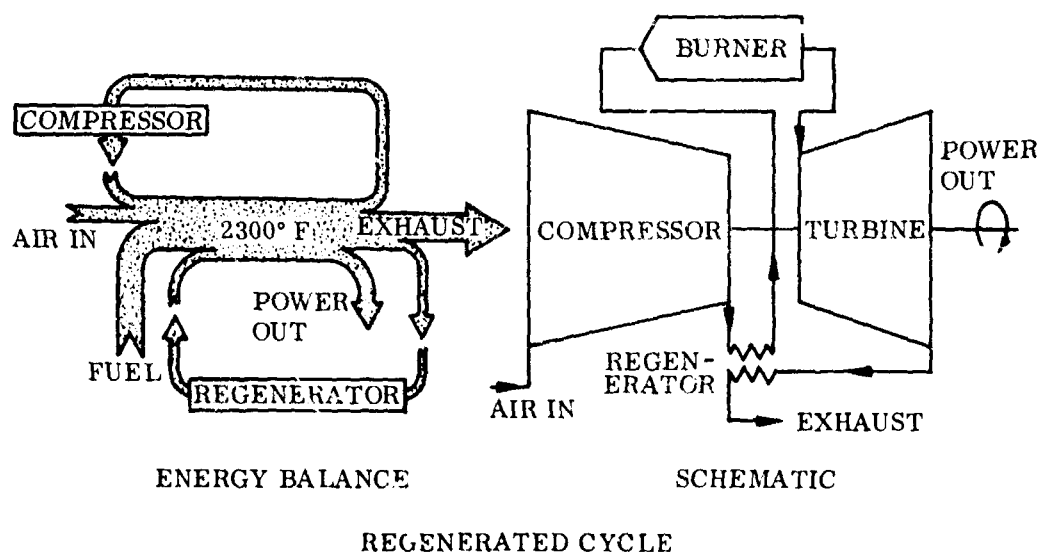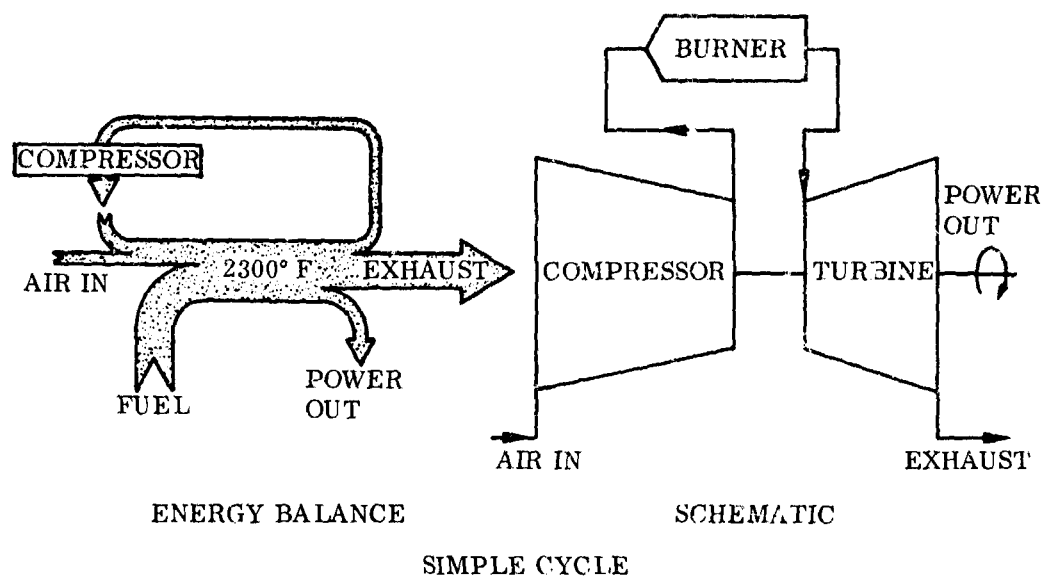
REGENERATED CYCLE

Figure 1. Energy Flows in Gas Turbines.

6
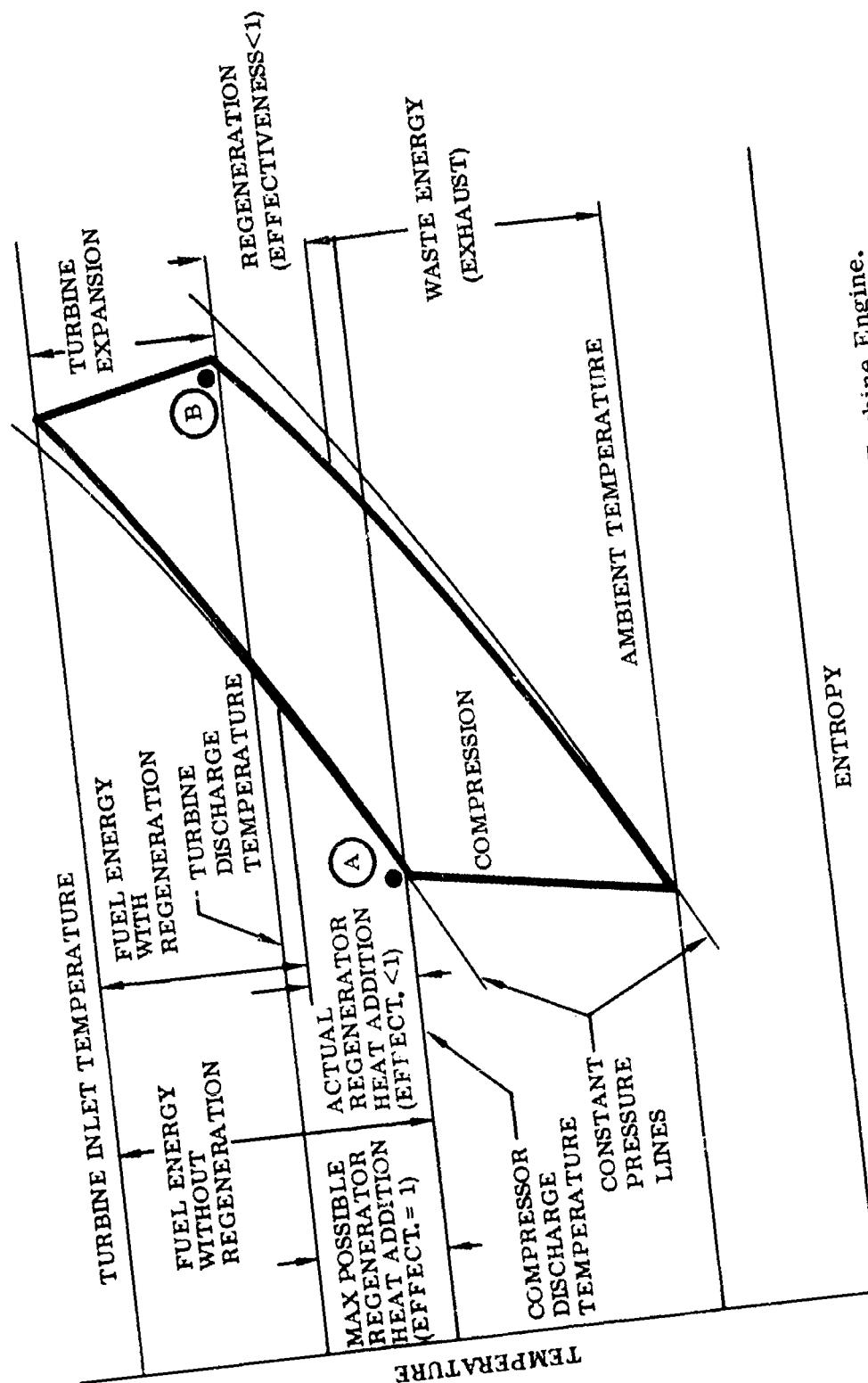
Figure 2. Thermodynamic Cycle of Gas Turbine Engine.

7

Figure 3. Specific Fuel Consumption, Simple Cycle Versus Regenerated Cycle.
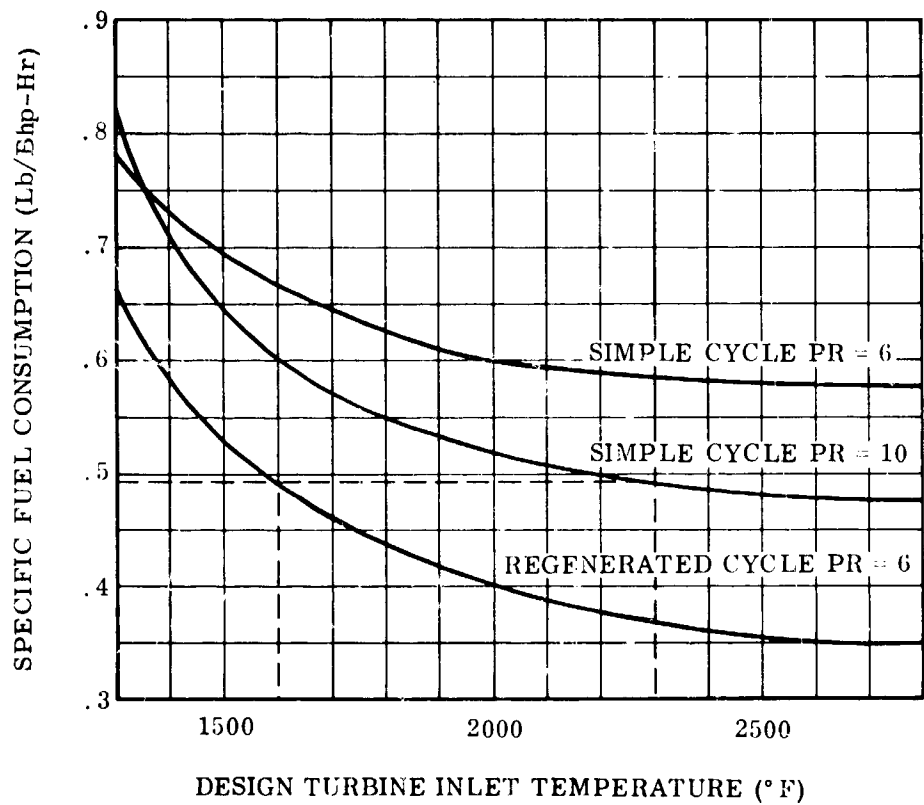
Compressor	$\eta_c = 0.80$		Regenerator:	
Gas Producer Turbine	$\eta_{TT} = 0.86$		Effectiveness	$\epsilon = 0.75$
Power Turbine	$\eta_{TS} = 0.83$		Pressure Drop	$\Delta P/P = 0.06$
Burner Loss	$(\Delta P/P)_B = 0.05$			

8

leads to a large and heavy regenerator. This weight-to-effectiveness relationship was of prime importance and led to the advanced tubular-core construction.

The advantages of regeneration for aircraft missions can be demonstrated by considering the logistics aspects shown in Figure 4. Here the payload in ton-miles carried per pound of fuel is compared for the regenerated and the nonregenerated engine. As can be seen, even for short missions the improvement obtained by regeneration is substantial. The optimum fuel consumption for this case would be 0.36 pound per horsepower-hour. From continued analyses of performance projections and considerations of economics, manufacturing and the various types of possible missions, a design point specific fuel consumption of 0.38 was selected.

The selection of turbine inlet temperature and compressor pressure ratio to obtain the desired specific fuel consumption of 0.38 pound per brake horsepower-hour was made from detailed cycle analyses. Figure 5 depicts the parametric curves obtained from these studies. It is apparent that optimum specific power and minimum specific fuel consumption occur at different conditions. In addition, the desired 0.38 pound per brake horsepower-hour specific fuel consumption can be achieved with a range of combinations of pressure ratios and turbine inlet temperatures. To assist in the selection, the optima of specific power and specific fuel consumption were plotted in Figure 6. The maximum turbine inlet temperature was dictated by potential improvements in materials and was selected as 2300°F. The optimum pressure ratio then was determined from Figure 6. For maximum specific power, the optimum pressure ratio is 10:1, for minimum specific fuel consumption, it is 7.8:1. A design-point pressure ratio of 10:1 was selected for the following reasons:

- Maximum specific power is desired because it results in the smallest, lightest engine.

- At part power the pressure ratio of a gas turbine engine characteristically decreases, and the operating point thus shifts towards the minimum specific fuel consumption condition, resulting in improved part-power specific fuel consumption.

Although the pressure ratio chosen was slightly higher than optimum for the best specific fuel consumption, it can be seen from Figure 5 that the minima of the curves are very flat. The exact difference can be determined from Figure 7, which plots the percentage increase in specific fuel consumption for pressure ratios higher than optimum at a number of turbine inlet temperatures. At the selected turbine inlet temperature of
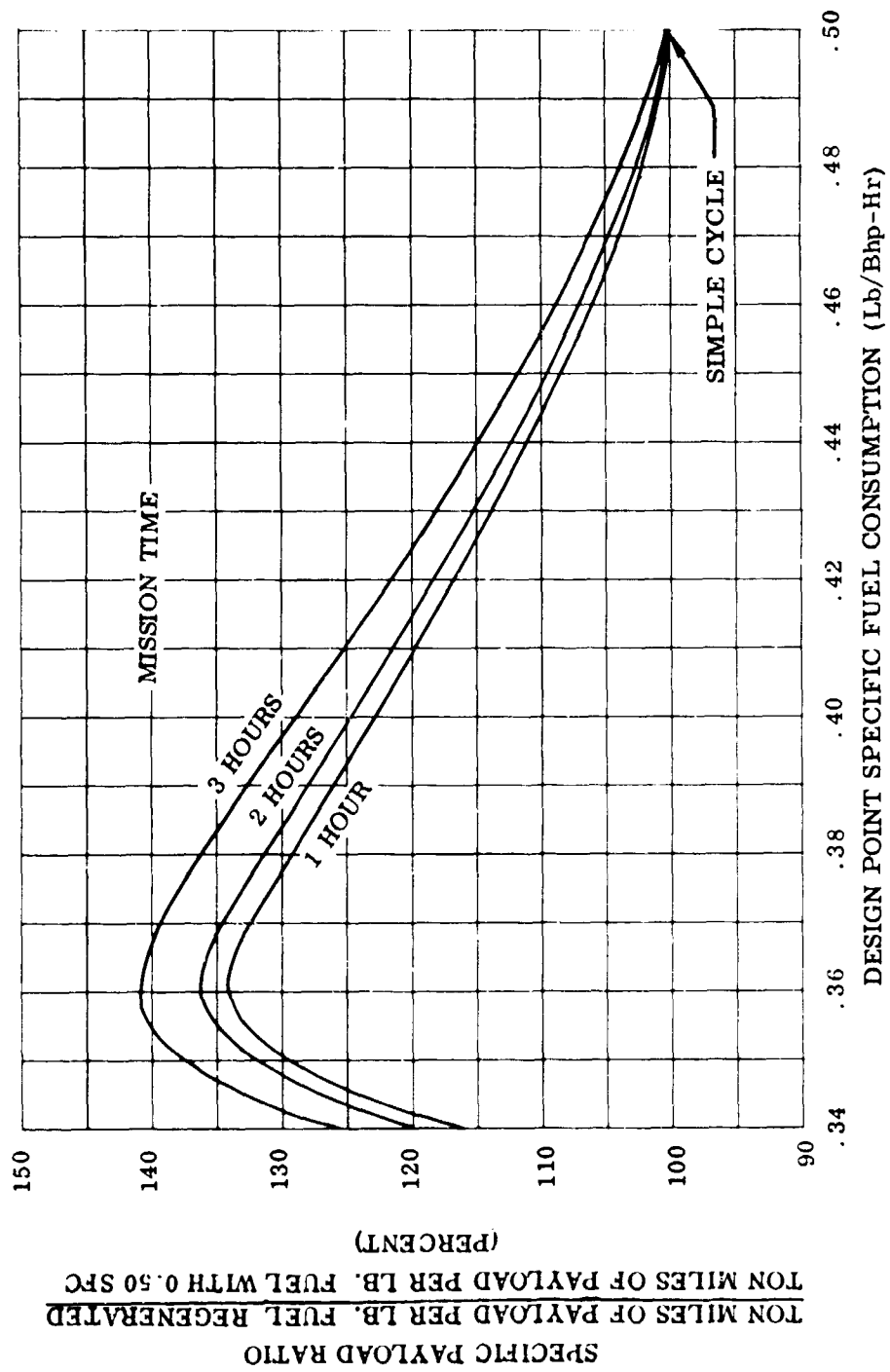
Figure 4. Increase in Payload With Regeneration.
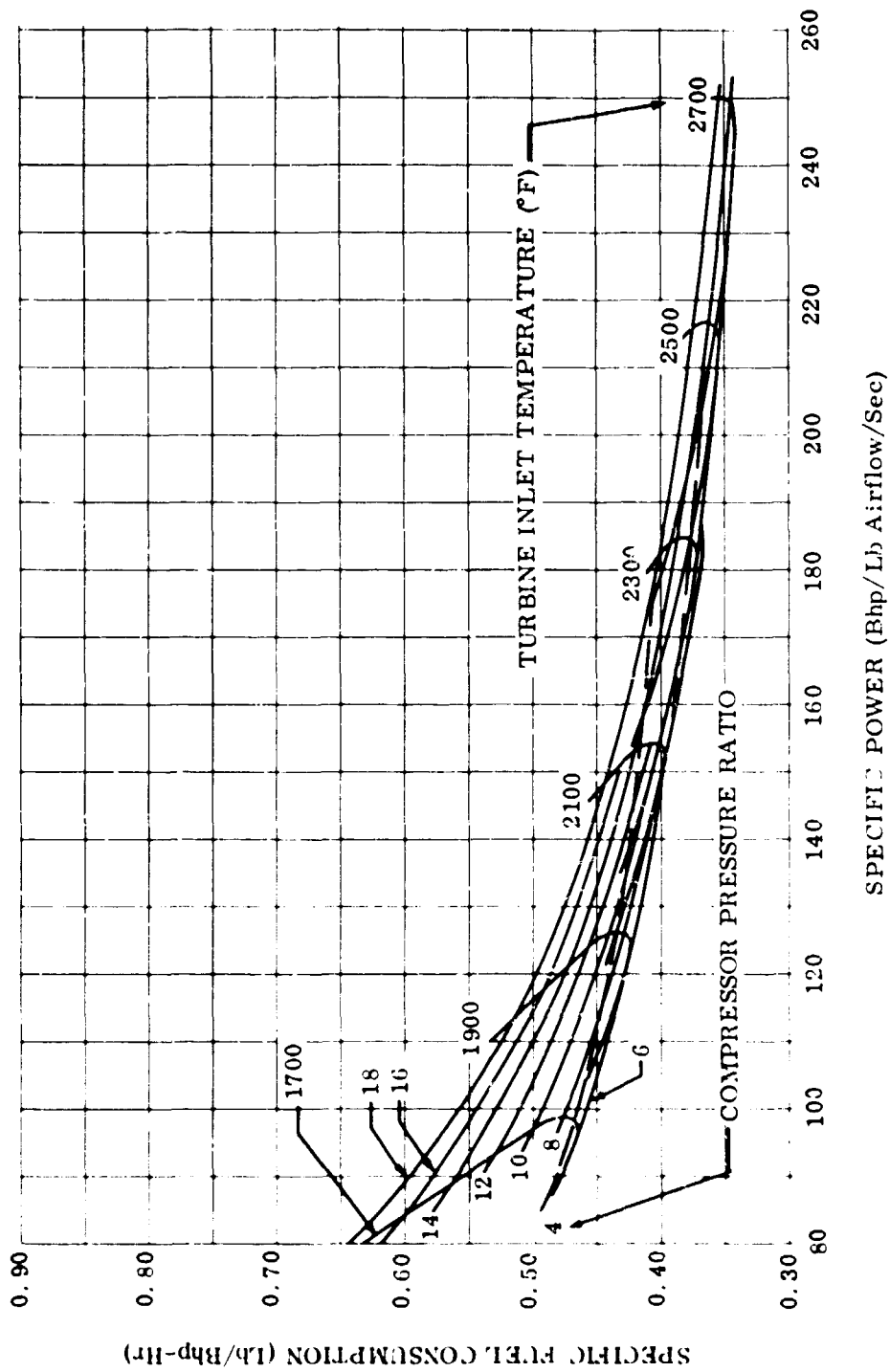
Figure 5. Effect of Gas Temperature on Regenerative Engine Cycle Performance.
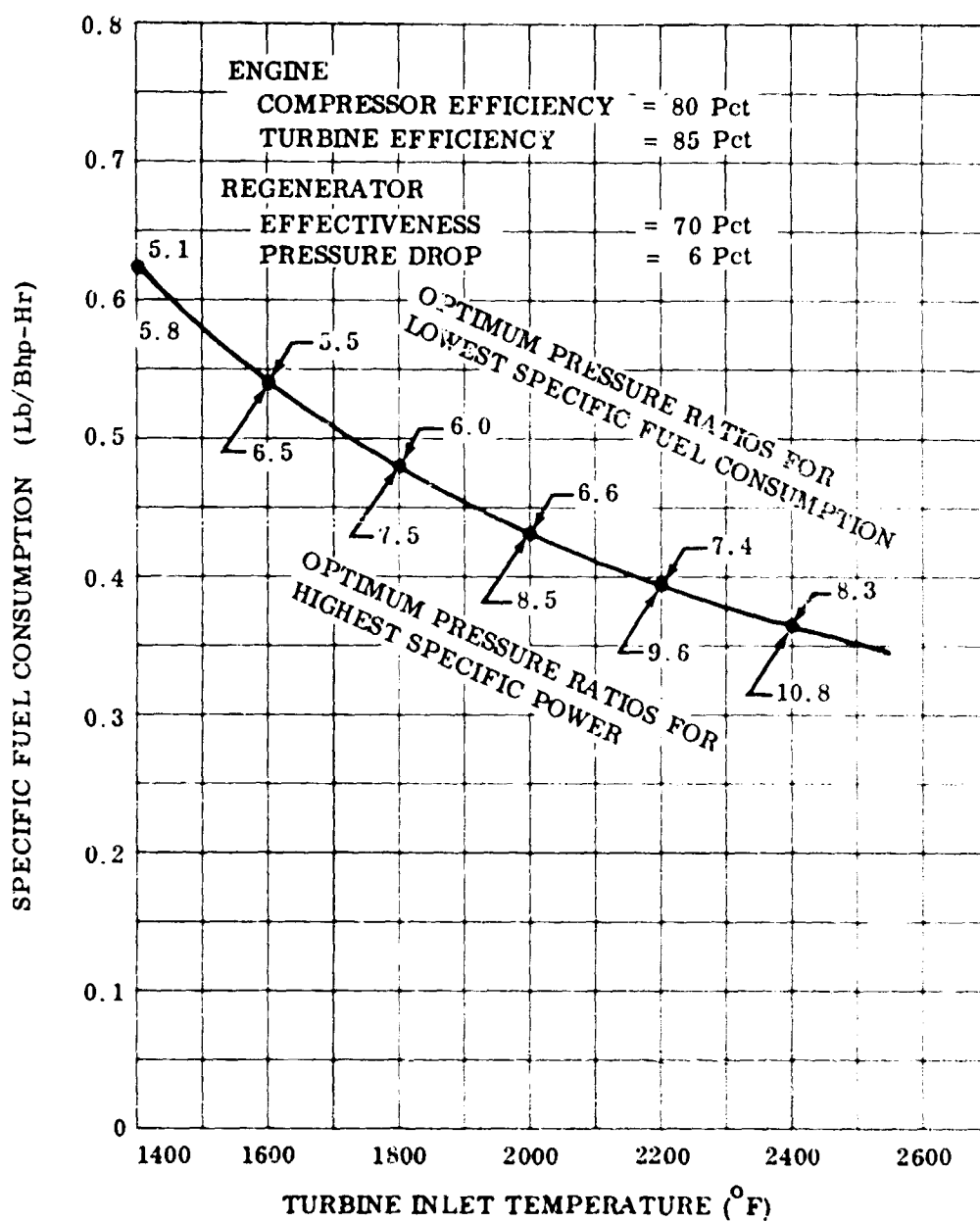
Figure 6. Ultimate Specific Fuel Consumption Performance.
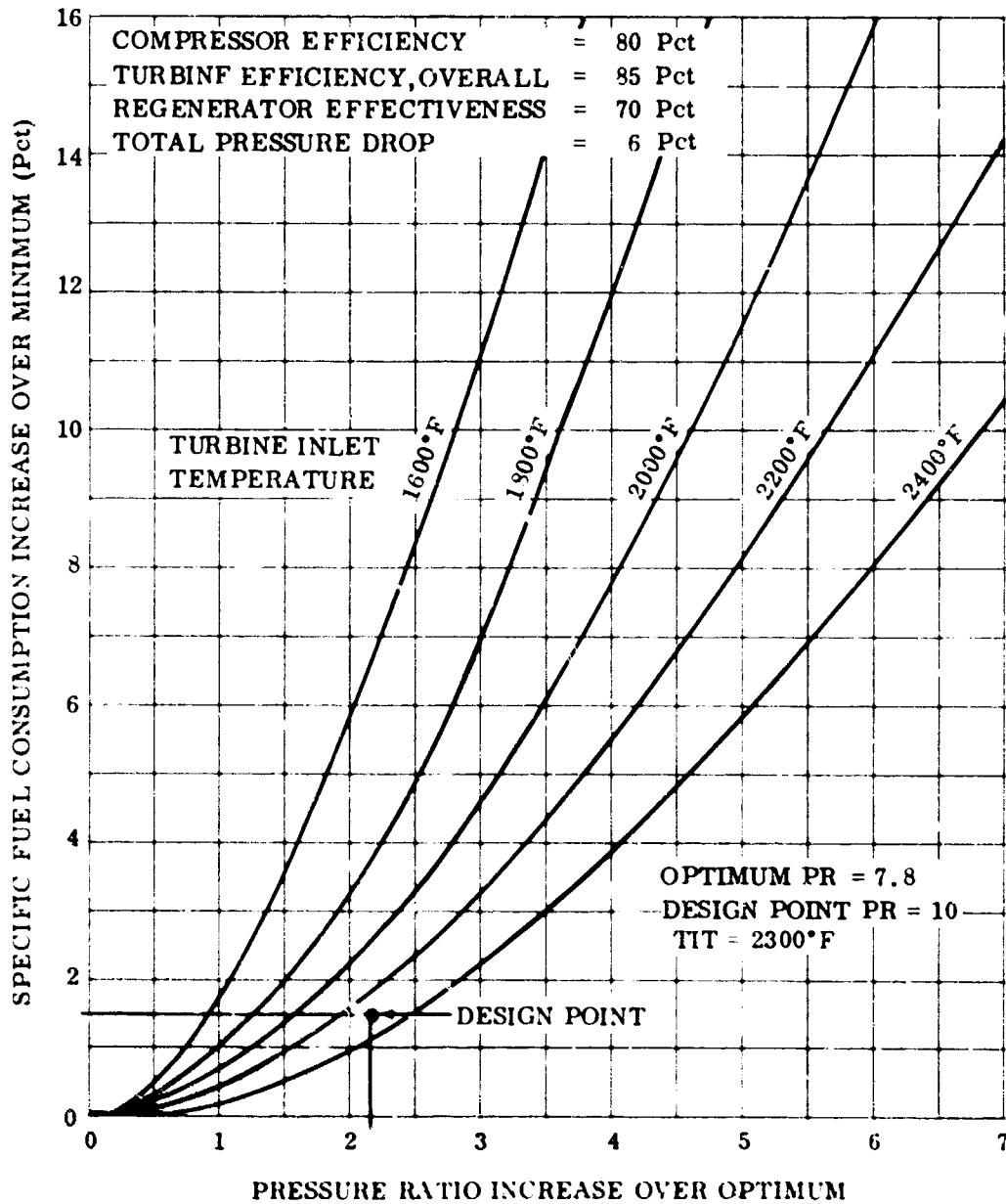
Figure 7. Specific Fuel Consumption Increase for Off-Optimum Compression Ratio.

2300°F, the difference is small and in the order of 1.5 percent of the minimum, or approximately 0.006 pound per brake horsepower-hour. Pressure ratio deviations have a much more pronounced effect at lower turbine inlet temperatures.

To obtain a 0.38 pound per brake horsepower-hour specific fuel consumption with a turbine inlet temperature of 2300°F and a pressure ratio of 10:1, a regenerator with an effectiveness in the 65- to 73-percent range and a pressure drop in the 3- to 10-percent range is required, as illustrated in Figure 8. Low pressure drop is desirable because of its influence on maximizing specific power and producing the smallest and lightest engine and regenerator. On the other hand, compact, lightweight regenerators are obtained by using high-density core surfaces with small passage sizes, which, in turn, tend to increase pressure drop. By analyzing surfaces of varying compactness, the final selection of a regenerator with 70-percent effectiveness and 6-percent total pressure drop was made, representing a desirable balance of size, weight, and performance.

Two types of core construction were evaluated in more detail in preliminary analyses: tubular types and plate-fin types. It was found that while plate-fin type cores could readily meet the performance goals, they did not show the desired low weight, a very essential requirement in Army aviation applications. Figure 9 shows the weight-volume-performance relationships of state-of-the-art plate-fin matrices. The high weight is the result of the fins, which are secondary heat transfer surfaces. They add their full share of weight but have a reduced heat transfer effectiveness because of the long conduction paths along the fins. This consideration led to the conclusion that the way to a compact, lightweight regenerator was the use of a core with all primary heat transfer surface.

Such a core construction is available in the tubular design where each wall has hot gas on one side and cold air on the other. Conventional tubular heat exchangers use tubes of relatively large diameter and correspondingly heavy walls. A study of compactness versus tube diameter was made and the results are shown in Figure 10. There is a hyperbolic dependency of the area density (compactness), and it can be seen that substantial gains are made at tube diameters below 0.25 inch. The constant, C, shown in the figure, depends on tube spacing only. The selection of the exact tube diameter below 0.25 inch is governed by manufacturing and core shape considerations. The smaller the tube diameter, the shorter the tubes will be for a given pressure drop. The effect is twofold: First, the no-flow length has to be increased to maintain the same frontal area and, thus, the same pressure drop in the fluid flowing across the tubes; this effect is shown in Figure 11. Second, the

14
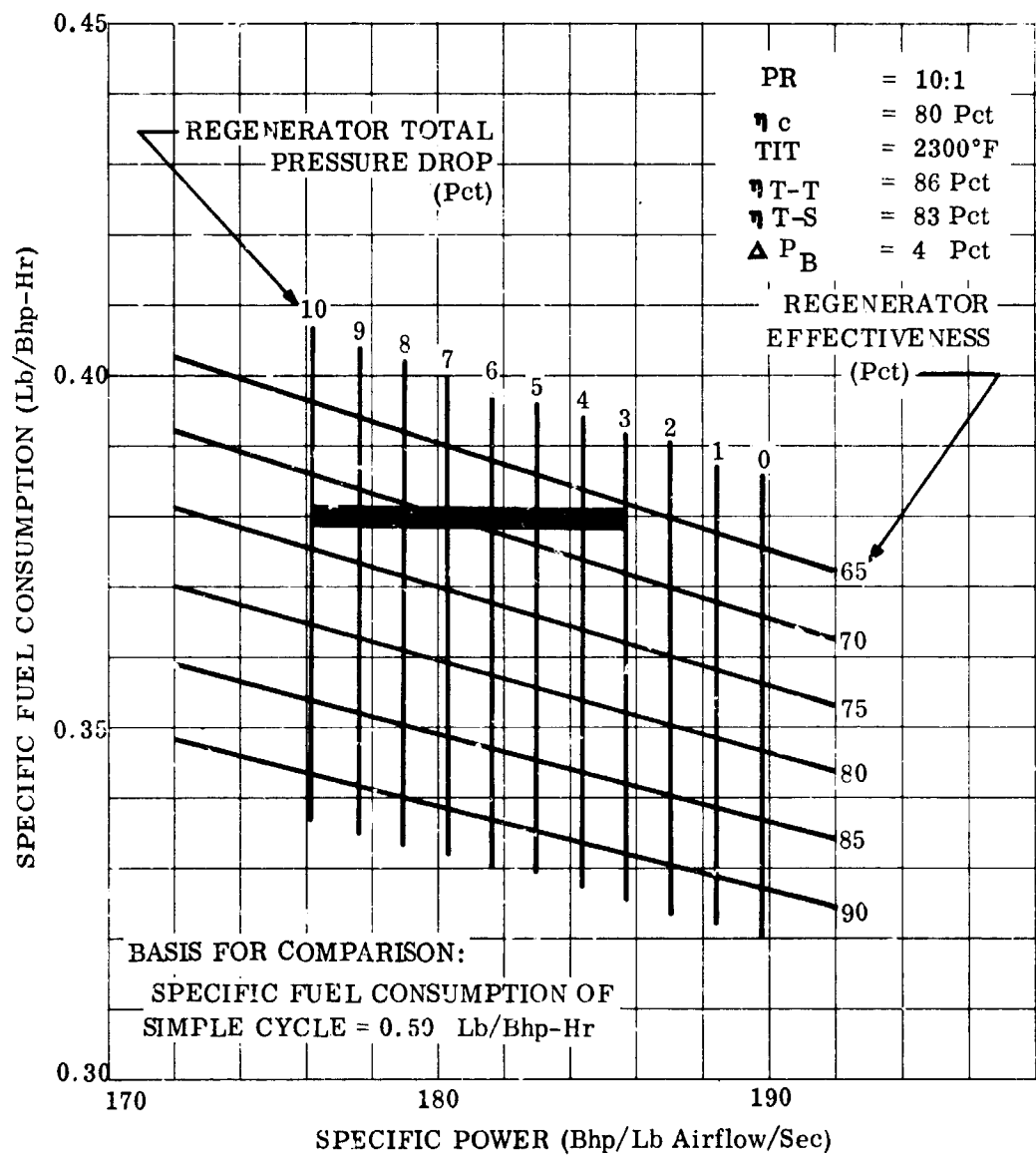
Figure 8. Specific Fuel Consumption and Specific Power
as Function of Regenerator Performance.
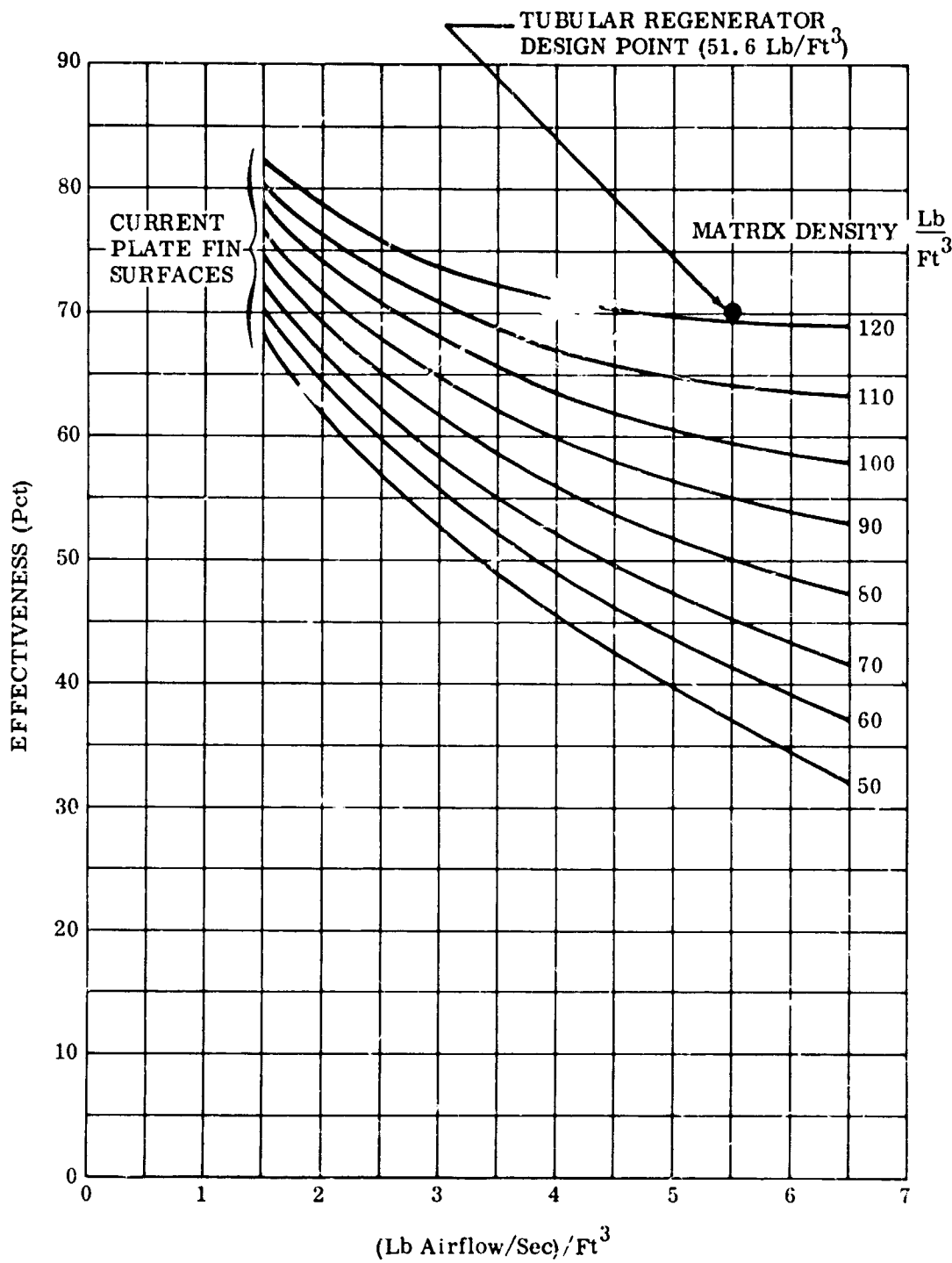
Figure 9. Regenerator Comparison.

16

EFFECT OF MINIATURIZATION

πDL HEAT TRANSFER AREA $4 \pi \dfrac{D}{2} \dfrac{L}{2} = \pi DL$

$\dfrac{\pi D^2}{4}$ FREE FLOW AREA $4 \dfrac{\pi}{4} \left(\dfrac{D}{2} \right) 2 = \dfrac{\pi D^2}{4}$

$D^2 L$,   VOLUME $\left(2 \dfrac{D}{2} \right)^2 \dfrac{L}{2} = \dfrac{D^2 L}{2}$

$a = C \dfrac{1}{D_o}$ $C = 25.2$

$a \ (FT^2/FT^3)$

D_o (In.)
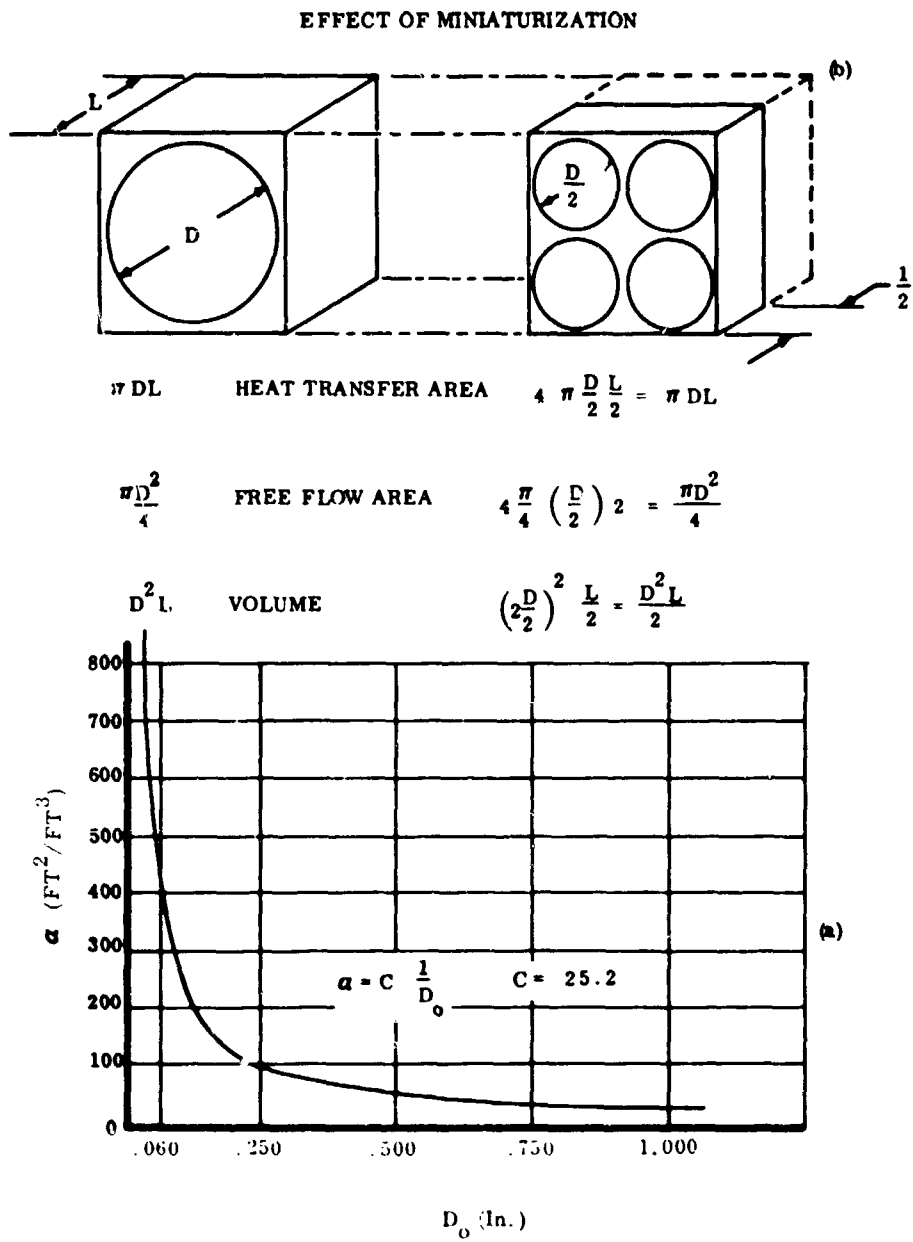
Figure 10. Core Compactness Versus Tube Diameter.

17
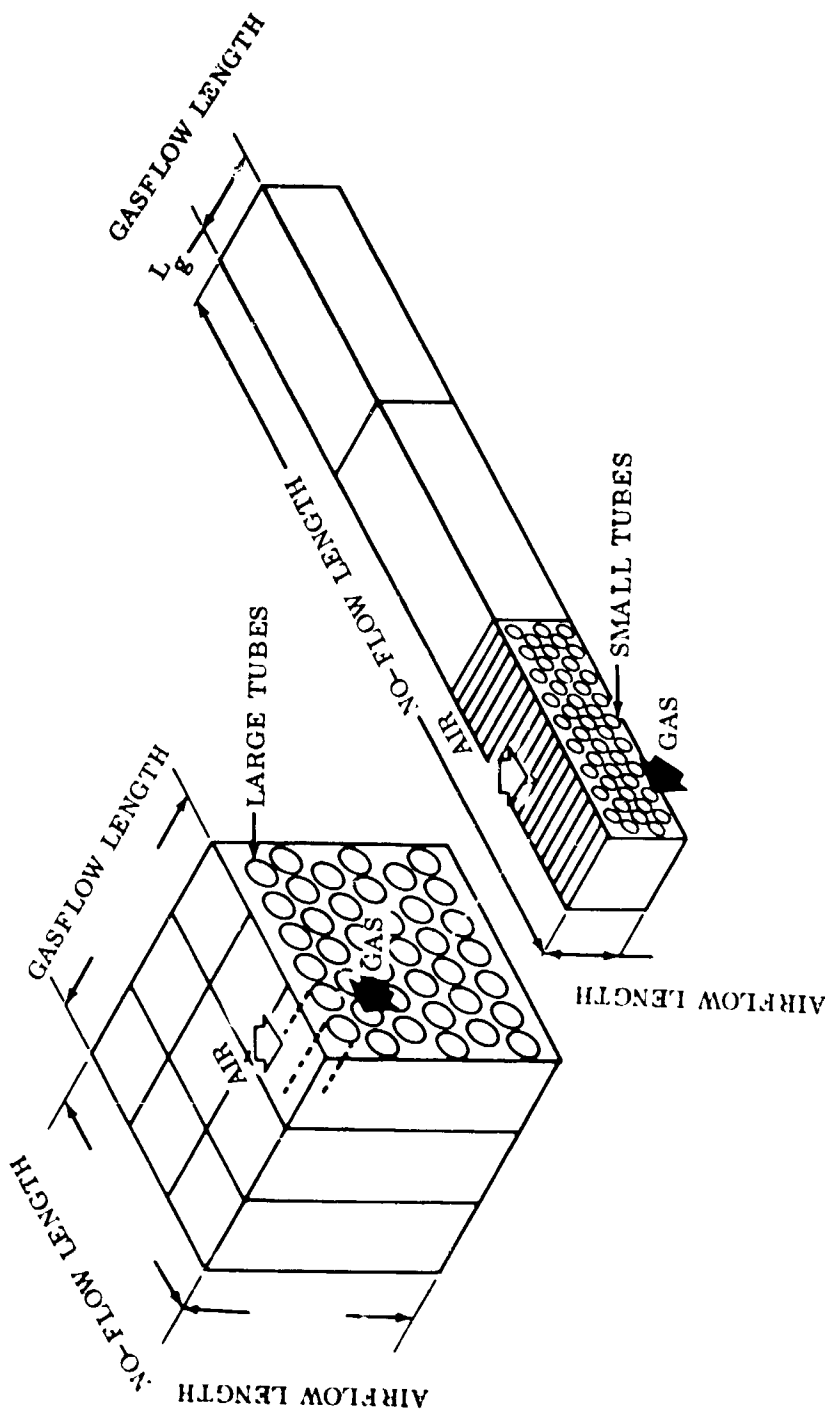
Figure 11. Effect of Tube Diameter on No-Flow Length.

number of tubes increases inversely proportional to the tube diameter, and more pieces need to be formed and assembled. With these factors being taken into consideration, a tube diameter of 0.060 inch was selected for the research program; it was reasoned that this size would lead to the necessary evaluation of the concept from a performance and manufacturing viewpoint.

State-of-the-art tubular regenerators are customarily built by inserting and brazing the individual tubes into drilled header sheets. This method of assembly becomes impractical with the large number of small tubes resulting from the compactness requirement. The difficulty is overcome by the Boeing-developed concept where the tube ends are expanded into a rectangular or hexagonal shape, these ends being brazed to form an integral header after assembly. This concept holds the promise for fully automated manufacturing, which would enhance the economic advantage of the regenerated engine. The application of the concept is illustrated in Figure 12. Subdividing the core into individual cores or modules facilitates the handling of thermal stresses, provides flexibility in design, and allows the individual replacement of damaged cores.
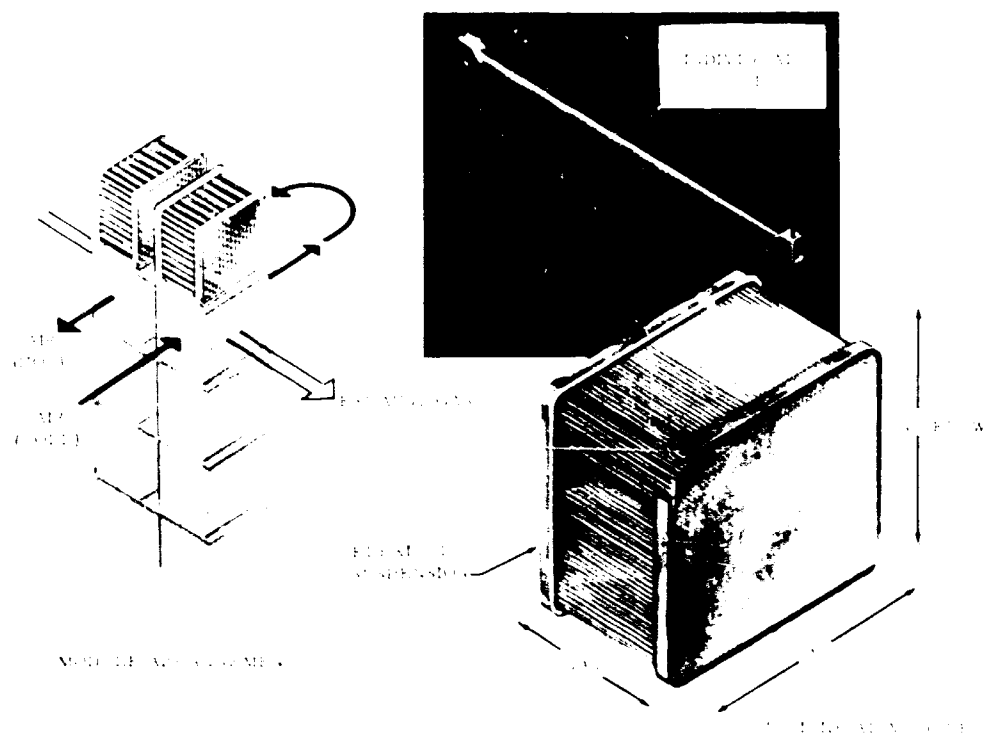
Figure 12. Boeing Small-Diameter Tubular
Regenerator Concept.

The design goals developed from the study of all the aspects presented above are detailed below:

Engine Application: 2300°F turbine inlet temperature
10:1 pressure ratio

Regenerator:

	Tubular core	
	Tube diameter	0.060 In.
	Area density	420 Ft^2/Ft^3
	Effectiveness	70 Pct
	Total pressure drop	6 Pct
	Core specific volume	0.2 Ft^3/Lb Airflow/Sec
	Core specific weight	10 Lb/Lb Airflow/Sec
	Maximum working pressure (air)	150 Psia
	Maximum temperature during transients	1800°F
	Maximum steady-state gas temperature	1350°F
	Specific regenerator weight (including core, manifolds, ducts and structure)	20 Lb/Lb Airflow/Sec
	Leakage	0 Pct

ANALYTICAL STUDIES

This portion of the program included the mathematical investigations necessary to support the design. Analytical work was aimed at defining a regenerator that would be compatible with a gas turbine engine having a 2300°F turbine inlet temperature and a 10:1 compressor pressure ratio. The characteristics of the engine cycle used as a model are shown in Table I.

TABLE I
ENGINE CHARACTERISTICS

Turbine Inlet Temperature, TIT	2300°F
Compressor Pressure Ratio, PR	10:1
Compressor Discharge Pressure	147 Psia
Compressor Discharge Temperature	650°F
Turbine Discharge Temperature	1316°F
Regenerator Gas Side Discharge Pressure	14.7 Psia
Compressor Efficiency, η_c	80 Pct
Gas Producer Turbine Efficiency, η_{gpt} (total-to-total)	86 Pct
Power Turbine Efficiency, η_{pt} (total-to-static)	83 Pct
Burner Efficiency, η_B	98 Pct

The analytical studies included the following:

- Effects of regeneration on engine performance

- Regenerator performance

- Stress studies

EFFECTS OF REGENERATION ON ENGINE PERFORMANCE

When a fixed-matrix regenerator is installed on a gas turbine engine, there are two parameters which affect the engine's performance. These are the effectiveness, ϵ, and the total pressure drop, $\Delta P/P$.

The effectiveness is defined as:

$$\epsilon = \frac{T \text{ air out} - T \text{ air in}}{T \text{ gas in} - T \text{ air in}}$$

It essentially represents the ratio of the actual heat transferred to the maximum possible heat which could be transferred in a true counterflow heat exchanger of infinite size.

For practical purposes, when the pressure drops of the fluids on the air and gas sides of a heat exchanger are expressed as percentages, $(\Delta P/P_1)_A$ and $(\Delta P/P_1)_G$, a 1-percent air side pressure drop has the same effect on the thermodynamic cycle as a 1-percent gas side pressure drop. In this regard, the split between the two pressure drops is not important. As a result, analyses in this section are given in terms of total pressure drop when effects of regeneration on engine performance are being studied.

In prior studies, Boeing prepared a cycle analysis computer program to evaluate the performance of regenerated versus simple-cycle engines using various component efficiencies, pressure ratios, and turbine inlet temperatures for values of regenerator effectiveness and total pressure drop. Results of this study, in percent reduction in specific fuel consumption (Δsfc) versus regenerator effectiveness for various total pressure drops, are presented in Figures 13 through 21 for engines with various turbine inlet temperatures and compressor pressure ratios. Figure 22 presents the percent loss in shaft horsepower versus regenerator pressure drop for each of these cycles. Of particular interest to this program are the curves for an engine cycle of 2300°F TIT and 10:1 pressure ratio, which is the model cycle for this study, and the 1800°F, 6:1 cycle, which corresponds to the current level of technology for small gas turbine engines.

22
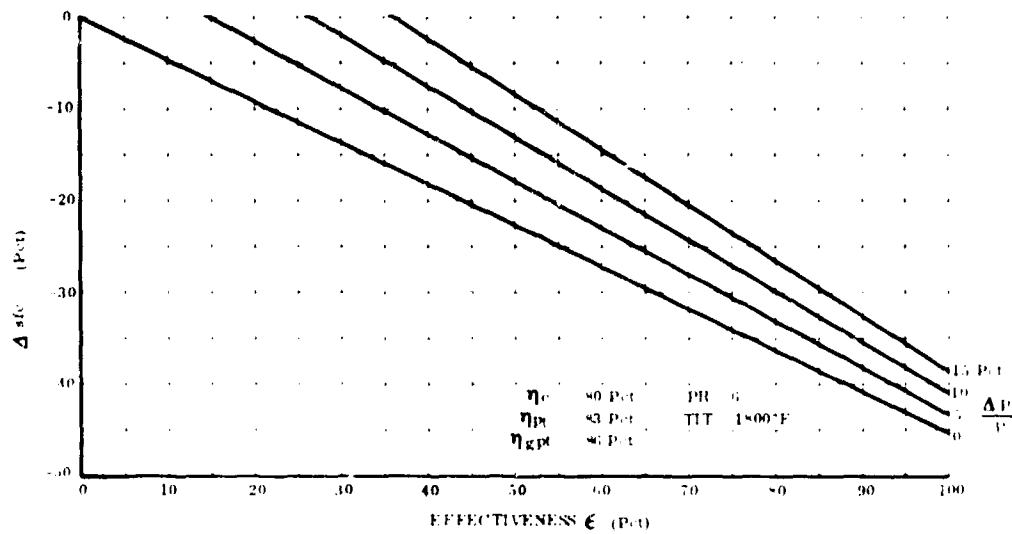
Figure 13. Fuel Flow Change by Adding Regenerator
to Basic Gas Turbine Engine.
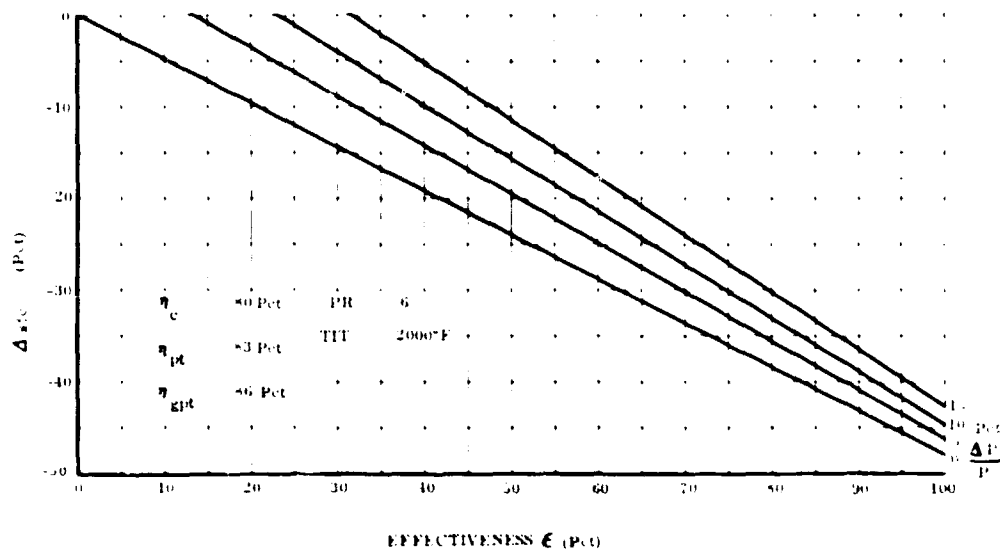
Figure 14. Fuel Flow Change by Adding Regenerator
to Basic Gas Turbine Engine.

23
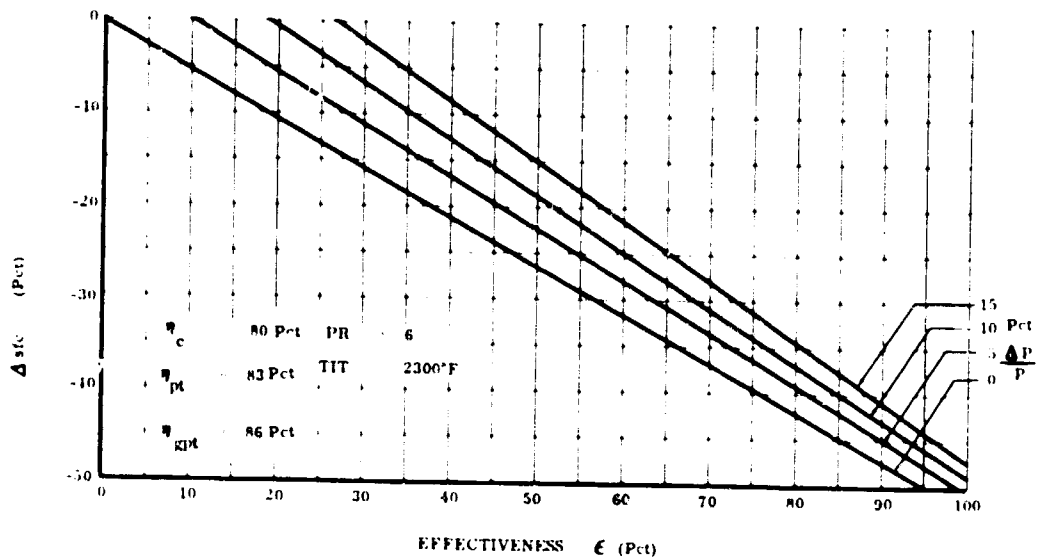
Figure 15.   Fuel Flow Change by Adding Regenerator
to Basic Gas Turbine Engine.
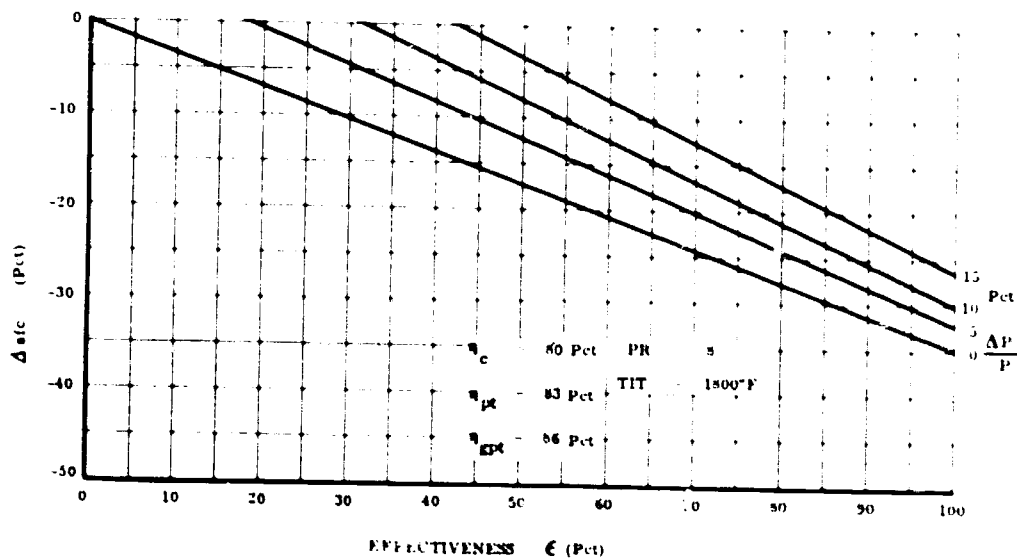
Figure 16.   Fuel Flow Change by Adding Regenerator
to Basic Gas Turbine Engine.

24
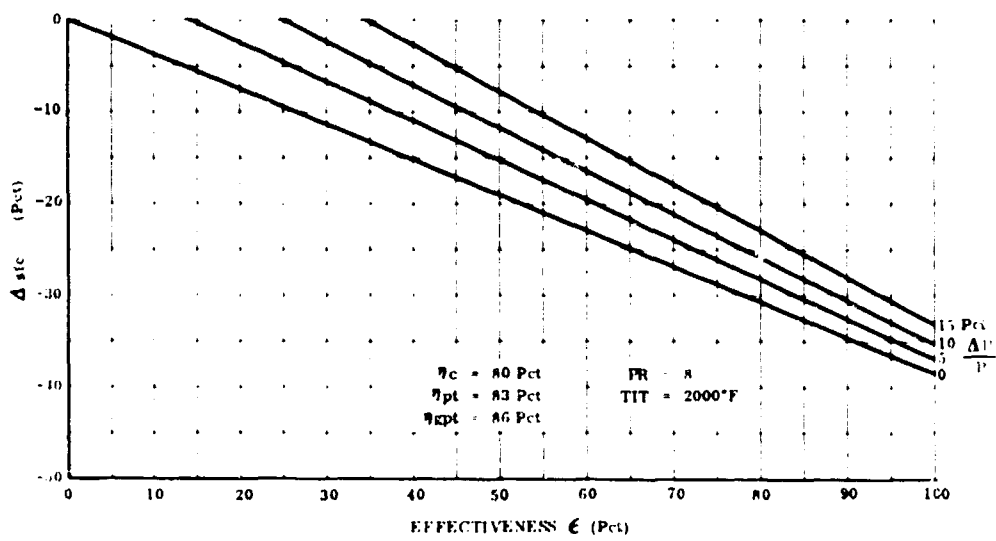
Figure 17.   Fuel Flow Change by Adding Regenerator
to Basic Gas Turbine Engine.
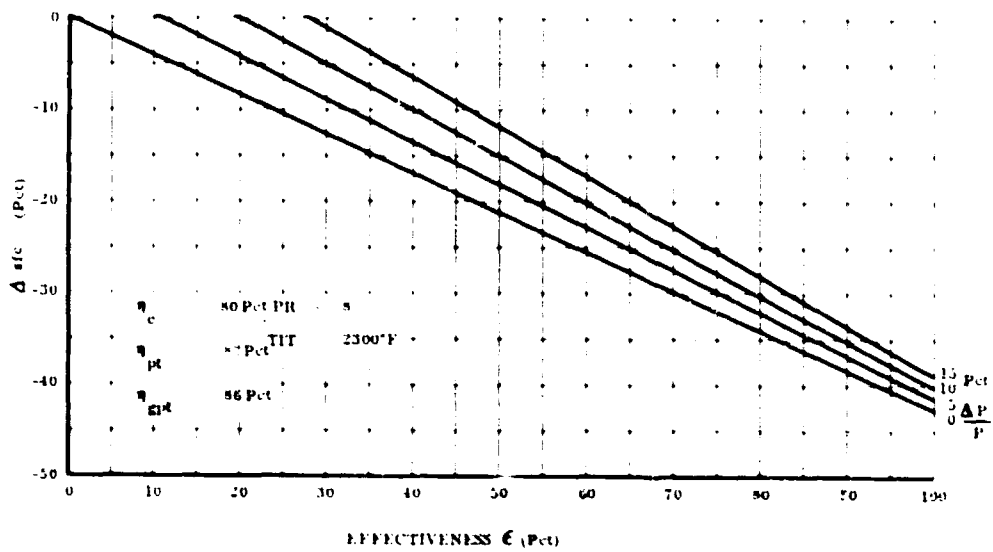
Figure 18.   Fuel Flow Change by Adding Regenerator
to Basic Gas Turbine Engine.
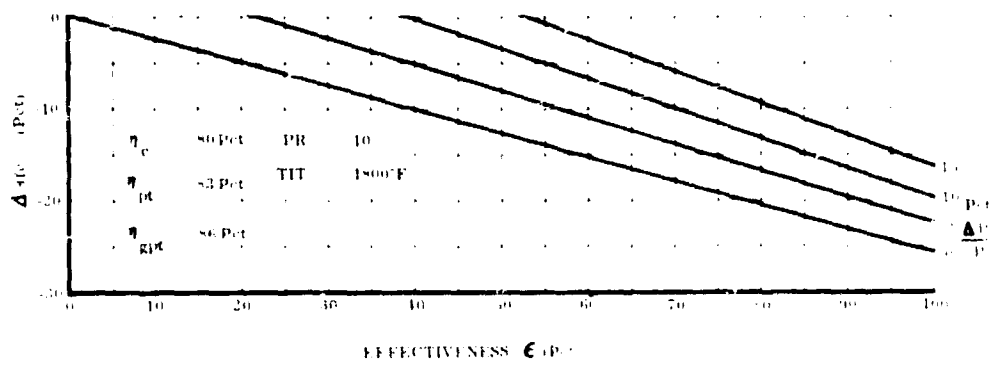
Figure 19. Fuel Flow Change by Adding Regenerator
to Basic Gas Turbine Engine.
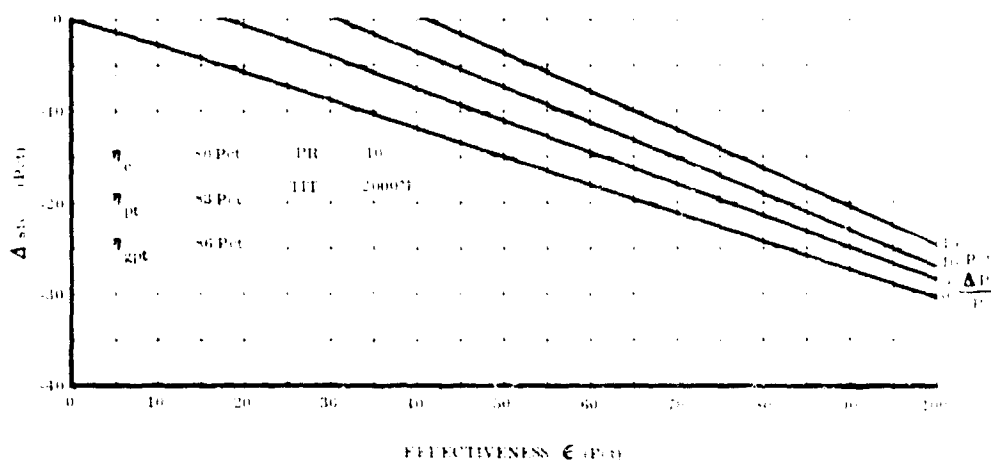
Figure 20. Fuel Flow Change by Adding Regenerator
to Basic Gas Turbine Engine.
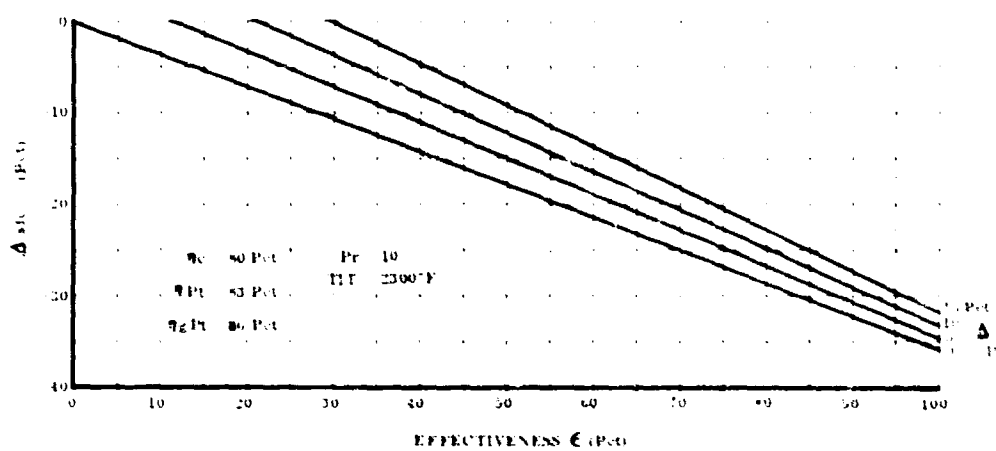
Figure 21. Fuel Flow Change by Adding Regenerator
to Basic Gas Turbine Engine.

26
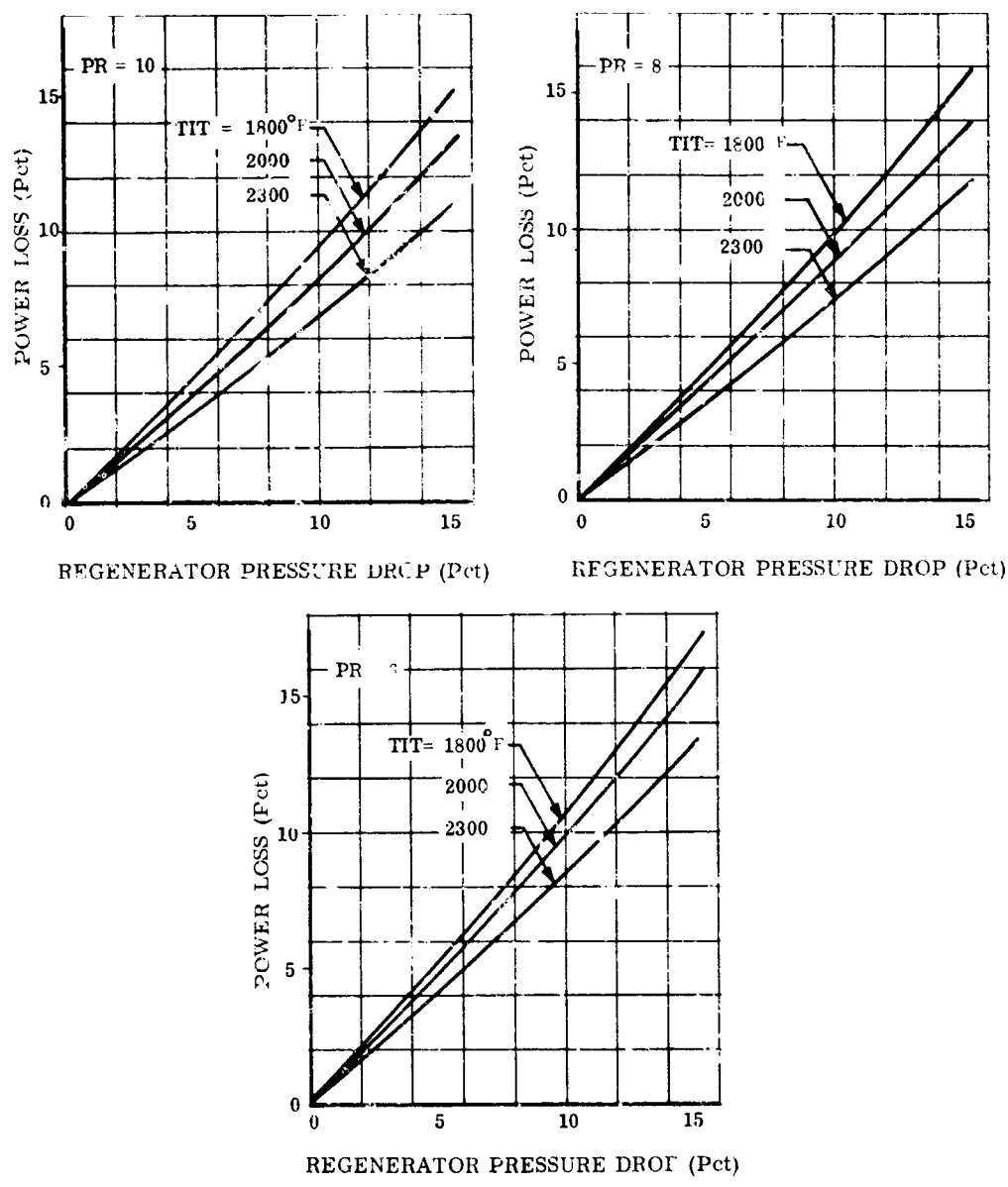
Figure 22. Engine Power Loss Versus Regenerator
Pressure Drop.

REGENERATOR PERFORMANCE

Selection of Optimum Core Geometry

Optimum geometry, from the standpoint of performance, is that geometry which achieves a desired engine specific fuel consumption with a minimum of heat exchanger volume, weight, and total pressure drop. An optimum cross-flow, fixed-matrix regenerator has minimum volume and minimum total pressure drop with the same geometry. For studying the relationships between geometric and performance parameters, a digital computer program was prepared, making it possible to predict the optimum core dimensions of tubular regenerators. For a fixed core design (tube diameter, spacing, etc.) and fixed fluid condit. ns, this program predicts regenerator effectiveness, total pressure drop and optimum air and gas flow lengths as functions of specific no-flow length. With the program, a map of regenerator performance was generated. This map, shown in Figure 23, indicates that the design goals of 70-percent effectiveness and 6-percent pressure drop can be achieved with a two-pass, cross-counterflow core having a 21.5-inch specific no-flow length, 4.2-inch airflow length and a 1.5-inch gas-flow length. To determine the necessary tube length, 0.15 inch should be added to the 1.50-inch gas-flow dimension to account for the expanded ends (as should be done to all gas-flow lengths presented). The resulting volume of this regenerator is 0.175 cubic foot per pound per second of airflow. It should be noted that the optimization presented by Figure 23 gives the minimum no-flow length for a 70-percent effectiveness and a 6-percent pressure drop. Use of larger diameter tubes will shorten the no-flow length; however, the core volume and weight will increase, as shown in Figure 24. A single-pass arrangement with 0.060-inch-diameter tubes would enable the use of a much shorter no-flow length; however, the volume would be substantially larger to obtain the required heat transfer surface, and the thermal s_r ses would be much higher because of more extreme temperature gr _ients. Another way to reduce the specific no-flow length and still obtain the same reduction in specific fuel consumption is to use a regenerator with a higher pressure drop but a compensating higher effectiveness. Figures 25 and 26 present such a trade-off for tubes with 0.054-inch inside diameter and 0.003- and 0.005-inch wall thicknesses, respectively. On both figures, the reduction in engine specific fuel consumption chosen for the example was a constant 22.5 percent. Figure 24 shows that with straight tubes, this reduction in specific fuel consumption can be obtained at a 69-percent effectiveness and a 6-percent pressure drop with a 21-inch no-flow length. Similarly, other points which can be selected, such as 71-percent effectiveness and an 8-percent pressure drop with a 16-inch no-flow length, also reduce sfc 22.5 percent.

$$Ntu = \frac{UA}{W_A \, c_{pA}}$$
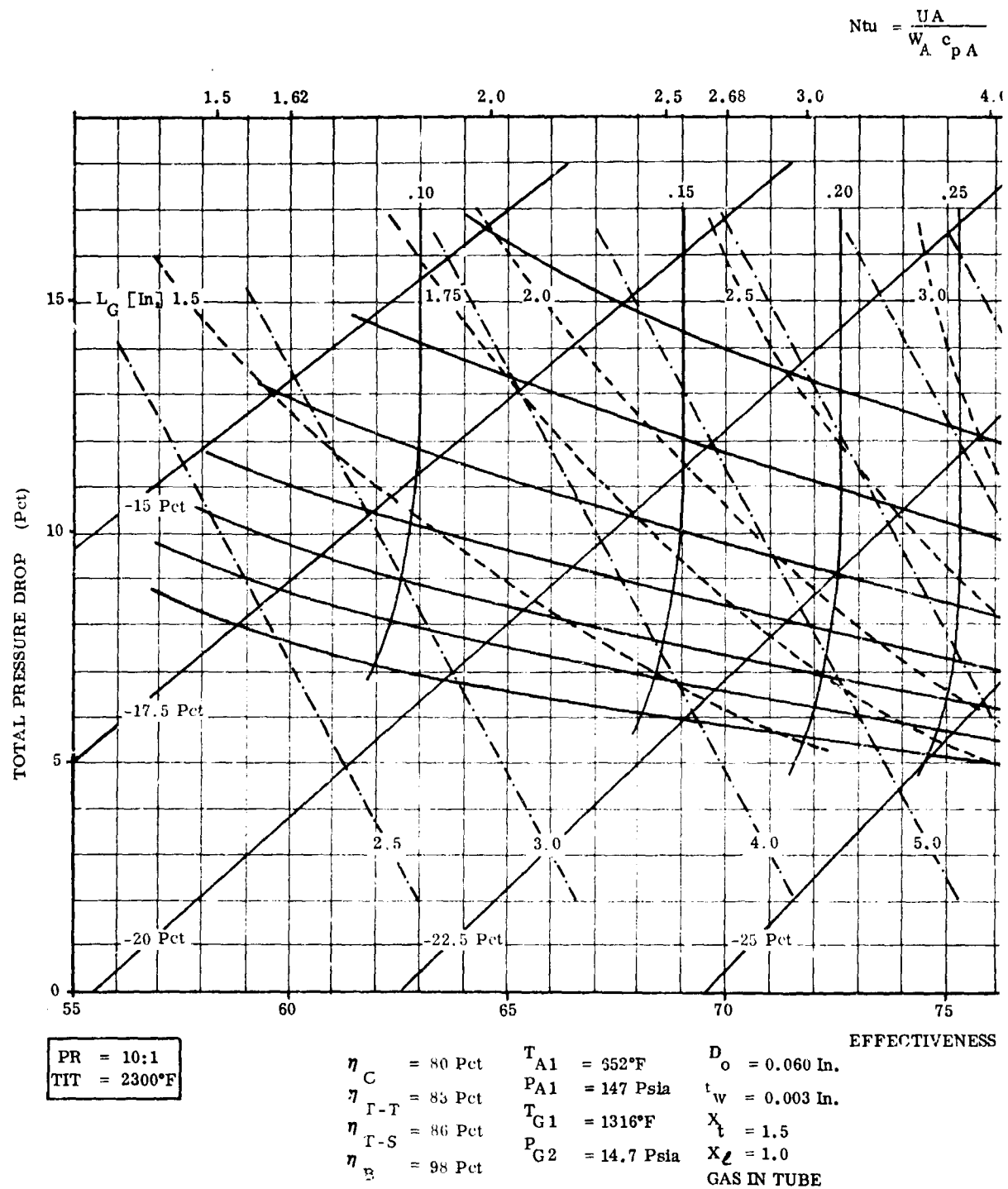
Figure 23. Regenerator Performance Map.

29

A

| 4.0 | 5.0 5.45 6.0 | 7.0 | 8.0 | 10.0 | 20.0 |

.30   .40   .50   .60 .70 V_{spec} $[Ft^3/(Lb/Sec)]$

4.0

L_{NF} In./(Lb/Sec)

10

12

14

16
18
20
22

6.0   7.0   8.0   9.0   10.0   11.0 L_A [In]

-27.5 Pct   -30 Pct   Δ SFC

5   80   85

ENESS ε (Pct)
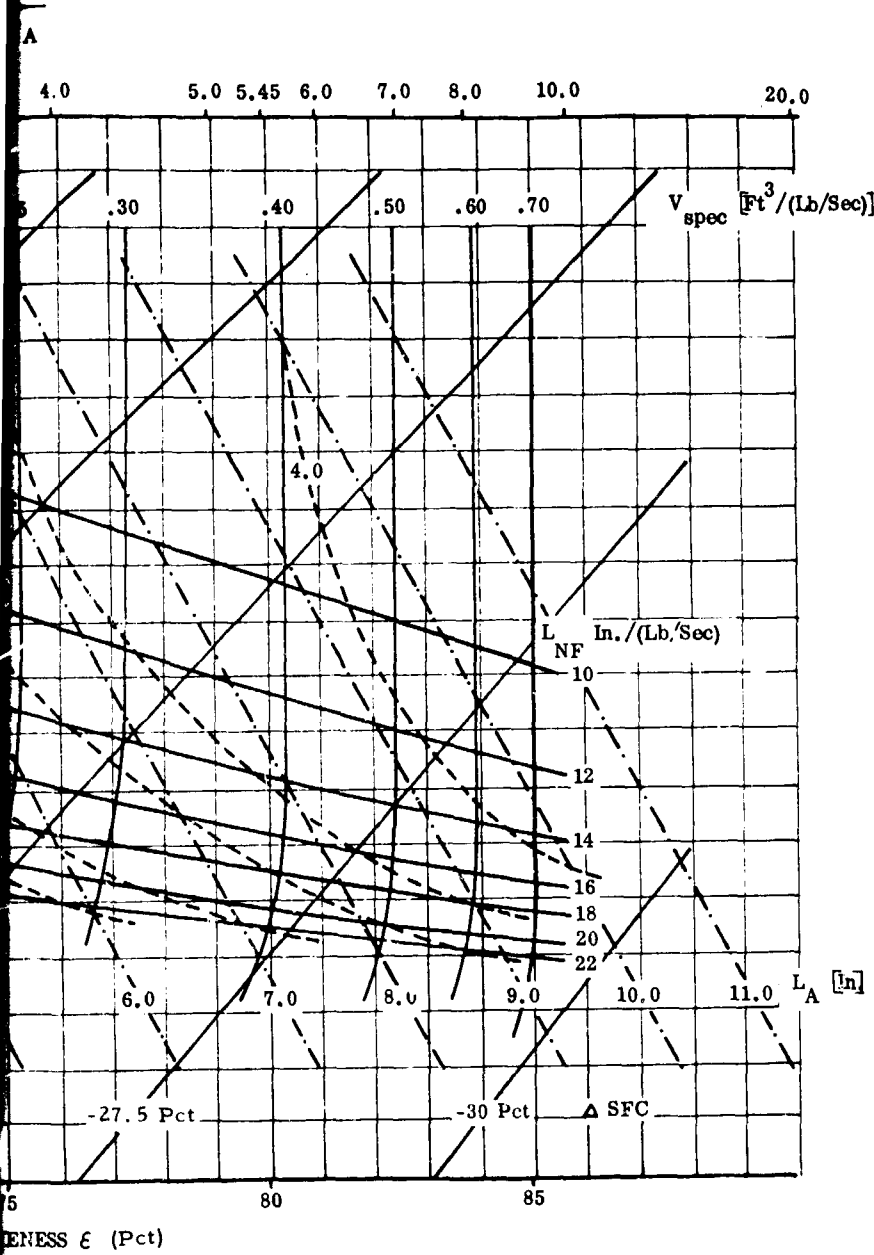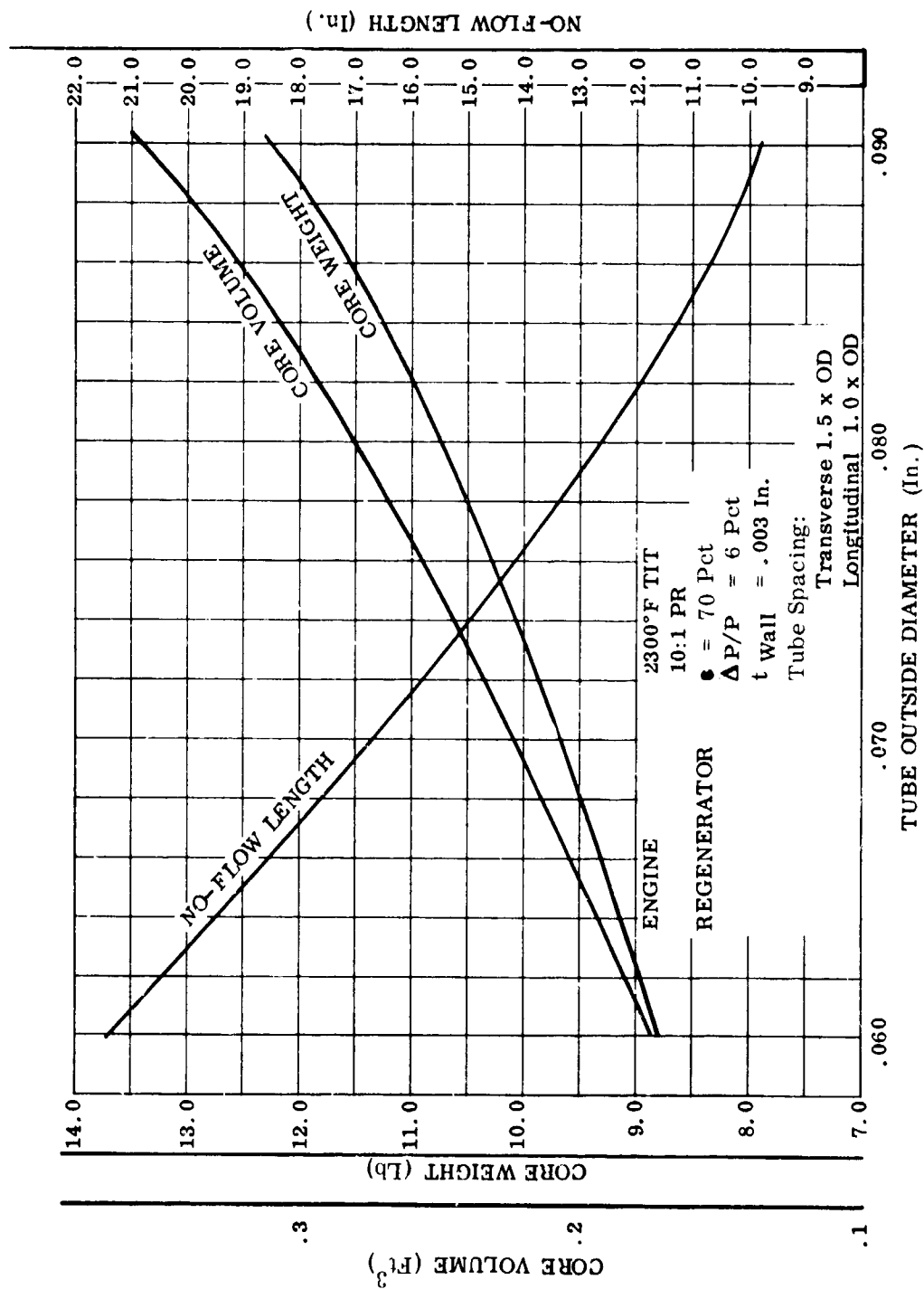
Figure 24. Influence of Tube Diameter On No-Flow Length, Core Volume and Weight (Based on One Lb/Sec Airflow)

31
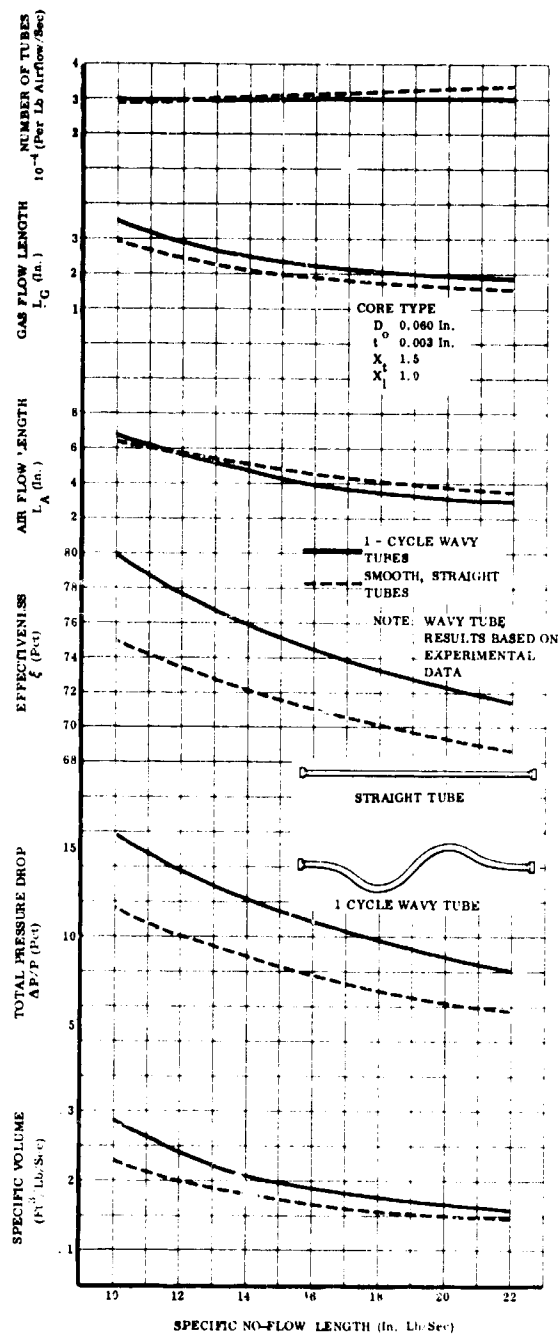
Figure 25. Optimum Regenerator Designs
For Model Engine With 22.5
Percent Reduction of Specific
Fuel Consumption.

32
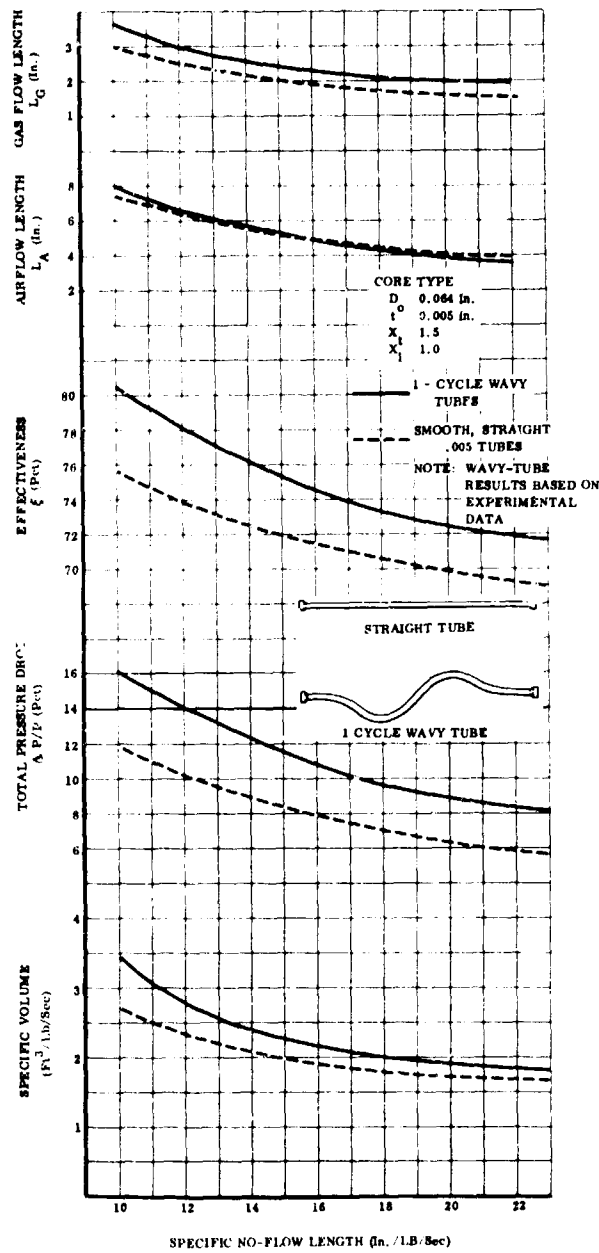
Figure 26. Optimum Regenerator Designs
For Model Engine With 22.5
Percent Reduction of Specific
Fuel Consumption.

33

Figure 27 presents similar results predicted for a Boeing T50 engine with a 25-percent reduction in specific fuel consumption. The straight tube heat transfer and pressure drop data used for all these curves were taken from Reference 1, pages 123 and 127. Figures 25 and 26 include the results of wavy-tube core element tests, which are described later in this report.

Part-Load Performance

As the power output of a gas turbine is reduced, the changes in airflow rate, cycle temperatures, and pressures affect the performance of the regenerator. Table II shows the estimated part-power fluid conditions as determined from prior routine cycle analyses for an engine designed for 2300°F TIT and 10:1 PR at full power. Based on these air and gas conditions, the part-load performance of a regenerator with a full-power effectiveness and pressure drop of 70 percent and 6 percent, respectively, was calculated using the computer program mentioned in the previous section. These results are presented in Figure 28.

TABLE II
PART-LOAD AIR AND GAS CONDITIONS
DESIGN POINT 2300° F, 10:1 PR

Power Level Pct	Compressor Discharge Pressure Psia	Compressor Discharge Temperature °F	Exit Gas Pressure Psia	Exit Gas Temperature °F	Air-flow Pct
100	147	652	14.7	1316	100.0
90	139	635	14.7	1275	96.5
80	132	615	14.7	1235	92.5
70	124	595	14.7	1185	89.0
60	116	570	14.7	1130	84.5
50	107	545	14.7	1070	80.0
40	97	520	14.7	1000	75.0
30	87	485	14.7	915	70.0
15 (idle)	78	415	14.7	750	60.7

34
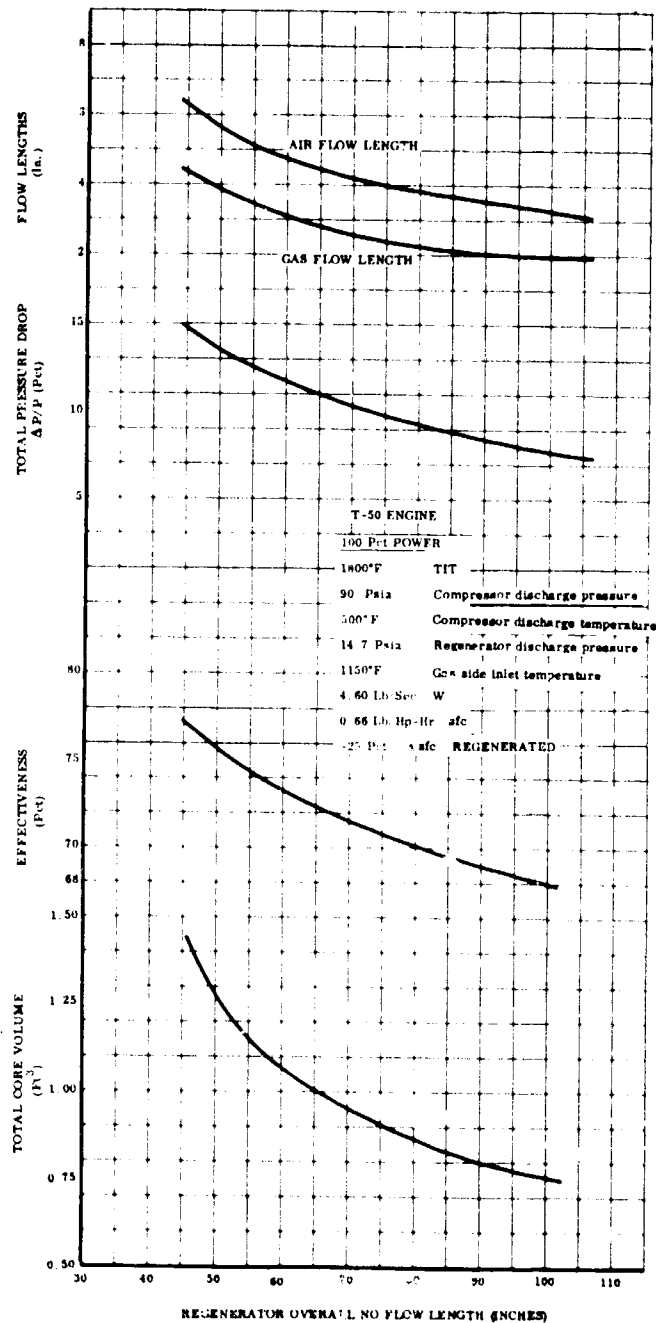
Figure 27. Optimum Regenerator Designs For T50 Engine With 25 Percent Reduction of Specific Fuel Consumption.

35
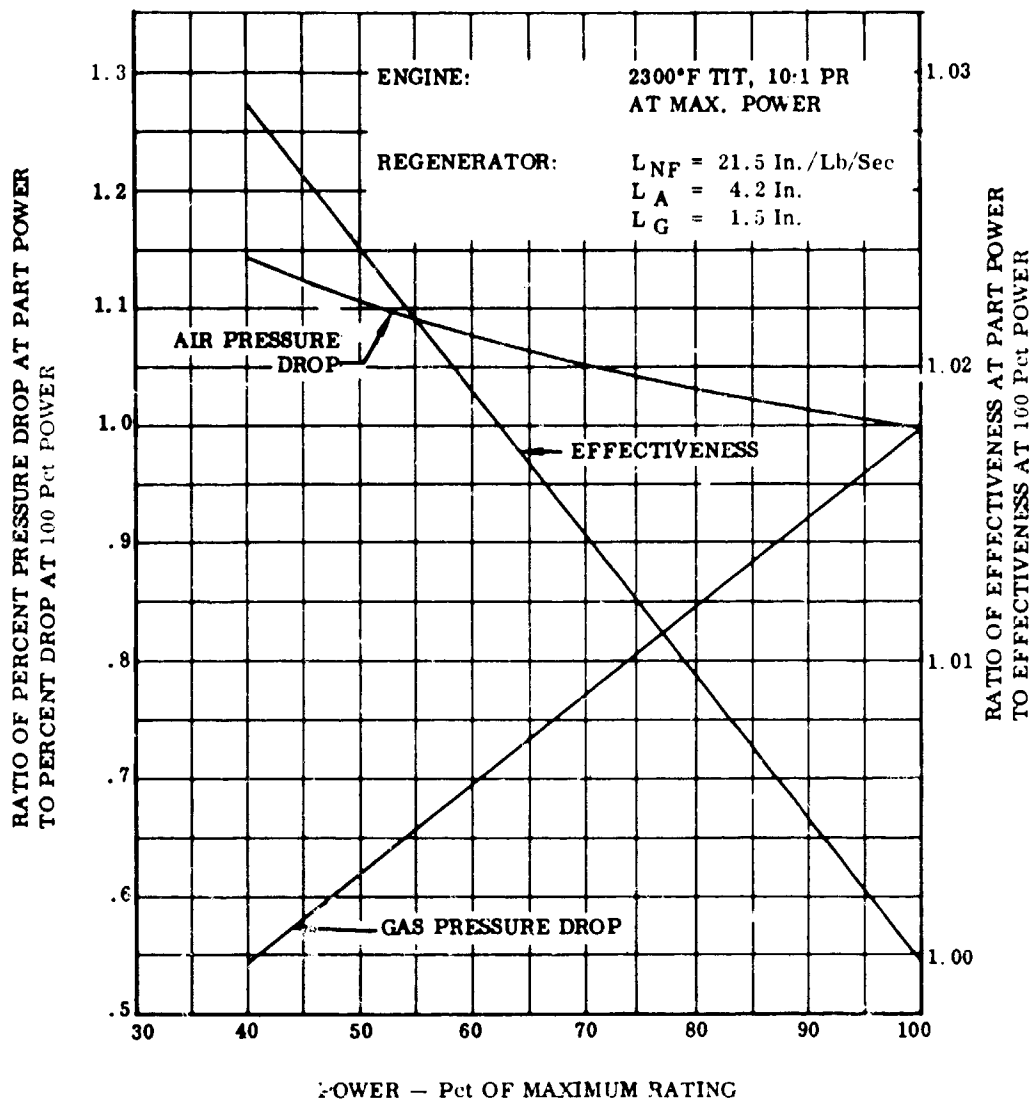
Figure 28.   Regenerator Part-Power Performance.

Wrap-Around Regenerators

In many regenerator designs, it is desirable to package the regenerator cores in a circular or wrap-around arrangement. Figure 29 shows this type of regenerator schematically, and Figure 30 shows schematic layouts of two wrap-around regenerators on a Boeing T50 engine. In the designs shown, the free-flow area of the air stream changes radially because of the wedge-shaped section of the flow path. A computer program, which was developed to evaluate the performance of this type of design, computes performance by dividing the heat exchanger core into many small segments and by calculating the changes in fluid temperatures and pressures as the fluids move from segment to segment. Figure 31 shows the percentage increase in pressure drop of a wrap-around core as the inside radius is decreased. As can be seen, at an inside radius of 5 inches, the pressure drop has increased by a ratio of 1.035:1 over a rectangular core (core with an infinite inside radius). It has been found that virtually no change in the effectiveness is seen as the inside radius is decreased. On this basis, it has been concluded that if the inside radius is greater than 5 inches, box-shaped results can be used, provided that the no-flow length is evaluated as the average of the inside and outside circumference.
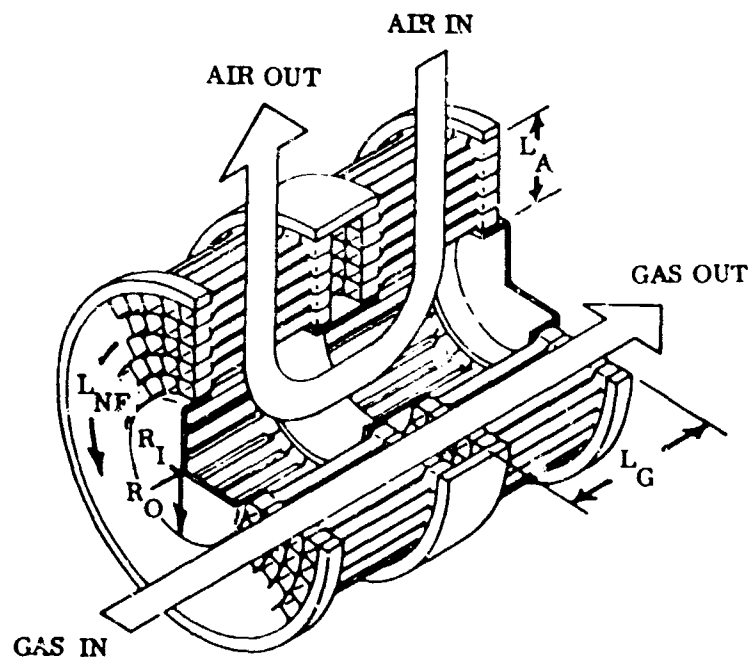
Figure 29. Wrap-Around Regenerator.
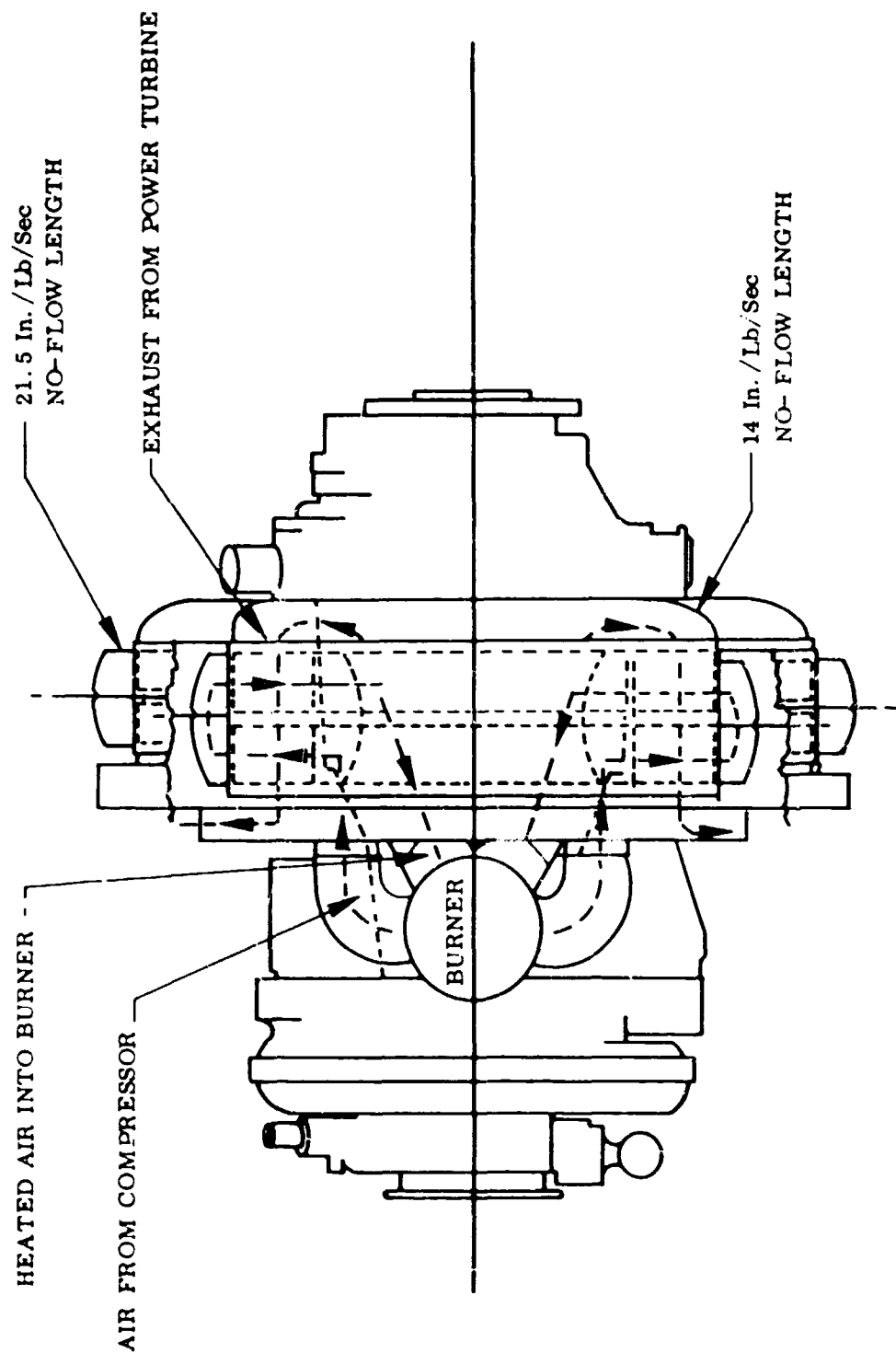
Figure 30. Boeing T50 Engine With Wrap-Around Regenerators.
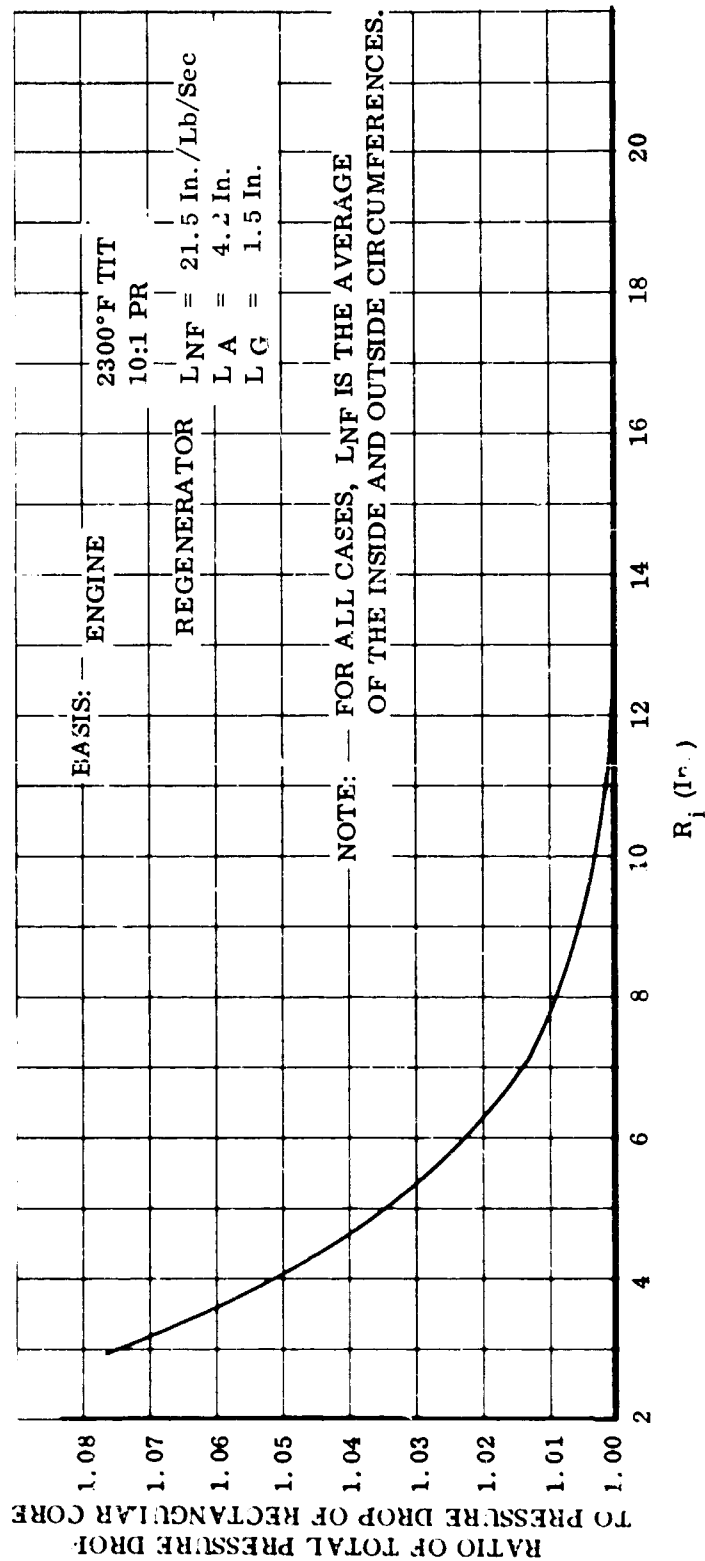
Figure 31. Influence of Inside Radius on Pressure Drop of Wrap-Around Regenerator.

Temperature Profiles at Regenerator Faces

Although the temperature profiles of the fluids are uniform at the inlets of a cross-flow heat exchanger, the profiles are nonuniform at the outlets due to the nature of the heat exchange behavior. The effectiveness of such heat exchangers has reference to the mixed mean inlet and outlet fluid temperatures.

The computer program which was developed to calculate the performance of wrap-around regenerators computes, as part of its procedure, the temperature profiles at the outlets of the regenerator. For single-pass regenerators, the predictions of this program are quite accurate. Figure 32 shows predicted and measured temperature profiles for a single-pass cross-flow regenerator core tested in the thermal shock rig (these tests are discussed later).

Figure 33 shows predicted temperature profiles for a two-pass, cross counterflow design. For two-pass arrangements, analytical techniques assume that each fluid becomes fully mixed between passes so that as each fluid enters the second pass, its temperature profile is uniform. Although the validity of this assumption at first may appear questionable, it has an almost insignificant effect on calculated performance (effectiveness and pressure drop). It can, however, affect the shape of the temperature profiles shown in Figure 33.

Interpass Pressure Loss

In most two-pass, cross-counterflow regenerator installations, it is necessary that one of the interpass connections be a 180 turn. Normally, this turn is taken with the higher density air at low velocity head to minimize pressure losses. As part of this program, an investigation of this loss was made, and based on studies of the literature, a loss of three times the velocity head was assumed as a maximum. To confirm this assumption, a full-size turning duct was built and flow tested. The results of the test are shown in Figure 34 in the form of loss coefficient versus velocity head. As can be seen, the measured losses are only about one-third of the maximum predicted. When these losses are converted into pressure drop for a typical regenerator installed on the model engine (2300°F TIT, 10:1 PR), a value of approximately 0.03 percent results, which then must be added to the core pressure drop.

The conclusion reached is that the turning losses themselves can be made insignificant in magnitude for the actual regenerator; however, it will be necessary that the specific duct be properly designed to ensure correct flow distribution at the inlet to the second pass.
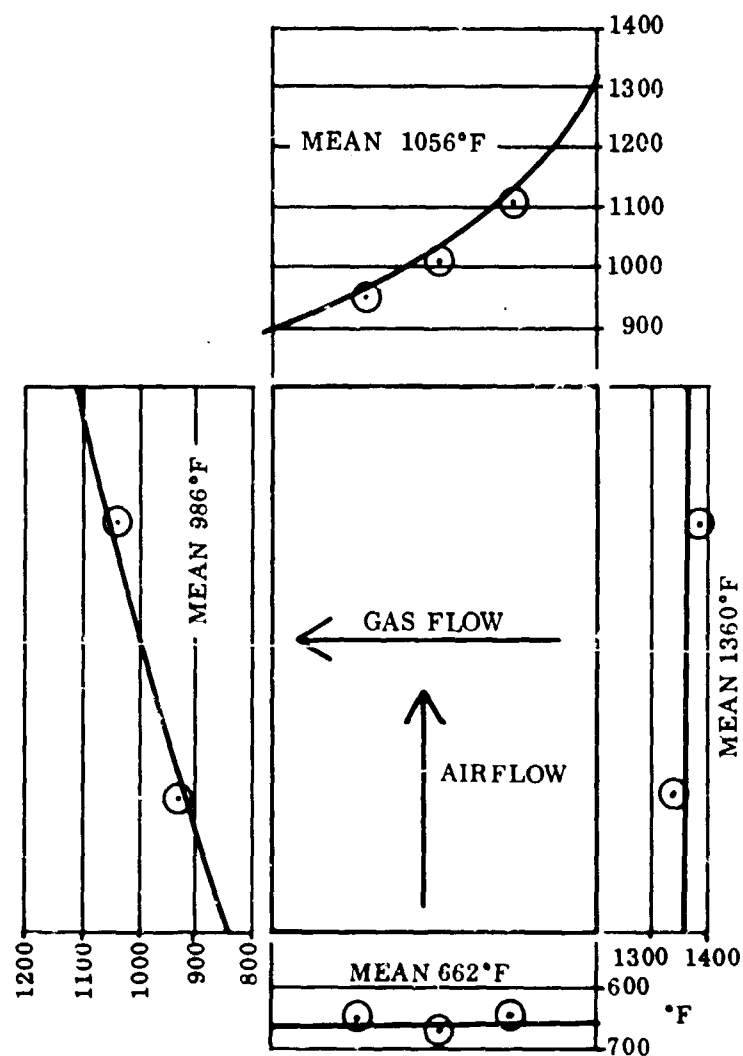
Figure 32. Single-Pass Temperature Profiles
(Test data based on thermal shock rig per-
formance tests on second straight-tube
module.)

41
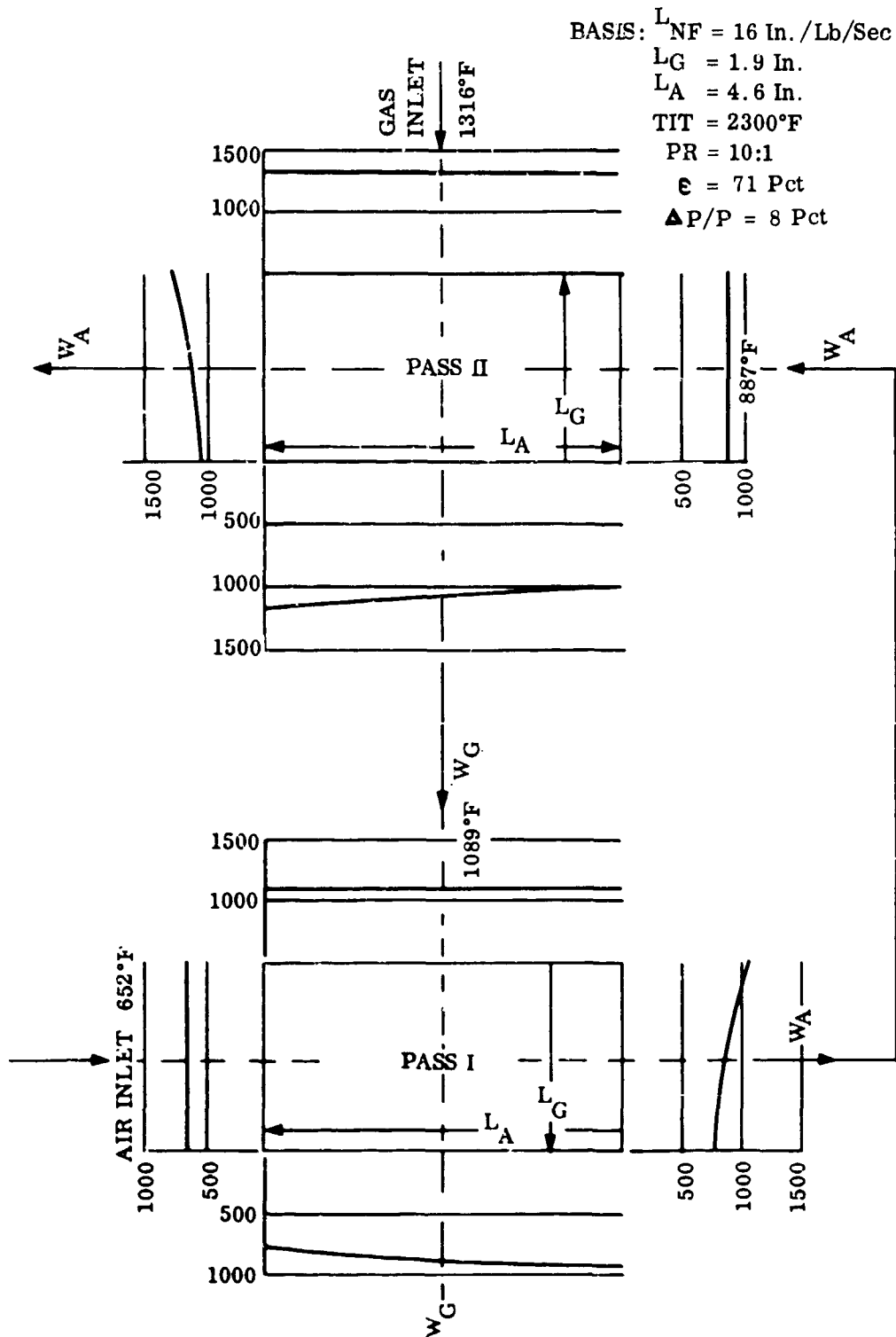
Figure 33. Regenerator Temperature Profiles Assuming Complete Mixing Between Passes.

UNIFORM INLET
PRESS. PROFILE

STATIC & TOTAL
PRESS. TAPS

FLOW STRAIGHTENER

D

FLOW

R

R/D = 0.5

TEST SETUP

TEST GEOMETRY

TOTAL LOSS COEFFICIENT K_T, VS. INLET VELOCITY HEAD

$$\text{VELOCITY HEAD} \quad \frac{\rho V^2}{2g_c} \quad \text{(In. water)}$$
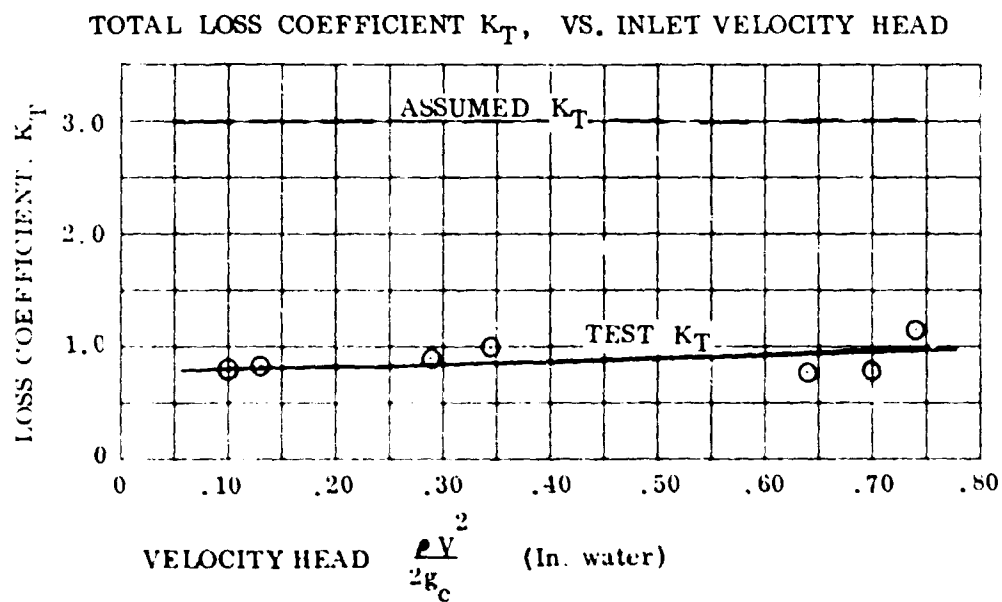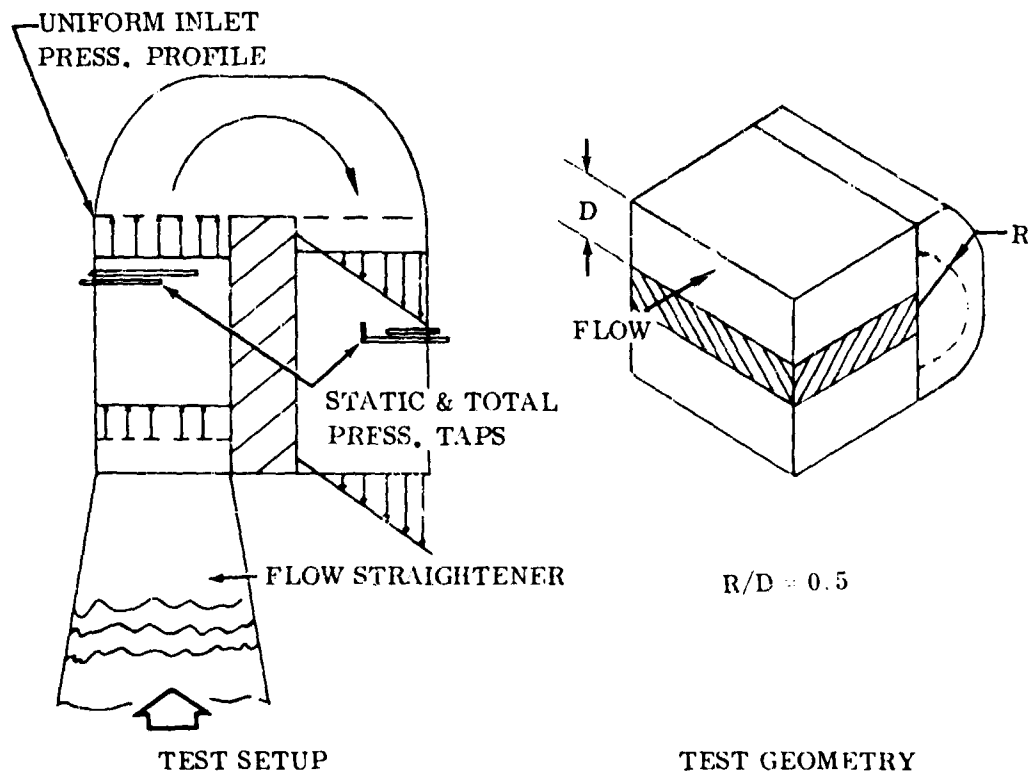
Figure 34. Duct Turning Losses.

43

Selection of Tubular Test Surfaces

It was recognized that flow through the tubes would be laminar and have values of Reynolds number less than 2000, mainly because of the small tube diameter and the necessity to hold the flow rate low enough to give acceptable pressure drops. On the other hand, flow across a tube bundle is turbulent because the fluid flows over a series of unfaired cylindrical shapes. Because of this difference in flow character, the inside heat transfer coefficient is on the order of one-third to one-fourth the coefficient on the outside, and almost all the resistance to heat transfer will occur on the inside surface of the tubes. As a result, worthwhile improvements in performance would be achieved if the inside heat transfer coefficient were increased by turbulence promotion. To achieve the improvement, consideration was given to surface modifications which would produce inside turbulence. In addition, tubular surface modifications which tended to reduce thermal stresses were of interest.

A literature survey was undertaken to help select various tubular surface modifications which might show performance advantages over smooth, straight tubes. The results of this survey are shown in Figure 35 as $\Delta P / \Delta P_{smooth}$ versus h/h_{smooth}, and designs which showed worthwhile increases in heat transfer capability without undue increases in pressure drop were identified. This survey indicated that crosswise dimples and spiral strips which produce a vortex-type flow were the most promising and led to selection of the ring-dimpled and spiral-dimpled tubes as test items. These tubes, along with the others which were initially selected, are pictured in Figure 36.

Analysis, details of which are presented in Appendix I, indicated that performance of straight, smooth tubes would be improved if the tubes were bent into a wave shape. This analysis was supported by the performance data of a wavy-fin, plate-fin surface given in Reference 1, page 215. In addition, wavy tubes are springy when subjected to an axial load, and lower stresses result, since force interactions between adjacent tubes are less than for straight tubes (discussed under STRESS STUDIES). The first wavy tube had the form of a 1-1/2-cycle wave.

The ring-expanded tube also was considered for its potential stress-relieving characteristics. Later, this design was discarded because of anticipated manufacturing difficulties.

Studies detailed in Appendix I showed that surface roughness would have little effect at laminar Reynolds numbers (less than 2000) unless the roughness was at least one-tenth the tube diameter. Therefore, the tubes tested had surface roughness between one-tenth and one-fifth of the tube inside diameter.
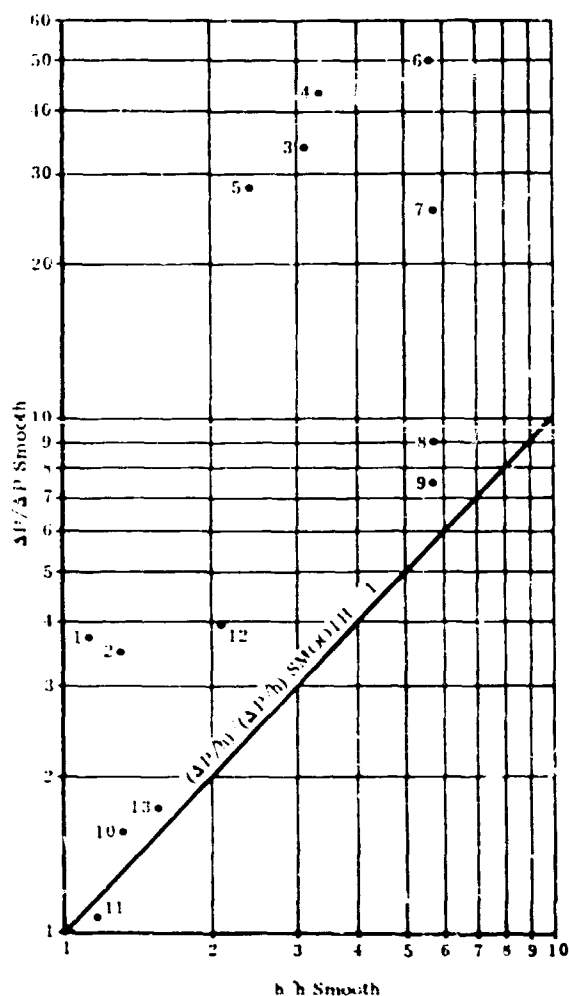
Configuration
Number — Description

1	7" Pitch Spiral Strip in 2 5/8" Tube
2	2 1/4" Pitch Spiral Strip in 2 5/8" Tube
3	3" Pitch Spiral in 2 5/8" Tube
4	Propeller Shaped Baffle in 2 5/8" Tube
5	Wire Spiral in 2 5/8" Tube
6	3/4" Pellets in 3" Tube
7	9/16" Pebbles in 3" Tube
8	0.5" Balls in 3" Tube
9	1" Balls in 3" Tube
10	2.5" diam twist Spiral Strip in 0.5" Tube
11	1.0 and 7.0 diam twist Spiral Strip in 0.5" Tube
12	Flattened - Dimpled Tube
13	Flattened - Dimpled Tube Ratioed to Single, Flattened Tube to Evaluate Effects of Dimples

References

1. Allan P. Colburn and W. Julian King, Relationship Between Heat Transfer and Pressure Drop, Industrial and Engineering Chemistry, Aug. 1931

2. Thomas H. Chilton and Allan P. Colburn, Pressure Drop in Packed Tubes, Industrial and Engineering Chemistry, Aug. 1941

3. Frank Kreith and David Margolis, Heat Transfer and Friction in Turbulent Vortex Flow, Applied Sciences Research, Section A, Vol. 8

4. W. H. Green and L. S. King, The Influence of Tube Shape on Heat Transfer in Air to Air Heat Exchangers, A.S.M.E. Transactions, Feb. 1946

Figure 35. Summary Of The Effects Of Turbulence-Promoting Devices Inside Tubes.
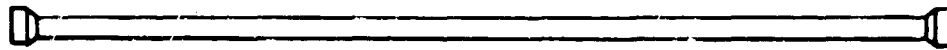
SMOOTH TUBE
$L/D_i = 50$

RING DIMPLED TUBE
$L/D_i = 50$, DIMPLE: SPACING 2.5 D_i, DEPTH .095 D_i

SPIRAL DIMPLED TUBE
$L/D_i = 50$, DIMPLE: SPACING 2.4 D_i, DEPTH .095 D_i

1-1/2-CYCLE WAVY TUBE
$L/D_i = 52$ $r/R = 9.6$

RING EXPANDED TUBE
$L/D_i = 50$, RINGS: SPACING 4.75 D_i, DIAMETER 1.75 D_i

Figure 36. Modified Tubular Surfaces.

The use of 0.060-inch-diameter tubes, flattened to an elliptical cross-section to reduce the pressure drop in flow across tube banks, also was considered; however, while the external pressure drop could be decreased in this way, the interior pressure drop increased sufficiently to nullify any gains. As a result, it was concluded that this approach would be of little value.

Module Metal Temperatures

To evaluate the steady-state thermal stress in the regenerator cores, it is necessary that the temperature of the core elements be known. The program that was developed to evaluate the performance of wrap-around regenerators also calculates the temperatures of the tube walls at points throughout the modules. The basis of this calculation is shown in Appendix II. Figure 37 shows some representative metal temperatures in both passes of a regenerator for the model engine (2300 F TIT, 10:1 PR). The program calculates temperatures only in regions where the tube is heated by gas on the inside and cooled by air on the outside. The region in the vicinity of the expanded ends presents a more complex situation in that expanded ends are heated from within but have virtually no external cooling. This causes the expanded ends to approach very nearly the gas temperature. However, the tube wall just adjacent to the expanded end is cooled; and due to the thin-walled material, which allows very little axial heat conduction, a very steep temperature gradient can result. The temperature gradient shown in Figure 38 was evaluated by assuming the worst possible conditions (calculated by the method described in Appendix II) and applied to point (A) in Figure 37. The gradient at point (B) is about the same, but the absolute values of temperature are less.

STRESS STUDIES

To understand structural requirements and to establish a design, a study was undertaken to determine where the maximum stresses occur in a regenerator module. The results of this study are given in Table III, and the analyses are detailed in Appendix III.

The compressive hoop stress, resulting from high pressure outside the tubes (as shown in Figure 39), is quite low and would not cause structural problems. Other calculations indicated that buckling of the tube wall due to this type of loading would not occur. The longitudinal stress, resulting from axial tension in the tubes due to pressure (Figure 40), is also low. The remainder of the stresses listed in Table III result from uneven thermal growth of the regenerator system. As shown in Figure 41, uneven expansion of the module as a whole tends to bow the tubes slightly.
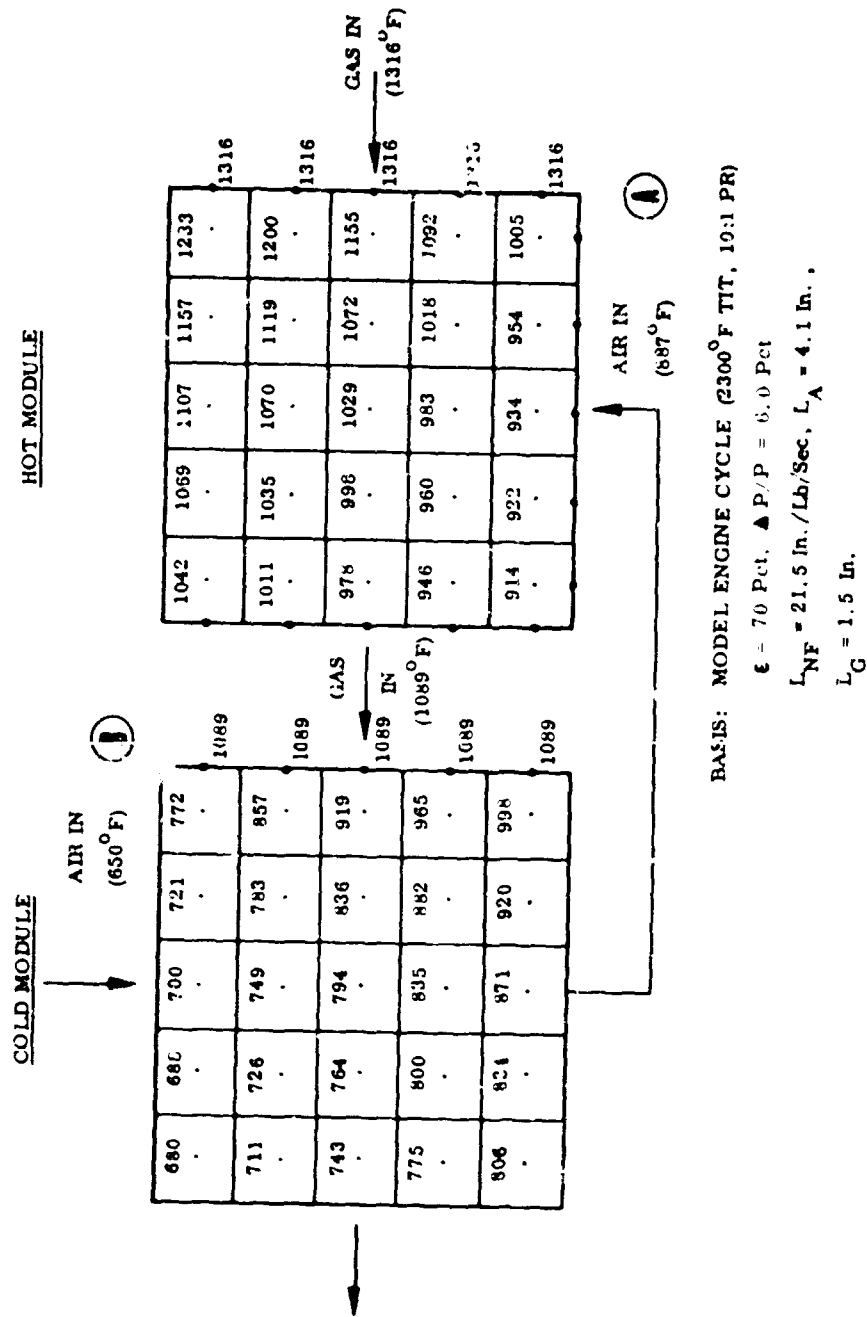
Figure 37. Module Metal Temperature Distribution.
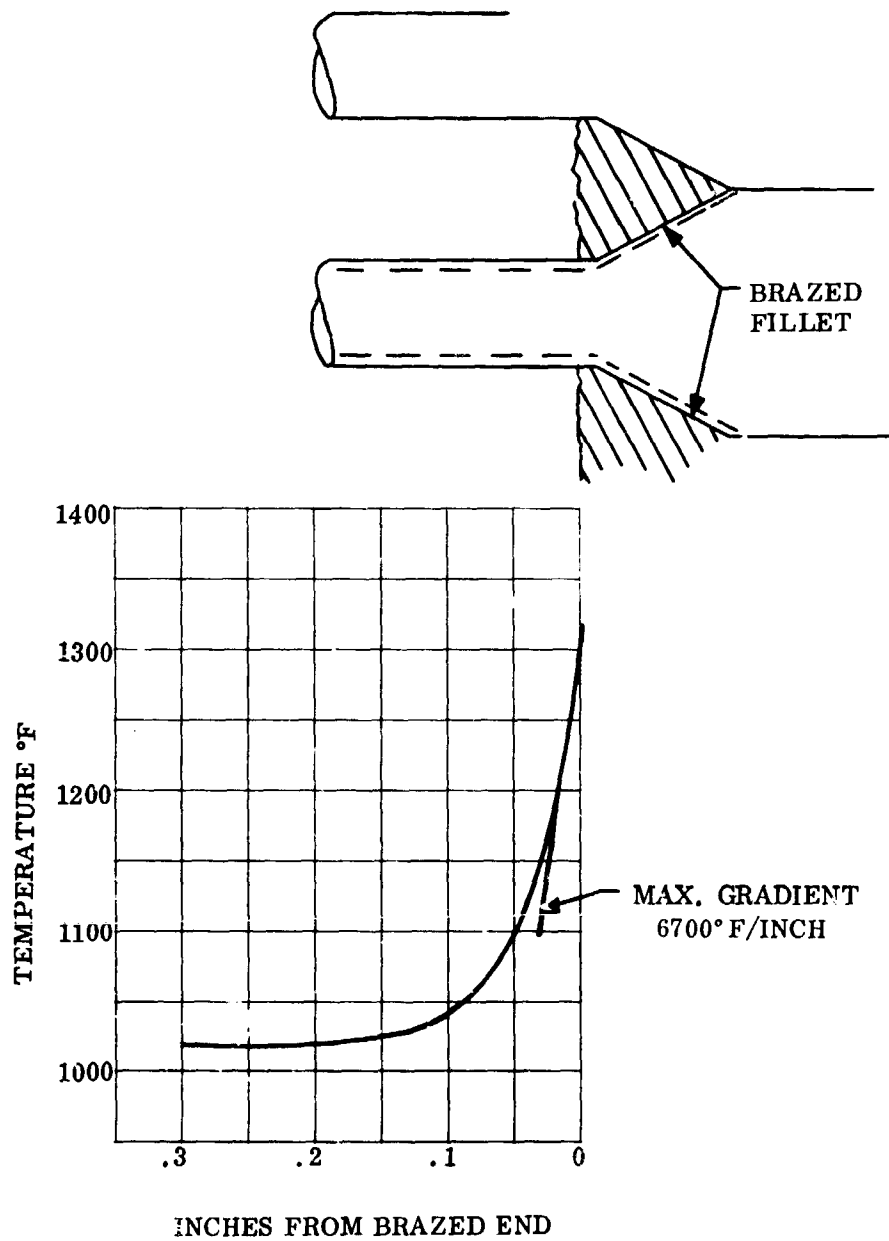
Figure 38. Temperature Gradient At Tube End.

This deformation results in bending stresses in the tube wall. The bending moment also results in small shear stresses at the faces of the expanded ends. These stresses are low enough to be ignored.

TABLE III
NOMINAL STRESSES IN MODULE

Compressive hoop stress due to pressure	1300 Psi
Longitudinal tension due to pressure	635 Psi
Stress from bending of tubes due to uneven thermal expansion	465 Psi
Shear stress at tube ends due to uneven thermal expansion	22 Psi
Stress due to thermal gradient near braze	20,500 Psi maximum
Suspension stresses due to differential expansion between module and manifolds (500°F temperature difference)	15,000 Psi

HIGH
PRESSURE
OUTSIDE
TUBE

LOW PRESSURE
INSIDE TUBE
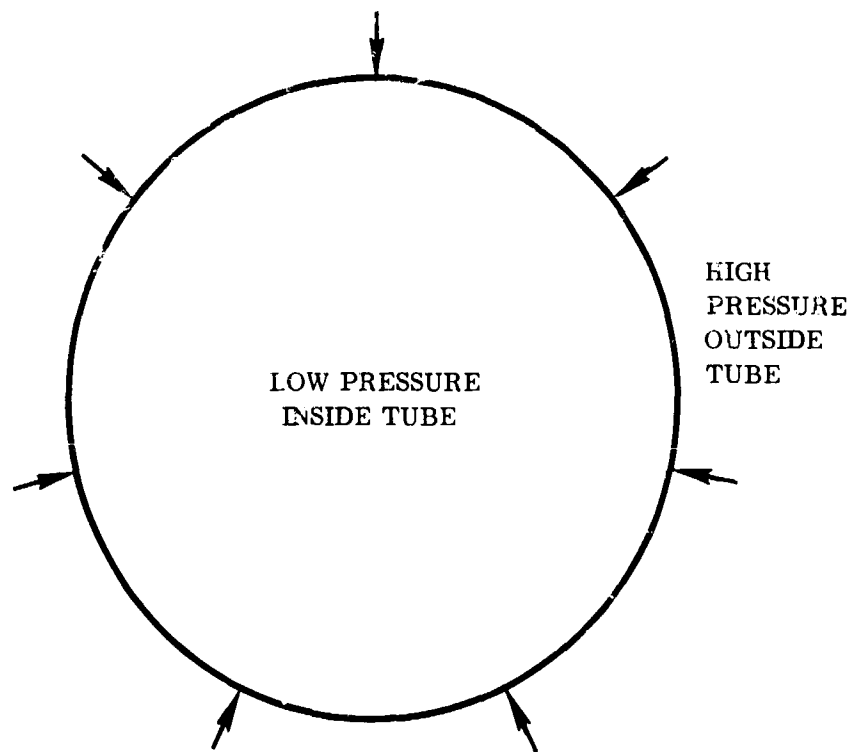
Figure 39.   Hoop Stress Loading.

50
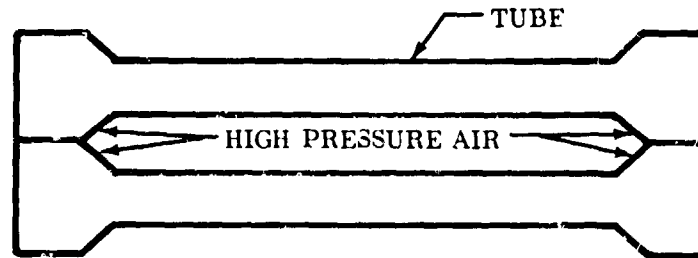
Figure 40. Tension in Tubes Due To Fluid Pressure.
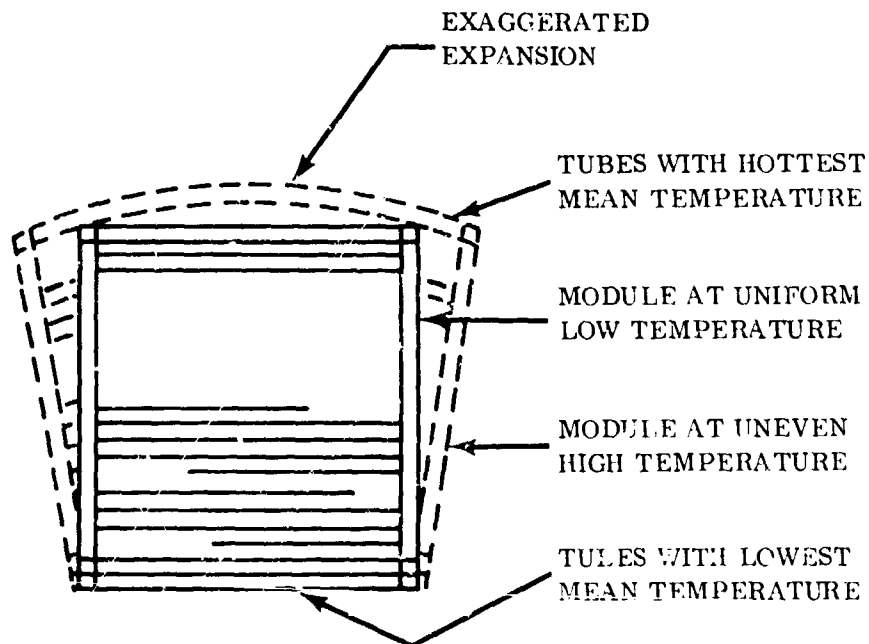
Figure 41. Exaggerated Bowing of Tubes Caused
by Uneven Thermal Expansion.

51

A stress resulting from a thermal gradient near the brazed, expanded end was studied. Figure 42, showing the joint which was considered, compares two cases - one in which a desirable braze has a small, rounded fillet, and one in which the alloy has a square fillet. A thermal gradient (up to 6700°F/inch) arises because the cylindrical part of each tube is heated from within and cooled by outside air, but the tube's expanded end, also heated from within, has virtually no external cooling. The expanded end therefore has a much higher equilibrium temperature than the rest of the tube. The transition between these two temperatures occurs over a very short distance, resulting in the predicted high gradient. As shown in Figure 43, the gradient causes the tube to become conical in shape. Where the conical section joins the braze alloy, the tube wall bends sharply, causing a high stress level. Good control of brazing alloy would produce the type of joint shown in Figure 42b with substantially lower stress.
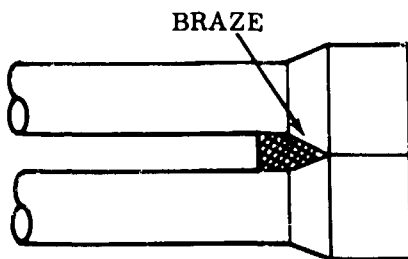
Figure 42a. Excessive Braze Causing High Stress Level
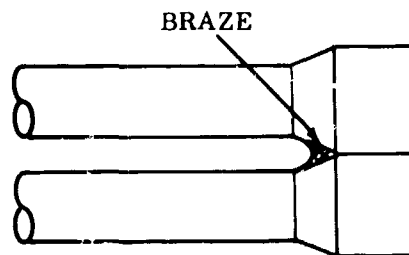
Figure 42b. Desired Braze

Figure 42. Brazed Fillets.

Calculated stresses for a suspension along the straight side of the module are approximately equal to the materials elastic limit. Stresses in corners are not readily amenable to known methods of calculation but were estimated to exceed the elastic limit of the flexure material (15,000 psi). The uncertainty of this stress calculation left the functioning of corners in question. Since it is known that thin-gauge high-strength materials can function satisfactorily after being initially deformed by a thermal stress, a test of the flexure was judged to be the best way to determine adequacy.

A study of the flexibility of the wavy tubes was made in order to design modules using either no flexible suspension or a suspension with more restricted movement. Reference 2, page 323, presents a method by

LARGE EXPANSION
DUE TO HIGH END
TEMPERATURE

BRAZE FILLET

SHAPE OF TUBE
BEFORE HEATING

LESSER EXPANSION
DUE TO LOWER
TEMPERATURE RISE

REGION OF
HIGH STRESS
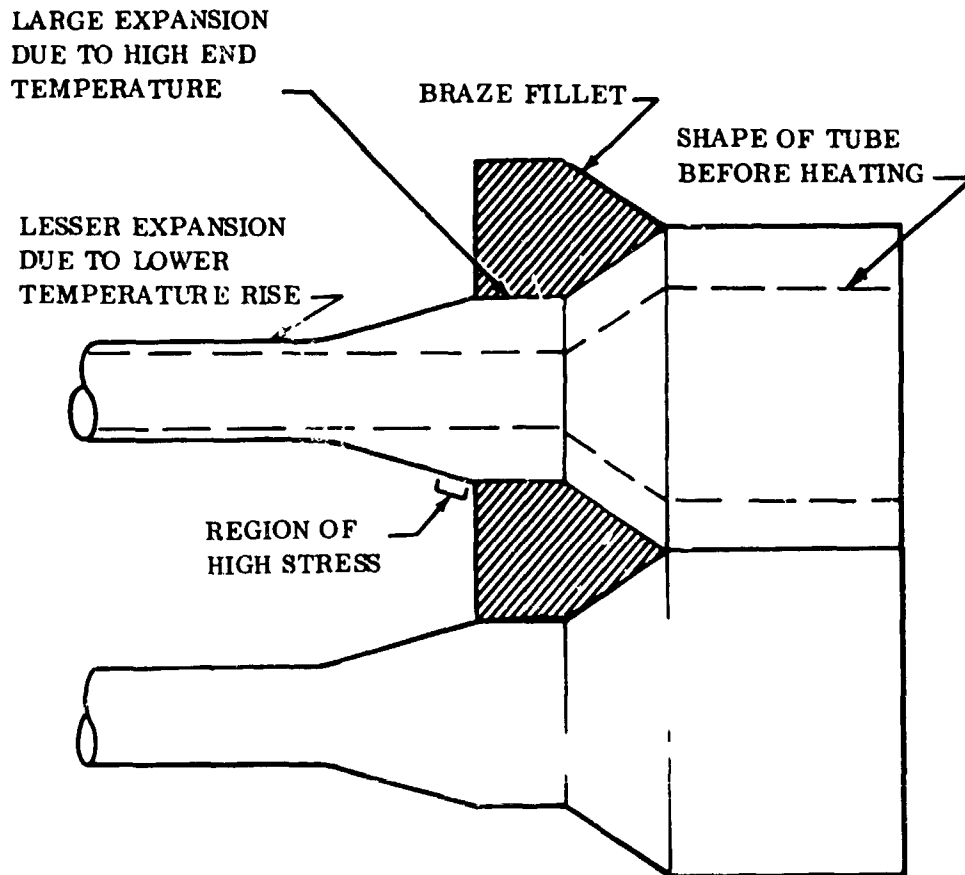
Figure 43. Exaggerated Effects of Tube End At Higher
Temperature Than Tube Body.

which the end loads and the maximum bending moment in an arbitrarily
curved pipe subjected to an axial displacement can be evaluated, and
Appendix III gives details of this analysis. From the maximum bending
moment, the maximum stress can be calculated readily. The end load
and maximum stress were then calculated for a straight tube (treated
as a column) subjected to the same axial displacement. It was found
that the maximum stress in a 1-cycle wavy tube is about 25 percent
lower than that in a straight tube. The end load is about one-seventh
that for a straight tube.

TEST CORE ELEMENT DEVELOPMENT

Heat transfer and pressure drop characteristics of modified tubular sur-
faces were investigated to identify types that would produce performance
better than smooth, straight tubes. A previous literature survey
(Figure 35) assisted in some tube modifications but gave no quantitative
data in the low Reynolds number (laminar flow) range of interest. To
obtain quantitative results, two test rigs were constructed: a steady-state
rig for testing flow through tubes and a transient-type rig for flow across
banks of tubes.

Two rigs were required (as established by data presented in Reference 3)
because it is not possible to construct one rig which has the required
accuracy for both types of flow. A parameter known as the Ntu (Ntu =
Ah/Wc_p) is used to describe the heat transfer size of a surface. That is,
it ratios the heat transfer capacity (Ah) to the fluid capacity (Wc_p).
Another parameter, the error magnification factor, which is the ratio of
the error in the desired result to the error in a measured quantity, is
presented as a function of Ntu for steady-state and transient types of heat
transfer test rigs in Figure 44. As can be seen, the transient type of rig
is inaccurate in the 1.5 to 3.0 range of Ntu, and steady-state testing is
inaccurate at Ntu's above 3.0. Since flow across tubes results in Ntu's
above 3.0, transient testing was the logical choice of rig. The Ntu's of
flow-through tubes are in the 1.0 to 3.0 range, making steady-state
testing the best choice.

SINGLE TUBE TESTS

The steady-state test rig for performance testing of flow through tubes is
diagrammed in Figure 45 and pictured in Figure 46. This rig was
designed to test a single tube of 1/4-inch diameter as opposed to testing
a 0.060-inch tube, since the larger size is easier to make and test. The
wall of the tubular surface under test was maintained at constant tempera-
ture by circulating high-velocity (6 gallons per minute) hot water around
the tube. Since the water flow rate was at least 2000 times the airflow
rate, changes in water temperature were negligible. Air was drawn into
the tube from the room, heated by convective heat transfer from the tube
wall, and then passed through the flow meter and blower. The inlet air
temperature was measured just ahead of the tube inlet with a precision
mercury thermometer. The air temperature was measured after the
test section with a 0.001-inch cooper-constantan thermocouple. These
data, together with the flow rate and water temperature, permitted
calculation of the Colburn factor j versus Reynolds number (see Appendix
IV for calculating procedures). Measurement of the pressure drop
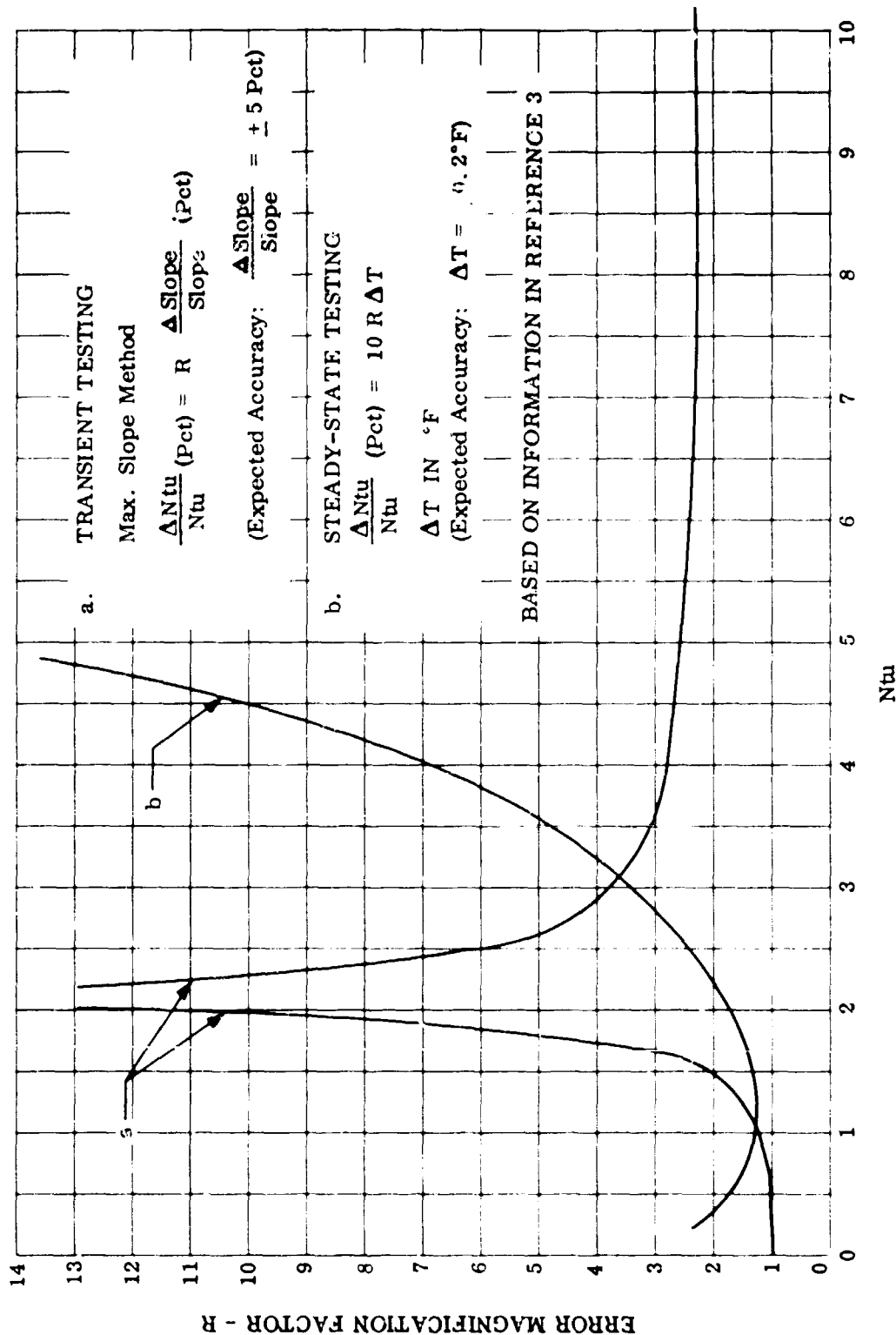
Figure 44. Error Magnification Factor Versus Ntu.

TRANSIENT TESTING

Max. Slope Method

$$\frac{\Delta Ntu}{Ntu} \ (Pct) = R \ \frac{\Delta Slope}{Slope} \ (Pct)$$

(Expected Accuracy: $\frac{\Delta Slope}{Slope} = \pm 5 \ Pct$)

STEADY-STATE TESTING

$$\frac{\Delta Ntu}{Ntu} \ (Pct) = 10 \ R \ \Delta T$$

ΔT IN °F

(Expected Accuracy: $\Delta T = 0.2°F$)

BASED ON INFORMATION IN REFERENCE 3

ERROR MAGNIFICATION FACTOR - R

Ntu

55
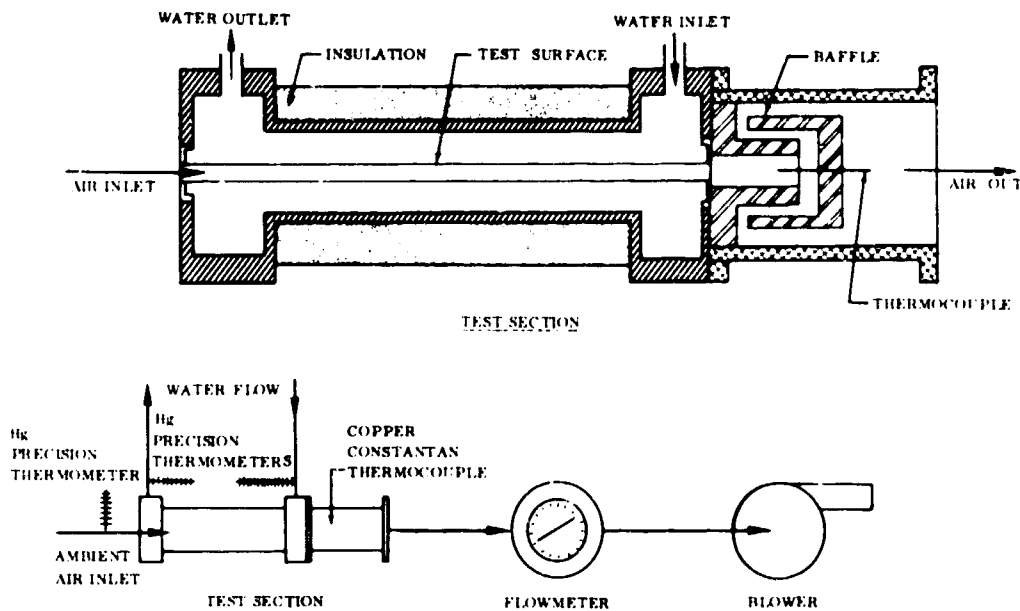
Figure 45. Steady-State Test Rig.

across the test section and the flow rate permitted calculation of the friction factor f versus Reynolds number.

Initially, five tubular surfaces were constructed. These included a straight, smooth tube to be used as a basis for comparison, a ring-dimpled tube, a spiral-dimpled tube, a 1-1/2-cycle wavy tube, and a ring-expanded tube as described previously. After initial tests, wavy tubes were found to have desirable characteristics, and two more wavy tubes were constructed, one with 1 cycle and another with 1/2 cycle. The tube shapes are pictured in Figure 47. In addition, three straight tubes having internal surface roughness were tested with particles of one-fifth of the tube diameter, one-tenth, and mixed in size. The particles (sand) were irregular in shape and were cemented to the tube wall. These tubes are shown sectioned in Figure 48.

Complete results of these tests are given in Appendix V in the form of friction factor and Colburn factor versus Reynolds number. When presented in this form, the results do not depend on tube diameter. Figure 49 presents the results in the form of gas side heat transfer coefficient versus gas side pressure drop. This figure is valid only for tubes with a 0.054-inch inside diameter. Heat transfer coefficients of the various surfaces were compared at the targeted gas side pressure drop of about 3 percent.
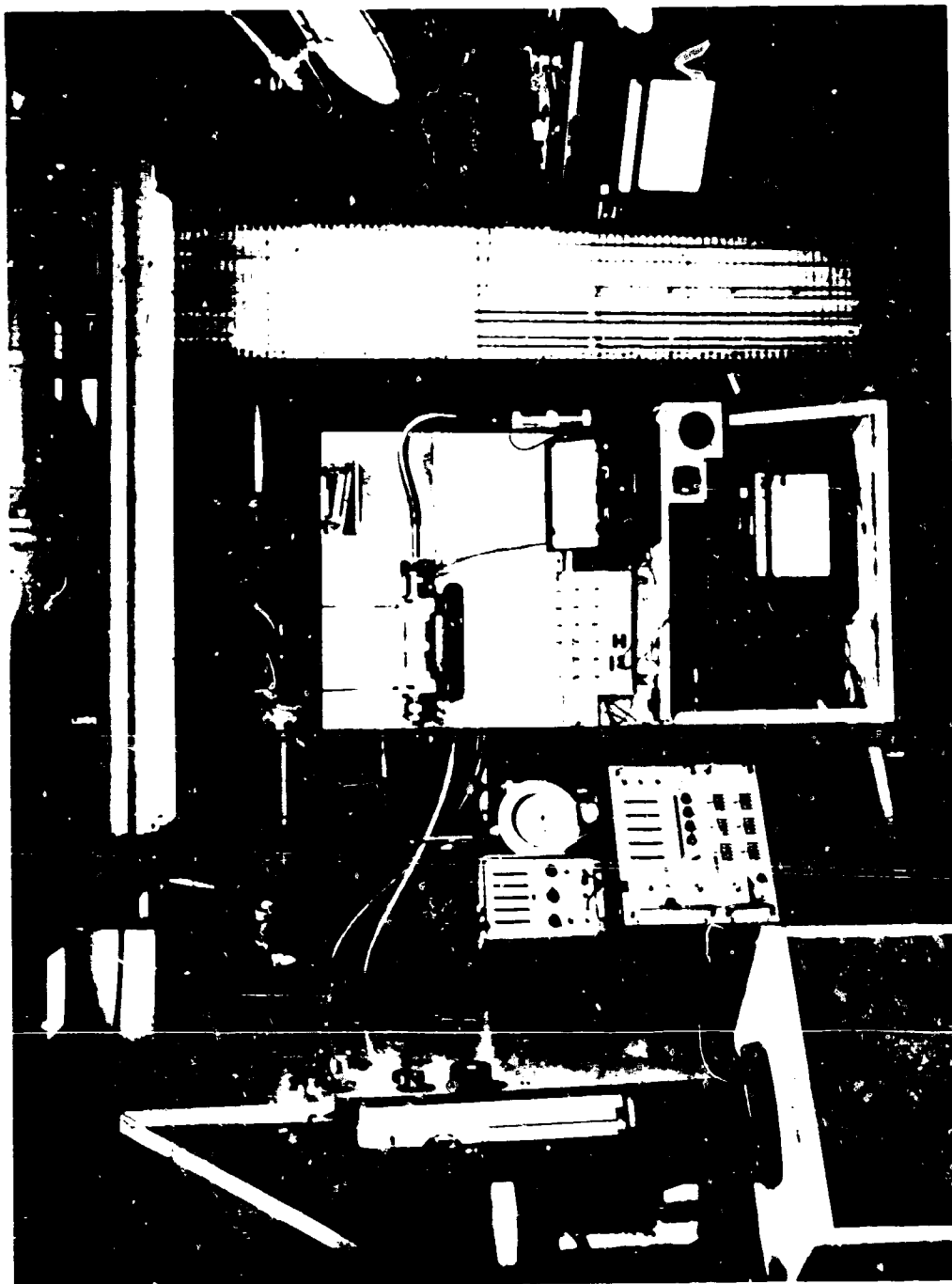
Figure 46. Steady-State Test Rig.

STRAIGHT TUBE, FLARED ENDS

RING-DIMPLED TUBE

SPIRAL-DIMPLED TUBE

1-1/2-CYCLE WAVY TUBE

RING-EXPANDED TUBE

1/2-CYCLE WAVY TUBE

1-CYCLE WAVY TUBE
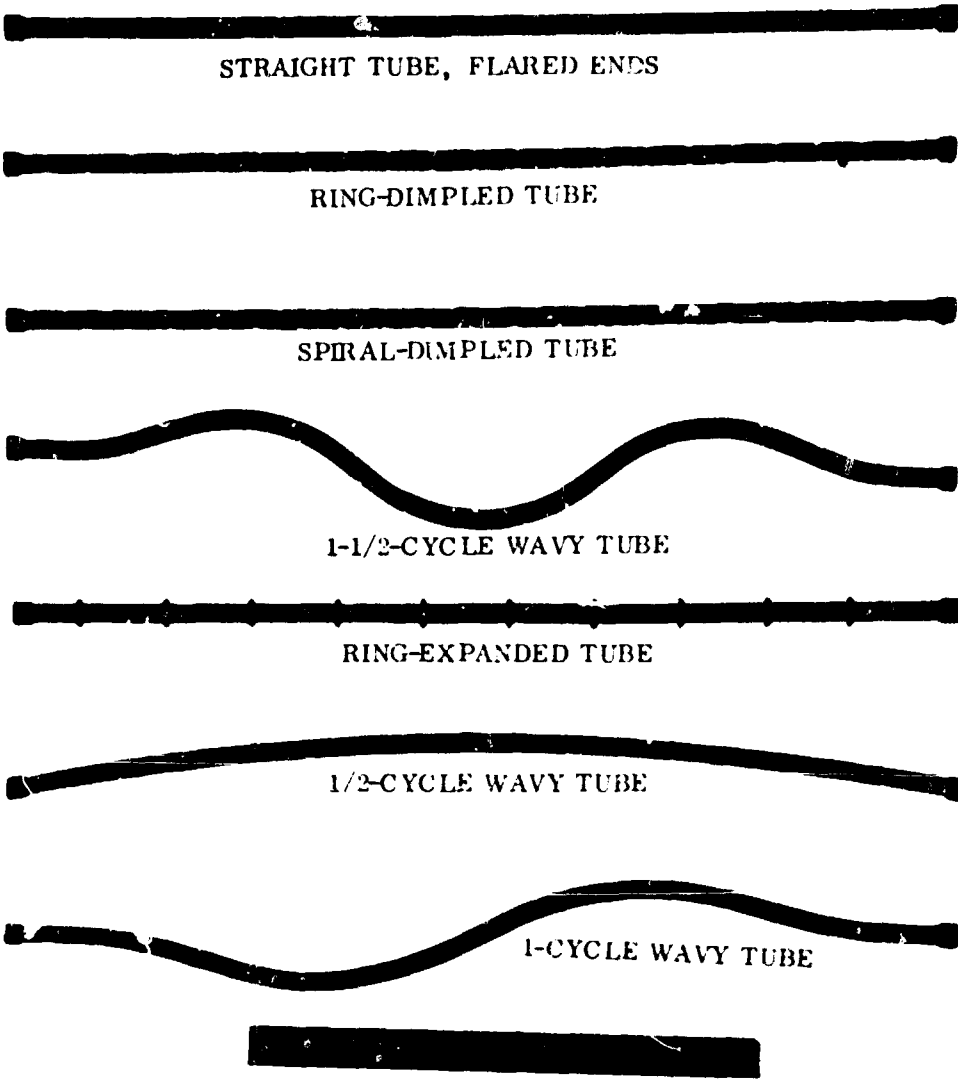
Figure 47. Modified Tubular Surfaces.

PARTICLES 1/10 TUBE I D

PARTICLE 1/5 TUBE I D

PARTICLES MIXED FROM 1/5 - 1/10 TUBE I D
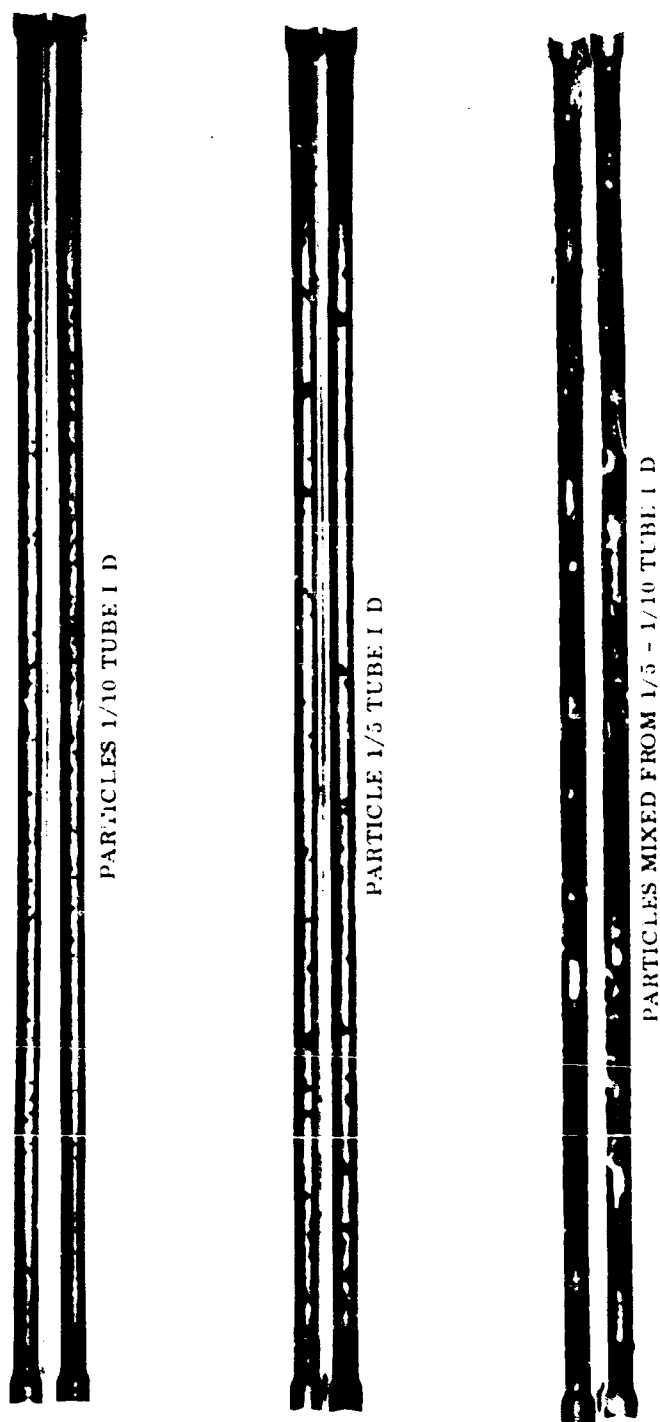
Figure 48. Surface-Roughened Tubes.

(1) STRAIGHT, SMOOTH TUBE   (4) 1/2-CYCLE WAVY TUBE (7) SURFACE-ROUGHENED TUBE, PARTICLES 1/5 ID
    AND RING EXPANDED TUBE (5) RING-DIMPLED TUBE   (8) SURFACE-ROUGHENED TUBE, PARTICLES 1/5-1/10 IC
(2) 1-1/2-CYCLE WAVY TUBE   (6) SPIRAL-DIMPLED TUBE   (9) SURFACE-ROUGHENED TUBE, PARTICLES 1 10 ID
(3) 1-CYCLE WAVY TUBE

BASED ON: 1316°F GAS AT 14.7 PSIG
           0.2 FT³/LB/SEC OF CORE
           .054-INCH ID TUBES
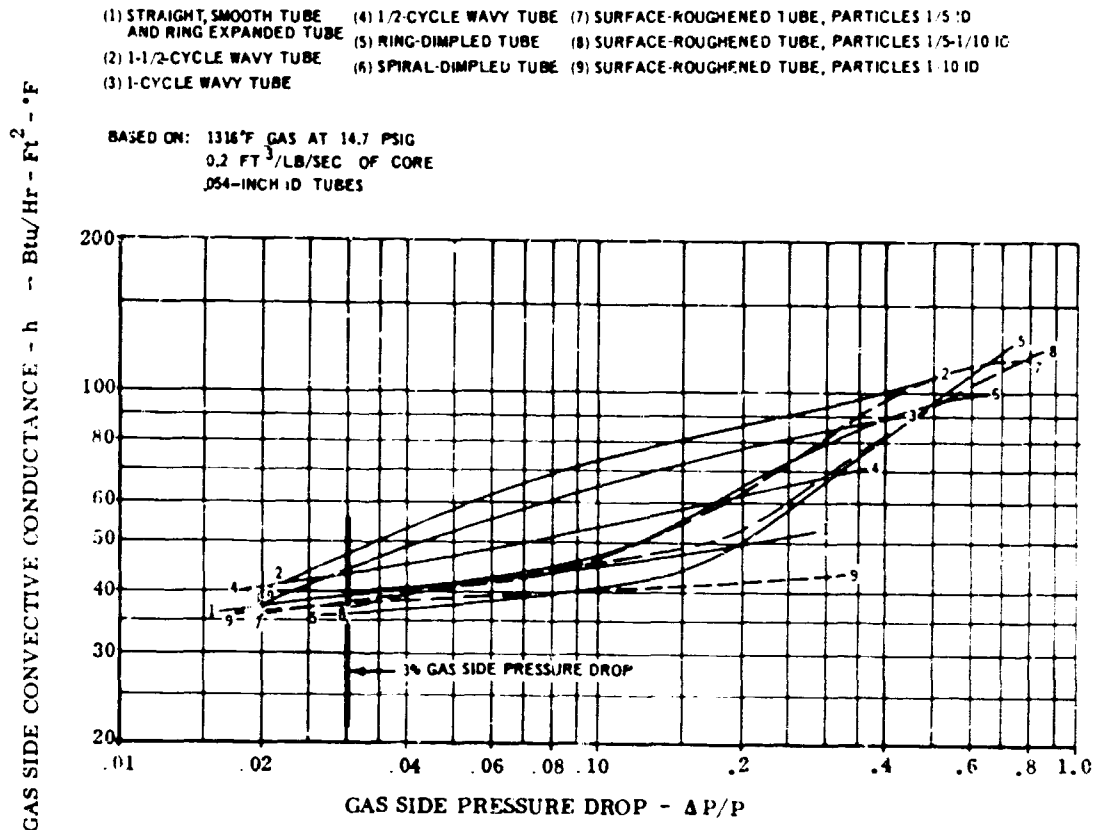
Figure 49. Characteristics of Modified Tubular Surfaces.

As can be seen, wavy tubes have significantly higher heat transfer coefficients. As discussed in Appendix I, this improvement results from secondary flows in the tube which cause the fluid in the boundary layer to mix with the fluid in the tube center. None of the remaining surfaces show any significant gains, inasmuch as the increases in heat transfer coefficient were offset by increased pressure drop. To achieve low pressure drop with the other surfaces, the Reynolds number was reduced so much that the heat transfer coefficient dropped to almost the value of a smooth tube.

It should be noted that these conclusions are restricted to 0.054-inch-inside-diameter tubes. Some of the modifications which did not show promise in this size range might well appear worthwhile for larger tubes.

Recognizing that straight tubes showed only a fair performance level but would be the simplest to manufacture and that the wavy tubes had the best performance with potential for desirable thermal stress characteristics,

it was concluded that both types should be evaluated further. Accordingly, the straight- and wavy-tube configurations were selected for follow-on module tests. Although the 1-1/2 -cycle wavy tube had the best performance, the 1-cycle wavy tube was easier to integrate into a module, since the tubes nest together better. As a result, 1-cycle tubes were selected as a good compromise.

TUBE BANK TESTS

A transient test rig was constructed to measure the heat transfer and pressure drop characteristics of flow across tube banks (Figures 50 and 51). A transient-type rig was selected to provide heat transfer and pressure drop data because it can be readily adapted to accommodate a wide variety of compact-type surfaces and yield the most accurate results. The technique (described in Reference 3) uses the principle of measuring the transient rate of temperature change of air flowing over a heated surface. The rate of maximum temperature change is related to the surface heat transfer coefficient. Figure 52 shows a temperature-time chart typical of the data from this rig.
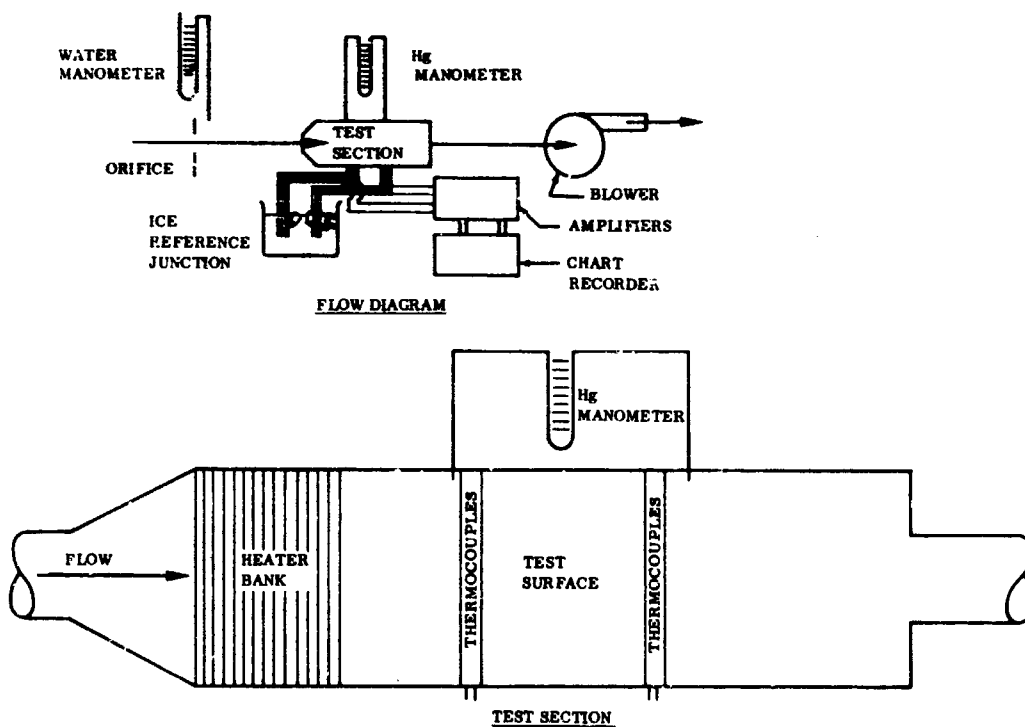
Figure 50. Transient Test Rig.
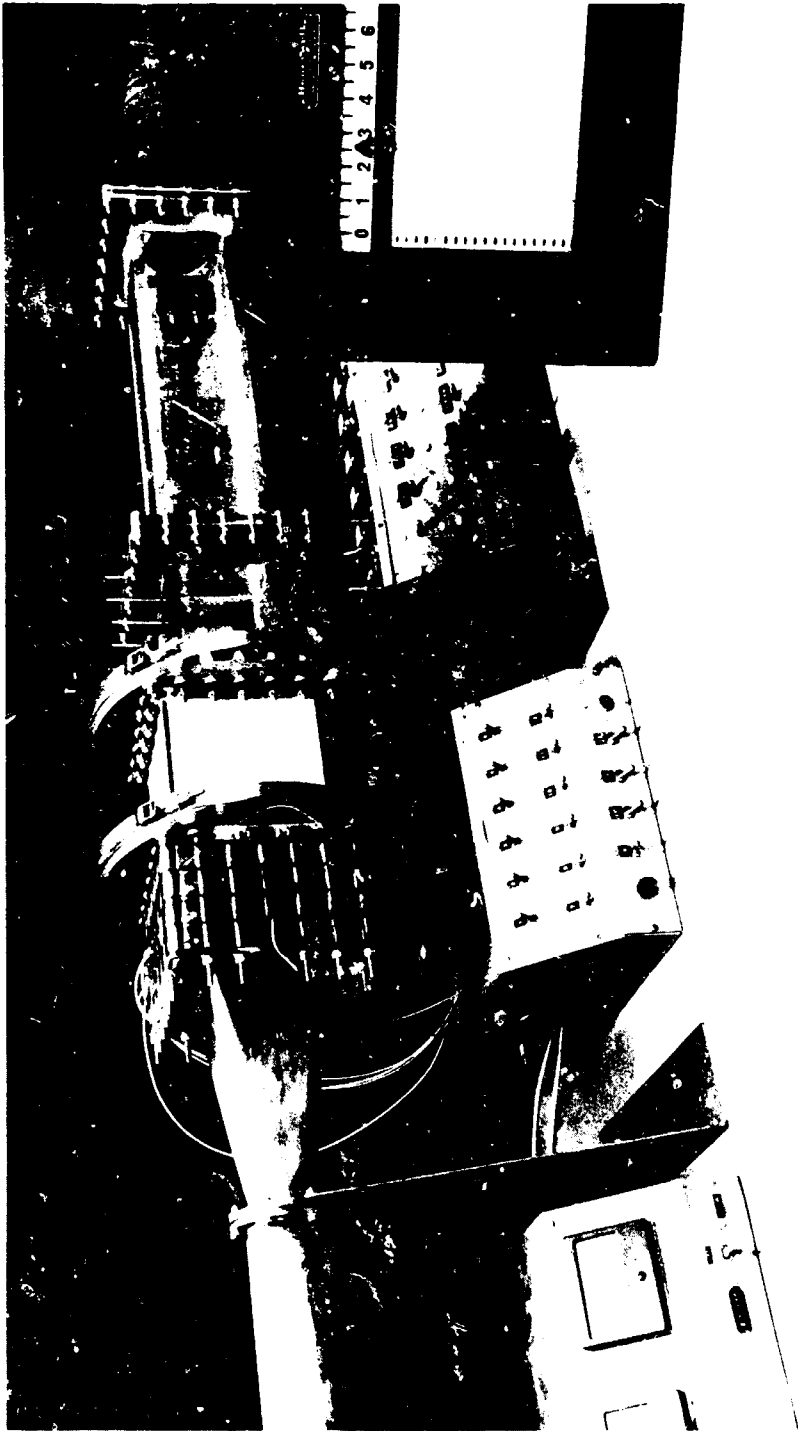
Figure 51. Transient Test Rig.
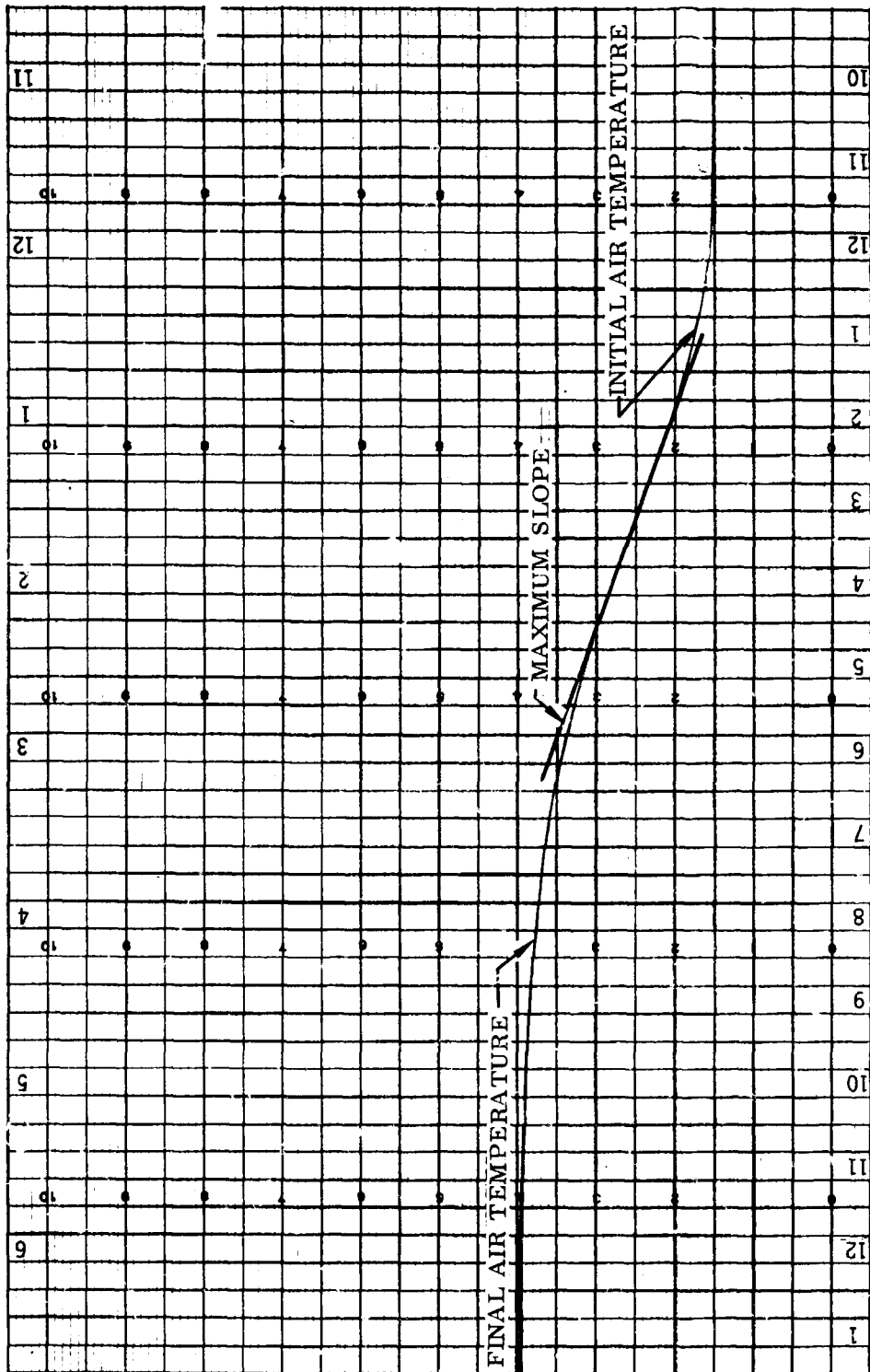
Figure 52. Typical Outlet Temperature Response.

Heat transfer and pressure drop data were taken on both straight- and wavy-tube banks. These results, given in Figure 53, in the form of f and j versus N_R, show that relative to the straight-tube module, the wavy-tube module is high in pressure drop and low in heat transfer. A probable factor was nonuniform flow distribution across the module, caused by the geometry of the design; at certain locations along the waves, it is unavoidable that flow space between tubes varies. In addition, the module had some tubes slightly misaligned. The apparent sensitivity of the wavy-tube module to local changes in flow area could be alleviated best by increasing the tube spacing in the longitudinal (airflow) direction; however, this change would have the disadvantage of increasing core volume.

It should be noted that the low heat transfer performance across wavy tubes has little effect on overall performance. The heat transfer coefficient inside the tubes is much smaller and consequently presents almost all of the heat transfer resistance. The effect of the high friction factor, however, will be reflected directly in total pressure drop.
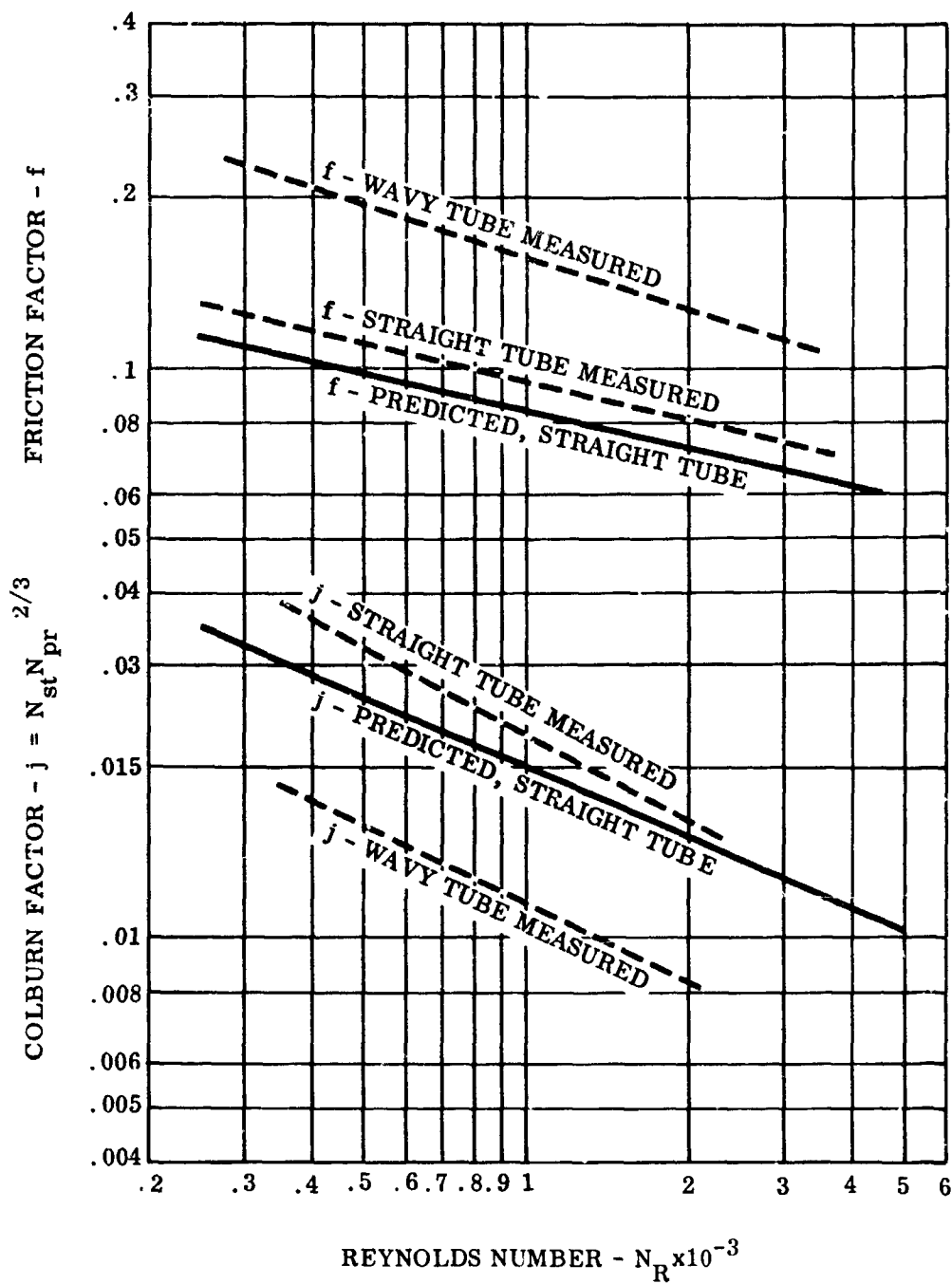
Figure 53. Heat Transfer and Pressure Drop Characteristics
for Flow Across Banks of Straight and 1-Cycle
Wavy Tubes.

65

FULL-SIZE MODULE DEVELOPMENT

The background material obtained from analytical studies and element tests was used during the major part of the regenerator program, which consisted of the design, fabrication, and testing of single modules of a full-sized regenerator. Although a complete regenerator uses many modules, the necessary fabrication techniques and performance and structural characteristics of individual modules were evaluated to identify specific problem areas representative of a complete heat exchanger.

This section describes activities involved in the development of full-size modules including:

● Design

● Selection of tube materials and brazing alloys

● Fabrication

● Testing and evaluation

● Manufacturing research

DESIGN

From the preceding analytical studies and single-tube tests, it was determined that straight and wavy tubes had the best overall balance of parameters for regenerators utilizing small diameter tubes. Indications were that the designs would have the advantages of high heat transfer capacity per unit volume, light weight, and good structural characteristics. Straight- and wavy-tube designs are shown in Figures 54 and 55.

The tubes selected had an outside diameter of 0.060 inch and a 0.003-inch wall thickness. To eliminate the need for inserting a large number of tubes into a more conventional, perforated header sheet, the design called for the ends of the tubes to be expanded into a rectangle so that they would nest together, forming an air-tight face (see Figure 12). The tubes were arranged in an offset design with a center-to-center spacing of 0.060 inch in the air-flow direction and 0.090 inch in the transverse (no-flow) direction. The selected design called for the gas to flow inside the tubes and the air outside. This selection had several advantages. The main advantage was that the high heat transfer coefficient outside the tubes (about four times that inside) would result in a mean tube temperature closer to the temperature of the air, as diagrammed in Figure 56.

66

$$\frac{3.030}{3.020}$$

$$\frac{3.020}{2.990}$$

SEE DETAIL I-

.060
±.001 OD

.003
WALL

.062 (REF)
(TYP)

.03R

.03R

$$\frac{.060}{.050}$$ FLAT (TYP)

30°

$$\frac{4.}{4.}$$

$$\frac{.0915}{.0900}$$

$$\frac{.020}{.015}$$ R(TYP)

$$\frac{.0615}{.0000}$$
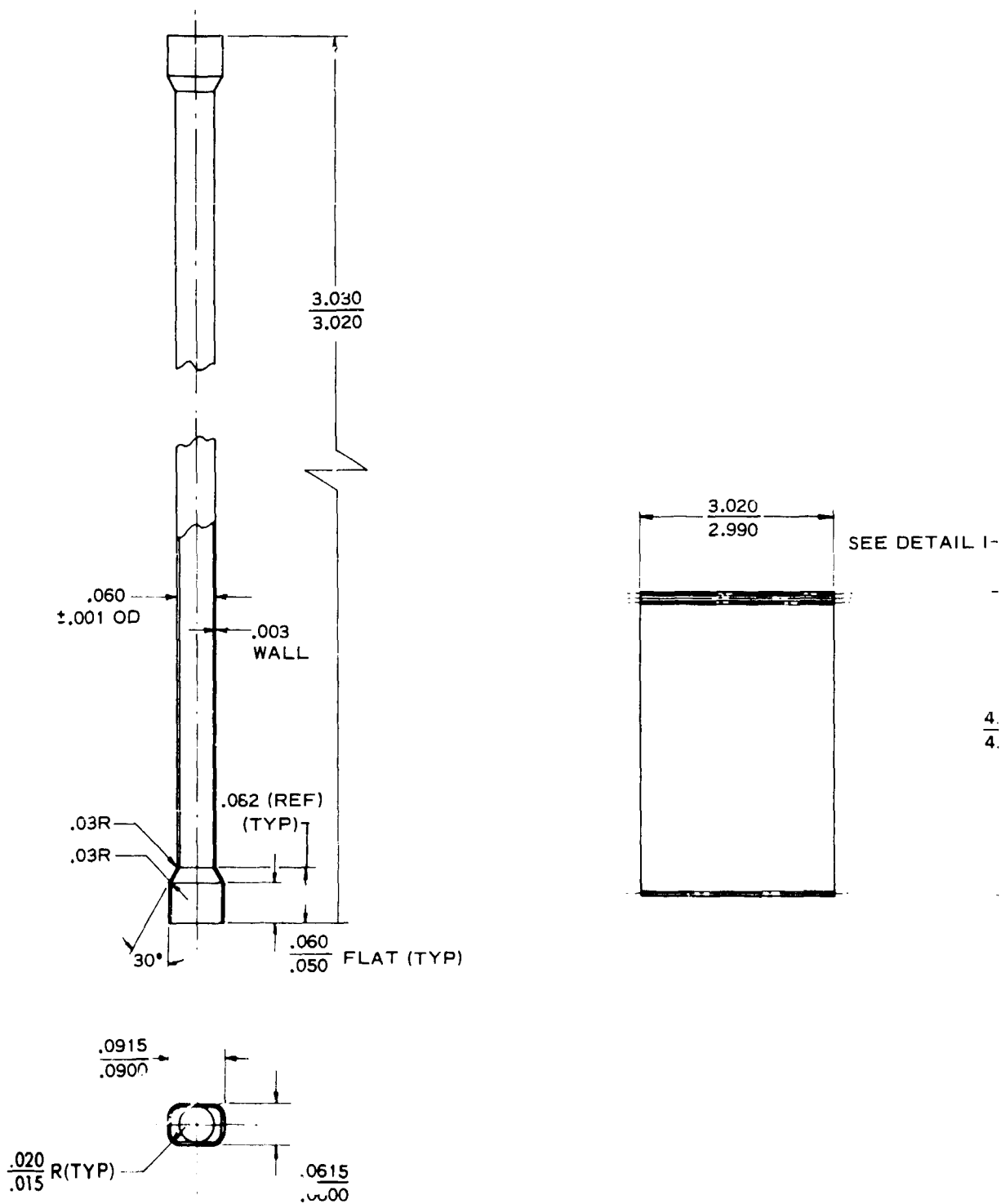
Figure 54. Straight-Tube Module Design.

67

FOR OFFICIAL USE ONLY

.090 (TYP)

.045 (TYP)

SEE DETAIL III

.060 (TYP)

SEE DETAIL II

DETAIL I

3.960
3.950

IL I

4.500
4.485

.100   .045
.090   .043

.060
.058

DETAIL II

.050   .010

.020
.015 R
TYP

.170

.230

.045

.090

.0:0 (REF)

.180   DETAIL III

2

.2175

.757

1.22R

3.015
2.995

1,813

.061 OD
.059
.003 WALL

.030R

.077 (REF)

1.22R
(TYP)

.12

.020 R (TYP)
.015

.0615
.0600

.2175

.0915
.0900
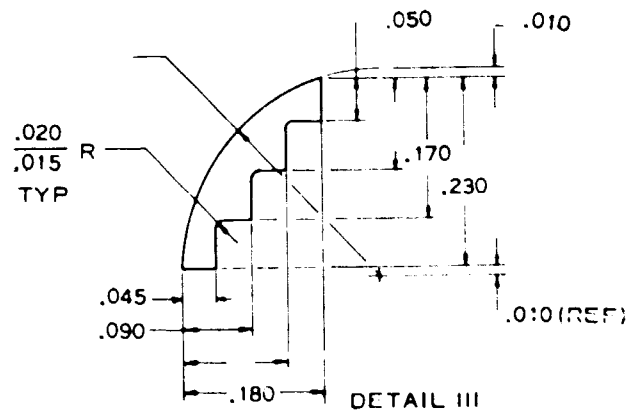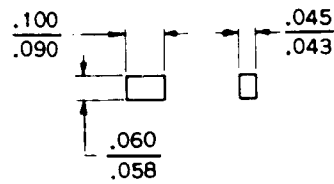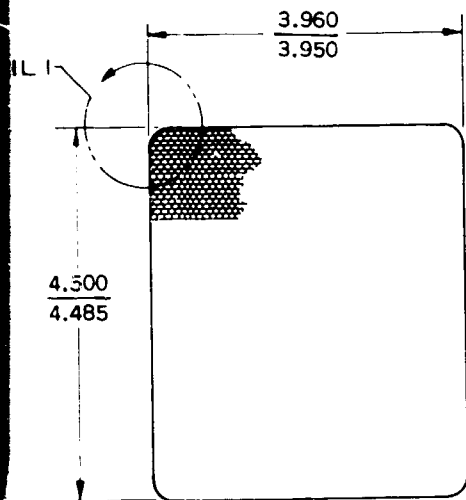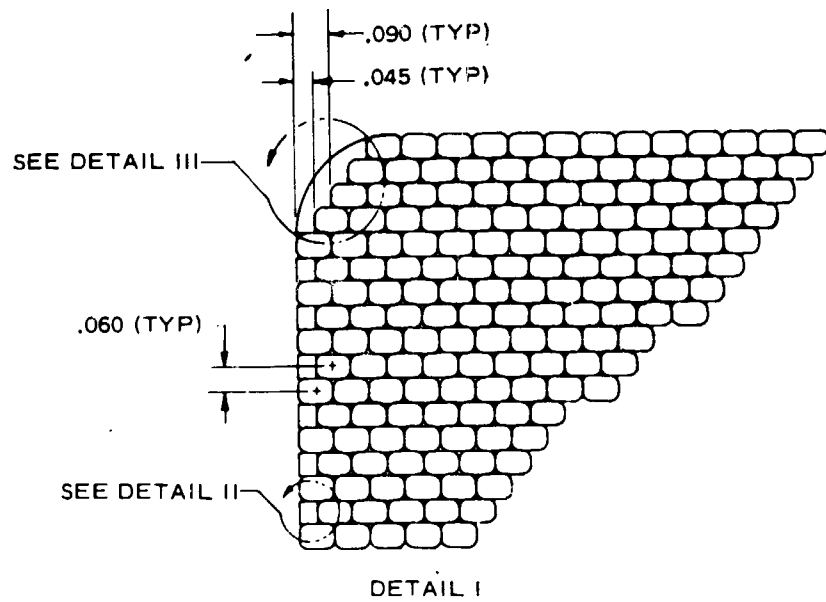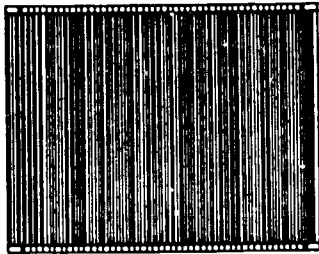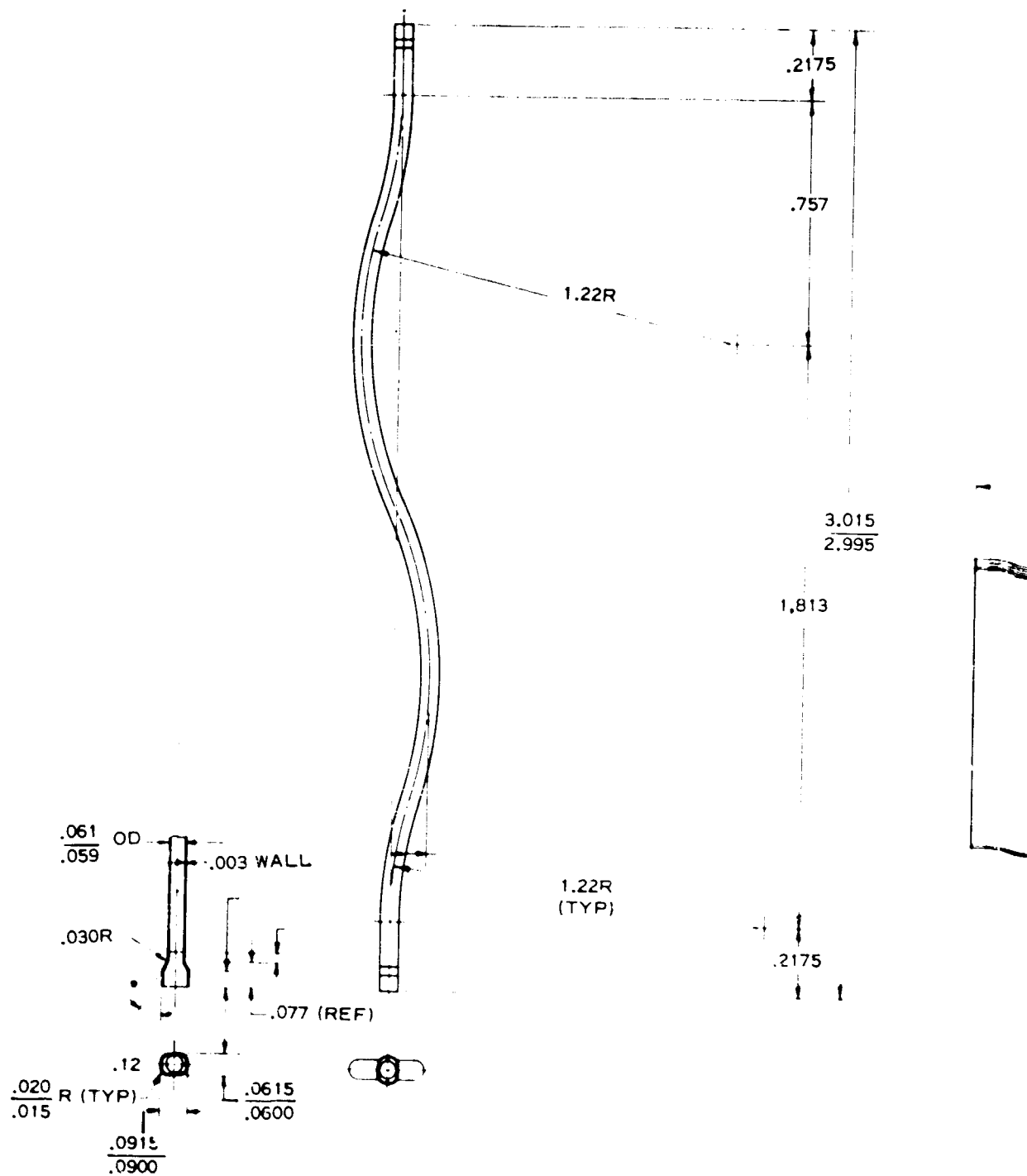
Figure 55. Wavy-Tube Module Design.

69

.090 (TYP)

.045 (TYP)

SEE
DETAIL III

.060
TYP

SEE DETAIL II

DETAIL I

3.020
2.990

SEE DETAIL

3.960
3.950

.045
.043

4.500
4.485

.100
.090

.060
.058

DETAIL II

.050   .010

.25R

.110

.170

.020 R
.015
TYP

.230

.045

.090

.010 (R

.135

.180

DETAIL III

2
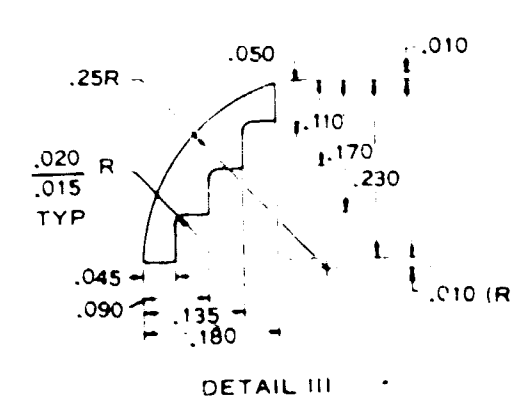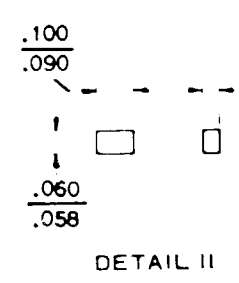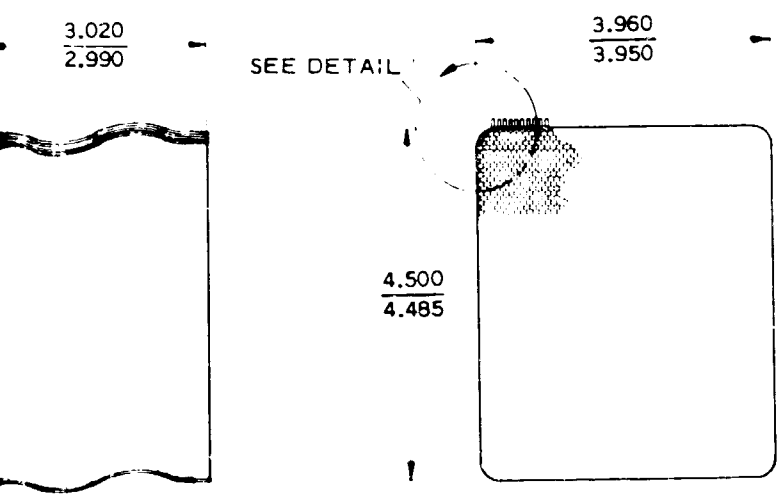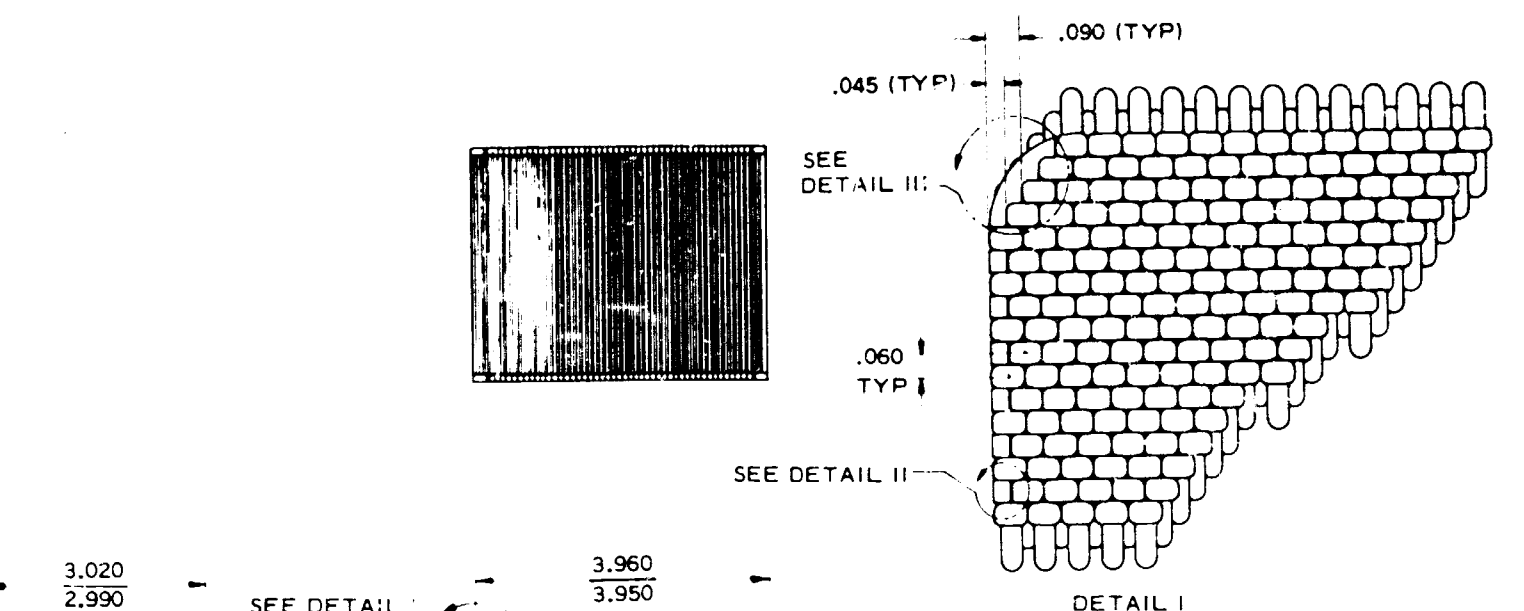
CASE I - GAS INSIDE TUBE
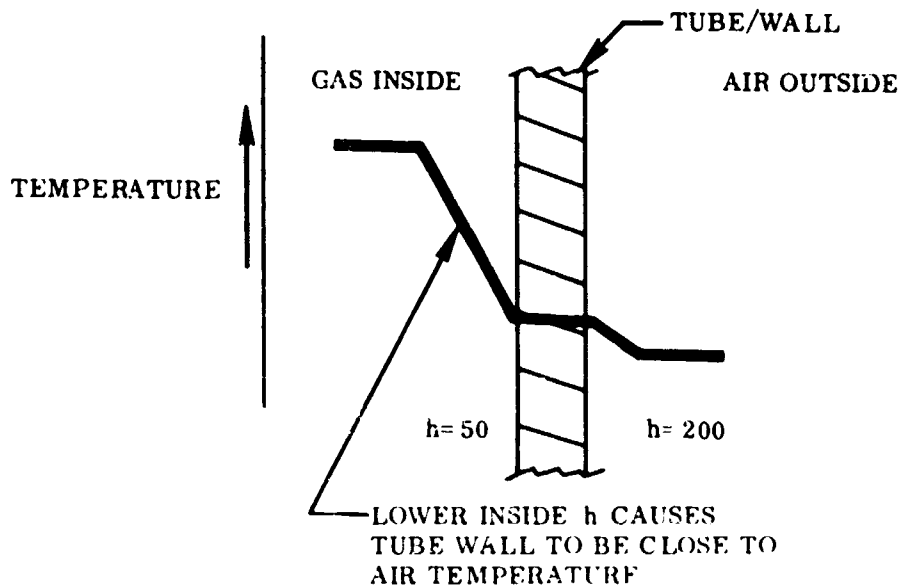
CASE II - AIR INSIDE TUBE
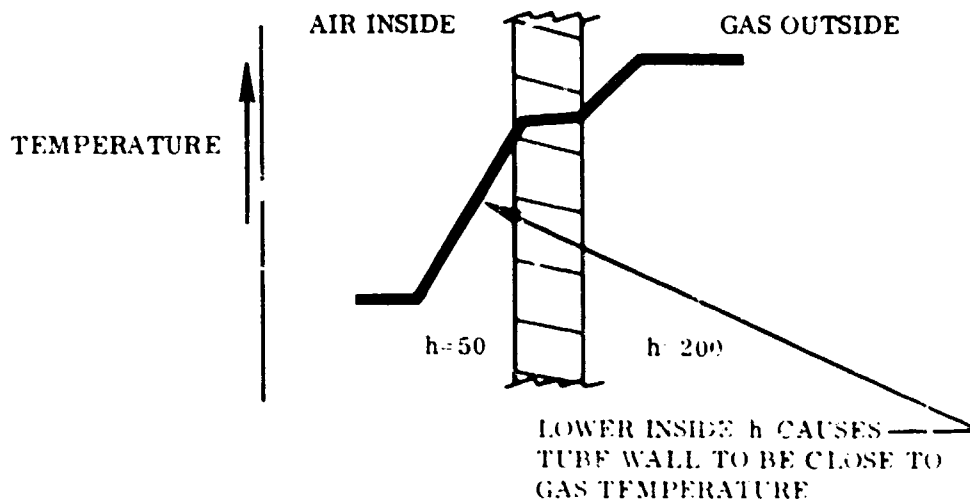
Figure 56. Effect of Gas Flowing Inside Tubes.

In addition, the absence of wake or turbulent regions in laminar flow through tubes would produce less tendency to foul. Further, less blockage of flow areas and less effect on increase of pressure drop would result if deposits occurred inside the tubes rather than outside. Finally, if partial fouling were to occur, cleaning inside tubes could be accomplished more easily from the ends.

The heat exchanger core was divided into a number of modules, each one supported by a flexible suspension as shown in Figures 57 and 58. This arrangement was aimed at minimizing thermal stresses by virtually eliminating end loads on the tubes and isolating thermal growth of the supporting structure from the tube bundle.

To eliminate leakage of air around the tube bundles, a sealing pillow was designed (Figure 59) to fit along the two sides of each module. The pillow was constructed of Fibrefrax layers enclosed in a casing of fine stainless steel wire gauze. The arrangement had high resistance to flow through it and provided compressive flexibility, ensuring a snug fit and good seal.
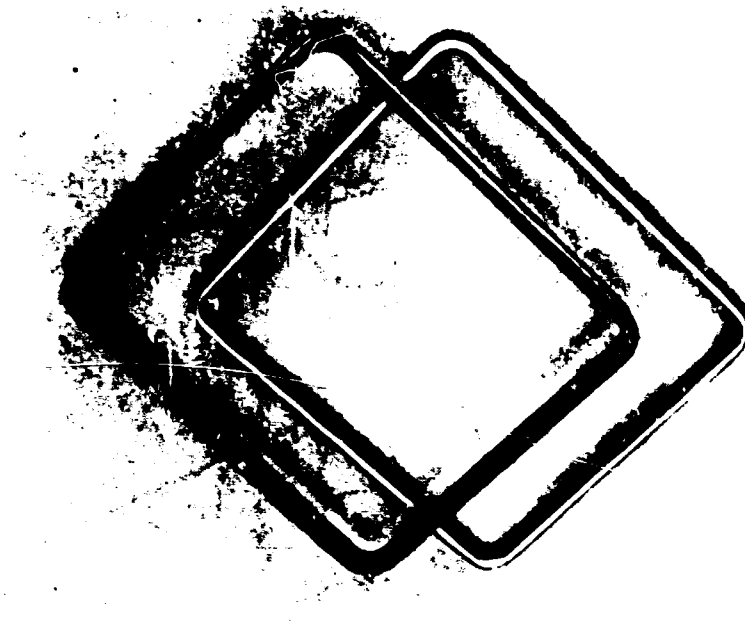
Figure 57.   Flexible Suspension.
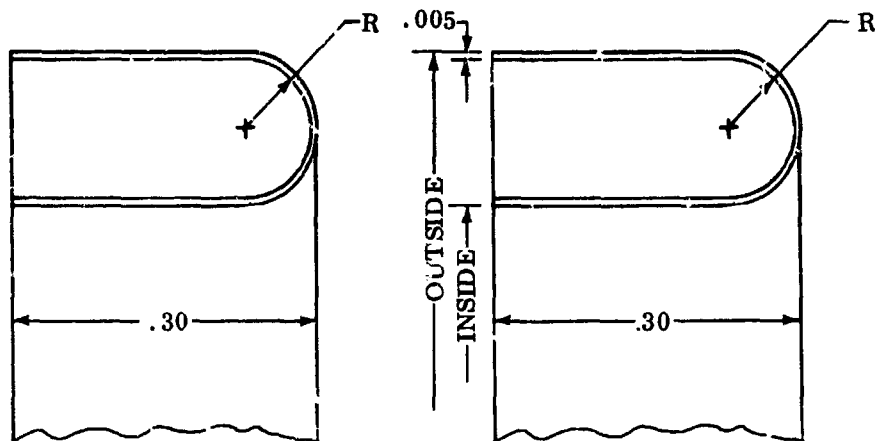
SECTION A-A
THRU CORNER

SECTION B-B
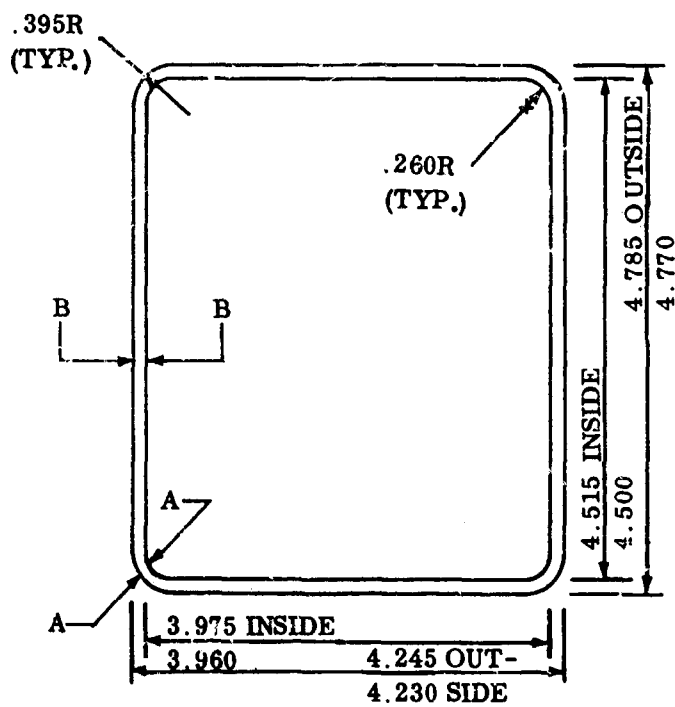
Figure 58.   Flexible Suspension.

FINE STAINLESS
STEEL MESH

A - A

FIBREFRAX CORE

PILLOW

FLEXIBLE SUSPENSION

TUBES

AIRFLOW PERPENDICULAR
TO PLANE OF PAPER
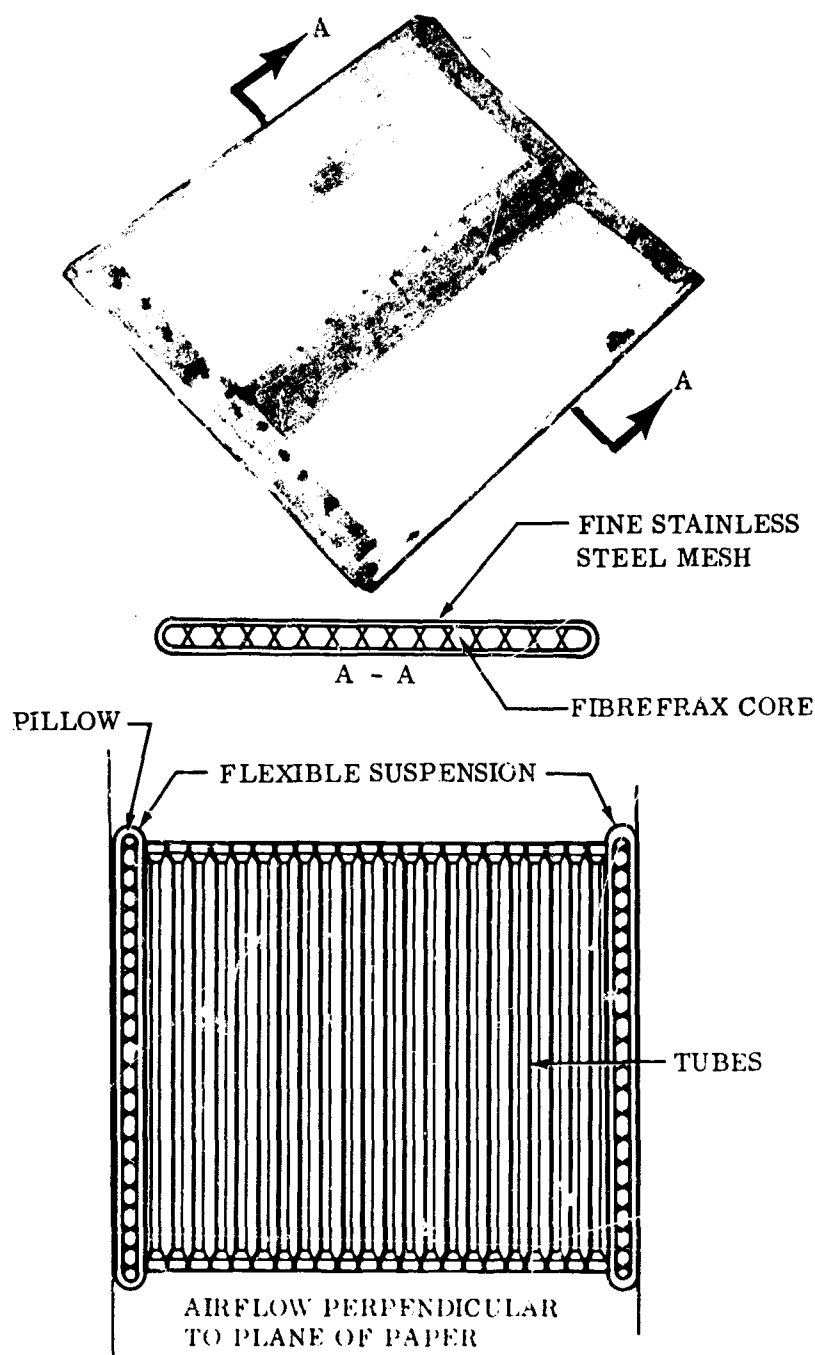
Figure 59.   Sealing Pillow Showing Installation.

74

SELECTION OF TUBE MATERIALS AND BRAZING ALLOYS

Tube Materials

In the selection of the tube material for this regenerator application, the most important criteria were judged to be good oxidation resistance at up to 1500°F, good ductility for forming, suitability for brazing, and availability at low cost. Early stress calculations available at the time that the material was selected indicated that high strength would not be required. A study of available data showed that AISI types 316L and 347 were the lowest cost suitable materials. Published property data showed that these materials have a yield strength at 1350°F of at least 15,000 pounds per square inch (page 22 of Reference 4), and their oxidation resistance is adequate for use at up to 1500°F (Reference 5).

When stainless steel is heated to a sufficiently high temperature, new grains appear in the metallographic structure. The new grain size and the rate at which the grains form depend on a number of variables, including amount of previous deformation, original grain size, and composition of the alloy.

If an alloy is exposed to temperatures above those necessary to produce recrystallization, growth proceeds by absorption of grains and is especially noticeable following recrystallization of severely deformed materials. Because of the variables involved, it is not possible to accurately predict the temperature at which recrystallization and grain growth occur. For cold-worked stainless steels, temperatures above 1850°F generally produce grain growth: required brazing temperatures are above 2000°F.

Brazing Alloys

Extensive tests were undertaken to determine suitable brazing alloys for the tubular-type regenerators. Initially, flow and erosion tests were performed with eight different brazing alloys in combination with parent materials of types 347 and 316L stainless steel. Those alloys showing good brazing alloy flow with the least erosion of the base material were Engelhard 440, Palniro 7, Palniro 1, Coast Metals 62, and Engelhard 135. Additional brazing tests on type 347 stainless steel tube clusters showed that Engelhard 440 and Coast Metals 62 had the least erosion of the parent material.

Brazed pillow pressure tests at room temperature (as indicated by Figure 60) showed that Palniro 1 and Palniro 7 produced strong joints, that Coast Metals 62 and Engelhard 440 were weaker, and that Engelhard 135 was

75

TOP VIEW

SECTIONAL VIEW
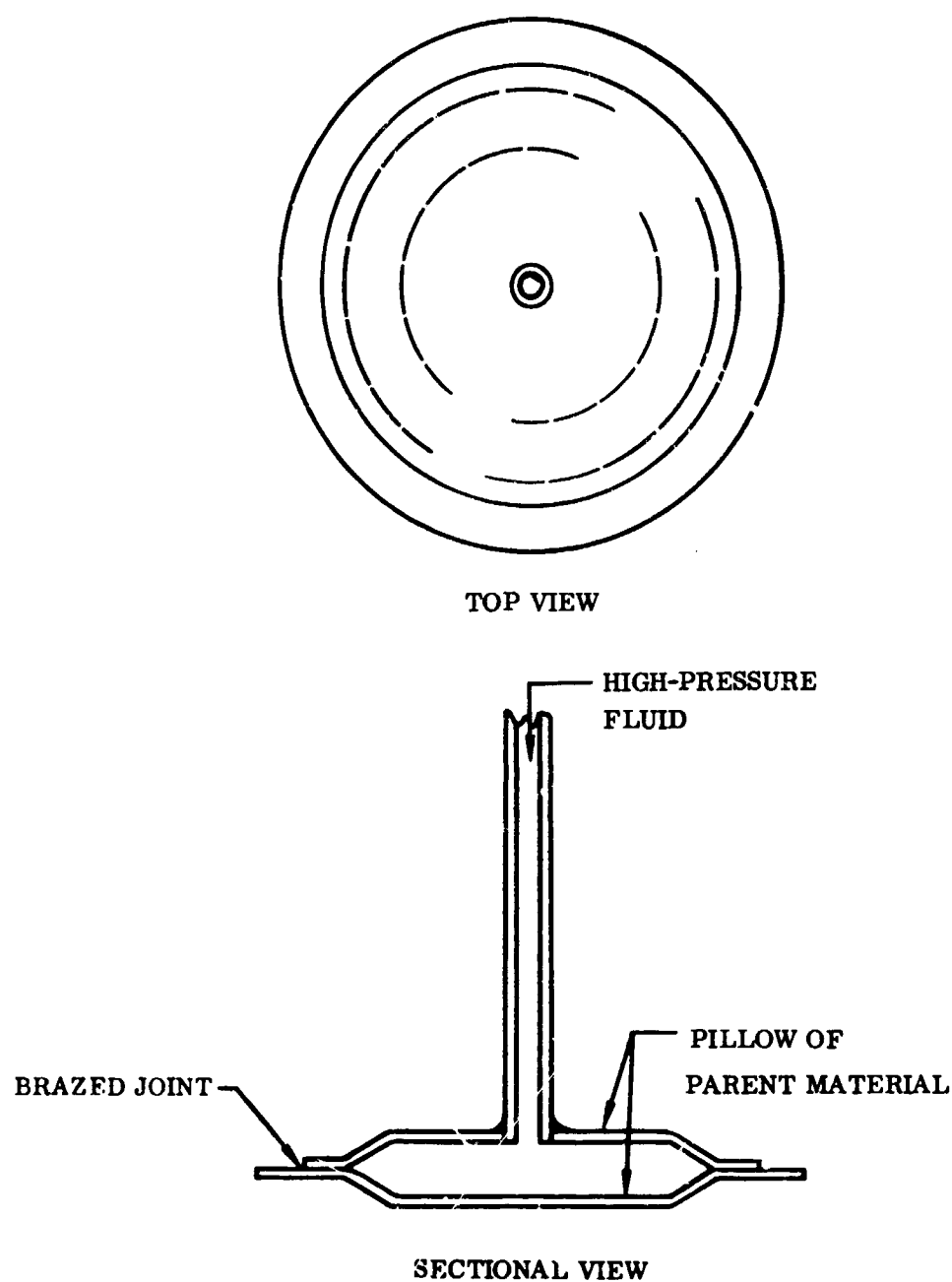
Figure 60. Brazed Pillow Test Specimen.

76

intermediate in strength. Since the important criterion was judged to be freedom from erosion (an erosive alloy could erode completely through the thin-walled tubing), Engelhard 440 was retained and compared with Palniro 1, Coast Metals 62, and Palniro 7 for joint strength at elevated temperatures. Again, Engelhard 440 was weaker than the other alloys but was judged to have sufficient strength for the application (8000/9000 psi at 1350°F).

Electron microprobe studies confirmed that Engelhard 440 produced the least penetration into the parent material. Coast Metals 62 showed no erosion, but a brittle network at the grain boundaries produced by boron content of the alloy was considered likely to impair resistance to fatigue damage. As a result of these studies, Engelhard 440 was selected as the most suitable brazing alloy. Figure 61 shows some typical brazes obtained in these studies. The complete results of these brazing alloy tests are presented in Appendix VI.

MODULE FABRICATION

The carbon content of initial deliveries of types 347 and 316L stainless steel was above specified maximum values and produced severe carbide precipitation at the grain boundaries during metallurgical tests. The supplier felt that it would be difficult to reduce carbon content to the required level for type 316L but that it would be possible to meet the specification for type 347. Later deliveries of type 347 showed the required improvement in the carbon content (Table IV), and on this basis, it was decided to manufacture all modules from AISI type 347 stainless steel.

The tubes were first cut to length by the electro-discharge machining technique to avoid burrs. Initial attempts at forming tube ends were unsuccessful, the reason being that it was expected that the rectangular shape could be produced with one punch in a single expanding operation. This method resulted in split-tube ends and a high rejection rate. To eliminate the deficiency, the procedure was corrected by forming the ends in two operations, using the punch and die sets shown in Figure 62. End forming was performed in two hand-operated machines. The first machine (Figure 63) preformed the tube ends into a round shape and upset the tube end uniformly to maintain a constant wall thickness. A second, similar, machine finish-formed the ends to their final rectangular shape. Straight tubes, so formed, were suitable for evaluation of experimental assembly techniques and subsequent testing. Wavy tubes were formed on a semi-automatic machine, forming two tubes at a time (Figure 64). A description of the operation of this machine is contained in Appendix VII. Both the bending of the tube and the end forming were done on this machine.
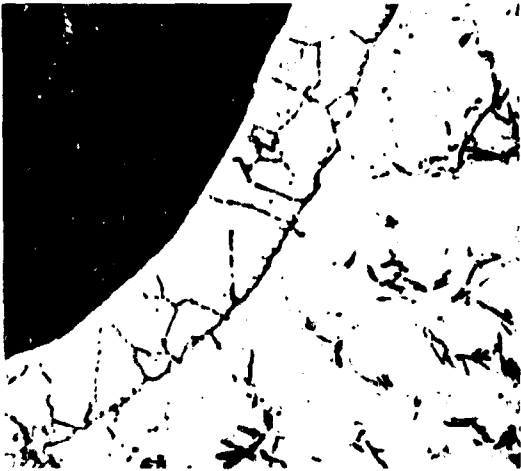
Figure 61a. Grain Boundary Pene-
tration by Coast
Metals 62
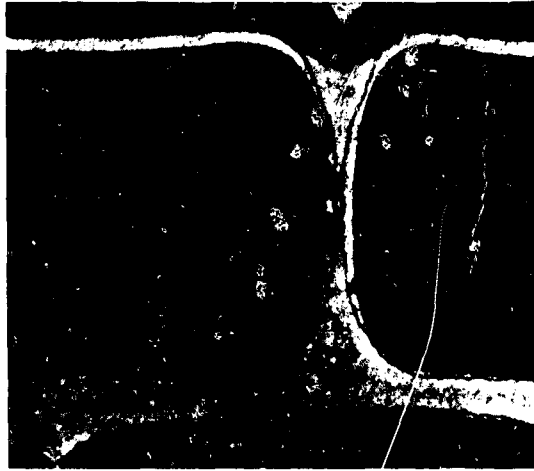
Figure 61b. Tube Wall Erosion by
Palniro 1 (Similar for
Palniro 7)
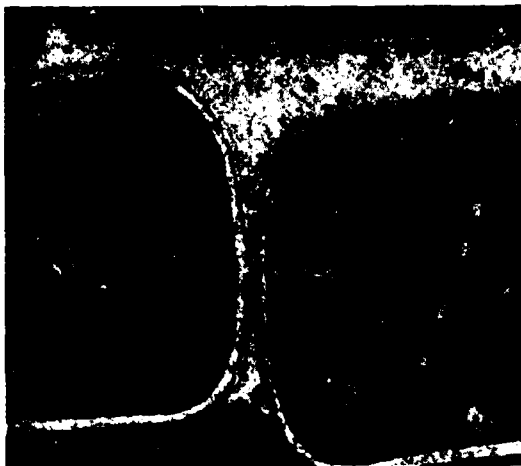
Figure 61c. Engelhard 440 Joints Showing no
Erosion or Penetration

Figure 61. Penetration and Erosion Characteristics
of Brazing Alloys.

78

TABLE IV
CARBON AND COLUMBIUM CONTENTS OF STAINLESS STEEL

| | 316 L | | 347 | | |
	Spec.	Delivery	Spec.	Early Deliveries (Handy & Harman)	Later Deliveries (Superior Tube)
Carbon	.03	.08	.08	.13	.077
Columbium	None Required	---	10 Times C Max. 1.1%	.80	.990

Due to springback of the wave and some die misalignment, these tubes were not as dimensionally accurate as desired, but by selecting the best tubes produced, a sufficient quantity was obtained to make a module.

The initial procedure selected to assemble the formed tubes into complete modules consisted of three steps. First. double-layer subassemblies of tubes were brazed into a fixture (Figures 65 and 66). Then sufficient double layers to make a full module were placed into a second fixture (Figures 67 and 68) and brazed together. This second fixture was a two-piece fixture with a movable upper half. Vistinex "A" was used for temporary bonding during both of these brazing operations. Next, the flexible suspension was brazed to the module. These operations, with successive brazes, were selected because it seemed more practical than assembly of tubes, fillers, and corners in a single brazing operation without temporary bonding.

Elimination of the first brazing operation by temporary bonding of the tubing with Vistinex "A" was tried without success because it has insufficient strength. Spot welding before brazing of tube ends was also tried, but metallographic examination indicated incomplete filling of the spotweld area with brazing material, which presents a severe stress concentration. This problem had to be overcome to make the spot-welding technique successful.
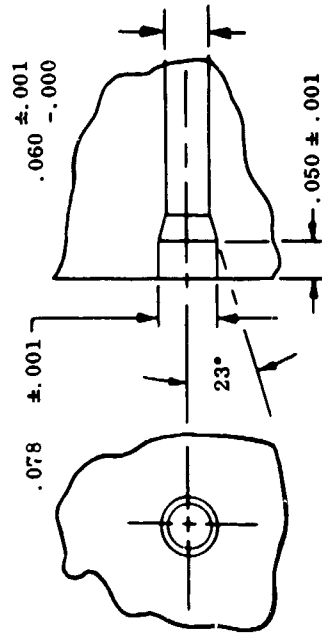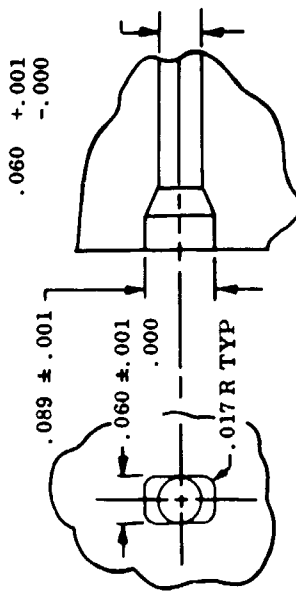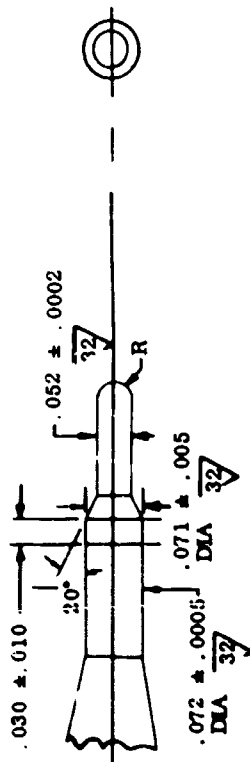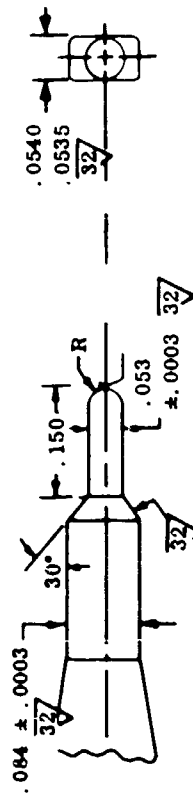
Figure 62. End Forming Punch and Die Sets.

80
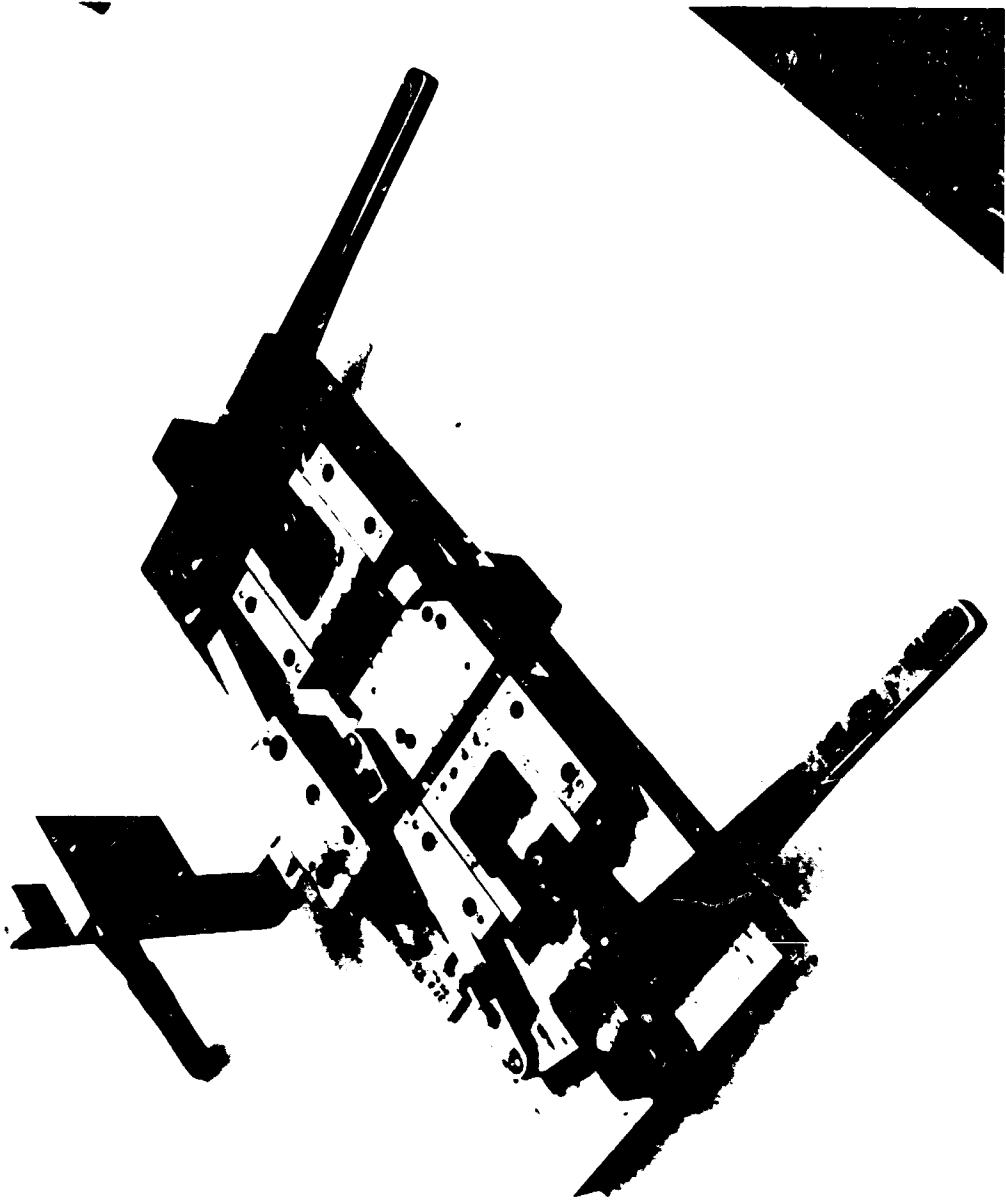
Figure 63. Straight-Tube End Forming Machine.
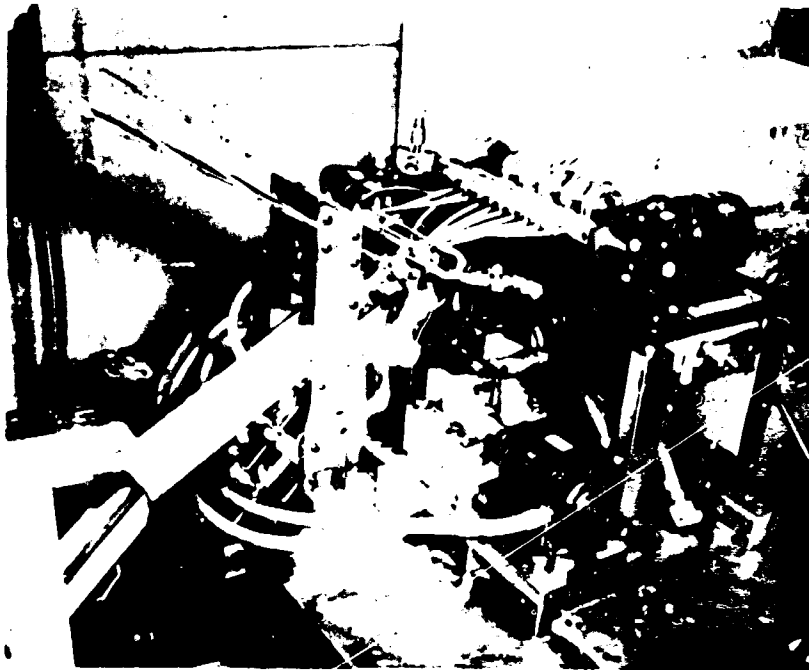
Figure 64.   Wavy-Tube Forming Machine.
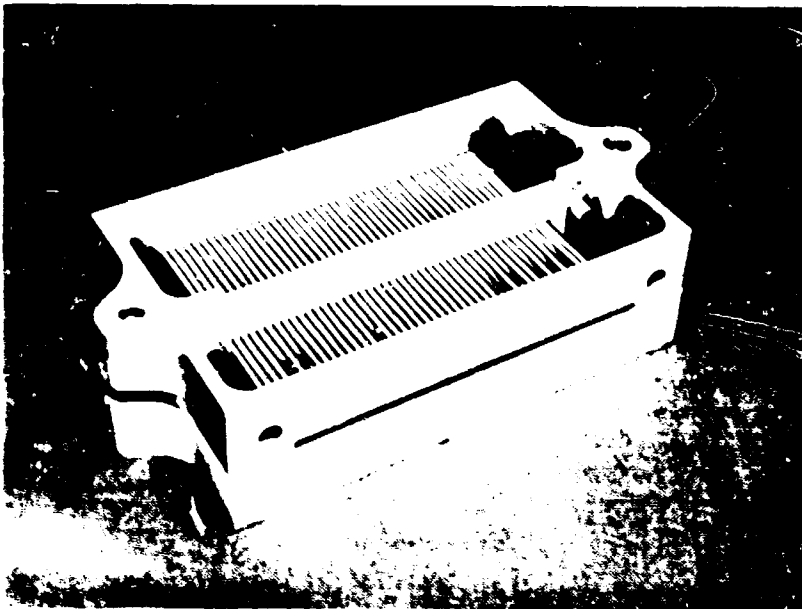
Figure 65.   Double-Layer Brazing Fixture.

3.960

3.018

.066
.062

066
.063

.090
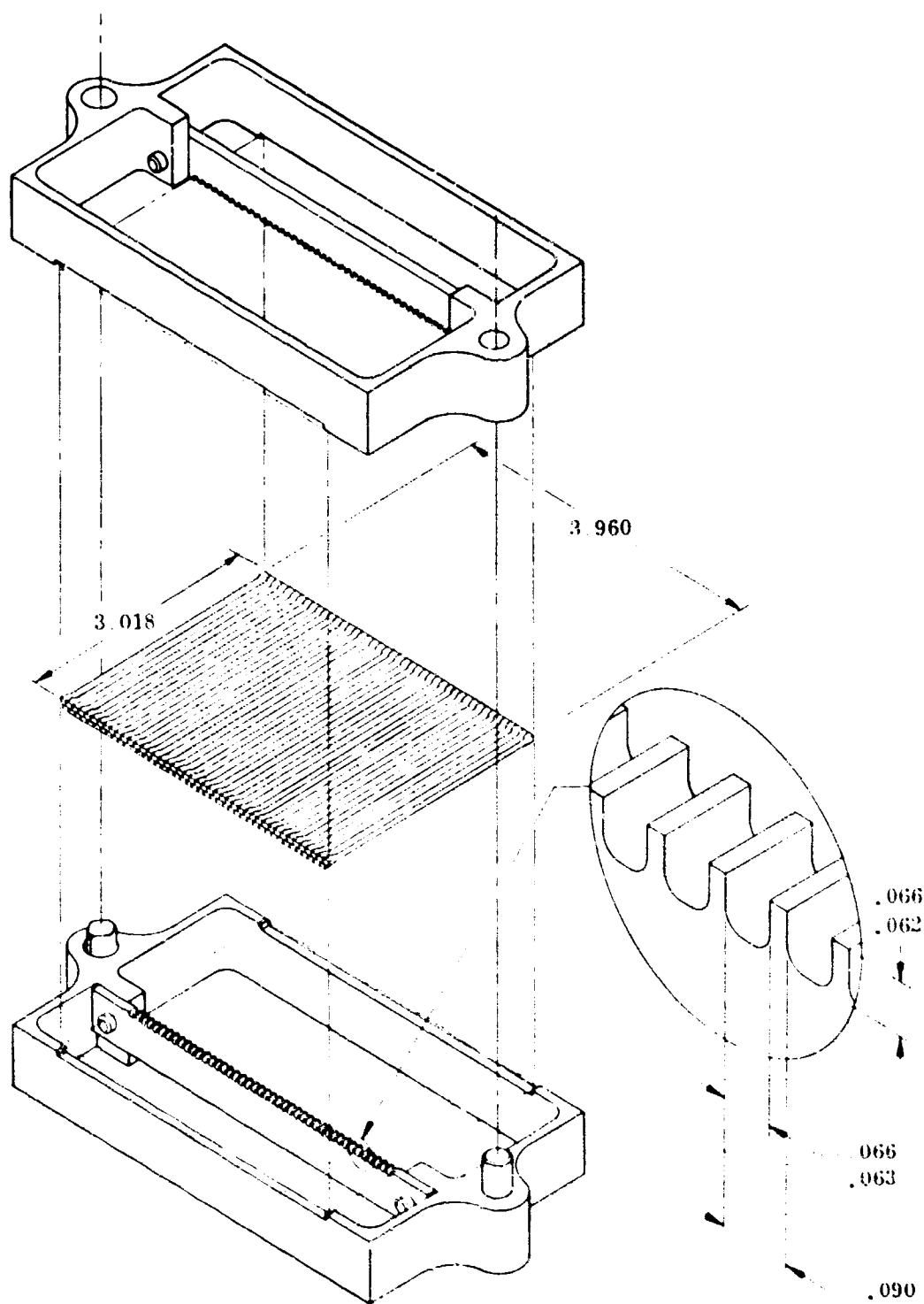
Figure 66. Double-Layer Brazing Fixture.

83
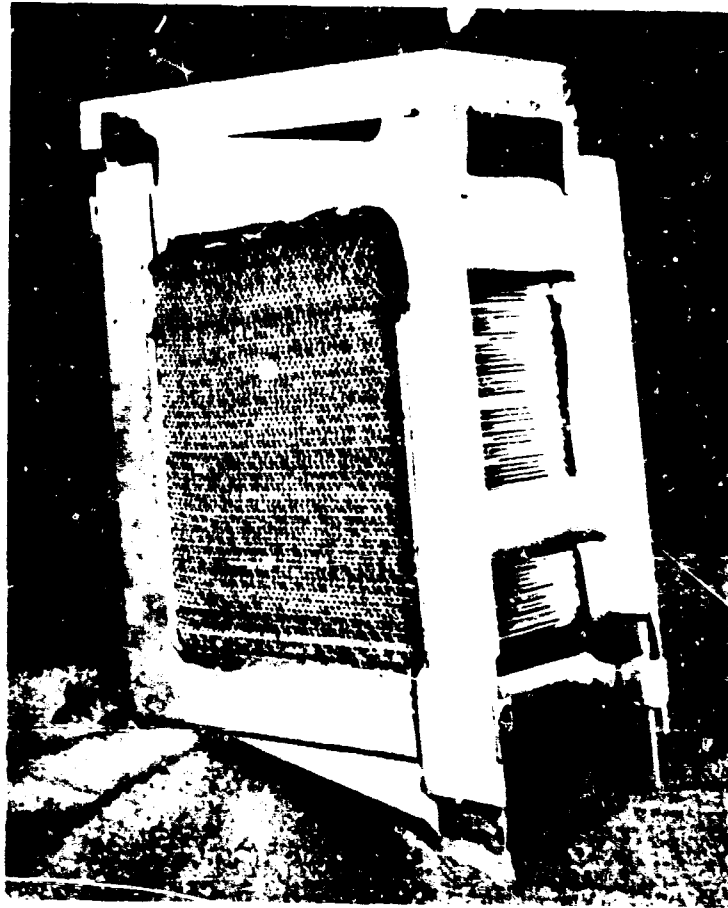
Figure 67. Complete Module Brazing Fixture.

Control of the amount of brazing alloy to avoid wall erosion was considered to be easiest if the alloy was applied in 0.002-inch foil strips between layers at the formed ends. The insertion of the foil strips resulted in a module height before brazing which was larger than the desired final module size. To maintain contact pressure during the brazing cycle and to accommodate the thermal expansion during heating, the fixture was built in two sections with the joints placed on a module diagonal. The fixture as a whole was tilted from the vertical to obtain lateral and vertical pressure from the weighted (three pounds), movable upper half. Guides constraining the direction of motion and stops were placed at the desired final module height

4.500
4.498

3.960
3.958

3.035
3.045

GUIDE JOINT
(4 PLACES)
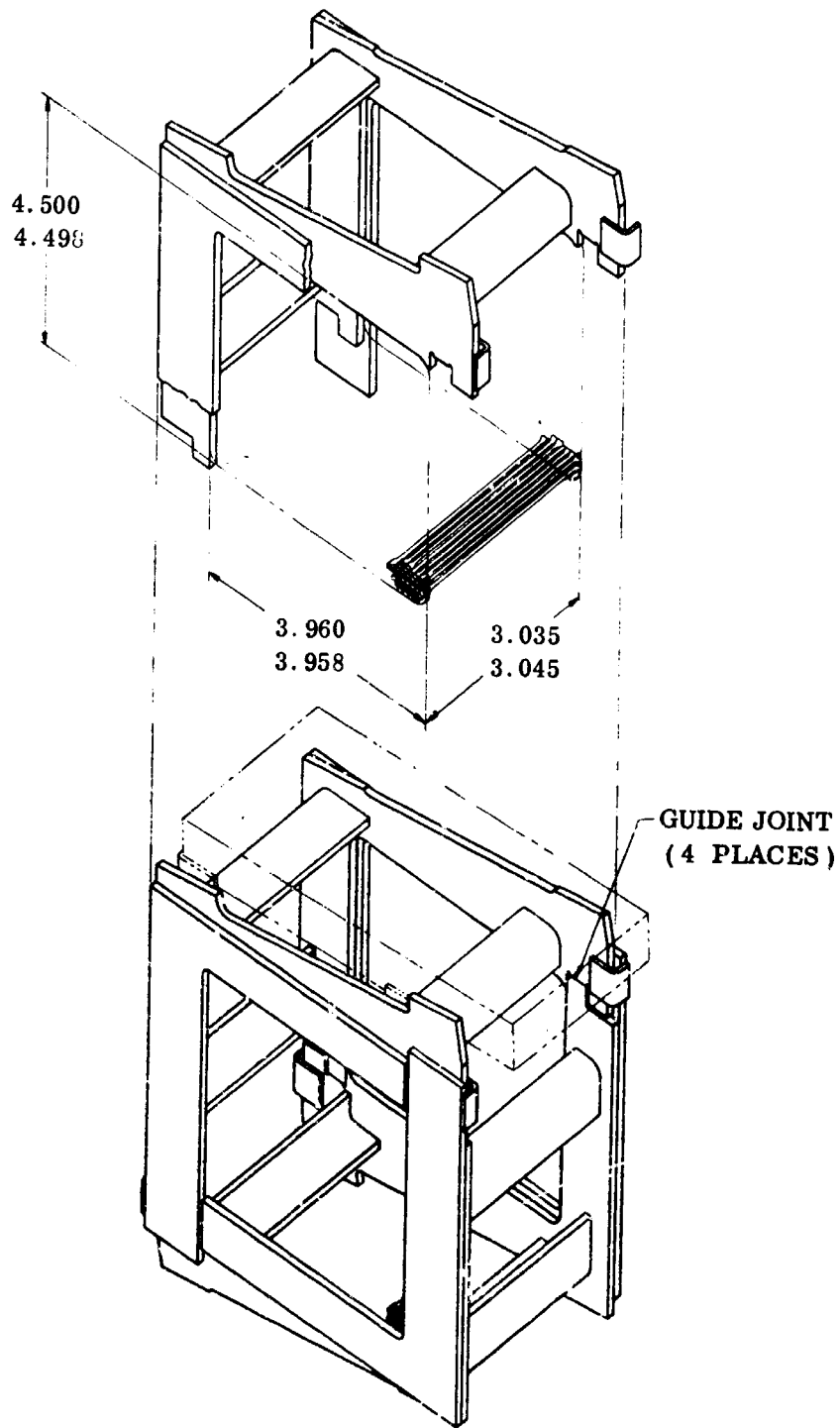
Figure 68.   Complete Module Brazing Fixture.

85

The brazing of double layer subassemblies was successfully demonstrated in the laboratory and later duplicated in experimental assembly; however, warping of the fixtures during brazing resulted in some rejections of sub-assemblies and required frequent rework of the fixtures. Enough subassemblies were produced, however, to start the second step. Brazing the double layers into a complete module in the two-piece fixture proved to be a difficult operation.

The first module brazed into this fixture is shown in Figure 69. As is evident from the picture, the brazing was incomplete, with gaps remaining between layers as well as between some tubes in same layer. From the appearance of the finished part, it was deduced that the weight of the upper half had led to local yielding of the lower tube layers before the assembly had reached the liquidus of the brazing alloy. Subsequently,
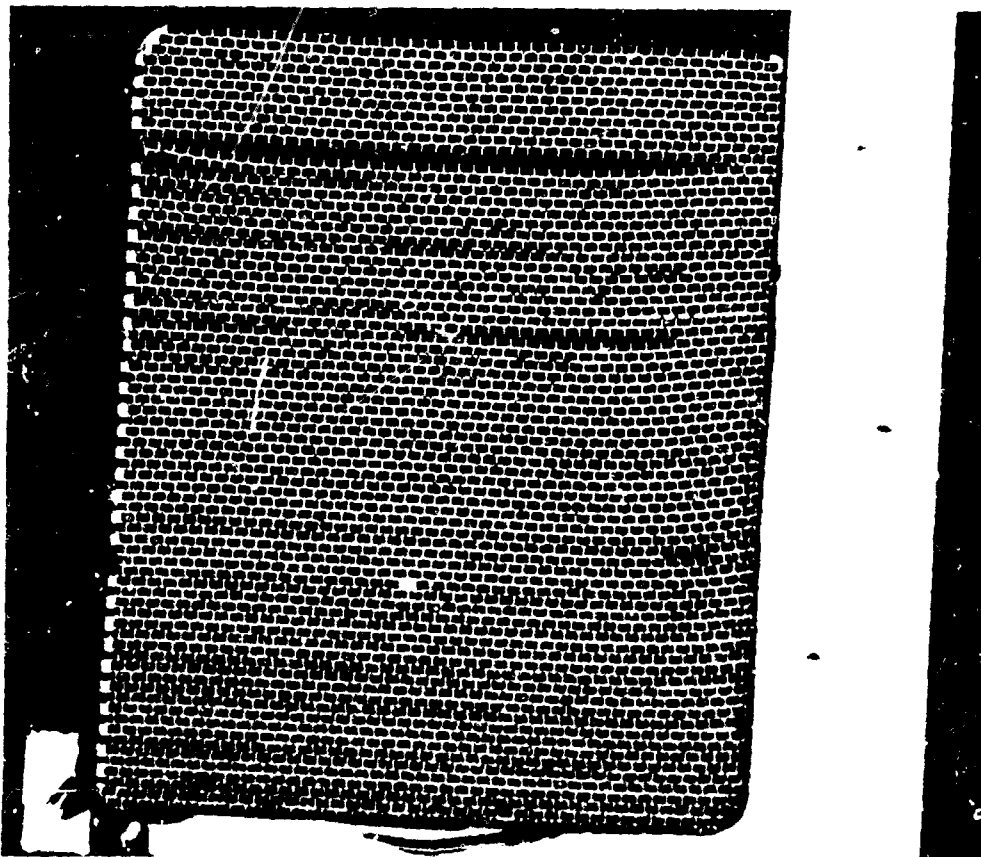
Figure 69. Module Brazed at Boeing.

during melting of the brazing alloy, the module shrank. The upper half of the fixture came to rest on its stops; but because of the yielded tubes, the module assumed a height smaller than that set by the stops, and contact pressure was lost. Without the pressure from the upper half, some of the tube layers hung up on the sides of the fixture, and gaps between layers developed. With these larger gaps, capillary action was reduced, and brazing alloy filtered downward. The result was an excess of alloy at the bottom and alloy deficiency at the top of the module.

Following this experience, several tests were conducted in which approximately 12 layers were brazed into the bottom of the same fixture with the remainder of the module height being taken up by a filler piece. In these tests, the weight on top of the fixture was varied. The tests led to the conclusion that the maximum weight permissible to avoid yielding of the bottom tubes was less than the minimum weight required to maintain adequate contact pressure on the top layers of the module. It was therefore apparent that this approach would require considerable development. As a result, an outside brazing specialist, The Pyromet Company, of San Carlos, California, was contacted. In parallel with Boeing, and assisted by prior Boeing studies, Pyromet found a successful technique that would correct the previous difficulties, as discussed below. Accordingly, all further brazing work was performed by the Pyromet Company.

Pyromet's approach was to spot-weld all components into a complete assembly which was self-aligning. Tubes were spot-welded into single layers by aligning them between flat plastic plates. The single layers were then assembled into a complete module and spot-welded to each other at about each fifth tube along the layers. As each layer was added, brazing alloy (Engelhard 440) in paste form was placed behind each joint, and a section of each tube behind the expanded end was coated with white stop-off. The suspension was then spot-welded to the tubes on each side and supported with ceramic fillers to maintain the proper fit-up and position during the brazing operation. Steel frames to hold the module in the test rig were then spot-welded to the suspension.

The spot-welding was done with two stored-energy-type machines. One was a Stryco Manufacturing Model SE-100; the other, a Federal Tool and Engineering Model DC-80-C. Tweezer electrodes were used, and the energy used was 5 watt-seconds for the tube-to-tube welds and 15-20 watt-seconds for the tube-to-suspension and suspension-to-frame welds.

The assembly was brazed in dry hydrogen in a sealed retort. The temperature was raised to 1800°F and held at this temperature for 15 minutes to equalize the temperature throughout the module. The temperature was then raised at a maximum rate of 400°F per hour to a point just above the

liquidus of the brazing alloy (2100°F). Immediately upon reaching this temperature the heat was turned off and the assembly was cooled in the retort. Brazing defects in the first brazing cycle were repaired in one or more additional cycles using silver-palladium alloys with lower melting points to avoid remelting of the original joints (Engelhard 431, melting at 2000°F, and Engelhard 428, melting at 1900°F). Figure 70 shows a typical heating curve as indicated by a thermocouple attached to the module.

Three modules were brazed by Pyromet: two with straight tubes and one with wavy tubes. The first module, when received by Boeing, showed sagging of the tubes and a large gap at the top (Figure 71). This condition was repaired by adding some tubes and by rebrazing (Figure 72). The sagging was avoided on the other modules by spot-welding the suspension to both the upper and lower tube rows and by supporting the suspension with ceramic fillers. The second module (Figure 73) showed no problems of sagging, but because some voids had occurred in the braze of the first module, extra brazing alloy had been added to the second to avoid a recurrence. Subsequent X-ray photographs showed that brazing alloy had filleted between the tubes for an average of 1/4 inch from each face. Several tubes were filleted two-thirds of the tube length. The excess brazing alloy constricted airflow and tended to increase thermal stresses as discussed earlier. On the third module (wavy-tube), the amount of brazing alloy was carefully controlled, and, as shown in Figure 74, the results were close to design expectations: experimental fabrication of this type of brazed module had thus been demonstrated.

TESTING AND EVALUATION

Vibration Tests

Vibration tests were run on the second straight-tube module and the wavy-tube module. Each module was installed in a housing and mounted on a shaker table at the Boeing Aero-Space Division Vibration Laboratory. The module was vibrated in a direction parallel to the tubes. An accelerometer was mounted at the tube ends to record the response of the module to the input vibrations.

Initial testing was done on the second straight-tube module as received from Pyromet and was aimed at determining the resonant or critical frequencies of the module. Sweeps at a 10g input level were made from 20 to 2000 cycles per second and over narrower ranges at slow rates. The resonant frequency was found to be shifting, and in a short time severe damage to the corners of the module suspension was apparent (Figure 75).

RETORT REMOVED
FROM FURNACE
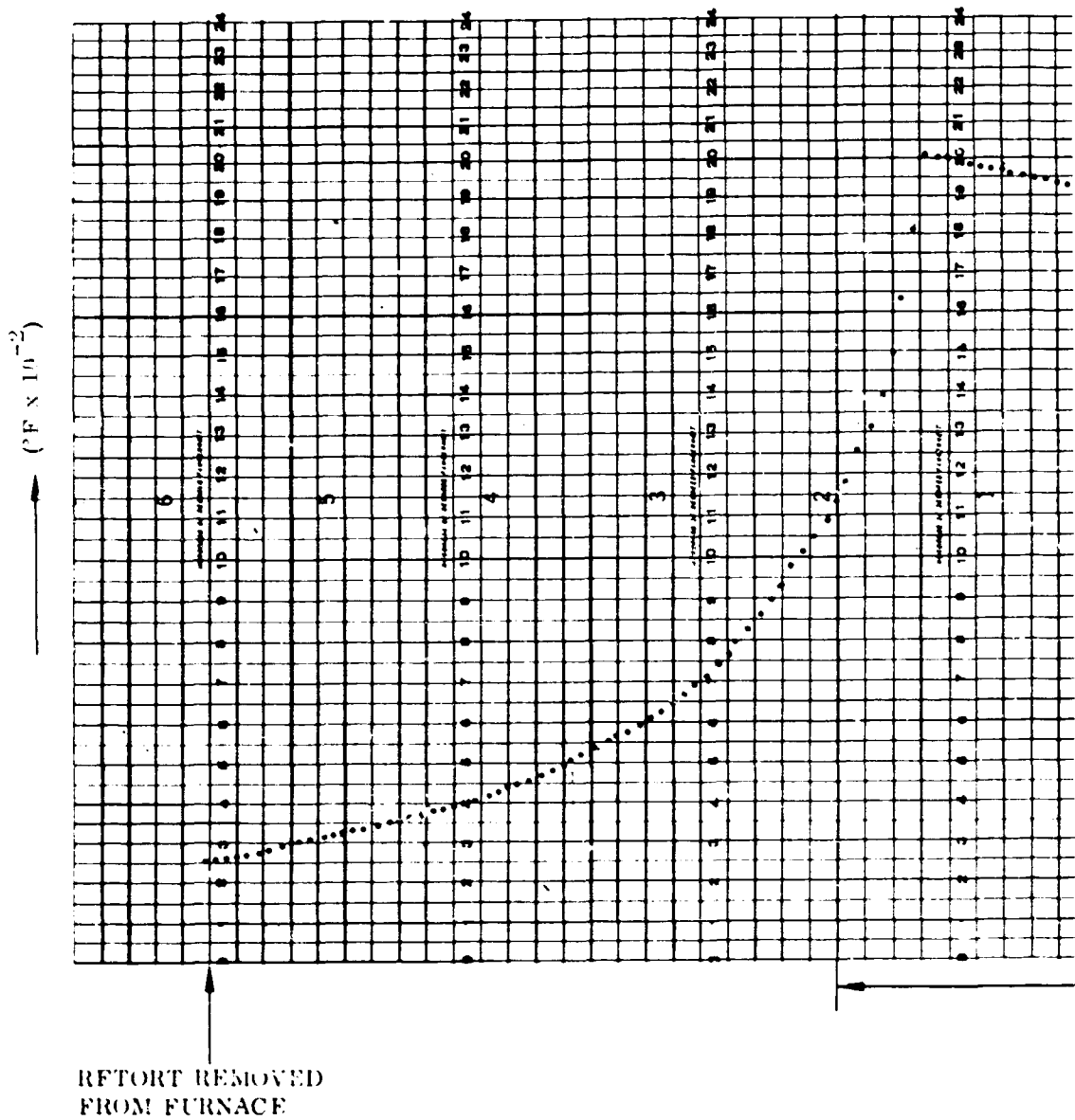
Figure 70. Pyromet Braze Cycle Temperature versus Time.
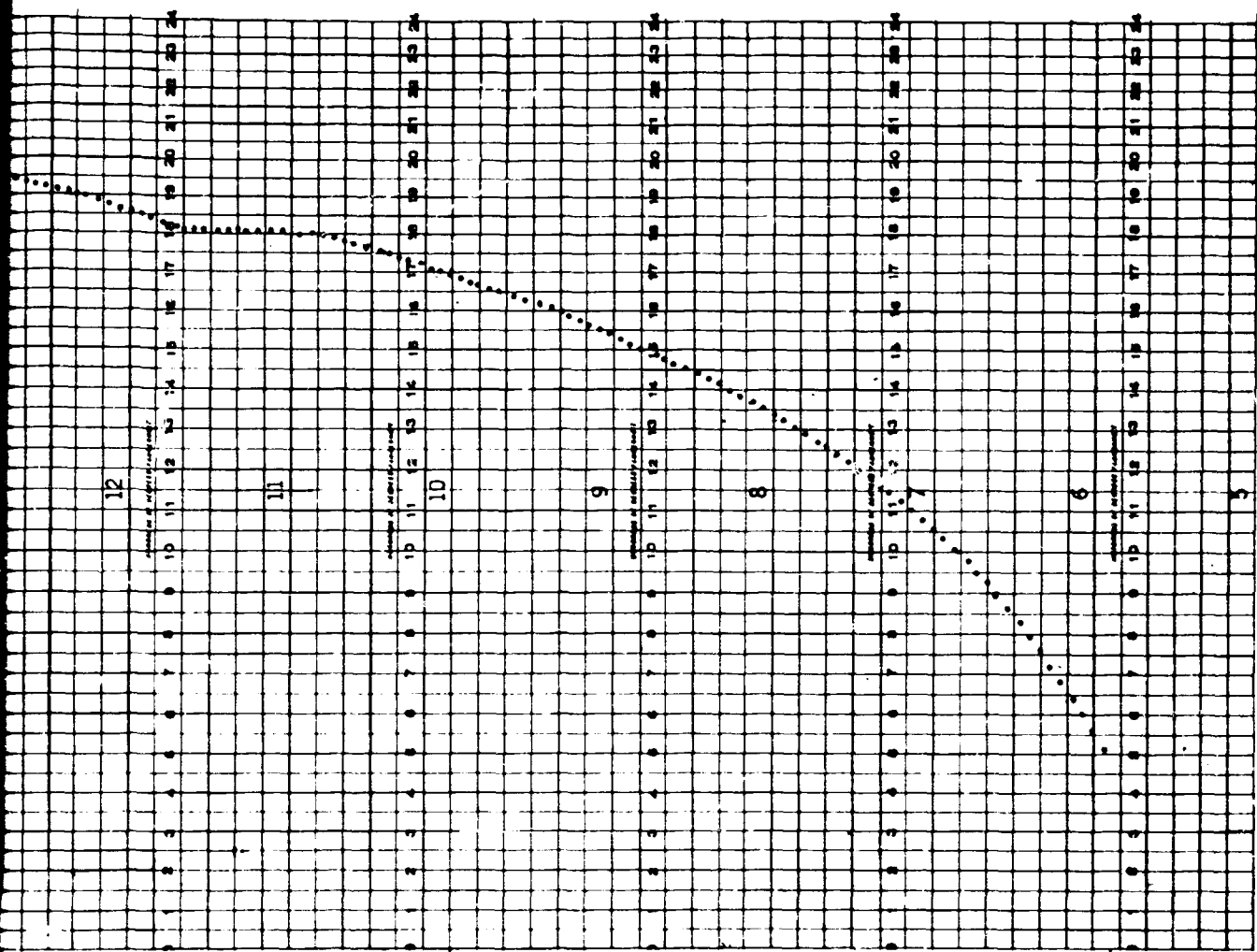
1 HOUR

RETORT PLACED
INTO FURNACE
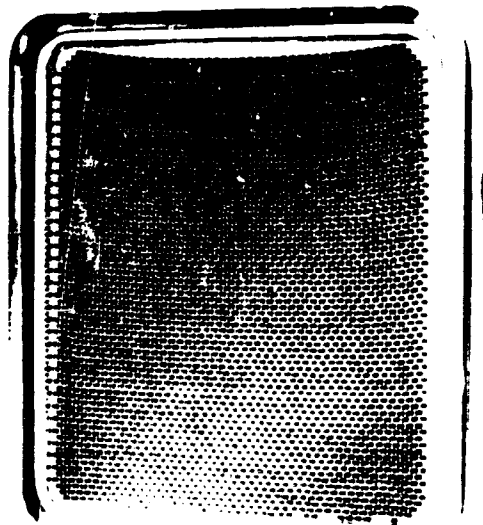
Figure 71.   First Straight-Tube Module
as Initially Received.
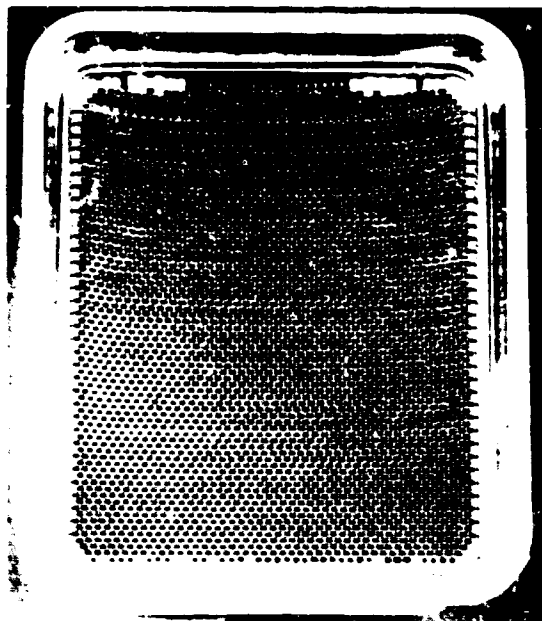
Figure 72.   First Straight-Tube Module
After Repair.
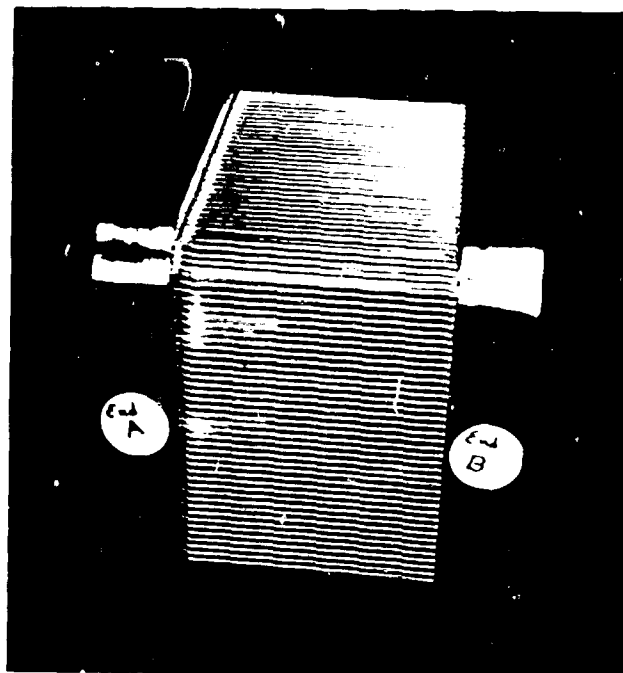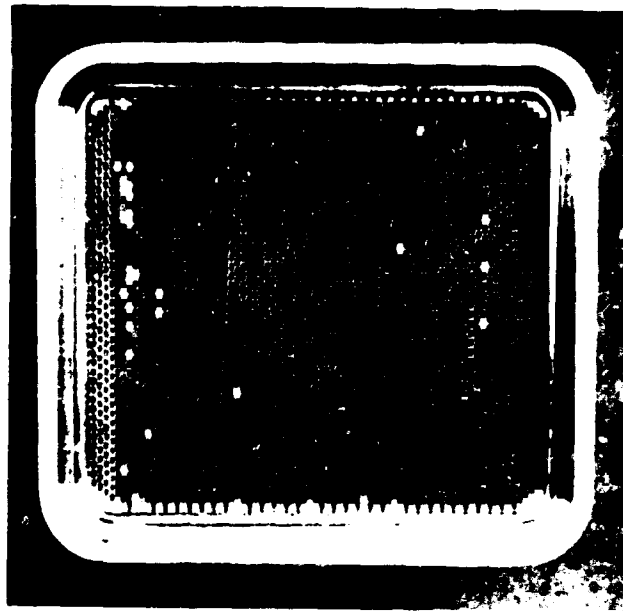
Figure 73. Second Straight-Tube
Module as Received.
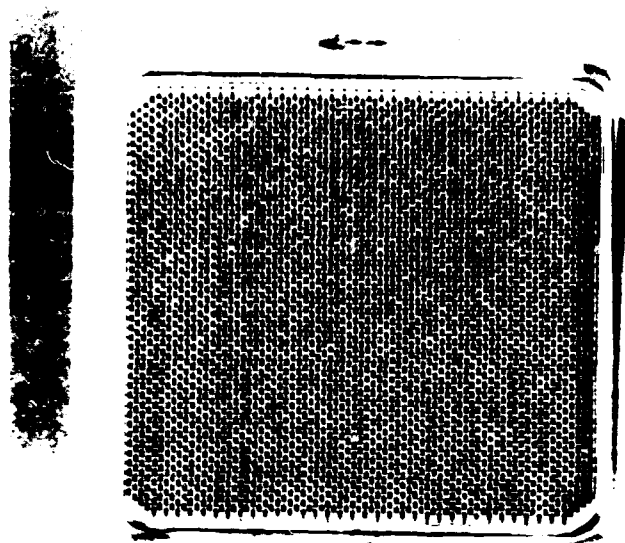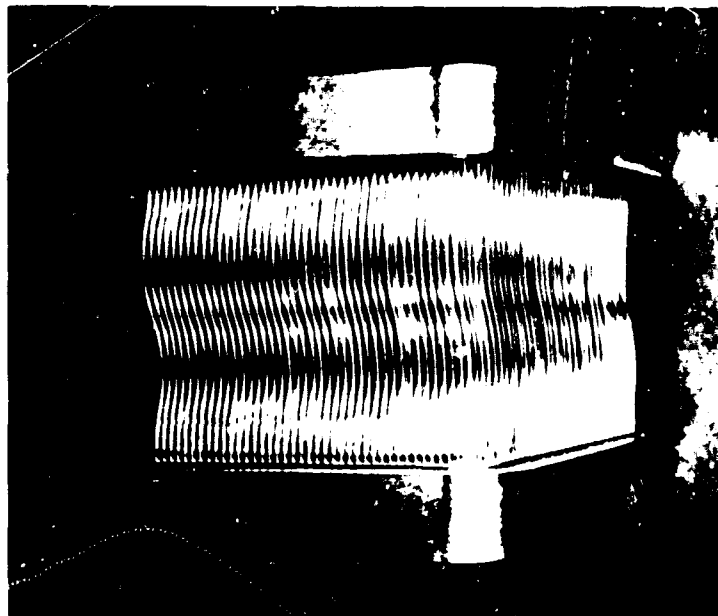
Figure 74. Wavy-Tube Module as Received.

93
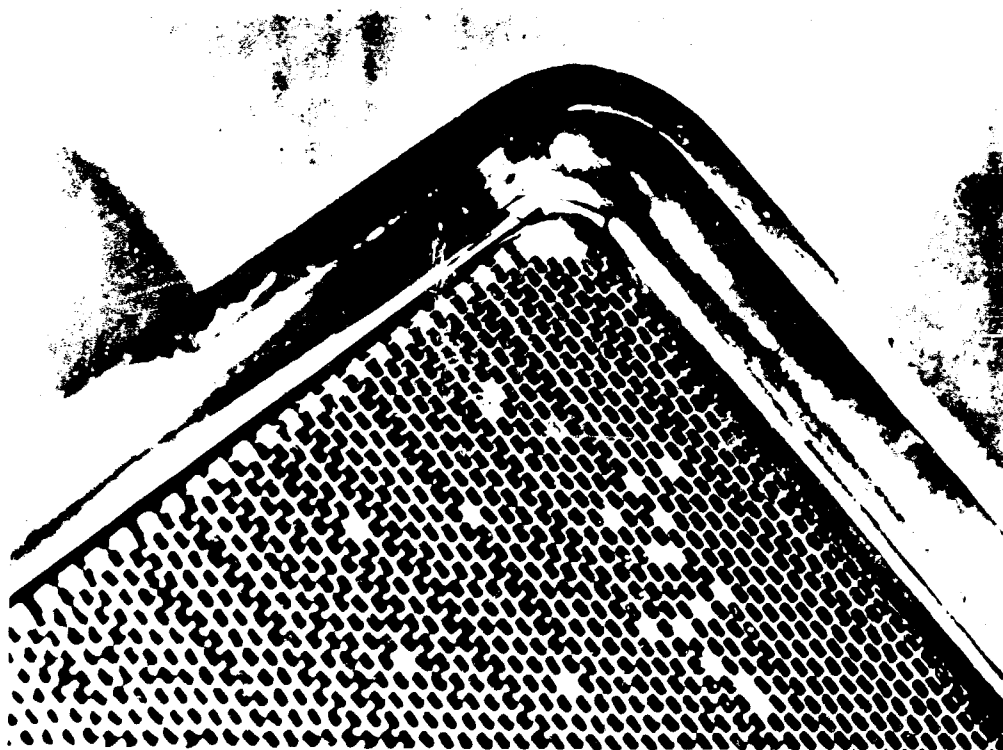
Figure 75. Damage to Corner of Suspension After
First Vibration Test.

It was concluded that this result was not representative of a module instal-
lation, especially in view of the fact that the test was conducted without
the air-side sealing pillows in place. These sealing pillows were expected
to provide some damping and to reduce vibration amplitudes. The suspen-
sion of this module was replaced, and pillows were installed for the next
series of tests, aimed at establishing vibration characteristics. Sine wave
sweeps were made from 20 to 2000 cycles per second at input g levels of
from 1 2 to 10. Output peak response and amplitude were recorded at
each input g level. Table V presents the results. The output response
pattern showed variations with time; and at the 10g input, failure in the
corner again occurred, this time within 4 minutes.

To correct the difficulty, the suspension was modified by inserting two
small steel spacers into one end and retaining them with epoxy cement
(Figure 76) as an expedient to assess changes in response. It was believed
that the inserts would restrain one end of the suspension, thus raising the

94

TABLE V
VIBRATION TESTS OF SECOND STRAIGHT-TUBE MODULE

	Input Accelero-meter g	Peak Response g	Frequency cps	1/2 Amplitude in.	Remarks
2nd Straight-Tube Module (no bypass pillows installed)	10	-	-	-	Failure occurred after a few min-utes of vibration in the critical region of 200-400 cps
2nd Straight-Tube Module (with by-pass pillows installed)	1	14.5	385	.00190	Response pattern changing with shake time and vibration input
	1/2	52.5	1109	.00080	
	1/2	20.0	1563	.00017	
	1/2	15.0	1541	.00012	
	1/2	21.0	1936	.00011	
	2	34.4	365	.00500	
	3	42.0	328	.00750	
	3	54.0	365	.01000	
	5	42.6	315	.00850	
	5	48.6	363	.00700	
	8	51.0	287	.01300	
	8	40.0	356	.00630	
	10	100.0	210	.04400	Failure occurred

resonant frequency and reducing displacement. The module with this modification was subjected to input levels of 2g's to 10g's over frequency ranges of 10 to 2000 cycles per second and 100 to 700 cycles per second, respectively. Results showed that neither the output displacement nor the resonant frequency was altered appreciably. It was reasoned that the inserts had little effect because the section formed by the brazed expanded ends of the tubes still was flexible; therefore, fixing the suspension locally had little effect on the motion of the whole section.

SPACER

FLEXIBLE SUSPENSION

SPACER

FLEXIBLE SUSPENSION
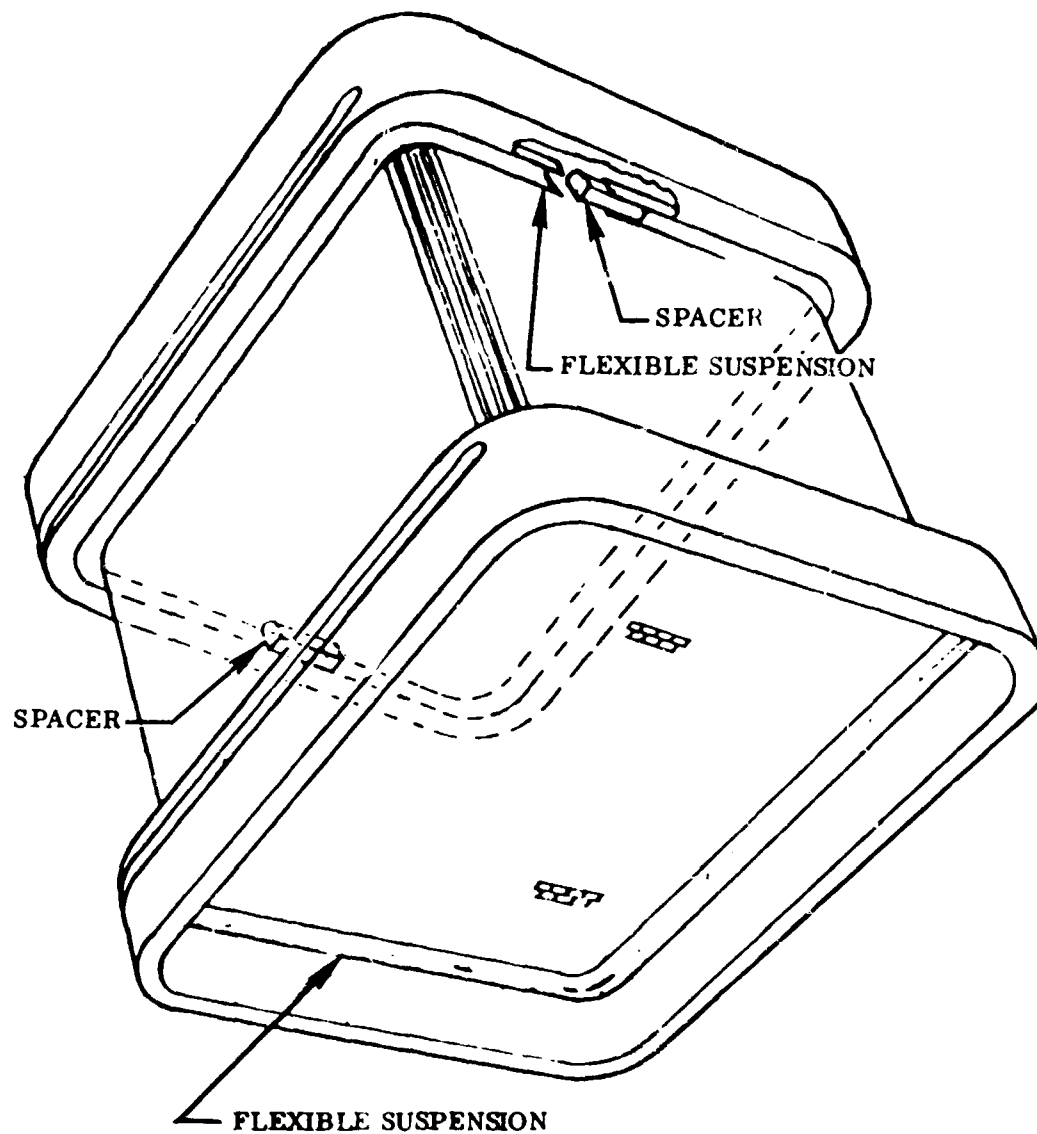
Figure 76.   Suspension With Steel Spacers.

Three other changes were tried, each one using stiffener guides running the full length of the module on two sides. In the first, the stiffener was connected to the frames by means of a piece of sheet metal, as shown in Figure 77. In the second, the sheet metal was replaced by four pieces of hard rubber; in the third, by some wire mesh bent into a tight accordion, as shown in Figure 78. None of these changes had any significant effect on the output response of the module.

On the basis of the above tests, the suspension was redesigned to be more flexible in the corners. The existing suspension was removed from the wavy-tube module, and the new design was brazed into position by Pyromet. The new suspension is shown in Figure 79. The wavy-tube module with this modified flexible suspension was subjected to vibration scanning tests similar to those conducted on the second test module. The bypass pillows were shimmed to give a tighter fit. The resonant frequency with this configuration was determined over a range of input levels from 1 through 10g's, and the maximum input level that could be sustained safely for about 4 minutes was established. No visible damage to module or suspensions was observed during the 1 through 9g input levels. The module was retested at the 5g level and produced the same resonant frequency as originally noted. The module was then subjected to a 10g input for a total of 5 minutes. A rerun at 4g's showed a slight shift in the resonant frequency, indicating possible suspension damage. A small crack (Figure 80) was visible after testing. The result of these vibration tests is included as Table VI. It can be concluded that in the design of an engine using this type of regenerator, effort should be directed towards minimizing engine-induced vibrations in the 380-500 cycles per second region.

To demonstrate the ability of the module to withstand an engine environment, the second straight-tube module was installed on a Boeing T50 engine for a 66-hour endurance test. No damage to the module suspension was apparent after testing. During the tests, an accelerometer was attached to the regenerator mounting, and the vibration characteristics were recorded at several engine speeds from 13,500 to 38,500 revolutions per minute. The data taken indicated an amplitude peak in the critical frequency range of the module. It was concluded that this peak resulted from resonance of the module, caused by random engine vibrations, which was fed back into the mounting. Analysis of the data indicated that this peak was greatest at 38,500 revolutions per minute, where its value was 1.85g's. This value is well below g levels where suspension failures and, consequently, engine-induced vibration problems would not be expected. However, since engine vibration characteristics are dependent on the complete engine package, it is recommended that specific regenerator vibration problems be solved in conjunction with the intended application.

97
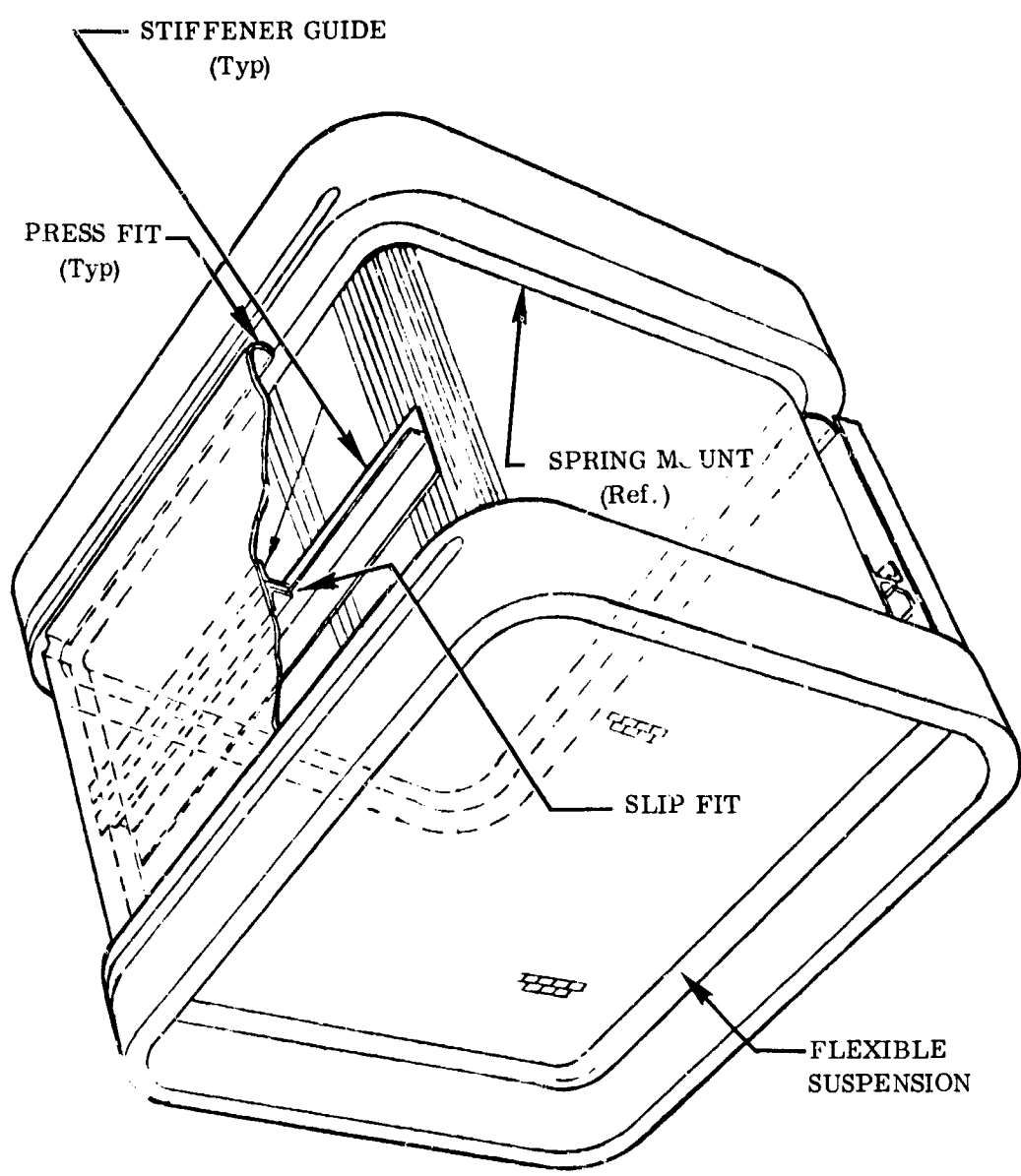
Figure 77. Module With Stiffener Guide.

HARD RUBBER

FRAME

FLEXIBLE
SUSPENSION

TUBES

RUBBER STIFFENING

STAINLESS STEEL MESH
BENT INTO TIGHT
ACCORDION

TUBES

STEEL MESH STIFFENING
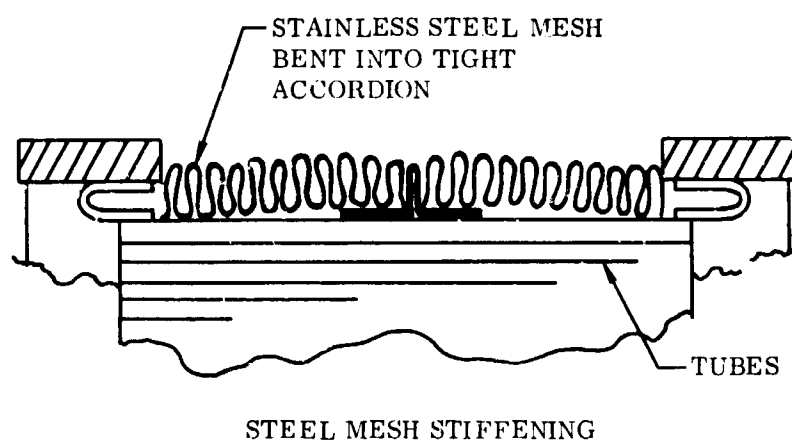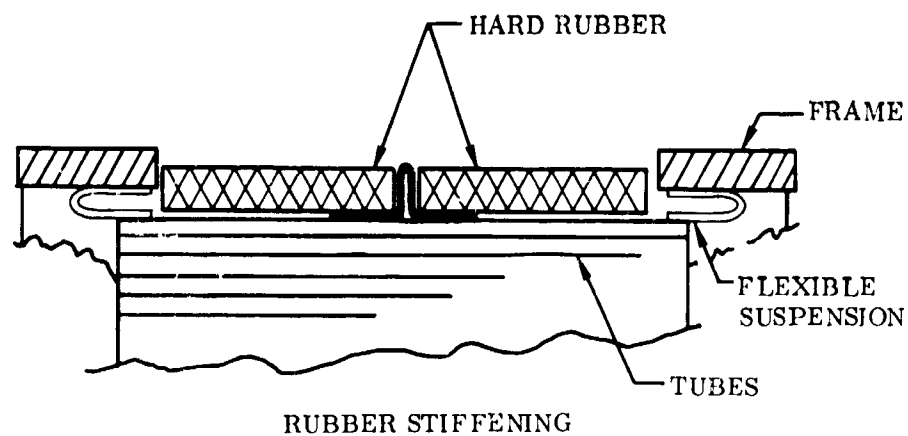
Figure 78.   Other Suspension Stiffening
Modifications.

.200 (REF)

.040R

.060R

.100R
SECTION B-B
(4 CORNERS
TYPICAL)

.065

.100R

.158

.030 R
(TYP)

.165

SECTION A-A
(ROTATED 90° CCW)

B

B

.468R
(TYP)

A

A
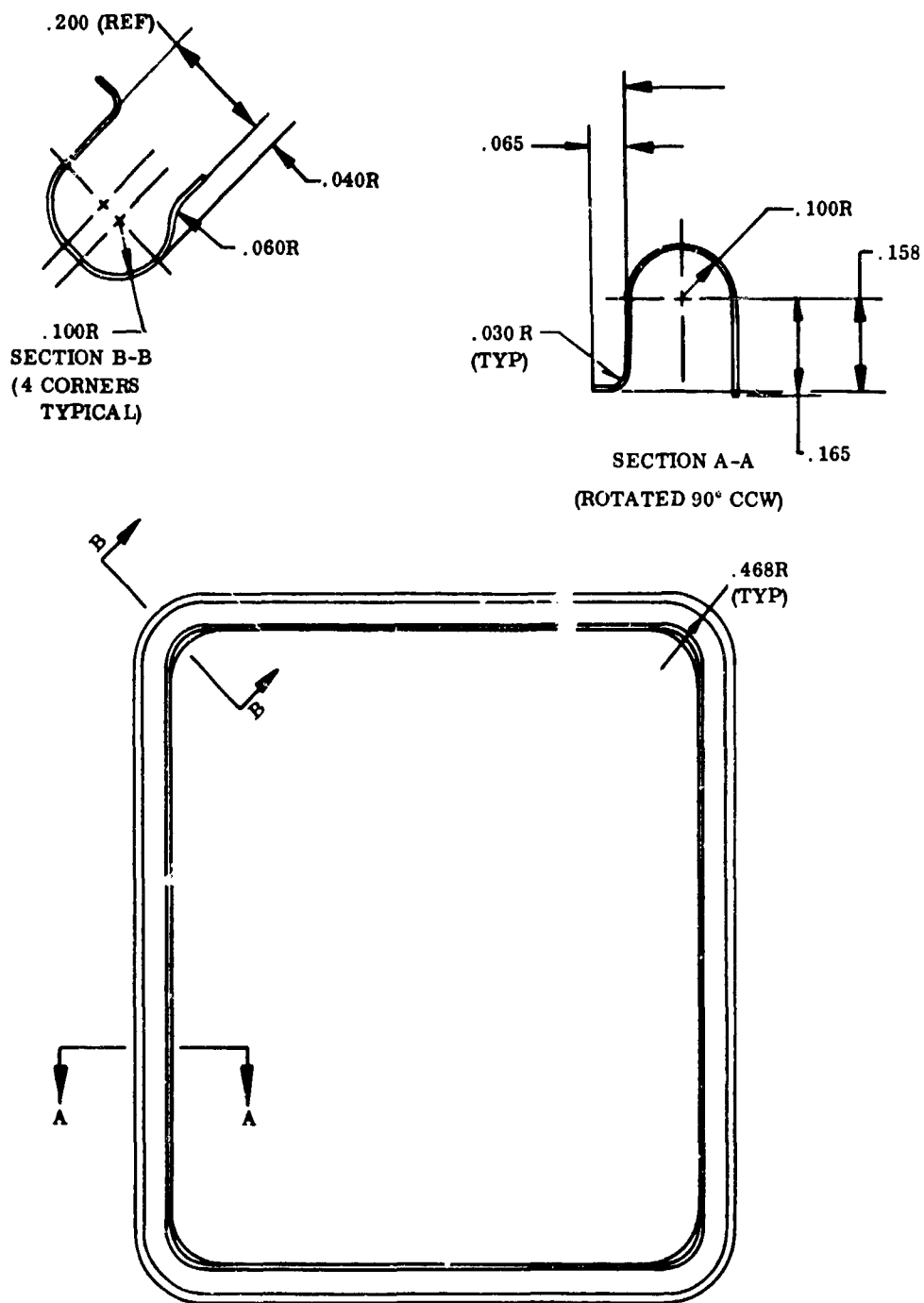
Figure 79. Modified Flexible Suspension.

100
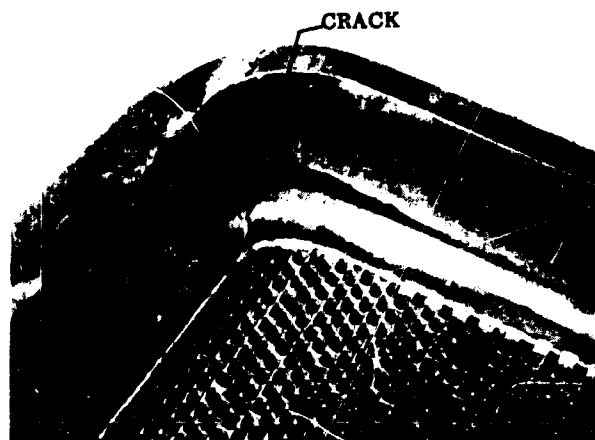
Figure 80. Crack in Modified Suspension.

TABLE VI
VIBRATION TEST OF WAVY-TUBE MODULE WITH MODIFIED SUSPENSION

Input Accel. (g)	Peak Response (g)	Resonant Frequency (cps)	Time At Res. Freq.
1	19	480	
2	29	430	
3	-	420	
4	30	405	2-1/2 Min.
5	43	380	2-1/2 Min.
6	47	385	4 Min.
7	53	370	4 Min.
8	54	355	4 Min.
9	56	350	4 Min.
5	44 (Retest)	380	Few Secs.
10	60	360	5 Min.
4	41 (Retest)	380	Few Secs.

101

Thermal Shock Rig

The thermal shock rig was designed as a multipurpose rig. The primary functions were to evaluate the ability of the modules to withstand thermal shock and to determine fouling and performance characteristics. A schematic of this rig is shown in Figure 81, and the actual hardware is pictured in Figure 82. This rig was designed to use up to 2 pounds per second of compressed air. Up to 1.5 pounds per second of air at pressures up to 100 pound per square inch could be heated by burning JP-5 in a burner of the type used in a small gas turbine engine. A portion of the combustion products could be bled off and mixed with high-pressure air to simulate fluid conditions experienced on the air (cooler) side of a gas
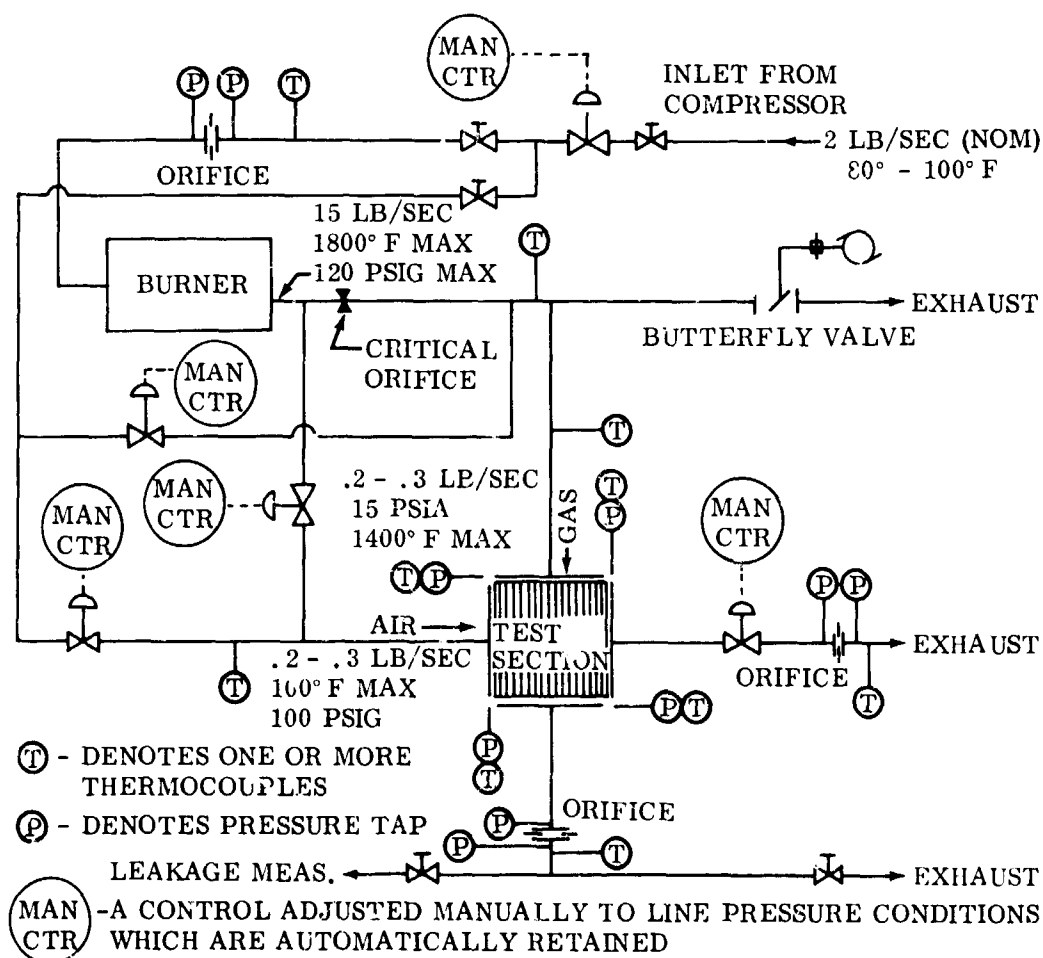
Figure 81. Thermal Shock and Fouling Rig.
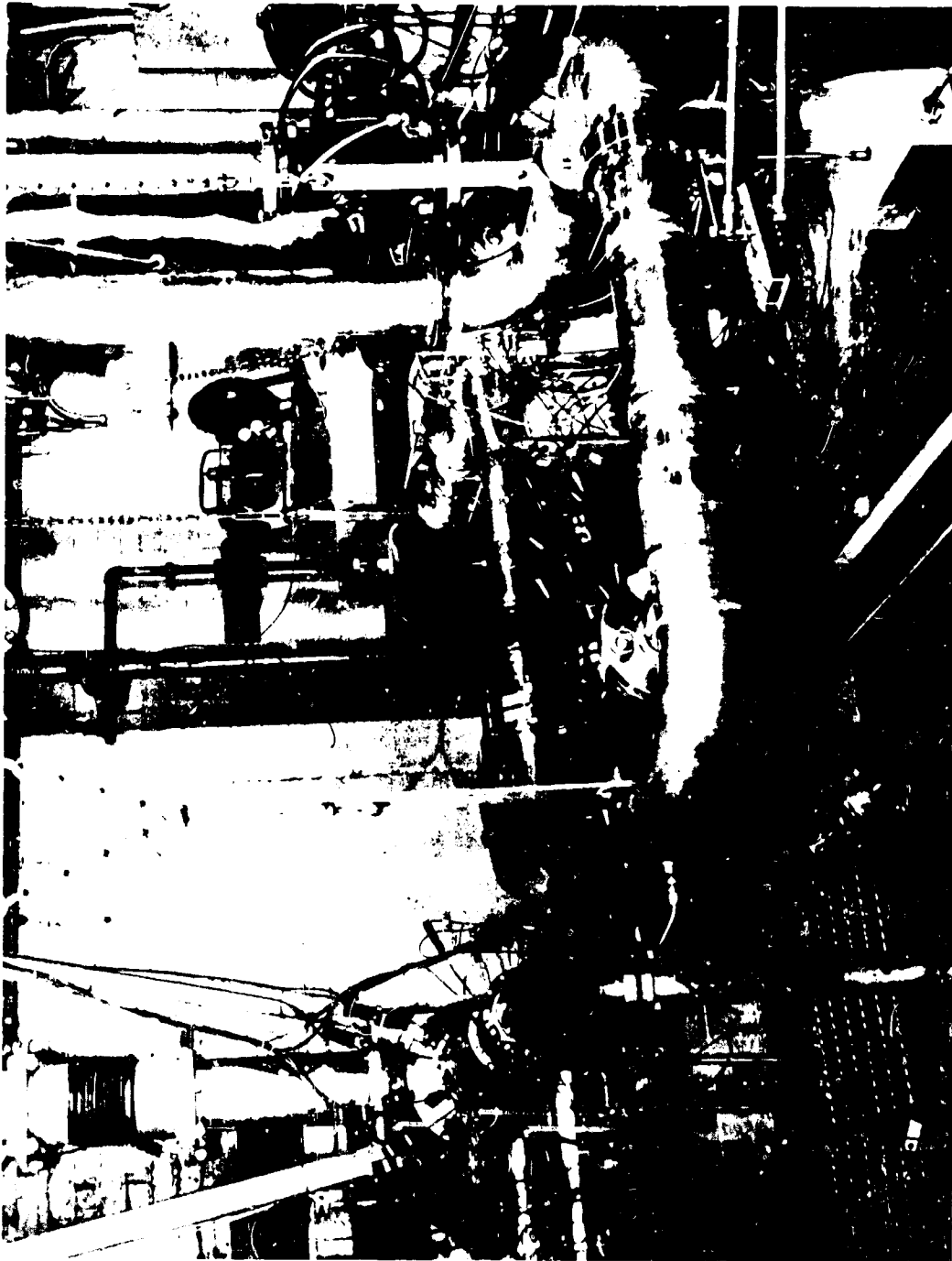
Figure 82. Thermal Shock and Fouling Rig.

turbine regenerator. This flow could be varied between 0.2 and 0.3 pound per second at pressures between 55 and 100 pound per square inch and at temperatures between 400° and 650°F. A range of temperature of the remaining burner flow (simulating turbine engine exhaust) from 750° to 1350°F could be achieved by regulating fuel flow to the burner. Part of this flow could be diverted to the gas (high temperature) side of the module by a butterfly valve. Gas flow through the test section could be varied from 0.2 to 0.3 pound per second. The rig could be operated through ranges of mass flow, temperature, and pressure to simulate all phases of engine operation from idle to full power. The only condition of the model engine (2300°F TIT, 10:1 pressure ratio) which the rig could not duplicate was the air-side pressure, which was limited to 100 pound per square inch by the supply pressure available to the test cell. During rig operation, the presence of products of combustion on the air side of the modules caused partial fouling of that side, a condition that would not normally occur in actual engine operation. It should also be noted that in each test a single module was subjected to simulated regenerator inlet gas and air temperatures rather than conditions matching the two-pass temperatures for which the modules were designed. Therefore, the test imposed considerably higher (more severe) temperature gradients than would be experienced in a two-pass, cross-counterflow system, and represent an extreme test of structural capability.

Fluid temperature changes through the module were determined from six thermocouples at each fluid inlet and outlet. Each thermocouple represented an equal area of the flow passage so that average temperatures could be determined. Air and gas pressures and pressure drops across the test module were determined from static pressure taps placed in constant area sections at gas and air inlet and outlet sections. Since entrance and exit measuring sections were of equal cross-sectional area and the flow Mach numbers were on the order of 0.1, the pressure drops could be considered as total to total. Figure 83 shows the module housing and indicates the location of pressure taps and thermocouples. Mass flows on the air and gas sides were measured with calibrated orifices. Table VII presents a description of testing performed on this rig, and Tables VIII and IX show the test schedules of the first straight-tube and the wavy-tube modules. The second straight-tube module was subjected only to performance tests, similar to the wavy-tube module. Appendix VIII presents data sheets typical of those taken on thermal shock rig testing.

NOTE:

T/C - THERMOCOUPLE

P/T - PRESSURE TAP
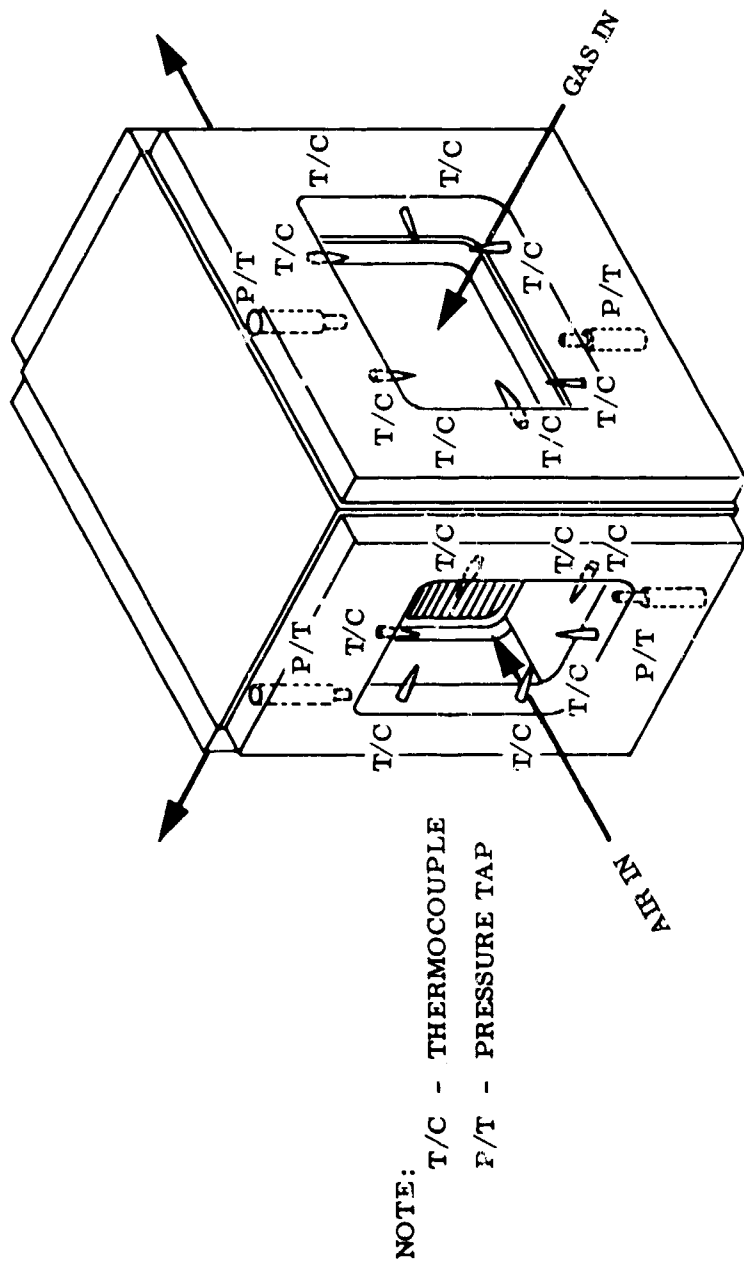
Figure 83. Thermal Shock Rig Housing Showing Instrumentation.

TABLE VII
DESCRIPTION OF THERMAL SHOCK TESTS

RUN NO.	DESCRIPTION
21	**Pressure Check** Hold pressure and flow at specified levels on one side (air or gas). Ambient temperature.
25	**Temperature Check** Hold temperature and flow at specified values on one side. Pressure at low level (close to ambient).
34	**Temperature Gradient Check** Hold temperature and flows at specified levels on both sides. Hold pressures close to ambient.
39	**Performance Measurements** Hold air and gas temperatures, flows, and pressures at specified values to simulate idle, 50 percent, and full-power levels. Hold until measurements stabilize.
42	**Thermal Shock** Stabilize at specified temperatures, pressures, and flows. Then turn burner off and on.
45	**Fouling Tests** Stabilize at temperatures, pressures, and flows to simulate idle, 50 percent, and full-power setting. Hold at each setting for 8 hours.
--	**Cyclic Test** Alternate between idle and full-power setting. Hold at each level for specified time. Change settings as rapidly as possible.
--	**Endurance Test** Hold at specified conditions for specified time. This test is designed to simulate an average of engine power settings.

TABLE VIII
FIRST STRAIGHT-TUBE MODULE
THERMAL SHOCK AND FOULING TEST PROGRAM

	RUN No.	AIR SIDE			GAS SIDE		
		Press psig	Temp °F	Max. Flow lb/sec	Press psig	Temp °F	Max. Flow lb/sec
Pressure Check							
a) Air Side	21	5	70	0.3	0	70	0
	22	45	70	0.3	0	70	0
	23	100	70	0.3	0	70	0
b) Gas Side	24	0	70	0	20	70	0.3
Temperature Check	25	5	300	0.3	0	70	0
a) Air Side	26	5	500	0.3	0	70	0
	27	5	700	0.3	0	70	0
b) Gas Side	28	0	70	0	0	300	0.3
	29	0	70	0	0	500	0.3
	30	0	70	0	0	700	0.3
	31	0	70	0	0	900	0.3
	32	0	70	0	0	1100	0.3
	33	0	70	0	0	1300	0.3
Temperature Gradient Check	34	10	300	0.3	0	500	0.3
a) Air and Gas Side Combined	35	10	500	0.3	0	700	0.3
	36	10	700	0.3	0	900	0.3
	37	10	700	0.3	0	1100	0.3
	38	10	700	0.3	0	1300	0.3
b) Performance Measurements	39	55	400	0.2	0	750	0.2
	40	85	550	0.25	0	1050	0.25
	41	100	650	0.3	0	1300	0.3
Thermal Shock	42	55	400	0.2	0	750	0.2
Air and Gas Side Combined	43	85	550	0.25	0	1050	0.25
	44	100	650	0.3	0	1300	0.3
Fouling Test	45	55	400	0.2	0	750	0.2
	46	85	550	0.25	0	1050	0.25
	47	100	650	0.3	0	1300	0.3
	48	100	650	0.3	0	1300	0.3
	49	85	550	0.25	0	1050	0.25
	50	55	400	0.2	0	750	0.2

Flow /sec	TIME BASE Rate sec	Hold min	TEST TIME INCLUDING TRANSIENTS Hours	NOTES	FLAG IDENTIFICATION
	▷1			▷2	▷1 Change pressures and temperatures slow
		5			
		5	1/2	▷3	▷2 Leak check after each run by using blind
		5			flange on gas inlet and bubble test on gas
0.3	▷1	5		▷4	outlet. 125 psia on air side.
		10		▷7	▷3 Limit airflow so pressure drop across te
	▷1	10		▷3	module does not exceed 15 in. Hg.
		10			
0.3		10	4-1/2		▷4 Limit gas flow so pressure drop across
0.3		10		▷2	test module does not exceed 40 in. WC.
0.3	▷1	10			
0.3		10		▷4	▷5 Turn burner on and off.
0.3		10			
0.3		10			▷6 Weigh clean test module before test; wei
0.3		10		▷2	module after each run if fouling occurs a
0.3		10			indicated by performance change.
0.3		10		▷2	
0.3	▷2	10			▷7 Run at each level for 30 minutes; change
0.3		10		▷4	between levels at maximum rate.
0.3		10	4		
0.2		30		Idle ▷7	▷8 Minimum pressures dictated by system
0.25	▷7	30		50% ▷3	back pressure.
0.3		30		100% ▷1	
0.2		10		10 cycles ▷2	▷9 Run at idle 10 minutes, 100% power
0.25	▷5	10	8-1/2	10 cycles ▷3	30 minutes; change conditions as rapidly
0.3		10		10 cycles ▷4	as possible.
0.2		480		Idle ▷2	
0.25		480		50%	
0.3		480		100%	
0.3	▷9	480	54-1/2	100% ▷3	
0.25		480		50% ▷4	
0.2		480		Idle ▷6	

2

TABLE IX
WAVY-TUBE MODULE
THERMAL SHOCK AND FOULING TEST PROGRAM

	RUN No.	AIR SIDE			GAS SIDE		
		Press psig	Temp °F	Max. Flow lb/sec	Press psig	Temp °F	Max. Flo lb/sec
Performance Measurements	39	55	400	0.2	0	750	0.2
	40	35	550	0.25	0	1050	0.25
	41	100	650	0.3	0	1300	0.3
Thermal Shock	42	55	400	0.2	0	750	0.2
Air and Gas Side Combined	43	85	550	0.25	0	1050	0.25
	44	100	650	0.3	0	1300	0.3
Endurance Test	--	100	620	0.3	0	1150	0.3
Cyclic Test	--	55	400	0.2	0	750	0.2
	--	100	650	0.3	0	1300	0.3
Fouling Test	45	55	400	0.2	0	750	0.2
	46	85	550	0.25	0	1050	0.25
	47	100	650	0.3	0	1300	0.3
	48	100	650	0.3	0	1300	0.3
	49	85	550	0.25	0	1050	0.25
	50	55	400	0.2	0	750	0.2

ow	Rate sec	Base Hold min	TEST TIME Hours	NOTES	FLAG IDENTIFICATION
		30		▷2 Idle	▷1 Change pressures and temperatures slowly.
	▷1	30		▷3 50%	▷2 Leak check after each run by using blind
		30		▷4 100%	flange on gas inlet & bubble test on gas
			13		outlet. 125 psia on air side.
		10		▷2 10 cycle	▷3 Limit airflow so pressure drop across test
	▷5	10		▷3 10 cycle	module does not exceed 15 in. Hg.
		10		▷4 10 cycle	▷4 Limit gas flow so pressure drop across
					test module does not exceed 40 in. WC.
Continues			25.5	▷7	▷5 Turn burner on and off.
					▷6 Weigh clean test module before test; weigh
		10			module after each run if fouling occurs as
	▷9	30	1		indicated by performance change.
					▷7 Run at each level for 30 minutes; change
		8 hr.		Idle	between levels at maximum rate.
		8 hr.		▷2 50%	▷8 Minimum pressures dictated by system
		8 hr.		▷3 100%	back pressure.
	▷1	8 hr.	57	▷4 100%	▷9 Run at idle 10 minutes, 100% power 30 minutes;
		8 hr.		▷6 50%	change conditions as rapidly as possible.
		8 hr.		Idle	

2

Fouling Tests

Series of runs of the thermal shock rig to evaluate fouling characteristics
(deposition of combustion products on the heat exchanger surfaces) were
made on the first (straight-tube) and the third (wavy-tube) modules. These
runs lasted 8 hours each with fluid conditions adjusted to simulate idle,
50-percent power, and full power of an engine with design points of $2300°F$
TIT ($1316°F$ exhaust gas) and 10:1 pressure ratio. Each run was at a
fixed, simulated power condition. The test module was cleaned prior to
the start of each run. Cleaning was required to remove the carbon buildup
on the outside (air side) of the tubes. This buildup is a characteristic of
the thermal shock rig (as previously explained) but is not typical of engine
operation. After the last run of the straight-tube module, an examination
showed that excessive carbon deposited on the outside of the tubes around
the sealing pillow had ignited, destroying a number of tubes, the pillow,
and part of the suspension, as shown in Figure 84.
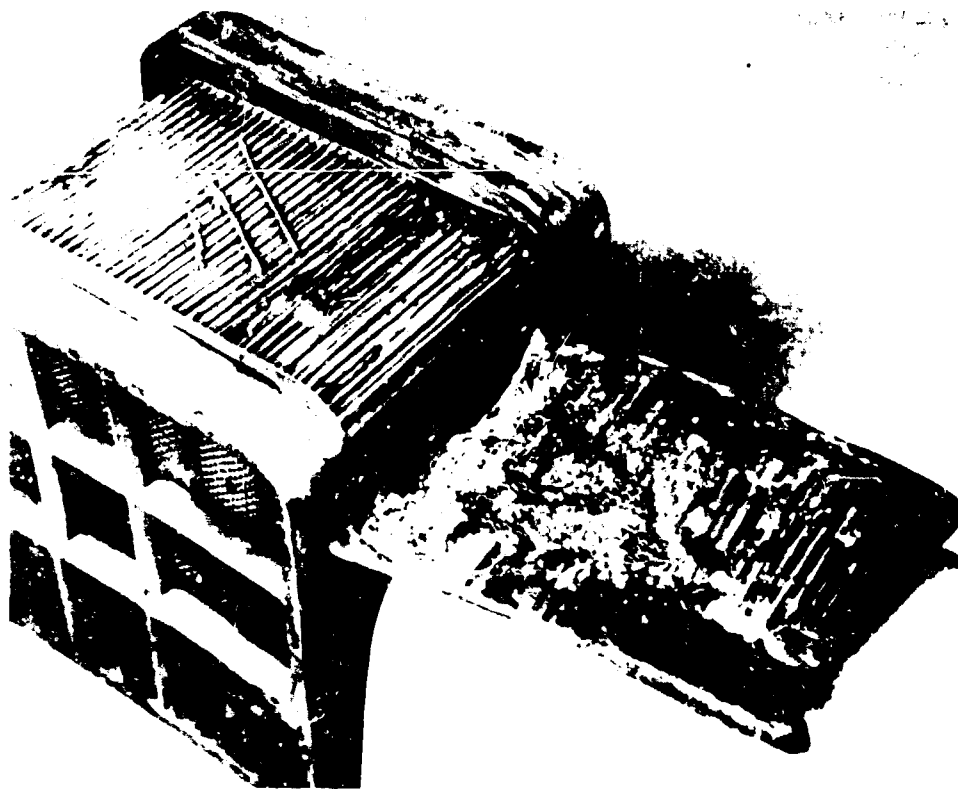
Figure 84. Damage to First Straight-Tube Module Due to
Combustion of Carbon Outside Tubes.

111

Figure 85 shows the effects of fouling on the gas side pressure drop of the first straight-tube module for idle, 50-percent, and full-power settings. Three other runs were taken on this module, but deterioration of the burner performance caused them to be unrealistic.

Figure 86 shows results of similar tests for the wavy-tube module. Pressure drop did not increase as rapidly as that of the straight-tube, primarily due to the improved combustion during these runs.

The gas side pressure drop is a good criterion of fouling because it reflects the decreased flow area due to deposition of a film. At idle conditions, over an 8-hour period, the pressure drop continually increased with time. At 50-percent power, the pressure drop increased and then leveled off, indicating that an equilibrium was reached. At full power, there was no fouling at all. In addition, a badly fouled module rapidly cleaned itself upon return to full power, as indicated by the dotted line in Figure 85. This cleaning action with resumption of high power is in keeping with heat exchanger fouling data obtained by others (Reference 6), indicating that deposits of carbon and heavy hydrocarbons can be dissipated

RUN NO.	CONDITION	RUN NO.	CONDITION
45	$W_G = 0.2$ Lb/Sec	47	$W_G = 0.30$ Lb/Sec
	$T_G = 750°F$		$T_G = 1300°F$
	Idle Power		100 Pct Power
46	$W_G = 0.25$ Lb/Sec	NOTE:	TRACE OF SMOKE VISIBILE ON RUNS 45 AND 46. RUN 47 CLEAR.
	$T_G = 1050°F$		
	50 Pct Power		
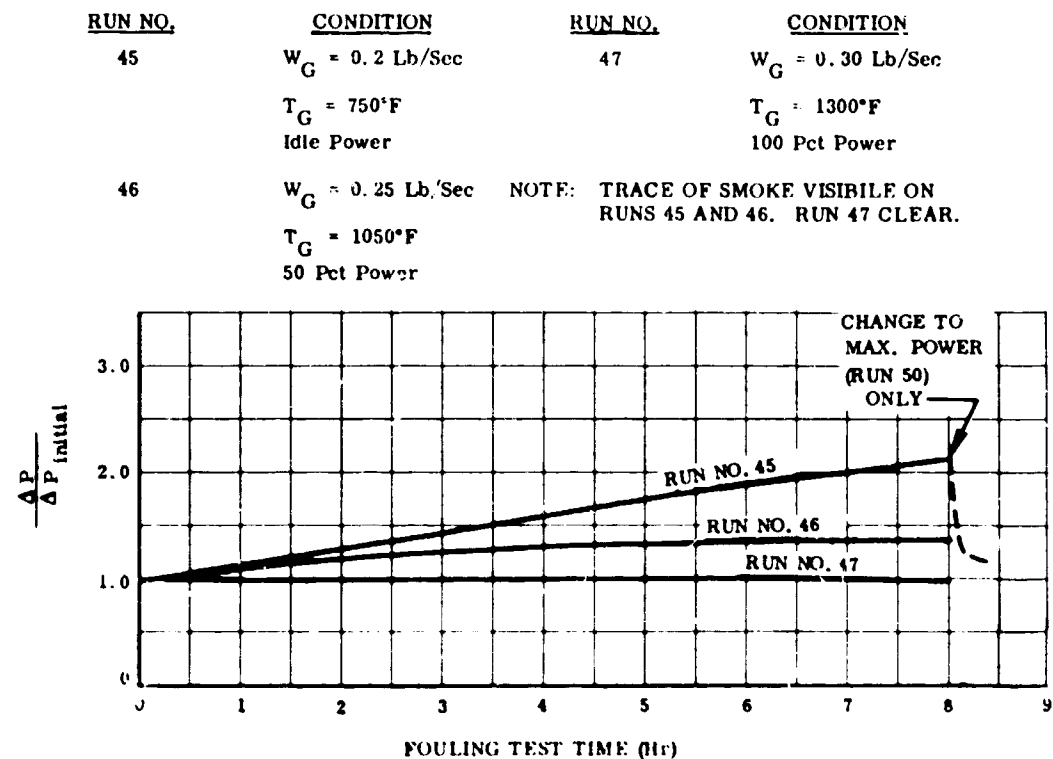
Figure 85. Gas in Tube Fouling Characteristics, Straight-Tube Module.

RUN NO.	CONDITION	RUN NO.	CONDITION
45	W_G = 0.2 Lb/Sec	47	W_G = 3 Lb/Sec
	T_G = 750°F		T_G = 1300°F
	Idle Power		100 Pct Power
46	W_G = 0.25 Lb/Sec		
	T_G = 1050°F		
	50 Pct Power		

NOTE: TRACE OF SMOKE VISIBLE IN COMBUSTION PRODUCTS ON RUN 45. OTHER RUNS CLEAR.
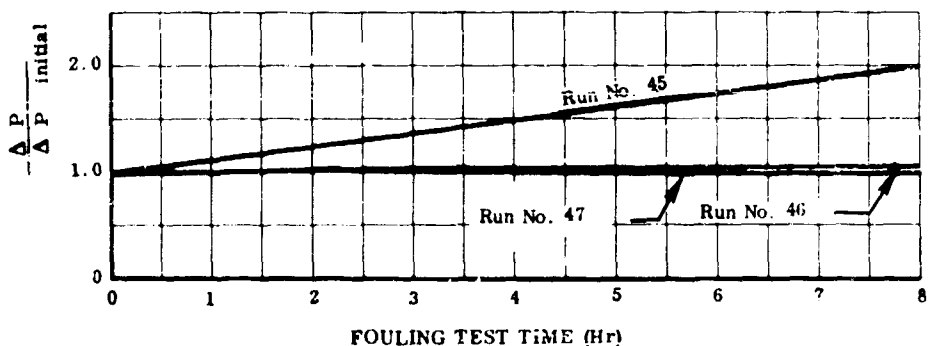
Figure 86. Gas in Tube Fouling Characteristics, Wavy-Tube Module.

when the base metal temperature exceeds 850°F. It can be concluded that the rate of pressure drop increase is a function of combustion cleanliness, which, in turn, will determine the length of time that an engine can be operated under fouling conditions.

Module Performance

Tests were run on the second straight-tube and the wavy-tube modules to establish the level of performance and to confirm prediction techniques. Fluid conditions for the tests and the geometry of the modules are presented in Table X. Measured performance and predicted performance of the test configurations are compared in Table XI. Table XII gives a comparison of the results which would be expected if the testing had been done on a two-pass arrangement with the modules as built.

Dimensions of the fabricated modules were sized to be compatible with the Boeing T50 engine cycle rather than the program model engine cycle; the reason was that it was planned initially to follow up the module development

TABLE X
MODULE PERFORMANCE TEST CONDITIONS AND GEOMETRY

Parameter	Straight Tube	Wavy Tube
$L_{no\ flow,\ specific}$ In./Lb/Sec	15.85	15.85
$L_{air,}$ In.	4.50	4.50
$L_{gas,}$ In.	*2.85	2.85
$L_{no\ flow,}$ In.	3.96	3.96
$T_{gas\ in,}$ °F	1360	1347
$T_{gas\ out,}$ °F	986	960
$P_{gas\ out,}$ Psia	16.33	16.9
$T_{air,}$ °F	662	654
$T_{air\ out,}$ °F	1056	1074
$P_{air\ in,}$ Psia	114.7	114.7

*For airflow through the module, the tube length dimension was reduced
to 2.625 inch from the 2.85 inch due to excessive brazing alloy flow
between tubes near each end.

TABLE XI
MODULE SINGLE-PASS PERFORMANCE

MODULE	EFFECTIVENESS (Percentage)		PRESSURE DROP (Percentage)	
	Measured	Predicted	Measured	Predicted
Straight-Tube	56	55.2	4.30	4.49
Wavy-Tube	59.5	64.2	5.35	5.28

114

TABLE XII
TEST MODULE EXPECTED TWO-PASS PERFORMANCE*

MODULE	EFFECTIVENESS (Percentage)		PRESSURE DROP (Percentage)	
	Prediction	Result Based on Test	Prediction	Result Based on Test
Straight-Tube	74	72	9	8.6
Wavy-Tube	77.5	74.5	10.6	10.7

*Results expected if test modules had been operated in a two-pass, cross-counterflow arrangement.

with the manufacture of a full-size regenerator to be tested on the T50 engine. Also, some of the fluid conditions differed slightly from those of the model engine cycle. To determine the module dimension which would be required to give the targeted performance with the model engine cycle, extrapolation formulae were derived (Appendix IX).

With the use of these formulae, test data for both the straight- and wavy-tube modules were extrapolated to a two-pass, cross-counterflow design having a 70-percent effectiveness and a 6-percent pressure drop. Table XIII, which presents a comparison of proposed goals and expected performance (extrapolated from test), shows that the desired performance level can be obtained with a 20-inch, no-flow length and a 0.21-cubic foot per pound of airflow per second volume with straight tubes or a 23-inch, no-flow length and a 0.19-cubic foot per pound of airflow per second volume with wavy tubes.

Thermal Shock Tests and Structural Behavior

Tubes

While parts of the thermal shock testing program were arranged specifically to subject the module to severe thermal shock for a finite time, the other portions of the test program also accumulated high thermal stress and oxidation corrosion time on the module. It is therefore appropriate to examine module durability with regard to total test time. A total of 72 hours was accumulated on the first straight-tube module, 10 hours on the second, and 95 on the wavy-tube module. Testing of the second

TABLE XIII
EXPECTED REGENERATOR PERFORMANCE BASED ON
EXTRAPOLATIONS FROM TEST DATA

	Proposed Goals	Straight-Tube Module	Wavy-Tube Module
Effectiveness, Pct	70	70	70
Total Pressure Drop, Pct	6	6	6
Specific Core Volume, $Ft^3/Lb/Sec$	0.20	0.21	0.19
Specific Core Weight, Lb/Lb/Sec	10	11.3	10.2
No Flow Length, In/Lb/Sec	-	20	23
Air Flow Length, In.	-	4.9	3.94
Gas Flow Length, In.	-	1.7	1.64

Performance based on: Model Engine Cycle (2300° F TIT, 10:1 PR)
Two-Pass Cross-Counterflow

straight-tube module in the thermal shock rig consisted only of performance measurements, adding little information regarding structural behavior.

Table VIII is a tabulation of the runs to which the first straight-tube module was subjected. Figure 37 is a history of the module leakage rate versus run time. When the module was received from Pyromet, the leakage (at 100 pound per square inch and 70°F) was found to be 0.005 pound per second. After run 38, with about 8 hours of accumulated running time, it had increased to 0.030 pound per second. Visual inspection at that time showed that approximately 18 cracks had occurred in tube walls at the tube and brazed joints. These cracks led to the stress analysis described previously, which indicates a high thermal gradient and high stress in this region.

After completion of run 41, more damaged tubes were found. Five of these were removed and given to the metallurgical laboratory for analysis. The laboratory found fracture surfaces too badly oxidized to establish the mechanism of failure. However, preferential oxidation was noted along the grain boundaries on the inside and outside of the tube. This observation indicated that some changes had occurred in the microstructure along

116
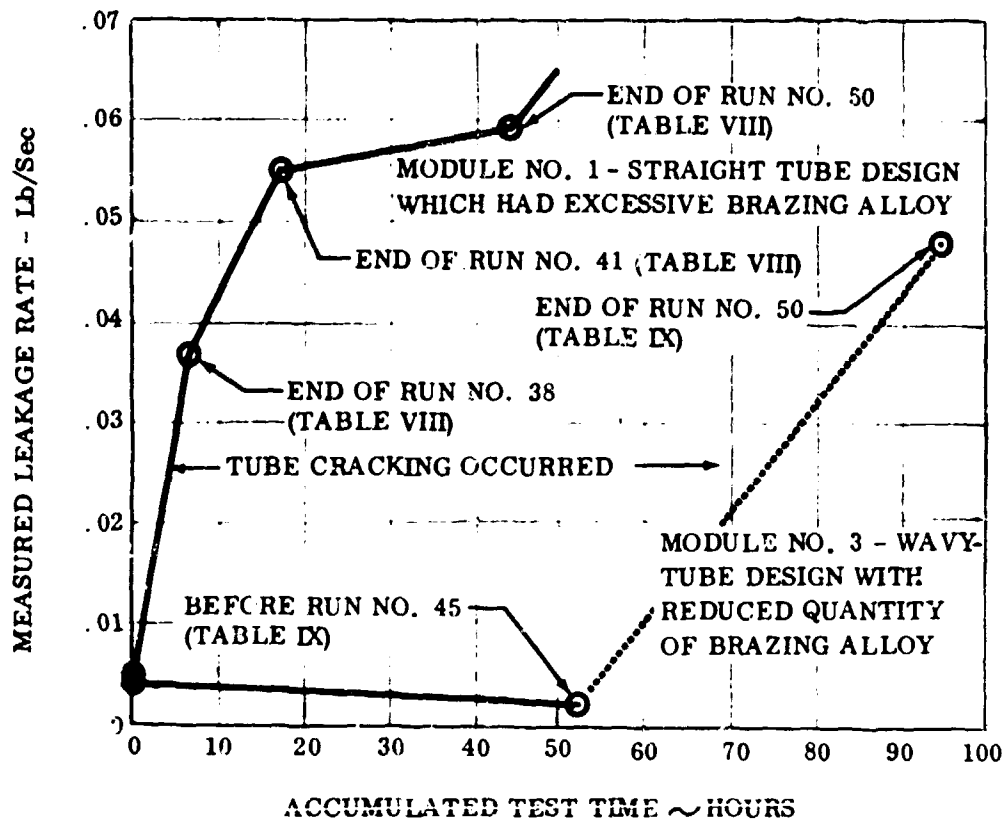
Figure 87. Module Leakage Rate With Test Time.

the crystal interfaces, with the most logical explanation being that chromium carbides had precipitated, resulting in chromium depletion and lower oxidation resistance in these areas. The suspected cause was a deficiency of columbium, which had been noticed in earlier tests of the tubing. A second condition noticed during the metallurgical investigation was localized oxidation under the brazing alloy. This oxidation was found to be the result of a chromium deficiency in the wall, the chromium having preferentially diffused into the brazing alloy. At the conclusion of run 50, the first module was again removed and examined. There appeared to be no further tube fractures; however, there was damage due to a carbon fire occurring in one of the bypass pillows (Figure 84) which was not related to module construction. This condition was discussed earlier under fouling tests. At the conclusion of 10 hours of testing of the second straight-tube module, two broken tubes were noted. The damage was similar to that suffered by the first module but to a lesser degree because of shorter total test time.

117

Table IX gives a run summary for the wavy-tube module. At the conclusion of 52 hours of testing on this module, it was removed for inspection. No cracked tubes were noted, and the leakage rate (0.002 pound per second at 100 pound per square inch and 70° F) was essentially the same as when the module was first received (Figure 87). The reduced amount of brazing alloy used in the assembly, combined with the lower stresses of the wavy tubes, apparently reduced the maximum stress to an acceptable level. At the completion of the remaining testing (fouling), an additional 43 hours had been accumulated on the wavy-tube module (total of 95 hours). The leakage rate had increased to 0.048 pound per second, although the module appeared to be in good condition. Close examination showed several broken tubes at random locations just behind the gas inlet face of the core (Figure 88). Since failures did not occur in the region of maximum stress,
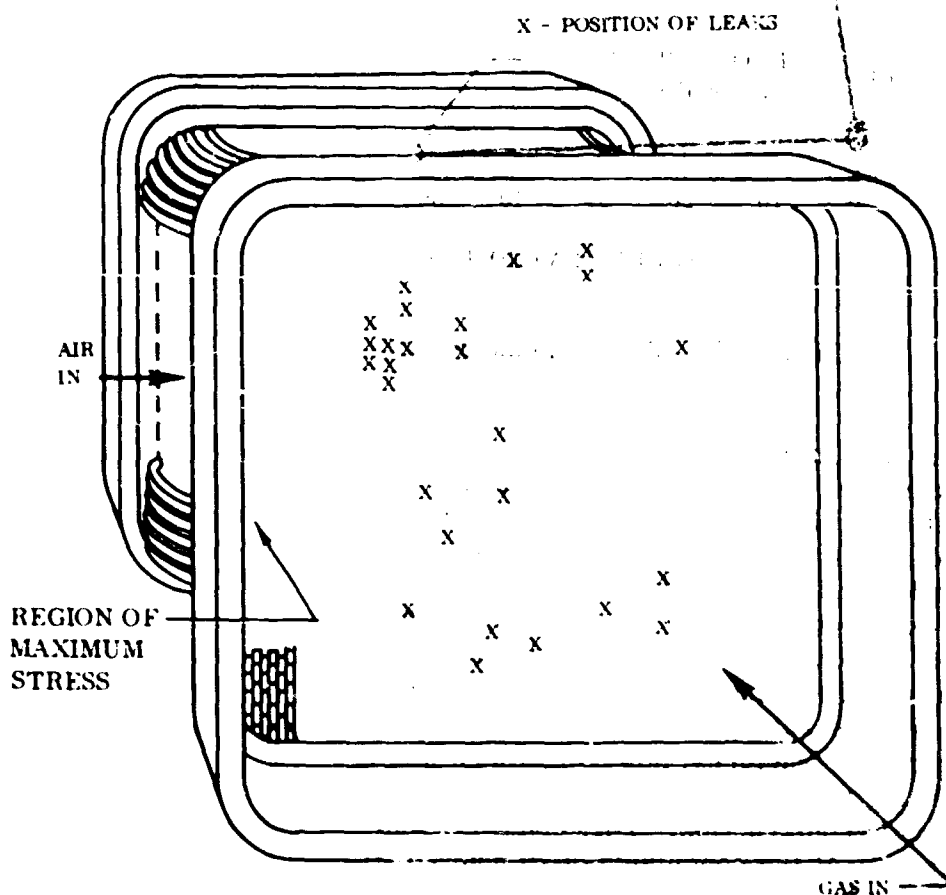
Figure 88. Wavy-Tube Module Leak Positions.
(After 95 Hours)

118

it was concluded that some other condition was causing tube failure. Therefore, sample sections of some of the broken tubes were cut from the module and metallurgically investigated. Examination showed intergranular oxidation at the region of the fracture (Figure 89). Continued studies led to the conclusion that failure was caused by moderate thermal stresses in tubes severely weakened by intergranular oxidation. Further study of the oxidation of the tube indicated that there were complicating factors involved.

First, there was some evidence of chromium carbide precipitation. As mentioned earlier, in unstabilized austenitic stainless steels exposed to temperatures between 800° and 1500°F, the carbon present in the alloy will combine with chromium and precipitate as carbides at the grain boundaries. This effectively depletes the adjacent areas of chromium, thereby reducing the oxidation and corrosion resistance of the grain boundary region. Stabilized austenitic stainless steels contain additives,
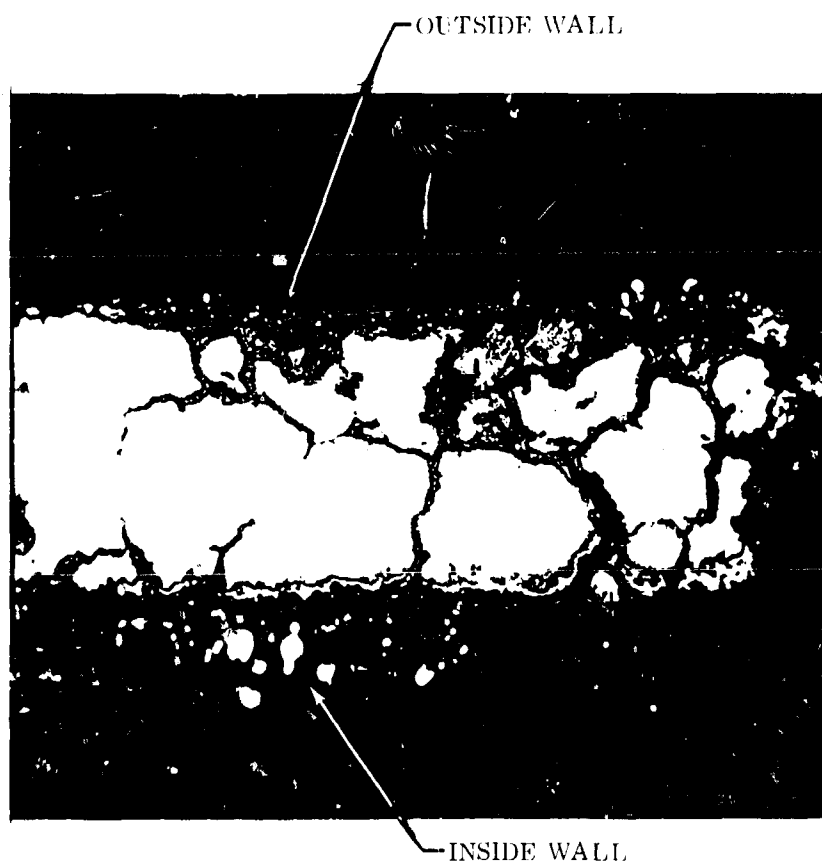
Figure 89. Intergranular Oxidation Near Tube
Fracture Point.

columbium in the case of type 347, which will preferentially combine with the carbon and thus prevent formation of chromium carbides, with resulting depletion of chromium at the grain boundaries. If the carbon should exceed the supply of columbium necessary for stabilization (ten times the carbon content), then the type 347 stainless steel again becomes susceptible to chromium carbide precipitation. Although precautions were taken to ensure that the tube material purchased was correctly stabilized, some evidence of carbide precipitation was evident in tubes from tests, indicating the possibility of local carbon pickup.

Second, some tube samples showed indications of sulfidation. A considerable amount of work has been performed at the Boeing Turbine Division on the phenomenon of sulfidation observed in gas turbine alloys. The term sulfidation attack is usually associated with operation in marine environments, where salt reacts with sulfur from fuels to form sodium sulfate. Sodium sulfate, either with or without some unreacted sodium chloride, deposits on metallic surfaces and initiates erosive attack. Examination of one of the failed tubes from the wavy-tube module revealed clear indications of sulfidation as shown in Figure 90. The areas denoted by "A" show the typical gray-colored chromium sulfides; the island-like appearance of the area "B" is typical or the advanced stage of a sulfidation-oxidation attack. Discussions with representatives of Battelle Memorial Institute and Phillips Petroleum Corporation failed to produce any

1000X   10 Pct NaNO$_3$ ETCH
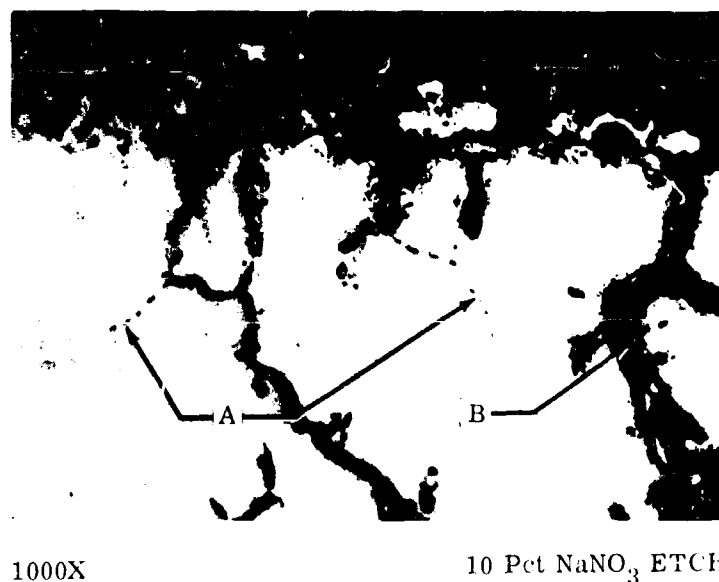
Figure 90. Sulfidation Attack.

120

information on sulfidation in austenitic stainless steels; available data appear to be confined to nickel- and cobalt-based alloys at temperatures of 1400°F and higher.

It has been found that localized stresses will influence the rate of oxidation of materials. This phenomenon has been explained as follows:

● Increased diffusion rates occur within the stressed areas, thereby increasing the frequency with which the metal and oxygen react.

● At the threshold stress, rate of metal deformation just exceeds the rate of growth of the oxides.

Since all tube failures have been observed in highly stressed regions, it is possible that the localized oxidation was accelerated by this stress.

The possibility of overheating of the tubes cannot be dismissed, although there was only one known overheat of the wavy-tube module. This overheat involved a rise in the gas temperature to about 1600°F for about 15 seconds. Because of the short duration, this condition would not be expected to cause failure.

Regardless of the mechanism which was primarily the cause of the oxidation of the tubes, it appears that type 347 stainless steel in the 0.003-inch thickness is not a suitable material for the application. In view of these findings, a test program to identify a better tube material was initiated and is discussed below in the section entitled "Material Corrosion Tests."

Suspension

During high-temperature testing, the flexible suspensions also were under observation. The initial design performed satisfactorily along the straight side but developed wrinkles at the corners which caused some pin holes to develop. To correct these defects and the problems during vibration tests, the flexible suspension was modified as shown in Figure 79. This modified suspension was installed on the second straight-tube module prior to initiation of the 66-hour T50 endurance test discussed previously. After this test, the suspension showed no visible signs of damage.

Material Corrosion Tests

Because of the oxidation of the stainless steel tubing during thermal shock and fouling tests of the first and third modules, a supplementary research program was undertaken to verify earlier results and to determine a more

suitable material. This program consisted of testing combinations of base materials and brazing alloys under conditions simulating an advanced gas turbine engine exhaust.

The rig used for test is diagramed in Figure 91. It consisted of a JP-5 burner (the one used in the thermal shock rig), a plenum chamber, a rotating specimen-holding disk and an exhaust hood. The plenum served to distribute a semicircular jet of hot gases equally. The disk rotated in a plane at right angles to the jet at 2 revolutions per minute and the material samples were mounted so that they alternately passed through the jet of hot gas for one-half revolution and ambient air for one-half revolution. The temperature of the jet was maintained close to 1400°F. The 1400°F temperature was selected to account for the temperature distribution which is typical of gas turbine operation.

Five materials were tested: AISI type 347 stainless steel, Hastelloy X, Haynes 25, Incoloy 800, and Inconel 625. Most of the samples consisted of two pieces of like material brazed together. Parent materials had thicknesses of 0.003, 0.005, and 0.008 inch. Brazing alloys used with these materials were Palmansil 5 and 7, 1700 CN, Nicrobraze 135 and 200, E 135, and Palniro 1.

It should be noted that while no difficulties were encountered in preparing the type 347, Hastelloy X, and Haynes 25 samples, brazing difficulties were encountered with Incoloy 800 and Inconel 625. The brazing problems with Incoloy 800 (poor wetting) were alleviated with the use of a flux. Use of a flux did not solve the poor flow problems in Inconel 625.

In addition to the foil samples, six bundles of AISI type 347 stainless steel tubes were tested with various brazing alloys. These bundles served as a basis for comparison with the module tests.

Table XIV presents the test results. The table shows that severe oxidation occurred on all stainless steel samples. Hastelloy X showed the best oxidation corrosion resistance, followed by Inconel 625 and Haynes 25.

The best brazing alloys were Palniro 1, Nicrobraze 200, and Nicrobraze 125, in that order. When consideration of brazing alloy cost is taken into account, Nicrobraze 200 would be the best choice. The best combinations were Hastelloy X with Palniro 1; Haynes 25 with Nicrobraze 200; and Hastelloy X with Nicrobraze 200. The most economical combinations, Incoloy 800 with Nicrobraze 200 or Nicrobraze 135, should not be discounted; they merit further study for use at slightly lower temperatures.

90 SPECIMENS
BOLTED TO PLATE
(4 SHOWN)

PLAN VIEW

EXHAUST
DUCT

TEST
SPECIMEN

PLENUM

EXHAUST
PORT

HOT GAS INLET DUCT

TURNTABLE DRIVE MOTOR

SIDE VIEW
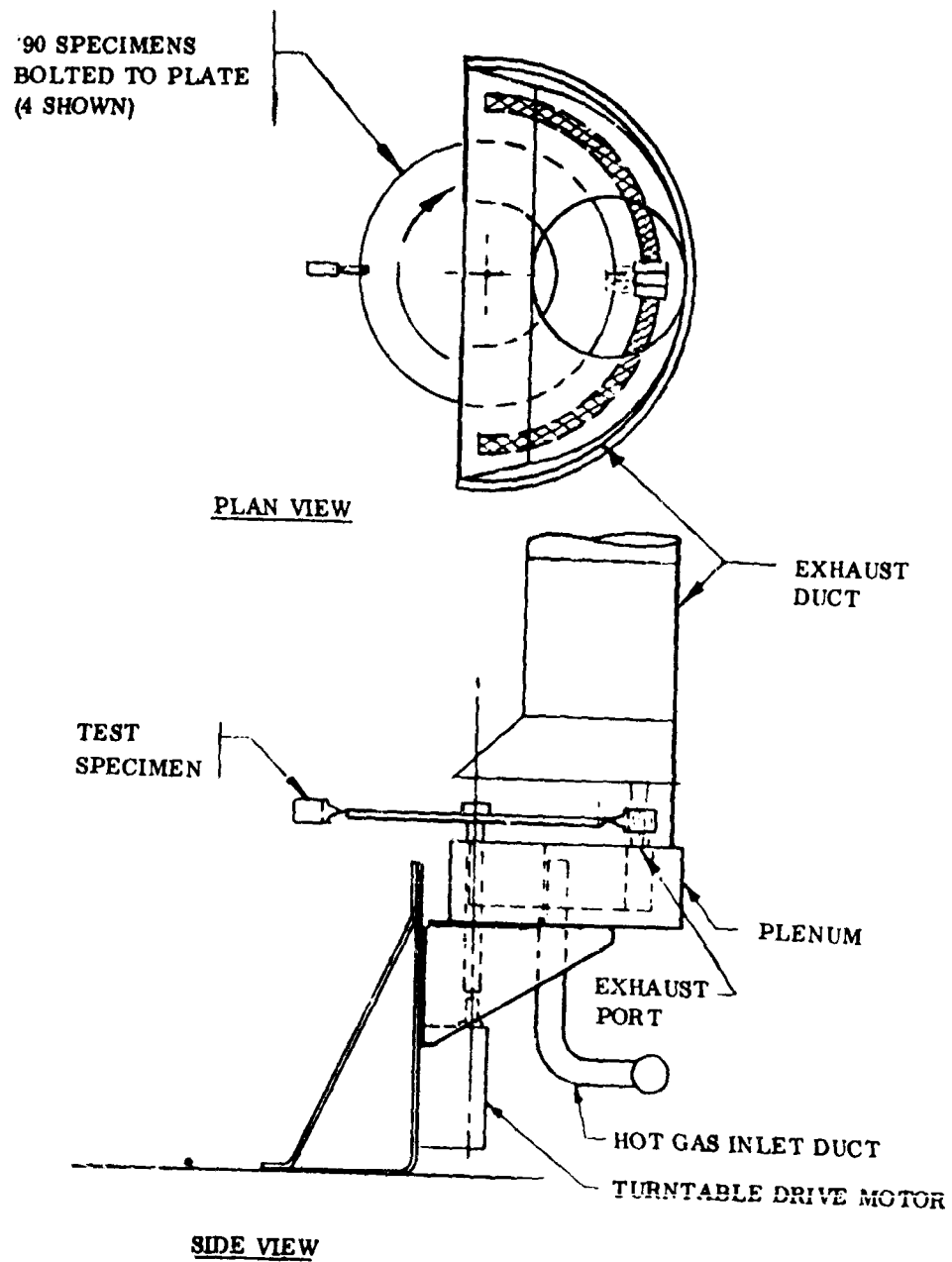
Figure 91. Oxidation and Corrosion Test Rig.

TABLE XIV
RESULTS OF MATERIAL CORROSION TESTS

MATERIAL	THICKNESS	BRAZING ALLOY	EFFECTS OF BRAZING	25 HOURS	50 HOURS	75 HOURS	100 HOURS
347 STAINLESS	0.003 Sheet		No Erosion	A2-6 Internal oxid. of feed fillet, full depth, approx. 0.003.	A2-8 Complete (0.003) oxid. of P/M on lead edge. Almost compl. elsewhere. Internal oxid. of brazed alloy fillets.	A2-6 Internal oxid. of brazed fillets. Surface oxid. full thickness on leading edge, 0.001 elsewhere, P/M.	A2-6 Complete oxid. of brazed fillets. Oxidation to 0.001 of P/M.
	0.003 Sheet	1700 CN	No Erosion, .001 Penetration	A1-2 Oxidation beneath brazing alloy; oxidation of feed fillet, 0.002; surface oxidation, approx. 0.0005, P/M.	A1-2 Complete oxid of feed and exit fillets, 0.003 in. Surface oxidation, up to 0.0075, P/M.	A1-3 Complete oxid. of feed and exit fillets, 0.003; surface oxidation, up to 001; through oxidation in one location, P/M.	A1-3 No brazed section on specimen. P/M oxidation completely through in some spots.
	0.003 Tubes	Palmanail 5					Complete oxidation in many locations (0.0015 from each side), P/M. Internal oxidation of braze.
	0.003 Tubes (as rec'd)	None			General oxidation mostly on outer surface to 0.0005 in.		Oxidation up to 0.001.
	0.003 Tubes (Pickled)	None			General oxidation mostly on outer surface to 0.00075.		Oxidation up to 0.001.
	0.008 Sheet	Palmanail 5	No Erosion or Penetration	C2-9 Oxidation Beneath exit fillet. Oxid. of feed fillet internally. Surface oxid. to max. depth of 0.001, P/M.	C2-9 Internal oxid. of brazed fillets. Surface oxidation of P/M to max. of 0.0015.	C2-10 Internal oxid. of brazed fillets. Surface oxidation of P/M to 0.002.	C2-10 Complete oxid. of brazed fillets. P/M oxidation up to 0.002. Some intergranular oxidation, P/M
	0.008 Sheet	Nicrobraz 200	0.002 Erosion, 0.001 Penetration	C5-16 General surface oxidation of P/M. Oxidation approx. 001 from each side. No oxidation of braze.	C5-16 No oxidation of brazing alloy. Parent material oxidation to 0.002 in.	C5-13 No significant oxidation of brazing alloy. Parent material oxidation.	C5-13 No oxidation of brazing alloy. P/M oxidation to 0.003.

SAMPLE NUMBER, HOURS OF EXPOSURE TO HOT EXHAUST GASES, AND EFFECT ON BRAZE AND PARENT MATERIAL

124

TABLE XIV (Continued)

MATERIAL	THICKNESS	BRAZING ALLOY	EFFECTS OF BRAZING	SAMPLE NUMBER, HOURS OF EXPOSURE TO HOT EXHAUST GASES, AND EFFECT ON BRAZE AND PARENT MATERIAL			
				25 HOURS	50 HOURS	75 HOURS	100 HOURS
HASTELLOY X	0.005 Sheet	Palniro 1	0.0015 Erosion	D6-6 No significant oxidation.	D6-6 No significant oxidation.	D6-7 No significant oxidation.	D6-7 No significant oxidation.
	0.005 Sheet		Little or no Erosion .001 Penetration	D1-21 Severe oxid. of brazed fillets, and parent metal beneath braze to depth of approx. 0.0005.	D1-21 Complete oxid of brazed fillets (0.003). Some oxid. in brazed penetration of P/M, 0.0005 max. No other significant oxidation, P/M.	D1-2 Complete oxid. of brazed fillets (0.003). Oxid. in full depth of brazed penetration of P/M (0.001).No other oxidation of P/M.	D1-2 Complete oxid. of brazed fillets and depth of brazed penetration int. P/M (0.0005 max.). No other oxidation, P/M.
	0.005 Sheet	Palniro 1	0.0015 Erosion	E6-13 No significant oxidation.	E6-13 Slight oxidation, less than 0.00025, one isolated spot of brazed alloy on flat section.	E6-16 one spot of oxidation on leading edge, 0.0003. Otherwise no significant oxidation.	E6-16 No significant oxidation.
	0.005 Sheet	Nicrobraz 135	0.001 Penetration	E3-9 No significant oxidation.	E3-9 No significant oxidation.	E3-11 Slight oxidation of braze approx. 0.0005. No other significant oxidation.	E3-12 Surface oxidation of brazed fillets (0.0005). No significant oxidation of P/M.
	0.006 Sheet	E 135	Little or no Penetration or Erosion	F4-17 Surface oxid. of brazed fillets, .002 plus some internal oxid. No oxidation parent material.	F4-17 Surface oxid. of brazed fillets 0.003, and some internal oxidation. No significant oxid. of P/M.	F4-20 Surface oxid. of brazed fillets to 0.003 plus 0.001 internal oxidation. No significant oxidation of parent material.	F4-20 Surface and internal oxidation almost completely through brazed fillets (0.005). No significant oxidation of P/M.
	0.006 Sheet	Nicrobraz 200	0.001 Penetration, 0.0025	F5-24 No significant oxidation.	F5-24 No significant oxidation.	F5-23 No significant oxidation.	F5-23 Slight surface oxidation of brazed fillets (0.005). No other significant oxidation.

TABLE XIV (Continued)

MATERIAL	THICKNESS	BRAZING ALLOY	EFFECTS OF BRAZING	SAMPLE NUMBER, HOURS OF EXPOSURE TO HOT EXHAUST GASES, AND EFFECT ON BRAZE AND PARENT MATERIAL			
				25 HOURS	50 HOURS	75 HOURS	100 HOURS
INCOLOY 400	0.003 Sheet	Palniro	0.002 Erosion	G6-6 Slight surface oxidation of brazed alloy. No significant oxidation of P/M.	G6-6 Insignificant oxidation of brazed alloy. Intergranular oxidation of P/M to 0.001.	G6-7 Insignificant oxidation of brazed alloy. Intergranular oxidation of P/M to 0.005.	G6-7 Slight oxidation of brazed fillets less than 0.0005. Intergranular oxidation of P/M to 0.001.
	0.003 Sheet	1700 CN	No significant Erosion 0.001 Penetration	G1-2 Severe oxid. of brazed fillets and penetration of P/M to dep.h of 0.001 No general oxid. of P/M.	G1-3 Complete oxid. of braze fillets (0.003) and penetration of P/M to 0.006. Oxid. of P/M elsewhere to 0.0005 including intergranular.	G1-4 Complete oxid. of brazed fillets 0.003 and penetration of P/M to 0.0015. Intergranular oxid. to 0.0005, up to 0.001 on leading edge, P/M.	G1-4 Complete oxid. oi brazed fillets intergranular oxid. of P/M to 0.001.
	0.005 Sheet	Palniro 1	0.002 Erosion	H6-13 Very slight surface oxidation of brazed alloy, less than 0.0005.	H6-13 Surface and intergranular penetration of P/M 0.001. One isolated penetration of 0.004*. braze not oxidized.	H6-15 No significant oxidation of braze. P/M oxidation, surface and intergranular to 0.001.	H6-15 No significant oxidation of brazed alloy. Surface and intergranular oxidation of P/M to 0.001.
	0.005 Sheet	Nicrobraz 135	0.002 Penetration	H3A-1 No significant oxidation.	H3A-2 Slight surface oxidation of P/M and brazed alloy to 0.0005.	H3A-4 Surface oxidation of braze to 0.0005. P/M oxidation to 0.0005.	H3A-2 Slight oxidation to brazed alloy. 0.0005. Intergranular oxidation to 0.0005 in P/M.
	0.006 Sheet	E 135	No significant Erosion or Penetration	I4A-5 Surface oxidation of brazed alloy 0.002 plus internal oxidation.	I4A-5 Surface oxidation of brazed alloy to 0.003 plus internal oxidation. Surface and intergranular oxidation to 0.001, P/M.	I4A-6 Surface oxidation of braze to 0.003. Internal oxidation 0.003. Surface and intergranular oxidation to 0.001, P/M.	I4A-6 Surface and internal oxidation of brazed fillets to full depth (0.005). Surface and intergranular oxidation P/M to 0.001.
	0.006 Sheet	Nicrobraz 200	0.0025 Penetration 0.003 Erosion	I5-24 No significant oxidation.	I5-24 No oxidation of brazed alloy. Surface and intergranular oxidation to 0.00015, P/M.	I5-22 No oxidation of brazed alloy. Surface and intergranular oxidation to 0.0075, P/M.	I5-22 No significant oxidation of brazed alloy. Surface and intergranular oxidation of P/M to 0.0005.

126

TABLE XIV (Continued)

MATERIAL	THICKNESS	BRAZING ALLOY	EFFECTS OF BRAZING	SAMPLE NUMBER, HOURS OF EXPOSURE TO HOT EXHAUST GASES, AND EFFECT ON BRAZE AND PARENT MATERIAL			
				25 HOURS	50 HOURS	75 HOURS	100 HOURS
INCONEL 625	0.003 Sheet	Palniro 1	0.0015 Erosion	M6A-1 Slight surface oxidation, P/M, roughening, less than 0.00025, P/M.	M6A-1 Slight surface oxidation and roughening, less than 0.00025, P/M.	M6A-4 Slight surface oxidation and roughening, less than 0.00025, P/M.	M6A-4 Slight surface oxidation of P/M, 0.00025. Brazed alloy, no significant oxidation.
	0.003 Sheet	1700 CN	0.001 Penetration	M1-5 Oxidation at braze fillets. No other oxidation.	M1-5 Complete oxidation of brazed alloy 0.003, and penetration into P/M, 0.001. No other significant oxidation of P/M.	M1-5 Complete oxidation of brazed alloy, 0.003, and 0.001 penetration. No other significant oxidation of P/M.	M1-5 Complete oxidation of brazed fillets and P/M penetration (0.001). No other significant oxidation of P/M.
	0.005 Sheet	Palniro 1	0.0015 Erosion	N6-14 Very slight surface oxidation. P/M.	N6-14 Very slight surface oxidation, less than 0.00025, P/M.	N6-15 Surface oxidation less than 0.00025, P/M.	N6-14 No significant oxidation.
	0.005 Sheet	Nicrobraz 135	Less than 0.0005 Erosion. 0.0015 Penetration	N3A-1 Slight surface oxidation of brazed alloy.	N3A-1 Slight surface oxidation of brazing alloy, 0.0005. No significant oxidation of P/M.	N3A-4 Slight surface oxidation of braze, 0.0005. No significant oxidation of P/M.	N3A-3 Brazed alloy oxidation less than 0.0005. No significant oxidation of P/M.
	0.006 Sheet	£ 135	No Erosion or Penetration	O4A-5 Surface oxidation of brazing alloy. P/M surface oxidation less than 0.0005.	O4A-5 Oxidation of brazing alloy 0.003. Parent material oxidation 0.00025.	O4A-7 Braze alloy oxidation 0.002 surface, 0.004 internal. Parent material oxidation 0.00025.	O4A-7 Surface and internal oxidation of brazed fillets 0.004. P/M oxidation 0.00025.
	0.006 Sheet	Nicrobraz 200	0.0015 Penetration 0.006 Erosion	05-21 No significant oxidation.	05-21 Slight oxidation of parent material, 0.0004.	05-23 No significant oxidation.	05-23 Slight oxidation of braze, 0.0004, and P/M, 0.00025.

TABLE XIV (Continued)

MATERIAL	THICKNESS	BRAZING ALLOY	EFFECTS OF BRAZING	SAMPLE NUMBER, HOURS OF EXPOSURE TO HOT EXHAUST GASES, AND EFFECT ON BRAZE AND PARENT MATERIAL			
				25 HOURS	50 HOURS	75 HOURS	100 HOURS
HAYNES 25	0.003	Palniro 1	0.002 Erosion	J6-5 Slight surface oxidation, less than 0.0005, P/M. Brazed alloy okay.	J6-5 Slight surface oxidation, less than 0.0005, P/M. Brazed alloy okay.	J6-7 No significant oxidation.	J6-7 Slight surface oxidation of brazed alloy and P/M. 0.0025.
	0.003	1700 CN	No significant Erosion. Slight Penetration.	J1-1 Severe oxidation of brazed alloy fillets, full depth 0.003. Surface oxid. of P/M less than 0.0005.	J1-1 Complete oxidation of brazed fillets (0.003). Surface oxidation of P/M less than 0.0005. (Lamination in P/M.)	J1-2 Complete oxidation of brazed fillets. Oxidation in P/M brazed penetration to 0.0005. P/M general oxidation to 0.00025.	J1-2 Complete oxidation of brazed fillet and brazed penetration in P/M (0.0005). Slight surface oxid. of P/M 0.00025.
	0.005 Sheet	Palniro 1	0.002 Erosion	K6-13 Slight surface oxidation less than 0.0005, P/M.	K6-13 Slight surface oxidation less than 0.0005, P/M.	K6-15 Surface oxidation of P/M up to 0.0005.	K6-15 Slight surface oxidation of brazed alloy and P/M 0.00025.
	0.005 Sheet	Nicrobraz 135	0.001 Penetration	K3-9 Slight surface oxidation, less than 0.0005, P/M.	K3-9 Slight surface oxidation, less than 0.0005, P/M and brazed alloy.	K3-10 Slight surface oxidation P/M and brazed less than 0.005.	K3-10 Slight oxidation of brazed alloy and P/M 0.0025.
	0.006 Sheet	E 135	No significant Erosion or Penetration	L4-17 Surface oxidation of braze fillets, 0.002 plus some internal oxidation.	L4-17 Surface oxidation of brazed fillets, 0.002 plus 0.002 Internal oxid. Parent material oxidation less than 0.0005.	L4-13 Surface oxidation of brazed fillets, 0.002 plus 0.002 internal oxid. Parent material surface oxidation less than 0.0005.	L4-13 Surface and internal oxidation of brazed fillets to 0.004. No significant oxidation of P/M.
	0.006 Sheet	Nicrobraz 200	0.001 Penetration	L5-21 No significant oxidation.	L5-21 No significant oxidation.	L5-23 No significant oxidation.	L5-23 No significant oxidation.

128

MANUFACTURING RESEARCH

The concept of using small tubes with expanded ends to form a heat exchanger was conceived as a means of dealing with a large number of small parts by automated methods. while providing high performance and structural integrity. The elimination of header sheets, which allows assembly without the need to insert a large number of tubes into precisely located, close-tolerance holes, appeared to provide the requisites for automated fabrication and hence for low cost heat exchanger construction. A study was conducted to determine practical methods of automated fabrication. The successful fabrication techniques used to construct the experimental modules clearly showed that two primary areas of manufacture needed extensive study:

1. The fabrication of formed tubes.

2. The assembly of tubes into a module and the brazing.

To gain a better understanding of the magnitude of the manufacturing task and to identify possible high cost areas, an approximate target cost of a regenerator in production was established.

Cost Target

From these studies, a regenerator cost of $1,000 per pound per second of engine airflow was established as a target. It was felt that one-half of this cost should be allotted to tube manufacture, including the cost of raw tubing, and the other half to the remaining fabrication and assembly. Since there are 33,000 tubes for each pound per second of engine airflow, the target cost for each completely formed tube is $0.015. The remaining $500 per pound per second, therefore, must cover module assembly and brazing, fabrication of the housing, headers, and manifolds, and the final assembly.

Having established these target costs, it was then necessary to analyze the expected actual cost of the different items.

Expected Cost of Formed Tubes

To establish the expected cost of mass-produced, formed tubes, the experience gained during experimental manufacturing was combined with information derived from extensive consultations with all established tube mills in the United States.

For the experimental modules, seamless tubing of AISI 347 was purchased in random lengths. This tubing was cut to the required length by electro-discharge machining (EDM) to obtain a tube end free of burrs and deformation. Tests indicated that the burr-free end was an absolute prerequisite for the subsequent forming of the ends with punch and die sets. Tubes manufactured in this fashion were inherently expensive, primarily because the raw tubing in random lengths costs from $0.15 to $0.30 per foot, or from $0.05 to $0.10 per tube. The high cost of the tubing was thus identified as the first obstacle in achieving the established target cost.

Quotations obtained from the manufacturers for production quantities of AISI 347 tubing, both welded and seamless, indicated a lower limit of tube cost of approximately $0.15 per foot in quantities of 2 million feet or more per order. Since this far exceeded the permissible cost (if the target was to be achieved), representatives from the engineering and manufacturing departments visited all the prominent tube mills (Superior Tube, Uniform Tube, Bishop Platinum Works, Tube Division of Nuclear Metals) to discuss the problem with key personnel of these manufacturers.

In these discussions, it was established that all tube mills use the same basic process for the manufacture of small-diameter tubing. This process uses standard welded or seamless, heavy-wall tubing of large diameter, 0.25 inch being the smallest size of welded tubing produced today on a production basis. This larger, heavy-wall tubing is then reduced by successive drawing operations until the required diameter and wall thickness are attained. Annealing and straightening operations have to be performed between draws whenever the particular material has work hardened to the extent that a further reduction becomes impractical. AISI 347 allows several (3 or 4) draws with reductions from 20 to 30 percent per draw before annealing is necessary; Hastelloy X must be annealed after each draw of from 10- to 15-percent reduction. Therefore, it becomes readily apparent that this manufacturing process by its very nature is expensive. Further, it was indicated that increasing the quantity beyond the 2 million feet per order mentioned above does not contribute to lower costs. The reason is that this quantity represents the largest lot size which customarily is processed in a single work order.

It is safe to assume that this well-established process has been perfected to the ultimate, because in the United States alone, the yearly production of utility-grade, AISI 304 hypodermic tubing has reached a volume of from 300 to 500 million feet. The market is highly competitive, Japanese and European manufacturers with their lower labor costs setting the going market price of the product. Thus, every incentive to lower the

production costs is present; and it is unlikely that a breakthrough will occur because of the demand for regenerator tubing.

At this point it became obvious that the target cost for the formed tubes could never be attained by starting with tubing produced by the conventional methods, and that an alternative manufacturing process would be necessary.

All the conceivable alternates were discussed with the tube manufacturers and with representative companies engaged in the manufacture of high-volume, small-size articles, such as fasteners, eyelets, and costume jewelry.

One tube manufacturer has, under the pressure of foreign competition, developed a new proprietary process to form small-diameter tubes, with a relatively heavy wall, in short lengths up to a maximum of about 1.5 inches. This manufacturer attempted to form regenerator tubing from Hastelloy X by this new process but was unsuccessful. The conclusion was that it would take years and large sums of money to develop the process for the desired regenerator part. This conclusion clearly eliminated the process from further consideration, at least for the foreseeable future.

The discussion with the manufacturers of small formed, pressed, or stamped articles, of which Carr Fastener was a typical representative, yielded equally negative results.

Electron-beam welding of the small tubing directly from 0.003-inch-thick strip stock was discarded as impractical tor the following reasons: the difficulties encountered in achieving proper alignment of the thin edges before welding; the necessity of operating in a vacuum; the limited speed of the welding operation; and the lack of a practical way to eliminate the weld bead. Experience has shown that end forming of tubes with any imperfection is impossible; the weld bead resulting from electron-beam welding, no matter how small, would constitute such an imperfection.

Electro-forming of the complete tube was eliminated, not only because the process of electro-depositing of a heat-resistant alloy does not yet exist, but also because of the very basic fact that the metallurgical structure resulting from electro-depositing is inherently brittle. This brittleness is overcome by cold-working, which leads again to the expense of drawing operations.

131

It is possible that a powder metallurgical process will be developed in the future which could provide a method to manufacture finish-formed tubes directly. At present, processes of this type are not yet developed to produce parts from high-temperature materials.

The results of the overall tube cost investigation are well summarized by the following quotation, taken from a letter written by the Superior Tube Company of Norristown, Pennsylvania, on September 8, 1965:

> ". . . We understand that you are looking for fabricated parts including the end forming in the neighborhood of one cent per piece. All our efforts up till this time indicate strongly that such a price level very definitely will not be reached, especially since the analysis has been changed from the more commercially available 347 grade to seamless Hastelloy X. We are still actively pursuing the investigation, however, and will keep you advised of our progress. We felt it wise, however, to go on record again with our firm belief that we will not be down to the price level you feel must be reached to permit successful development of the project. Unfortunately, we cannot even hazard a guess at the moment as to the level we might be able to reach, if and when quantity production is ever demanded of us . . . "

Assuming for a moment that an ultimate cost of $0.15 per foot of Hastelloy X tubing, or $0.04 per tube, can be reached, and assuming an optimistic cost for end forming of $0.01 per tube, the most optimistic cost per formed tube is $0.05, which results in a cost for the formed tubes of $1,650 per pound per second. This cost exceeds not only the target cost of the formed tubes by more than a factor of three, but it exceeds the target of the whole regenerator by 65 percent.

Expected Cost of Module Assembly and Brazing

Simultaneously with the investigation of the cost of formed tubes, the assembly and the brazing of the modules were studied.

The present methods of assembly and brazing, as used in the experimental modules with many hand operations, are expensive. Cost of $4800 per pound per second of engine airflow ($800 per module) in large quantities has been estimated for just the assembly and braze. As indicated, an assembly and brazing target cost of well under $500 per pound per second must be found in order to make this surface competitive. Therefore, a considerable cost improvement must be made.

While some research on mass assembly and brazing methods has been conducted, an economical method has not been found to accomplish this task. On the basis of these studies, it has been concluded that the quantity production manufacture of tubular regenerators having tube diameters on the order of 0.060 inch and a wall thickness of about 0.003 inch will not be feasible in the near future. It must be stated, however, that future developments and demands, although not foreseeable, could well initiate the breakthrough necessary.

A quotation from one brazing specialist in September 1965 indicated that the brazing cost could be reduced from the previously quoted $800 per module to $475 per module on the mass production basis of 300,000 modules per year.

This cost, although representing about a 40-percent improvement, still would result in a cost of about $2,800 per pound per second--too far from the target. This quotation was based on consideration of design changes to permit application of the brazing alloy on the outer faces of the tubes; use of induction heating or quartz lamp heating in an inert atmosphere; and changes in brazing alloys. It should be noted that these cost figures are for assembly and brazing of the modules only, and do not include headers, ducts, or housings.

CONCLUSIONS

This program has demonstrated the size and weight advantages of using small tubes for compact, gas turbine regenerators. It has been shown that the design targets of 70-percent effectiveness and 6-percent pressure drop can be achieved with a straight-tube core of 0.21 cubic foot per pound per second with a 20-inch per pound per second no-flow length or a wavy-tube core of 0.19 cubic foot per pound per second and 23-inch per pound per second no-flow length. The results of thermal shock tests have indicated that the design has potentially good structural characteristics; however, thin-walled AISI type 347 stainless steel tubing was shown to be an unsuitable material for use in an exhaust gas environment of 1300°F and above, inasmuch as the tubes showed severe oxidation after relatively short test times. Later material tests show that Hastelloy X is a preferred material for the application when brazed with Palniro 1 or Nicrobraze 200. Haynes 25 and Inconel 625 are also satisfactory materials for use in an exhaust gas environment up to 1400°F.

Ways to manufacture this type of heat exchanger at reasonable mass production costs have not yet been found. The primary area of high cost has been identified as the manufacture of the tubing itself, and this problem must be overcome first. The other potential problem is in the assembly and brazing of the module; within the scope of the program, feasible methods have not been uncovered. To assess accurately overall assembly costs, far more extensive research of possible automated techniques will be necessary.

RECOMMENDATIONS

Due to the projected high cost of manufacturing this tubular-type regenerator in mass quantities, Boeing recommended that development work be suspended. Because the program has demonstrated that good performance can be obtained from a compact, lightweight heat exchanger and because it has shown a potential for good structural behavior under severe thermal shock, a monitoring of applicable new manufacturing processes should be continued. In the event that new and unforeseen methods of fabrication are discovered to enhance the future of the concept, it is recommended that the small-tube design be re-examined for improvements in end costs. Manufacturing breakthroughs, combined with one of the suggested materials, could make this tubular heat exchanger design of great value to the gas turbine industry; this is particularly true in aircraft, where light weight and small size are prime factors in logistics.

REFERENCES

1. Kays, W. M., and London, A. L., Compact Heat Exchangers, Second Edition, McGraw-Hill Book Company, New York, New York, 1964.

2. Den Hartog, J. P., Advanced Strength of Materials, McGraw-Hill Book Company, New York, New York, 1952.

3. Coppage, J. E., Heat Transfer and Flow Friction Characteristics of Porous Media, Technical Report No. 16, Department of Mechanical Engineering, Stanford University, Palo Alto, California, December 1, 1952.

4. The Elevated Temperature Properties of Stainless Steels, Special Technical Publication No. 124, American Society for Testing Materials, Philadelphia, Pennsylvania, January, 1952.

5. Aerospace Material Specification 5512, Society of Automotive Engineers, New York, New York, December 1, 1950.

6. Kohler, H. L., and Miller, J. A., Gas Turbine Regenerator Fouling, Progress Report Fiscal Year 1965, Technical Note No. 65T-2, United States Naval Postgraduate School Department of Aeronautics, Monterey, California, 1965.

7. Schlichting, H., Boundary Layer Theory, McGraw-Hill, New York, New York, 1960.

8. Roark, R. J., Formulas for Stress and Strain, McGraw-Hill, New York, New York, 1954.

9. Timoshenko, S., and Young, D. H., Elements of Strength of Materials, Van Nostrand, Princeton, New Jersey, 1962.

10. Timoshenko, S., and Woinowsky - Krieger, Theory of Plates and Shells, McGraw-Hill, New York, New York, 1959.

APPENDIX I

ANALYSIS OF MODIFIED SURFACES

WAVY TUBES

In most cases, producing turbulence in pipes will increase the friction factor (and pressure drop) and will increase the heat transfer coefficient by similar amounts. However, this situation will not hold for increases in the apparent friction factor caused by local constrictions. For curved tubes without constrictions, some turbulence could be expected with an increase in both heat transfer coefficient and friction factor due to secondary flows.

For any pipe flow, it is recognized that the velocity of the fluid is highest near the tube center and lowest at the tube walls due to the formation of a boundary layer at the wall. In a curved pipe, the fluid at the center experiences a greater centrifugal force due to its higher velocity. As shown in Figure 92, the curvature causes secondary flows in the tube — the fluid flow outward in the tube center and inward along the walls.

Figure 92. Secondary Flows in Curved Tube.

Reference 7, pages 529-530, discusses this behavior further and presents the following formula for increase in friction factor for flow in curved tubes:

$$\frac{f}{f_0} = 0.37 \ (N_D)^{0.36}$$

137

where N_D, the Dean Number, is defined as

$$N_D = 1/2 \, N_R \sqrt{\frac{R}{r}}$$

N_R is the pipe Reynolds number, R is the radius of the pipe, and r is the radius of curvature of the pipe.

In the case of the 1-cycle wavy tubes used for the program,

   r = 1.22 inches

   R = 0.027 inch

At a laminar Reynolds number of 1000,

$$N_D = 1/2 \times 1000 \sqrt{\frac{0.027}{0.122}}$$

$$N_D = 73.5$$

$$\frac{f}{f_o} = 0.37 \, (73.5)^{0.36}$$

$$\frac{f}{f_o} = 1.7$$

This calculation indicates a 70-percent increase in friction factor, and a corresponding increase in heat transfer coefficient would be expected.

The lowest performing wavy tube considered was the 1/2-cycle or bowed tube which had an R/r of 0.0046. However, it still indicated a 30-percent increase in friction factor.

It should be mentioned that the results of the single-tube tests confirmed the above analysis.

SURFACE-ROUGHENED TUBES

Work on surface-roughened tubes in the past (Nikuradse and others, Reference 7, page 521) has been mainly concerned with turbulent flow in which relatively small particles can have significant effects. The largest particles studied previously (3 percent of the tube inside diameter) have

very little effect at low, laminar Reynolds numbers (under 2000). In order
to cause mixing in laminar flow, which is quite stable, quite large
particles would be required.

The analysis used to determine the minimum particle size necessary to
produce mixing is as follows: The particle is assumed to be a sphere
which has a Reynolds number determined by its diameter and the local
stream velocity at one-half the particle diameter from the wall (Figure 93).
It is further assumed that worthwhile mixing will not occur until a wake
region is established behind the sphere, which is taken to be a particle
Reynolds number of 70 (based on information in Reference 7, page 17).
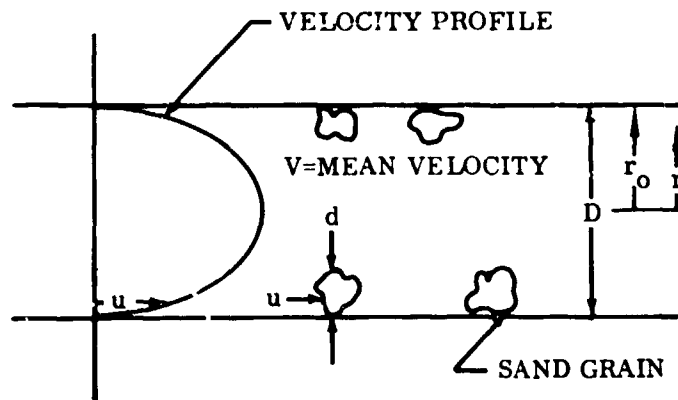
Figure 93. Surface Roughness in Tube.

From Reference 7, pages 68-69, the formula for the laminar velocity
distribution in a pipe can be derived as:

$$u = 2V\left[1 - \left(\frac{r}{r_0}\right)^2\right]$$

where u is the local velocity, V is the mean velocity, r_0 is the pipe radius,
and r is the distance from the pipe axis.

Assuming a particle of 1/10 the tube inside diameter, it protrudes a distance of 1/5 r_o. The distance from the tube axis to the particle center is then 0.9 r_o, so

$$u = 2V\left|1 - (0.9)^2\right|$$

$$u = 0.38V$$

The Reynolds number of the pipe is

$$N_{R\ pipe} = \frac{\rho VD}{\mu}$$

and of the particle

$$N_{R\ part.} = \frac{\rho ud}{\mu}$$

ρ and μ are the same for the particle and the pipe, so

$$N_{R\ part.} = N_{R\ pipe}\left(\frac{d}{D}\right) \times \left(\frac{u}{V}\right)$$

At a pipe Reynolds number of 2000,

$$N_{R\ part.} = 2000\,(1/10)\,(0.38)$$

$$N_{R\ part.} = 76$$

For d/D = 0.1, therefore, the influence of surface roughness will not be significant until N_R = 2000.

For a particle of 1/5 the tube diameter at $N_{R\ pipe}$ = 2000,

$$N_{R\ part.} = 288$$

At $N_{R\ pipe}$ = 1000 and d/D = 1/5,

$$N_{R\ part.} = 144$$

The conclusion reached was that the particles of at least 1/10 the tube inside diameter would be required to produce turbulence and that particles of 1/5 the tube diameter would be more than sufficient.

The tests did not show quite the expected results, however. The particles evidently did produce local turbulence which caused the flow to become fully turbulent at low Reynolds numbers (1000 - 1500) with consequent increases in pressure drop and heat transfer coefficient. However, at Reynolds numbers below the point of transition, there was little effect at all (not the modest increases expected). It is possible that increases in the heat transfer in this region were masked by the insulating effect of the glue used to retain the particles.

APPENDIX II

EVALUATION OF TUBE WALL TEMPERATURES

Separate methods for two different parts of the heat exchanger were used to evaluate the temperatures of the tube walls. The first method was used where the tube sees air and gas on opposite sides of the tube wall and sees no effect from the tube end. The second method was used for the region of the expanded end of the tube.

METHOD 1 (ALL EXCEPT TUBE END)

Consider the tube shown in Figure 94 with interior and exterior fluid temperatures, heat transfer coefficients and areas.

AIR $\quad T_A, \ h_A, \ A_A \quad \diagup \ T_W$

$T_G, \ h_G, \ A_G$

GAS
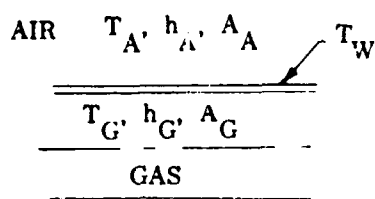
Figure 94. Tube Section
Showing Heat Transfer
Nomenclature.

The heat transfer from the gas to the tube wall is

$$q_1 = h_G A_G \left(T_G - T_W \right) \tag{1}$$

and the heat transfer from the wall to the air is

$$q_2 = h_A A_A \left(T_W - T_A \right) \tag{2}$$

with equilibrium

$$q_1 = q_2$$

$$h_A A_A \left(T_W - T_A \right) = h_G A_G \left(T_G - T_W \right) \tag{3}$$

Rearranging equation (3) gives

$$T_W = \frac{h_G A_G T_G + T_A h_A A_A}{(h_A A_A + h_G A_G)}$$

This equation thus calculates the local wall temperature as a function of the local fluid temperatures. The wrap-around regenerator computer program, discussed earlier, has this equation incorporated and thus calculates equilibrium tube wall temperatures.

METHOD 2 (TUBE ENDS)

Consider the tube end pictured in Figure 95 with the attached brazing alloy. For this problem, it is assumed that the tube end comes up to the temperature of the entering gas. This is a reasonable assumption, since the end has little area exposed to the airstream and since heat transfer coefficients on the gas side are high because a boundary layer is not yet fully developed.
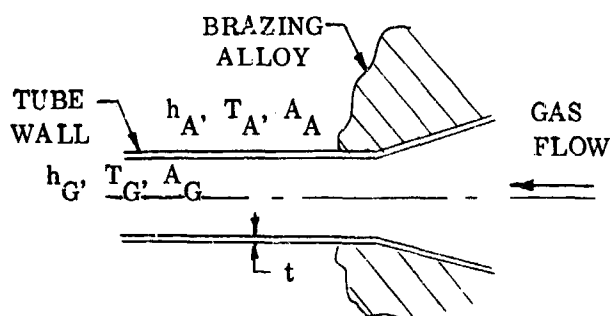
Figure 95.   Tube End Showing Heat
Transfer Nomenclature.

Figure 96 shows the manner in which the problem was set up.

143
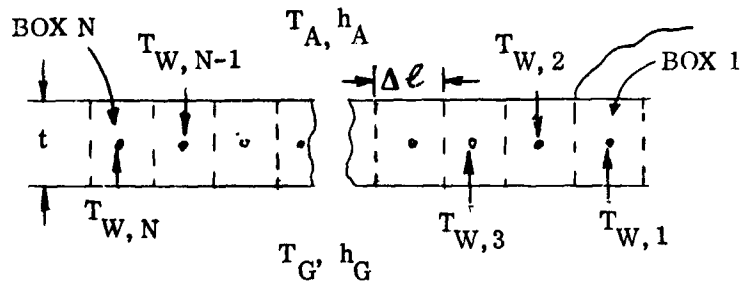
Figure 96. Tube Wall Section Showing Nomenclature.

$T_{W,1}$ was assumed to be equal to the gas inlet temperature and $T_{W,N}$ equal to the equilibrium temperature which would be calculated by Method 1. The distance between $T_{W,1}$ and $T_{W,N}$ must be long enough so that the method calculates values of T_W equal to $T_{W,N}$ a substantial distance to the right of box N (on the order of half the distance between Box 1 and Box N). That is, $dT_W/dx = 0$ halfway between Box 1 and Box N. If this is not the case, the distance is too short and must be lengthened for this problem; the distance used is 0.3 inch (100 times t), which was adequate.

Figure 97 shows the energy flows on a typical box, denoted I.
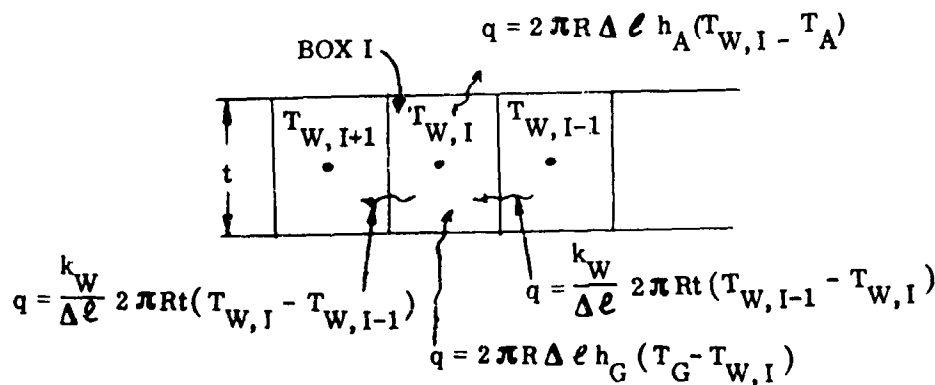
Figure 97. Tube Wall Section Showing Energy Flows.

Applying conservation of energy,

$$2\pi R \Delta \ell h_G (T_G - T_{W,I}) + \frac{k_W}{\Delta \ell} 2\pi R t (T_{W,I-1} - T_{W,I}) =$$

$$2\pi R \Delta \ell h_A (T_{W,I} - T_A) + \frac{k_W}{\Delta \ell} 2\pi R t (T_{W,I} - T_{W,I+1})$$

which with some rearrangement gives

$$T_{W,I-1}\left(\frac{k_W t}{\Delta \ell}\right) + T_{W,I}\left(-\Delta \ell h_G - \frac{k_W t}{\Delta \ell} - \Delta \ell h_A - \frac{k_W t}{\Delta \ell}\right) + T_{W,I+1}\left(\frac{k_W t}{\Delta \ell}\right) =$$

$$T_G (-\Delta \ell h_G) + T_A (\Delta \ell h_A)$$

If $N = 100$, there are 98 such equations and two boundary conditions

$$T_{W,1} = T_{G \text{ inlet}}$$

$$T_{W,100} = T_{W \text{ equilibrium}}$$

This set of equations was solved with the use of a standard matrix solving computer program, giving the result shown in Figure 38. The values of the constants were:

$$T_{W,1} = 1316°F$$

$$T_{W,100} = 980°F$$

$$k_W = 11.0 \text{ Btu/Hr} - \text{Ft} - °F$$

$$t = 0.003 \text{ In.}$$

$$\Delta \ell = 0.003 \text{ In.}$$

$$h_A = 200 \text{ Btu/Hr} - \text{Ft}^2 - °F$$

$$h_G = 50 \text{ Btu/Hr} - \text{Ft}^2 - °F$$

145

APPENDIX III

STRESS CALCULATIONS

NOMENCLATURE FOR STRESS ANALYSIS

A	Area	In.^{2}
D_o	Tube outside diameter	In.
E	Modules of elasticity	Psi
e	Basis of natural logarithm	-
F	Force	Lb
H	ΔH = differential expansion between module and housing, in direction L_A	in.
I	Moment of inertia	In.^{4}
K	Beam stiffness per unit length	Lb
L_A	Length of module in the airflow direction	In.
M	Moment, or	In.-Lb
	moment per unit width	In.-Lb/In.
p	Pressure	Psi
Q	Shear force	Lb/In.
R	Radius	In.
T	Temperature	°F
t	Wall thickness	In.
X_l	Pitch of tube spacing, transverse	-
X_t	Pitch of tube spacing, longitudinal	-
z	Distance from neutral axis to extreme fiber	-

146

α	Coefficient of thermal expansion	In./In.°F
β	Inverse of wave length	1/In.
δ, Δ	Prefix, denotes small increment of following unit	-
θ	Angular deflection	Radians
ν	Poisson's ratio	-
σ	Normal stress	Psi
τ	Shear stress	Psi

SUBSCRIPTS

B	Bending
H	Hoop
M	Mean
opt	Optimum
tot	Total

Additional symbols and subscripts are defined in the text, where used.

COMPRESSIVE HOOP STRESS IN TUBE

When a tube is subjected to external pressure, its wall develops a compressive stress. Such a stress is commonly known as a hoop stress and can be evaluated from formulas such as the following (Reference 8, page 268):

$$\sigma_H = \frac{pR}{t}$$

where p is the tube outside minus inside pressure.
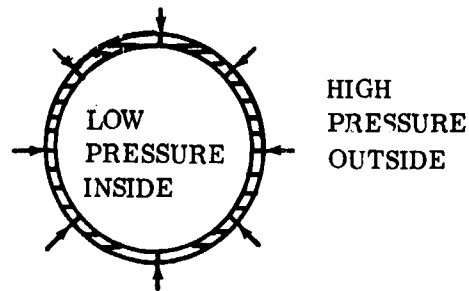
Figure 98.   Sketch Showing
Loading Creating Hoop Stress.

At the model engine (2300°F TIT, 10:1 PR) design point,

p = 147 - 14.7 = 132.3 Psi

R = (0.060 - 0.003)/2 = 0.0285 In. = mean radius

t = 0.003 In. = tube wall thickness

Substituting:

$$\sigma_H = 1257 \text{ Psi}$$

ELASTIC STABILITY OF TUBE WALL

If the external pressure on a tube becomes too great, it is possible for the wall to buckle.   The pressure needed to cause buckling can be calculated from a formula given in Reference 8, page 318.

$$p' = \frac{E}{4(1 - \nu^2)} \times \left(\frac{t}{R}\right)^3 \quad \text{for} \quad \ell > 4.9R\sqrt{\frac{R}{t}}$$

For this configuration,

E = 28. x 10^6 Psi

ν = 0.3

ℓ = 2.85 In.

148

$$4.9R\sqrt{\frac{R}{t}} = 0.43 < 2.85$$

$$p' = 8972.0 \text{ Psi} = \text{pressure level that would produce buckling}$$

Since the actual pressure in service will be about 132 pound per square inch, the tube wall is stable and there is no danger of buckling.

LONGITUDINAL TENSILE STRESS DUE TO PRESSURE

As shown in Figure 99, the end plate of a tube module consisting of the expanded ends of the tubes is subjected to a pressure imbalance. This imbalance is compensated for by tension in the tube walls.
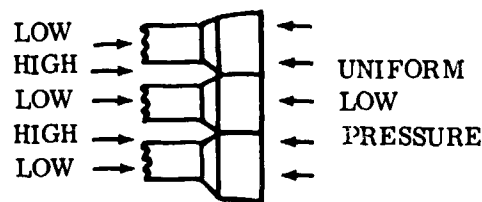
Figure 99. Sketch Showing
Loading Creating Hydraulic
Imbalance.

For each tube, the area over which this differential pressure acts is shown in Figure 100. It is given by the formula

$$A = X_t X_\ell D_o^2 - \frac{\pi}{4} D_o^2$$
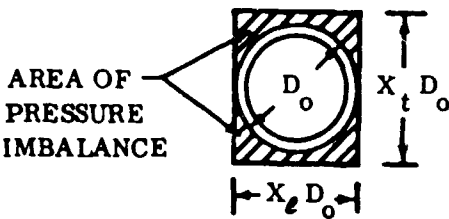
Figure 100. Sketch Showing
Area of Differential Pressure.

The force per tube is then

$$F = pA = p\left(X_t X_{\ell} D_o^{\ 2} - \frac{\pi}{4} D_o^{\ 2}\right)$$

and the stress is

$$\sigma = \frac{pA}{A_{Tube\ Wall}} = \left(X_t X_{\ell} - \frac{\pi}{4}\right)\frac{pD_o^{\ 2}}{2\pi Rt}$$

For the model engine design point,

$$X_t = 1.5$$

$$X_{\ell} = 1.0$$

$$D_o = 0.060\ In.$$

$$p = 132.3\ Psi$$

$$R = (D_o - t)/2 = 0.0285\ In.$$

$$t = 0.003\ In.$$

Substituting:

$$\sigma = 634\ Psi$$

STRESS FROM BENDING OF TUBES DUE TO UNEVEN THERMAL EXPANSION

In normal steady-state operation of a tubular regenerator, the mean temperature of individual tubes increases in the airflow direction. The hotter tubes expand more than the cooler tubes, and it is expected that a deformation like Figure 101 will result. The curved shape of the tubes which results will cause a bending stress to develop in the tube wall.

For a tubular regenerator with a 21.5-inch no-flow length, a 4.1-in. airflow length, and a 1.5-inch gas-flow length, the mean tube temperatures as functions of y have been calculated (by means of the wedge-shaped regenerator computer program).
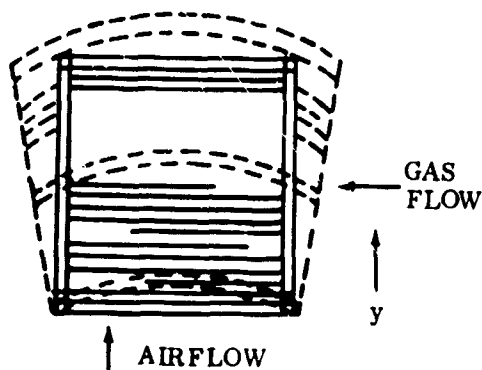
Figure 101. Exaggeratéd Bowing
of Tubes due to Thermal
Gradient. (Exaggerated for
illustration)

These values are:

y (In.)	T_{Mean} (°F)
0	924
0.205	939
0.41	953
0.615	967
0.820	981
1.025	994
1.230	1006
1.435	1018
1.640	1030
1.845	1041
2.050	1052
2.255	1063
2.460	1073
2.665	1082
2.870	1092
3.075	1101
3.280	1109
3.485	1118
3.690	1125
3.895	1133

The maximum gradient which results in the y direction is 15° F over 0.205
inch or 73.4° F per inch.

If two adjacent tubes are examined as in Figure 102, it can be seen that an angle 2θ results.
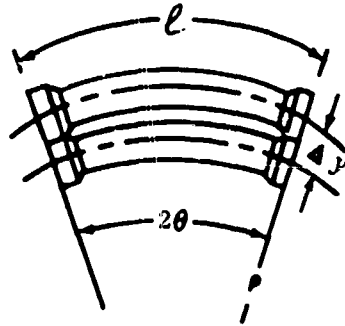
Figure 102. Bowing of
Tubes.

The elongation of a tube is

$$\delta l = l\alpha\Delta T; \qquad \Delta T = T - T_0$$

where α is the coefficient of thermal expansion.

The differential change in length between the two tubes is

$$\Delta(\delta l) = l\alpha\,(T_1 - T_2)$$

where the subscript 1 denotes the hotter tube and 2 denotes the colder tube.

If ρ denotes the radius of curvature of the inner tube, then

$$\Delta(\delta l) = (\rho + \Delta y)\,2\theta - \rho \times 2\theta$$

$$\Delta(\delta l) = 2\theta\Delta y$$

and

$$\theta = \frac{\Delta(\delta l)}{2\Delta y} = \frac{l\alpha\,(T_1 - T_2)}{2\Delta y}$$

Since

$$\frac{T_1 - T_2}{\Delta y} = \frac{dT}{dy}$$

then

$$\theta = \frac{1}{2} \alpha \frac{dT}{dy} \ell$$

For a uniform tube in bending,

$$M = \frac{EI2\theta}{\ell}$$

$$\left\{ \begin{array}{l} \text{Eq. 5.4, page 114, Reference 9,} \\ \text{gives } M = EI/R; \text{ since } \ell = 2R\theta, \\ \text{the equation at left results.} \end{array} \right\}$$

and

$$\sigma = \frac{MR}{I}$$

(Reference 9, page 114, Eq. 5.5)

so

$$\sigma = \frac{E\theta R}{\ell}$$

and

$$\sigma = \frac{ER}{\ell} \left(\frac{\ell}{2} \alpha \frac{dT}{dy}\right)2$$

$$\sigma = ER \alpha \frac{dT}{dy}$$

For this configuration,

$$E = 23 \times 10^6 \text{ Psi}$$

$$R = 0.0285$$

$$\alpha = 10^{-5} \text{ In./In.-°F}$$

$$\frac{dT}{dy} = 73.5° \text{F/In. (maximum)}$$

$$\sigma_{max} = 23 \times 10^6 \times 10^{-5} \times 0.0285 \times 73.5$$

$$\sigma_{max} = 480 \text{ Psi}$$

SHEAR STRESS AT TUBE END (RESULTING FROM BENDING ABOVE)

The above bending also must be taken by the expanded ends, which results in a shear stress. Figure 103 pictures this type of loading at the end.
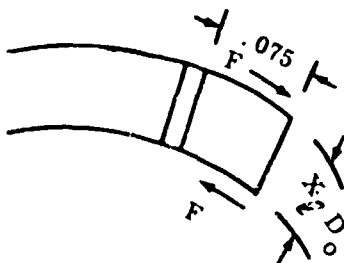
Figure 103. Region of Shear Forces at Tube End.

From the above,

$$\theta = \frac{l}{2} \alpha \frac{dT}{dY}$$

$$M = \frac{EI\theta}{l}$$

For this problem,

$$E = 23 \times 10^6 \text{ Psi}$$

$$I = 21.8 \times 10^{-8} \text{ In.}^4$$

$$l = 1.5 \text{ In.}$$

then

$$\theta = \frac{1.5}{2} \times 10^{-5} \times 73.5 = 5.5 \times 10^{-5} \text{ Radians}$$

and

$$M = \frac{23 \times 10^6 \times 21.8 \times 10^{-8} \times 55.0 \times 10^{-5} \times 2}{1.5}$$

$$M = 3.7 \times 10^{-3} \text{ In.-Lb}$$

154

Also,

$$M = FX_\ell D_0$$

$$F = M/(X_\ell D_0)$$

$$F = \frac{3.7 \times 10^{-3} \text{ Lb}}{0.060 \times 1.0} = 60 \times 10^{-3} \text{ Lb}$$

$$\tau = \frac{F}{A} = \text{shear stress}$$

$$\tau = \frac{60 \times 10^{-3}}{1.5 \times 0.060 \times 0.075}$$

$$\tau_{max} = 22 \text{ Psi}$$

STRESSES IN CURVED TUBES

One of the reasons that wavy tubes were considered for this program is that when subjected to axial loads, they are springy and require less force to compress axially and have lower resulting stresses than straight tubes. This was demonstrated by means of Spielvogel's Theorem, which is described in Reference 2, pages 323-325. Consider the curved pine shown in Figure 104. The pipe is built in at one end and is subjected to loading at the other end with forces X_0 and Y_0 and bending moment M_0.
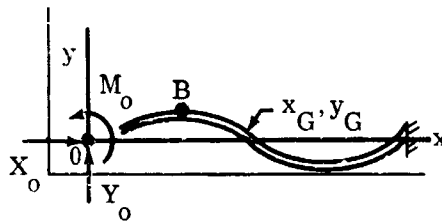
Figure 104.   End Loading on
Wavy Tube.

If x_G and y_G are the coordinates of the center of gravity of the pipe considered to be of "weight" $1/EI$ per unit length, then I_{xG}, I_{yG} and I_{xyG} are

155

the moments and product of inertia of the pipe about axes through the center of gravity x_G and y_G. The theorem states:

$$\Delta x = I_{xG}X_o - I_{xyG}Y_o$$

$$\Delta y = I_{yG}Y_o - I_{xyG}X_o \quad\quad (a)$$

$$M_o = x_G Y_o - y_g X_o .$$

This problem was solved for the 1-c⋯ wavy tubes. The following demonstrates the method.

As shown in Figure 105, the point x_G, y_G is through the center of the tube from symmetry.
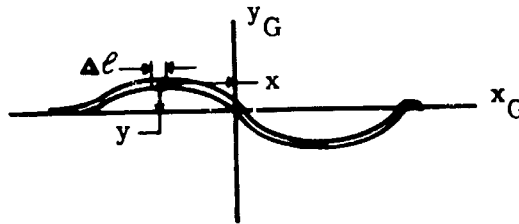
Figure 105. Evaluation of Moments
of Inertia of Wavy Tube.

The moments and products of inertia were evaluated graphically, as shown in Figure 105.

$$I_x = \sum_{\ell} \frac{\Delta \ell}{EI} y^2$$

$$I_y = \sum_{\ell} \frac{\Delta \ell}{EI} x^2$$

$$I_{xy} = \sum_{\ell} \frac{\Delta \ell}{EI} xy$$

The resulting solution for the wavy tube shown in Figure 104 with $E = 23 \times 10^6$ Psi and $I = 21.8 \times 10^{08}$ In.^{4} is

$$I_x = 0.00322 \text{ In./Lb}$$

$$I_y = 0.475 \text{ In./Lb}$$

$$I_{xy} = 0.0185 \text{ In./Lb}$$

$\Delta y = 0$ for the assumed type of loading (thermal expansion) substituting into equations (a) and rearranging.

$$X_o = 400 \Delta x$$

$$Y_o = -15 \Delta x$$

$$M_o = -22.5 \Delta x$$

These correspond to point O in Figure 104. The minus signs denote opposite sense from Figure 104.

X_o is the end load per tube for a deflection Δx. M is a maximum for the tube at point B, and has the value $37.7\Delta x$ inch-pound.

For a beam in bending,

$$\sigma = \frac{Mz}{I}$$

for

$z = 0.030$ In. (tube outside radius) and $I = 21.8 \times 10^{-8}$ In.^{4}

$$\sigma = 5.2 \times 10^6 \Delta x$$

To this must be added the simple compressive stress due to the end load. The cross-sectional area of the tube wall is

$$A = (R_o{}^2 - R_i{}^2) = 5.35 \times 10^{-4} \text{ In.}^2$$

and the compressive stress is

$$\sigma_{comp} = \frac{F}{A} = \frac{X_o}{A} = \frac{400}{5.35 \times 10^{-4}} = 0.75 \times 10^6 \Delta x \text{ Psi}$$

so the total maximum stress is

$$\sigma_{max} = (5.2 + 0.75)\ 10^6 \Delta x$$

$$\sigma_{max} = 5.95 \times 10^6 \Delta x\ \text{Psi}$$

For a straight tube in simple compression, with $E = 23.0 \times 10^6$ Psi,

$$\sigma = \frac{E \Delta x}{\mathit{l}}$$

$$\sigma = \frac{\Delta x \times 23 \times 10^6}{3.0} = 7.7 \times 10^6 \Delta x,\ \text{Psi}$$

For the end load on a straight tube,

$$F = \sigma A$$

$$F = 7.7 \times 10^6 \times 5.35 \times 10^{-4}$$

$$F = 4100 \Delta x$$

so the ratio of the wavy-tube to straight-tube end loads is

$$\frac{F\ \text{wavy}}{F\ \text{straight}} = \frac{400}{4600} = 0.087$$

STRESS DUE TO HIGH THERMAL GRADIENT AT TUBE END

Description of Problem

If there exists a heavy accumulation of brazing alloy at the tube end as shown in Figure 106, the tube behaves as a built-in column. As discussed previously in the analytical studies of this report, the equilibrium temperature of the tube wall is much lower than the temperature of the ends. The brazing alloy is approximately at uniform temperature due to its high area for internal conduction. Since the tube wall is thin, it permits little axial conduction; consequently, a high temperature gradient exists. As shown in Figure 107, the tube tries to assume a conical shape. The brazed end, being at a uniform temperature and quite rigid, holds the tube cylindrical. The forces cause the tube wall to take a sharp bend at the intersection and result in a high stress. The temperature gradient was calculated by the method presented in Appendix II. The following is the analysis of the resulting stresses.

158
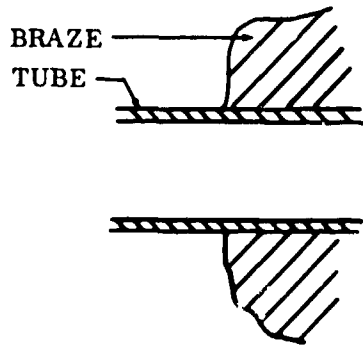
Figure 106. Brazing Alloy at Tube End.
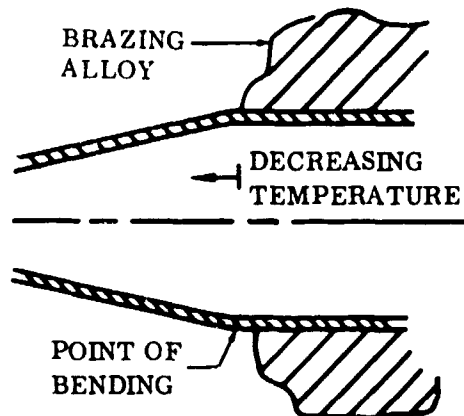
Figure 107. Bending of Wall at Tube End.

Problem Analysis

The thermal stresses in the tube near the end are calculated by the theory of thin-walled cylinders subjected to a rotationally symmetrical load. This theory is derived from "Beams on Elastic Foundation" which is discussed further in References 2 and 10.

Accordingly, the stresses in the tube wall are calculated for a thin, long section of the tube wall, which is treated as a beam, the remainder of the tube forming the elastic foundation. See Figure 108, taken from Reference 2.
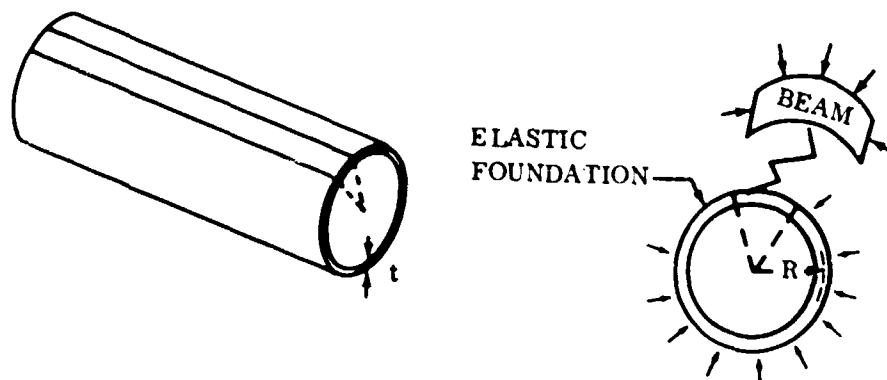
Figure 108. "Elastic Foundation" Method of Analysis.

159

If the width of the beam is made unity, the stiffness of the foundation becomes

$$K = \frac{Et}{R^2} \qquad (1)$$

and the stiffness of the beam becomes

$$EI = \frac{Et^3}{12(1 - \nu^2)} \qquad (2)$$

The differential equation for a beam on elastic foundation reads as follows:

$$\frac{d^4 y}{dx^4} + \frac{K}{EI} y = \frac{p}{EI} \qquad (3)$$

where

y = downward deflection of beam

K = stiffness of foundation

EI = stiffness of beam

p = downward loading per unit length, or
= pressure on tube outside per unit width

The general solution of this differential equation for the case of $p = o$ is

$$y = e^{\beta x} \left[C_1 \cos\beta x + C_2 \sin\beta x \right] + e^{-\beta x} \left[C_3 \cos\beta x + C_4 \sin\beta x \right] \qquad (4)$$

with the notation:

$$\beta^4 = \frac{K}{4EI} \qquad (5)$$

C_1 to C_4 are arbitrary constants.

The stresses near the tube end are now obtained by superposition of the deflections caused by a shear force Q_o and a moment M_o at the end and the deflection due to the temperature gradient; the beam loading is shown in Figure 109.
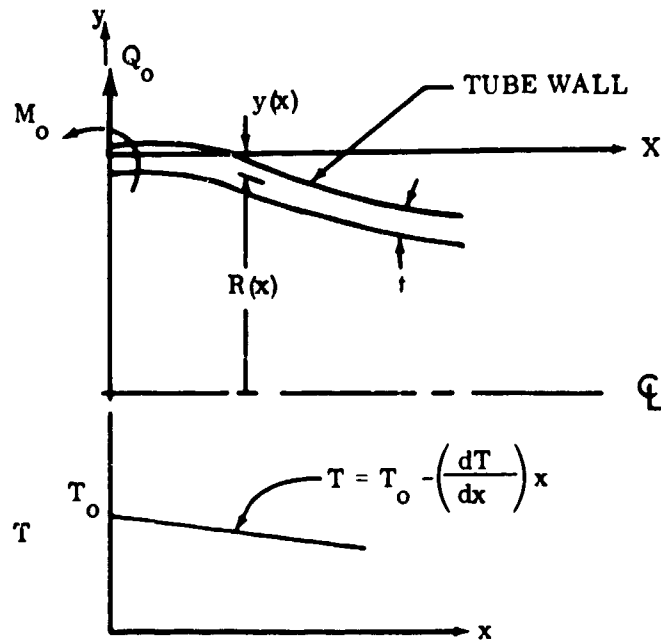
Figure 109. Loading of "Beam" (Tube Wall).

From Reference 2, page 154, we find for a semi-infinite beam, the deflection due to Q_o:

$$y = \frac{2\beta Q_o e^{-\beta x} \cos \beta x}{K} \tag{6}$$

and the deflection due to M_o from Reference 2, page 155:

$$y = \frac{-2\beta^2 M_o e^{-\beta x}}{K}(\cos \beta x - \sin \beta x) \tag{7}$$

The deflection due to the thermal gradient is

$$y = \alpha R\left(\frac{dT}{dx}\right)x \tag{8}$$

The total deflection of the beam is obtained by adding equations (6), (7), and (8):

$$y = \frac{2\beta Q_o}{K} e^{-\beta x} \cos \beta x - \frac{2\beta^2}{K} M_o e^{-\beta x}(\cos \beta x - \sin \beta x) + \alpha R\left(\frac{dT}{dx}\right)x \tag{9}$$

161

Differentiation of Equation (9) furnishes

$$y' = \frac{-2\beta^2 Q_o}{K} e^{-\beta x} (\cos \beta x + \sin \beta x) + \frac{4\beta^3 M_o}{K} e^{-\beta x} \cos \beta x + \alpha R\left(\frac{dT}{dx}\right) \quad (10)$$

Introducing now the boundary conditions at $X = 0$, namely, no deflection ($Y = 0$) and no change in angle ($y' = 0$), the values for Q_o and M_o are found to be as follows:

$$Q_o = \frac{-\alpha RK}{2\beta^2} \left(\frac{dT}{dx}\right) \quad (11)$$

$$M_o = \frac{-\alpha RK}{2\beta^3} \left(\frac{dT}{dt}\right) \; ; \quad (12)$$

or substituting K from Eq. 1,

$$Q_o = \frac{-\alpha Et}{2R\beta^2} \left(\frac{dT}{dx}\right) \quad (13)$$

and

$$M_o = \frac{-\alpha ET}{2R\beta^3} \left(\frac{dT}{dx}\right) \quad (14)$$

The total deflection at any point x is then determined by combining equations (9), (13), and (14).

$$y = \frac{-\alpha R}{\beta} \left(\frac{dT}{dx}\right) e^{-\beta x} \sin \beta x + R\left(\frac{dT}{dx}\right)x \quad (15)$$

Differentiation of equation (15) and the relationships

$$M_B = EIy'' \quad (16\ a)$$

and

$$Q = EIy''' \quad (16\ b)$$

162

yield, in conjunction with equations (2) and (5), the meridional moment and the shear force per unit length:

$$M_B = + \frac{\alpha t E}{2\beta^3 R} \left(\frac{dT}{dx}\right) e^{-\beta x} \cos \beta x \qquad (17)$$

$$Q = - \frac{\alpha t E}{2\beta^2 R} \left(\frac{dT}{dx}\right) e^{-\beta x} \left(\sin \beta x + \cos \beta x\right) \qquad (18)$$

Stresses

The forces and moments so calculated cause the following stresses in the beam element under consideration (width = 1).

a)   Meridional normal stress

$$\sigma_M = \frac{12 M_B y}{t^3} \qquad (19)$$
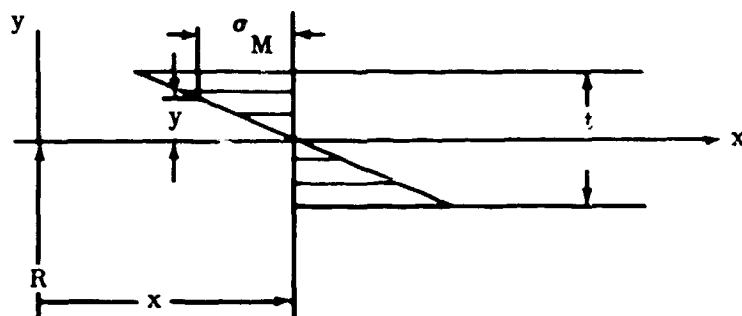
Figure 110.   Meridional Normal Stress Diagram.

b)   Meridional shear stress

$$\tau_{M \, max} = \phi \frac{Q}{A} = \frac{3}{2} \frac{Q}{t} \qquad (20)$$

163

where ϕ is a form factor (3/2 for the rectangular beam section under consideration, Reference 3, page 96, and Q/A the average shear stress in the section).
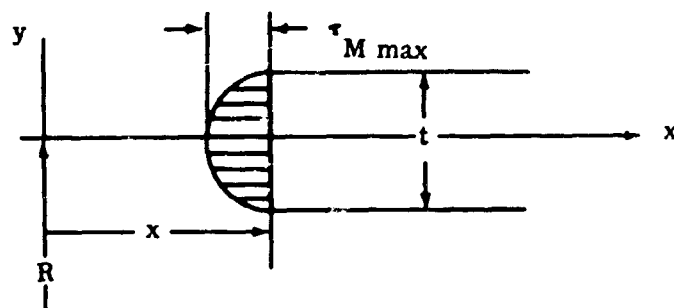
Figure 111. Meridional Shear Stress Diagram.

c) Tangential normal stress

$$\sigma_T = \nu \sigma_M + \sigma_H \tag{21}$$

where σ_H is a hoop stress caused by the term

$$-\frac{\alpha R}{\beta} \left(\frac{dT}{dx}\right) e^{-\beta x} \sin \beta x = \Delta R \text{ of equation (15)}$$

$$\sigma_H = \frac{\Delta R}{R} E \tag{22}$$

d) Tangential shear stress

$$\tau_T = 0 \tag{23}$$
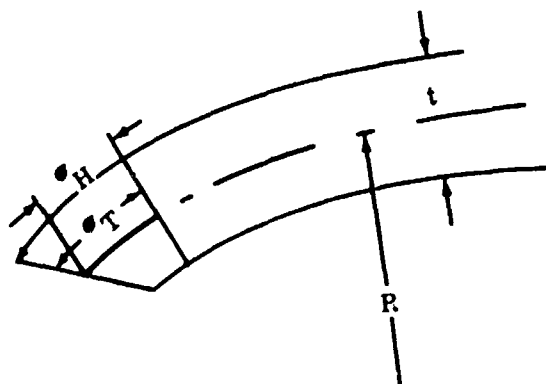
Figure 112.   Tangential Normal
Stress Diagram.

TUBE FAILURE

Using the Mises-Hencky failure theory (maximum deformation energy), tube failure will occur where

$$\sigma_{fail} = \sqrt{\sigma^2_M + \sigma^2_T + \sigma_M \sigma_T + 3\tau^2} \qquad (24)$$

reaches a maximum.

When considering the order of magnitude of the different stresses, σ_M is by far the largest stress, and it is permissible to set

$$\sigma_{fail} = \sigma_M$$

Looking at equation (17), it becomes apparent that the maximum stress occurs at $x = 0$.

Using the following values for calculation,

$$\alpha = 10^{-5} \text{ In./In.-}^\circ F$$

$$t = 3 \times 10^{-3} \text{ In.}$$

165

$$E = 2.3 \times 10^7 \text{ Lb/In.}^2$$

$$R = 6 \times 10^2 \text{ In.}$$

$$(dT/dx) = 6.7 \times 10^3 \text{ °F/In.}$$

$$\nu = 0.3$$

we find

$$\beta = \sqrt[4]{\frac{3(1-\nu^2)}{R^2 t^2}} = 139 \text{ In.}^{-1}$$

$$M_{B,\ x=0} = \frac{\alpha t\, E}{2\beta^3 R}\left(\frac{dT}{dx}\right) = 0.0302 \text{ In. Lb/In.}$$

$$\sigma_{max,\ x=0} = \frac{6M_B}{t^2} = 20,133 \text{ Psi} \approx \sigma_{fail}$$

The maximum thermal stress thus occurs at the end of the tube. Its order of magnitude is below the maximum permissible working stress.

SUSPENSION STRESSES

The original flexible suspension had a U-shaped cross section as shown in Figure 113 Initial calculation of the stresses along the straight sides of this suspension indicated that the stresses due to pressure exceeded the material's yield strength by an order of magnitude.

This result indicated that the suspension would yield, or balloon, as shown in Figure 114. This deformation by itself would not be harmful, but later tests showed that the ballooning led to the development of wrinkles in the corner, and eventually pinholes developed there.
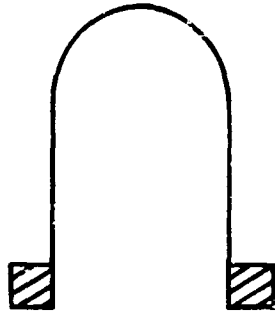
Figure 113. Flexible
Suspension as Installed.
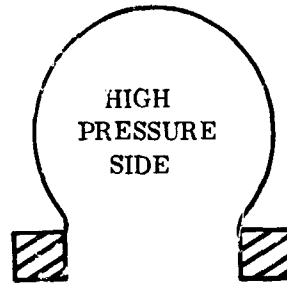
Figure 114. Flexible
Suspension After
Yielding.

These results, combined with problems in the corners resulting from
vibration, led to the design of a suspension which was of circular cross
section in the corner before installation. When installed, the sides also
ballooned permanently, but wrinkles did not develop. The following is an
analysis of a suspension with circular cross section. It also applies to
the original suspension after ballooning has occurred.

Stresses in Suspension With Circular Cross Section

This stress analysis is limited to the straight sides of the module. The
stress concentration effect in the corners cannot be calculated accurately,
but is reduced by larger radii.

The following assumptions are made:

1. The wall thickness is small compared to the radius of the cross
   section.

2. The deformations are elastic.

3. A section of unit width is analyzed.

4. There is no constraint from the corners in the section analyzed.

The configuration and the designations are shown in Figure 115.
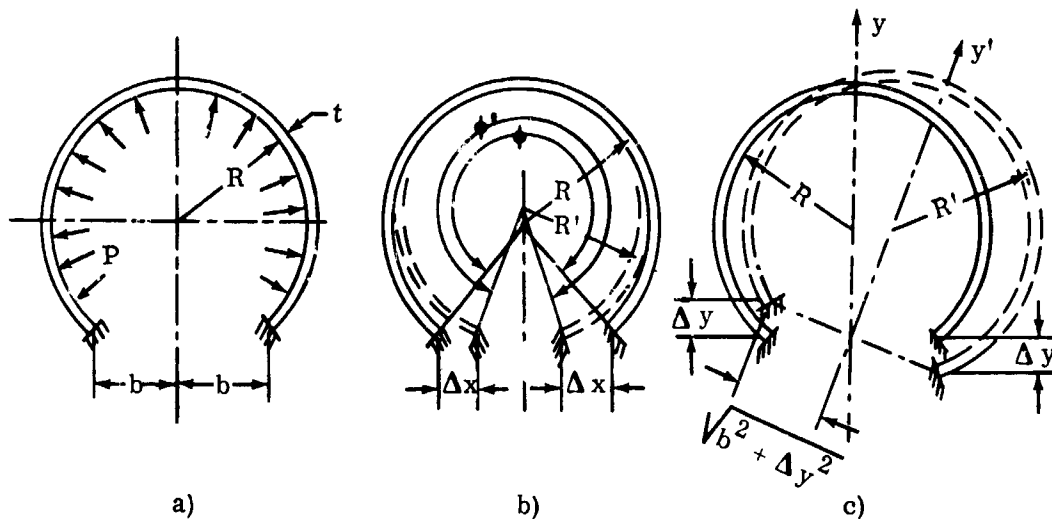
Figure 115.   Suspension Stress Analysis Nomenclature Diagram.

Stresses in the suspension are caused by three effects:

1.   Hoop stresses due to internal pressure (Figure 115a)

$$\sigma_H = \frac{pR}{t} \tag{1}$$

2.   Bending stresses due to a displacement Δx (Figure 115b)

3.   Bending stresses due to a displacement Δy (Figure 115C)

As can be readily seen from Figures (115a) and (115b), deflections Δx and Δy have basically the same effect, namely, a change in the distance between the ends; and, because the length of the neutral fiber remains unchanged during bending, a change in radius of curvature occurs such that

$$\phi R = \phi' R' \tag{2}$$

The rotation of the axis of symmetry in Figure (115c) from y to y' does not affect the bending moment in the cross section, except in the immediate vicinity of the point of attachment.   The local stresses at these points depend to such an extent on the unknown detail configuration, e.g., size and shape of brazed fillet, that a detailed analysis at this point would be meaningless.   It can be further seen that the effect of growth in the direction

168

of the tube axis (Δy) tends to counteract the effect of a growth at right angle to the tube axis (Δx) because:

$$b - \Delta x < b \qquad \text{(Figure 115b)}$$
$$\sqrt{b^2 + \Delta y^2} > b \qquad \text{(Figure 115c)}$$

The analysis of the bending stress is therefore limited to the case of a displacement Δx of Figure 115b.

Analysis of Bending Stress Due to Displacement Δx

For reason of symmetry, the analysis is performed on a half-section, as shown in Figure 116; and an end force F_o and an end moment M_o are applied at the section.

$$x = R \sin \alpha$$
$$y = R (1 - \cos \alpha)$$
$$ds = R d\alpha$$
$$\Delta x = -\Delta H$$
$$\phi = \frac{\phi}{2} = \pi - \arcsin \frac{b}{R}$$
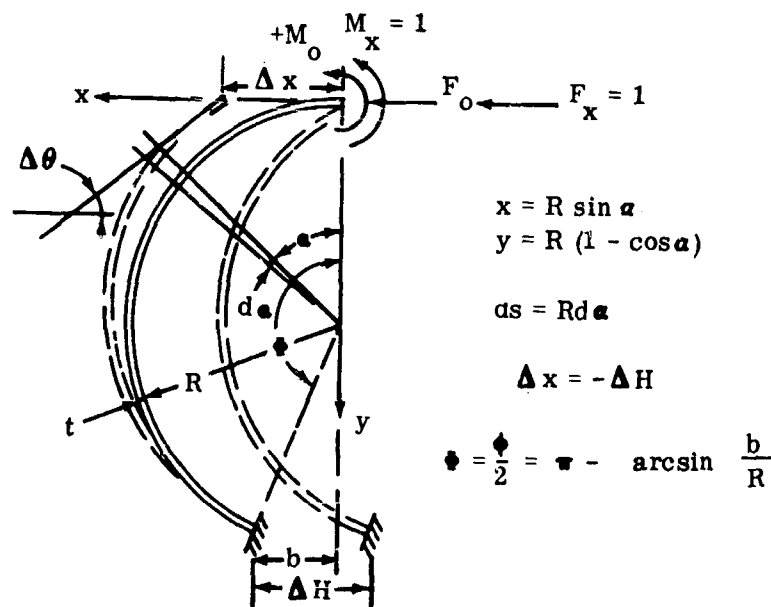
Figure 116.   Suspension Stress Analysis
Nomenclature Diagram.

The linear deflection Δx and the angular deflection $\Delta \theta$ under the effect of the end force F_0 and the end moment M_0 are now calculated by means of

169

equations (3) through (9); by substituting the boundary conditions, the values for F_O and M_O are computed. With F_O and M_O known, the bending moment and the bending stress at any point of the cross section can be calculated. The total stress in the suspension is obtained by superposition of the bending stress and the hoop stress of equation (1).

The deflections were calculated as follows:

Linear deflection Δx caused by moment M_O:

$$\Delta x_{M_O} = \frac{1}{EI} \int_0^\phi M_O M_{F_x} ds = \frac{M_O}{EI} \int_0^\phi R(1 - \cos\alpha) Rd\alpha \tag{3}$$

$$\Delta x_{M_O} = \frac{M_O R^2}{EI} \left(\phi - \sin\phi \right) \tag{4}$$

Linear deflection Δx caused by force F_O:

$$\Delta x_{F_O} = \frac{1}{EI} \int_0^\phi M_{F_O} M_{F_x} ds = \frac{F_O}{EI} \int_0^\phi R(1 - \cos\alpha) R(1 - \cos\alpha) Rd\alpha \tag{5}$$

$$\Delta x_{F_O} = \frac{F_O R^3}{2EI} (3\phi - 4\sin\phi + \sin\phi \cos\phi) \tag{6}$$

Angular deflection $\Delta\theta$ caused by moment M_O:

$$\Delta\theta_{M_O} = \frac{1}{EI} \int_0^\phi M_O M_x ds = \frac{M_O}{EI} \int_0^\phi Rd\alpha \tag{7}$$

$$\Delta\theta_{M_O} = \frac{M_O R}{EI} \phi \tag{8}$$

Angular deflection $\Delta\theta$ caused by force F_o:

$$\Delta\theta_{F_o} = \frac{1}{EI} \int_0^{\phi} M_{F_o} M_x \, ds = \frac{F_o}{EI} \int_0^{\phi} R(1 - \cos\alpha)R \, d\alpha \qquad (9a)$$

$$\Delta\theta_{F_o} = \frac{F_o R^2}{EI}\left(\phi - \sin\phi\right) \qquad (9b)$$

Adding linear and angular deflections, equations (4), (6), (8) and (9b), and introducing the boundary conditions:

$$\sum \Delta x = -H \qquad (10a)$$

$$\sum \Delta\theta = 0 \qquad (10b)$$

This yields:

$$\frac{M_o R^2}{EI}\left(\phi - \sin\phi\right) + \frac{F_o R^3}{2EI}\left(3\phi - 4\sin\phi + \sin\phi\cos\phi\right) + H = 0 \qquad (11a)$$

$$\frac{M_o R \phi}{EI} + \frac{F_o R^2}{EI}\left(\phi - \sin\phi\right) = 0 \qquad (11b)$$

From these two equations, we obtain the values of the moment M_o and the force F_o:

$$M_o = -\frac{2EIH}{R^2} \frac{\phi - \sin\phi}{2\sin^2\phi - \phi\sin\phi\cos\phi - \phi^2} \qquad (12a)$$

$$F_o = \frac{2EIH}{R^3} \frac{\phi - \sin\phi}{2\sin^2\phi - \phi\sin\phi\cos\phi - \phi^2} \qquad (12b)$$

171

From the geometrical relationships of Figure 116, we derive

$$\sin\left(\pi - \phi\right) = \frac{b}{R} = \sin\left(\phi\right) \tag{13a}$$

$$\cos\phi = -\sqrt{1 - b^2/R^2} \tag{13b}$$

$$\phi = \pi - \arcsin\left(b/R\right) \tag{13c}$$

The stiffness EI of the beam of unity width calculates to

$$EI = \frac{Et^3}{12\left(1 - \nu^2\right)} \tag{14}$$

The bending moment in any section now becomes:

$$M_B = M_0 + F_0 R\left(1 - \cos\alpha\right) \tag{15}$$

and the bending stress is given by

$$\sigma_{\alpha,\,max} = \frac{6\,M_B}{t^2} \tag{16}$$

or

$$\sigma_{B\,\alpha,\,max} = \frac{EtH}{R^2\left(1 - \nu^2\right)}\;\frac{\sin\phi - \phi\cos\phi}{2\sin^2\phi - \phi\,\sin\phi\cos\phi - \phi^2} \tag{17}$$

It can be seen from equation (17) that the bending stress reaches a first maximum at the center of the suspension and a second maximum at the point of attachment.

To determine which maximum is larger, let

$$\psi_0 = \psi \bigg|_{\alpha = 0} = \frac{\sin \phi - \phi}{2 \sin^2 \phi - \phi \sin \phi \cos \phi - \phi^2} \tag{18a}$$

$$\psi_\phi = \psi \bigg|_{\alpha = \phi} = \frac{\sin \phi - \phi \cos \phi}{2 \sin^2 \phi - \phi \sin \phi \cos \phi - \phi^2} \tag{18b}$$

The two functions are plotted in Figure 117 with b/R as abscissa. We see that the maximum stress occurs always at the point of attachment.

The total stress in the suspension is then

$$\sigma_{tot} = \frac{p\,R}{t} + \frac{EtH}{\left(R^2\,1 - \nu^2\right)} \psi_\phi \tag{19}$$

To select a suitable geometry, the minimum of equation (19) could be determined for given values of H and P; an approximate solution was developed by expressing ψ_ϕ as follows:

$$\psi_\phi = 0.295 \; (3.254)^{b/R} \tag{20}$$

Substituting equation (20) in equation (19), differentiating and setting the result equal to zero yields:

$$X = \frac{R^3}{(3.254)^{b/R} \left(2 + b/R \text{ In. } 3.254\right)} = 0.295 \; \frac{E\,t^2\,H}{\left(1 - \nu^2\right)P} \tag{21}$$

This expression is best solved graphically, plotting X versus R on log-paper with b/R as parameter, calculating the expression on the right-hand side, and reading the radius from the graph; the proper b/R-curve from which to read the radius is found by trial and error.

Execution of this procedure shows that useable values of b/R always fall in the range of 0.4 to 0.6. The effect of varying b/R in this range is small, and the alternate method presented below becomes practical and yields the desired result faster.
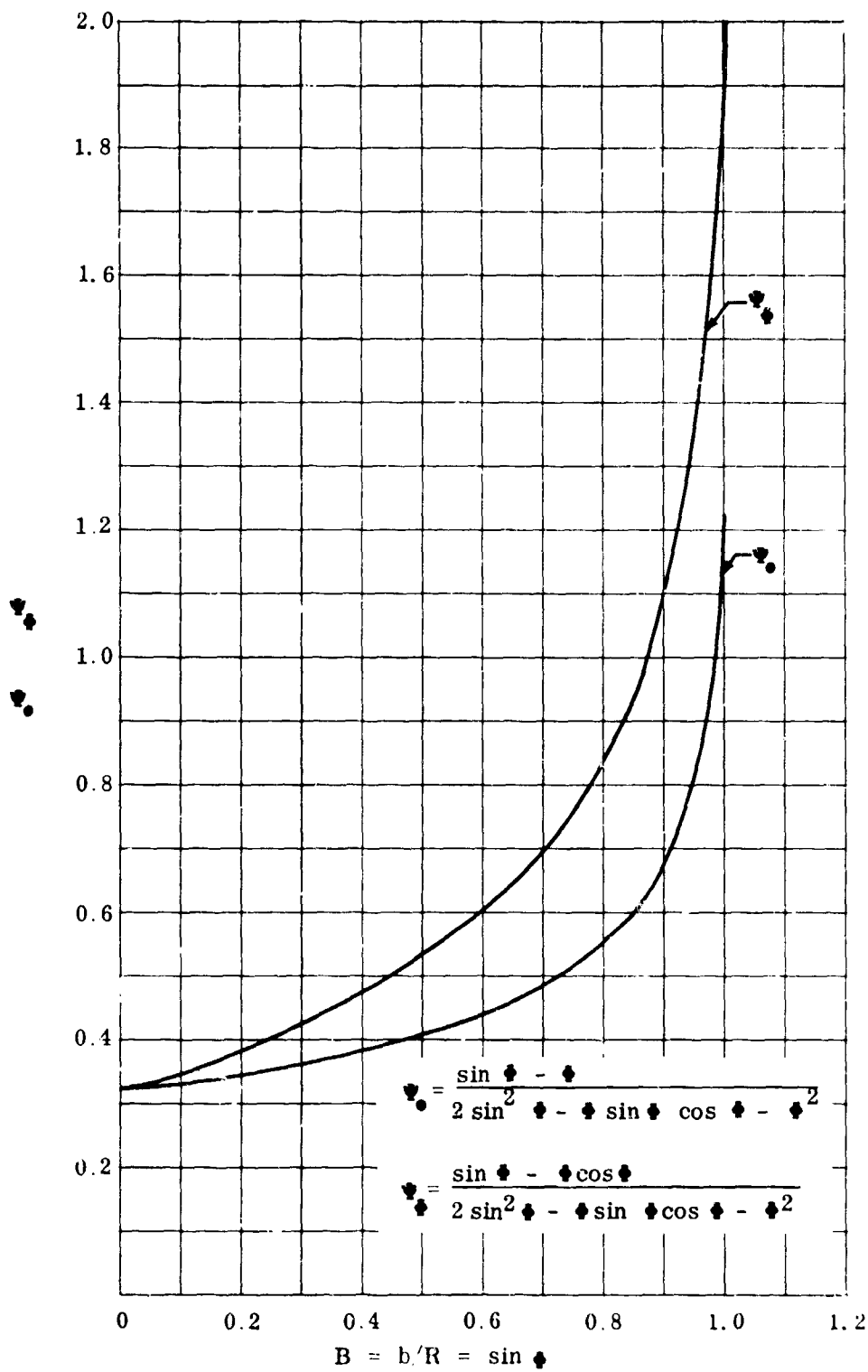
Figure 117. Suspension Stress Analysis Functions.

The alternate procedure is to select a ratio b/R, to read Ψ_ϕ from Figure 117 and to treat it as a constant in subsequent calculations. Differentiation of equation (19) and setting the resulting expression equal to zero then yields:

$$R_{opt} = \sqrt[3]{\frac{2E\Psi_\phi}{1-\nu^2}} \; \sqrt[3]{\frac{t^2 H}{P}} \tag{22}$$

Sample Calculation

The latter calculation is illustrated by the following:

We assume the following values and conditions:

$$E = 2.3 \times 10^7 \; Lb/In.^2$$

$$\nu = 0.3$$

$$\Delta T = T_2 - T_1 = 500° F \; (\text{see Figure 117})$$

$$p = P_{air} - P_{gas} = 135 \; Psi$$

$$L_A = 4.5 \; In.$$

$$\alpha = 10^{-5} \; In./in. \; °F$$

$$b/R = 0.5$$

The calculation proceeds as follows:

Thermal Expansion of Module

The displacement H, due to a temperature difference between module and frame, is shown in Figure 118.
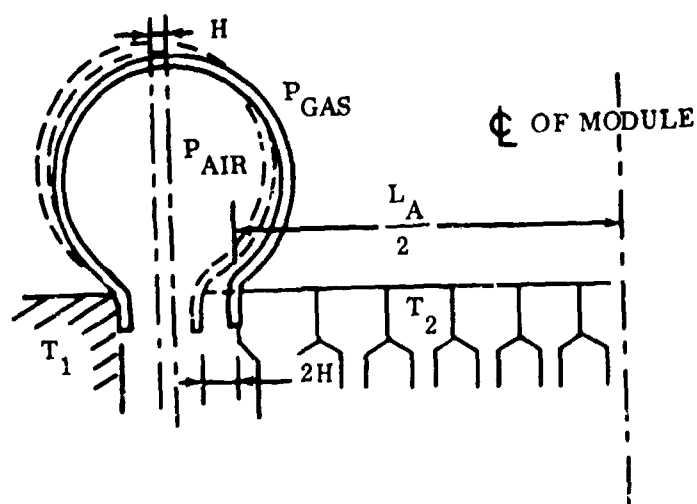
Figure 118. Displacement Due to Nonuniform
Thermal Expansion.

Thus,

$$H = 1/4 \ \alpha \ L_A \ \Delta T = 0.5625 \times 10^{-2} \ \text{In.}$$

Value of ψ_ϕ :

From Figure 117,

$$b/R = 0.5 \qquad \psi_\phi = 0.53$$

Values for R and t from equation (22):

$$R_{opt.} = \sqrt[3]{\frac{2 \times 2.3 \times 10^{+7} \times 0.53 \times 0.5625 \times 10^{-2}}{0.91 \times 135}} \ \sqrt[3]{t^2}$$

$$R_{opt.} = 1037.3 \ \sqrt[3]{t^2} \tag{23}$$

The optimum radius and wall thickness, t, are plotted in Figure 119.
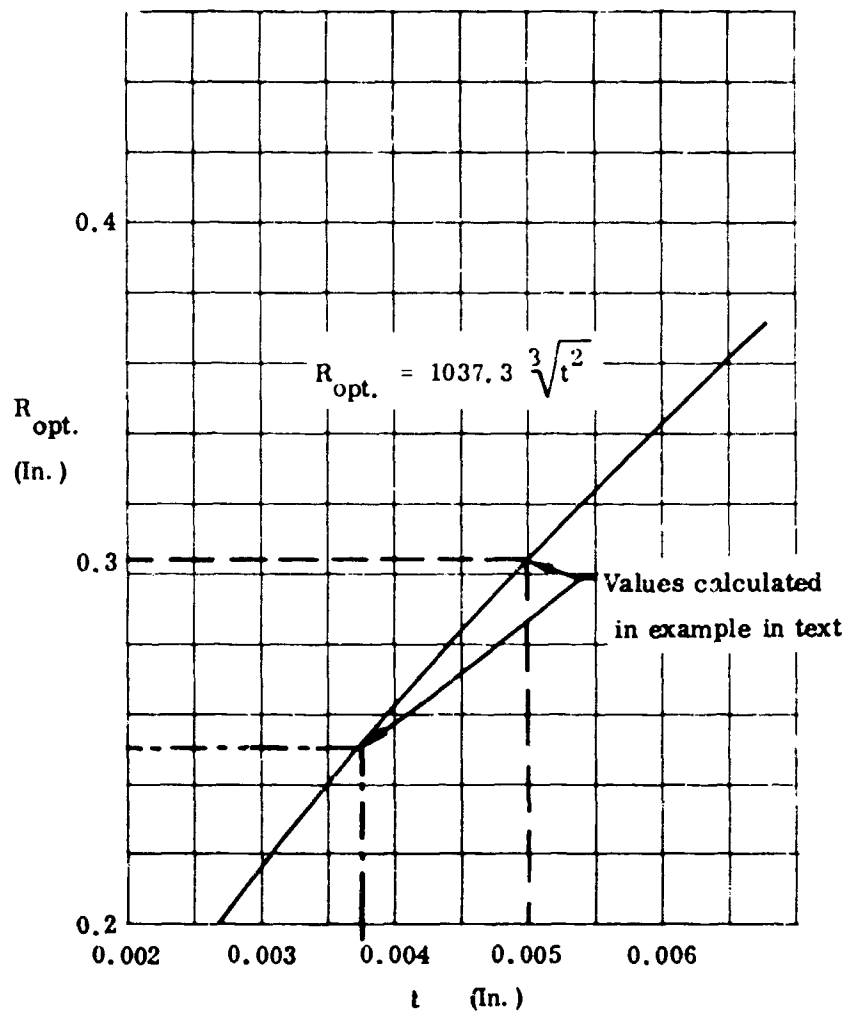
Figure 119. Optimum Suspension Radius
Versus Wall Thickness.

177

We see that selecting the radius at 0.25 inch to fit the existing hardware requires a wall thickness of 0.00375 inch, which is too thin for manufacturing reasons. Selection of the minimum practical thickness of 0.005 inch yields an optimum radius of 0.304 inch.

The stresses for this combination are as follows:

From equation (1) $\sigma_H = 8,208$ Psi

From equation (17) $\sigma_B = 4,077$ Psi

and $\sigma_{tot.} = 12,285$ Psi

To suit the existing hardware, we have to deviate from the optimum and we select:

$$R = 0.250 \text{ In.}$$

$$t = 0.005 \text{ In.}$$

The stresses, then, are as follows:

$$\sigma_H = 6,750 \text{ Psi}$$

$$\sigma_B = 6,028 \text{ Psi}$$

$$\sigma_{tot.} = 12,778 \text{ Psi}$$

Discussion of Results

From the results we see that the deviation from the optimum does not result in an excessive penalty; the effects of deviations are largely cancelled by their inverse effect on hoop and bending stress.

If manufacturing tolerances are taken into account, the stresses in the proposed circular suspension will be of the order of 15,000 pounds per square inch.

The stresses in the module corners will be higher, but they are not amenable to a simple analysis. Large corner radii will minimize the stresses in these areas.

APPENDIX IV

DATA REDUCTION METHODS FOR SINGLE-TUBE TESTS

The single-tube test rig is essentially a counterflow heat exchanger with the heat capacity of the airstream small compared to the heat capacity of the water stream. Air enters at $T_{A,1}$ and leaves at $T_{A,2}$. Water enters at $T_{W,1}$ and leaves at $T_{W,2}$. The resistance to heat transfer on the water side of the tubular surface is negligible when compared to the air side.

COLBURN FACTOR, j

For this configuration, Reference 1, page 19, shows that the effectiveness is

$$\epsilon = 1 - e^{-Ntu} \tag{1}$$

For the minimum heat capacity fluid (air), the effectiveness is given by

$$\epsilon = \frac{T_{A,2} - T_{A,1}}{T_{W,1} - T_{W,2}} \tag{2}$$

Combining (1) and (2),

$$\frac{T_{A,2} - T_{A,1}}{T_{W,1} - T_{A,1}} = 1 - e^{-Ntu} \tag{3}$$

With some rearrangement, (3) reduces to

$$\frac{T_{W,1} - T_{A,2}}{T_{W,1} - T_{A,1}} = e^{-Ntu} \tag{4}$$

Taking natural logarithms of both sides

$$Ntu = \ln\left(\frac{T_{W,1} - T_{A,1}}{T_{W,1} - T_{A,2}}\right) \tag{5}$$

The Ntu is defined as

$$Ntu = \frac{Ah}{Wc_p} \tag{6}$$

The Stanton number, N_{St}, is defined as

$$N_{St} = \frac{A_c h}{WC_p} \tag{7}$$

Combining (5), (6), and (7),

$$N_{St} = \frac{A_c}{A} \ln \left(\frac{T_{W,1} - T_{A,1}}{T_{W,1} - T_{A,2}} \right) \tag{8}$$

The Colburn factor is defined as

$$j = N_{St} N_{Pr}^{2/3}$$

Thus,

$$j = N_{Pr}^{2/3}, \frac{A_c}{A} \ln \frac{T_{W,1} - T_{A,1}}{T_{W,1} - T_{A,2}}$$

REYNOLDS NUMBER

The Reynolds number is defined as

$$N_R = \frac{WD_H}{A_c \mu}$$

μ, the viscosity, is evaluated from Reference 1, page 233, at the mean air temperature.

$$T_{M,A} = \frac{T_{A,1} - T_{A,2}}{2}$$

FRICTION FACTOR, f

From Reference 1, page 33, for an isothermal pressure drop corresponding to the method by which the data were taken,

$$\Delta P = \frac{W^2 v_1}{A_C^2 2g_C} \left((K_c + 1 - \sigma^2) + f \frac{A}{A_c} \right)$$

Rearranging,

$$f = \frac{A_c}{A} \left(\frac{\Delta P A_c^2 2 g_c}{W^2 v_1} - (K_c + 1 - \sigma^2) \right)$$

K_c is taken from Reference 1, page 93, at the Reynolds number and L/D corresponding to the test condition.

The data reduced by these formulae are then plotted in the form of f and j versus N_R.

APPENDIX V

RESULTS OF SINGLE TUBE TESTS
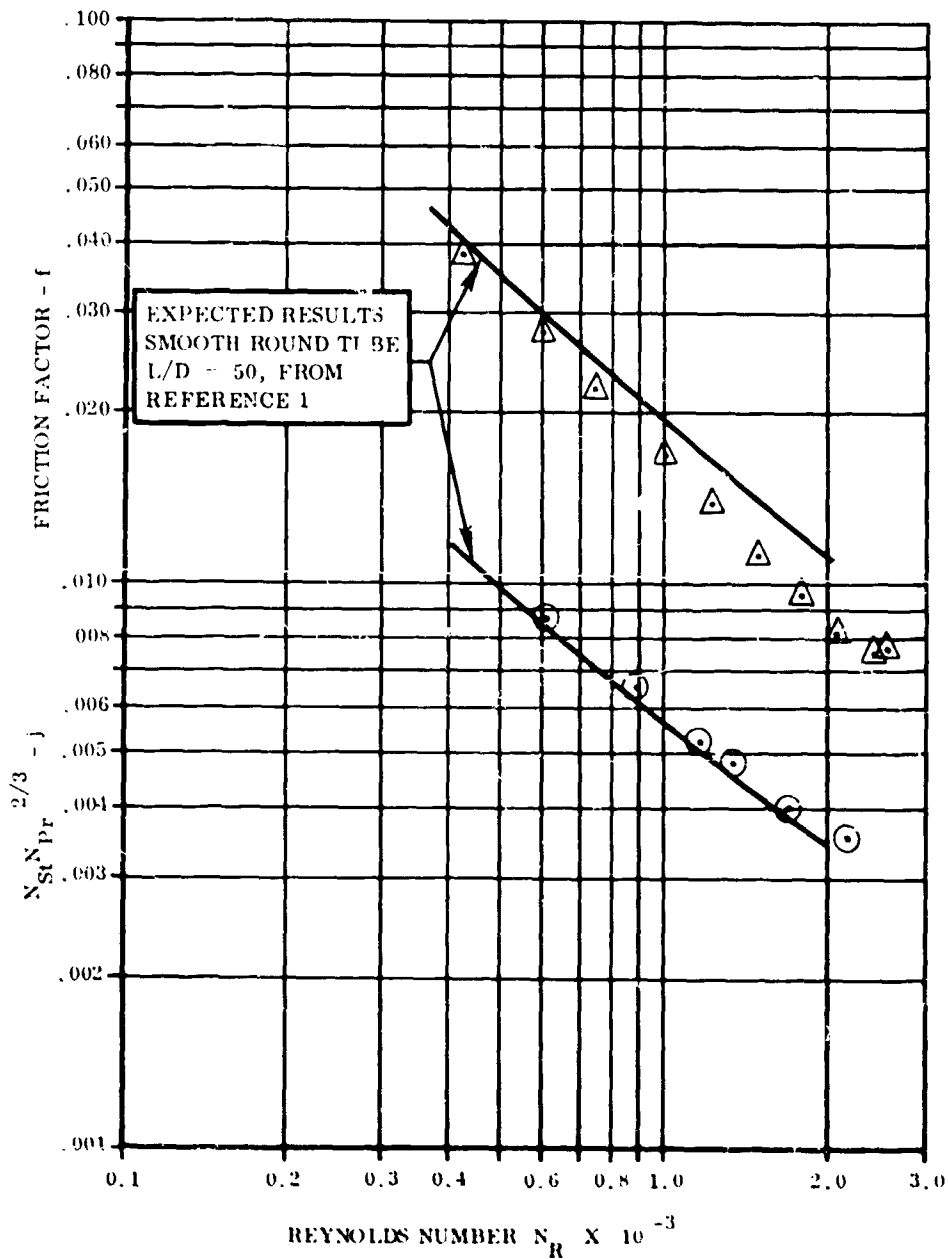
Figure 120. Heat Transfer and Pressure Drop Characteristics, Smooth Tube, Flared Ends.

182
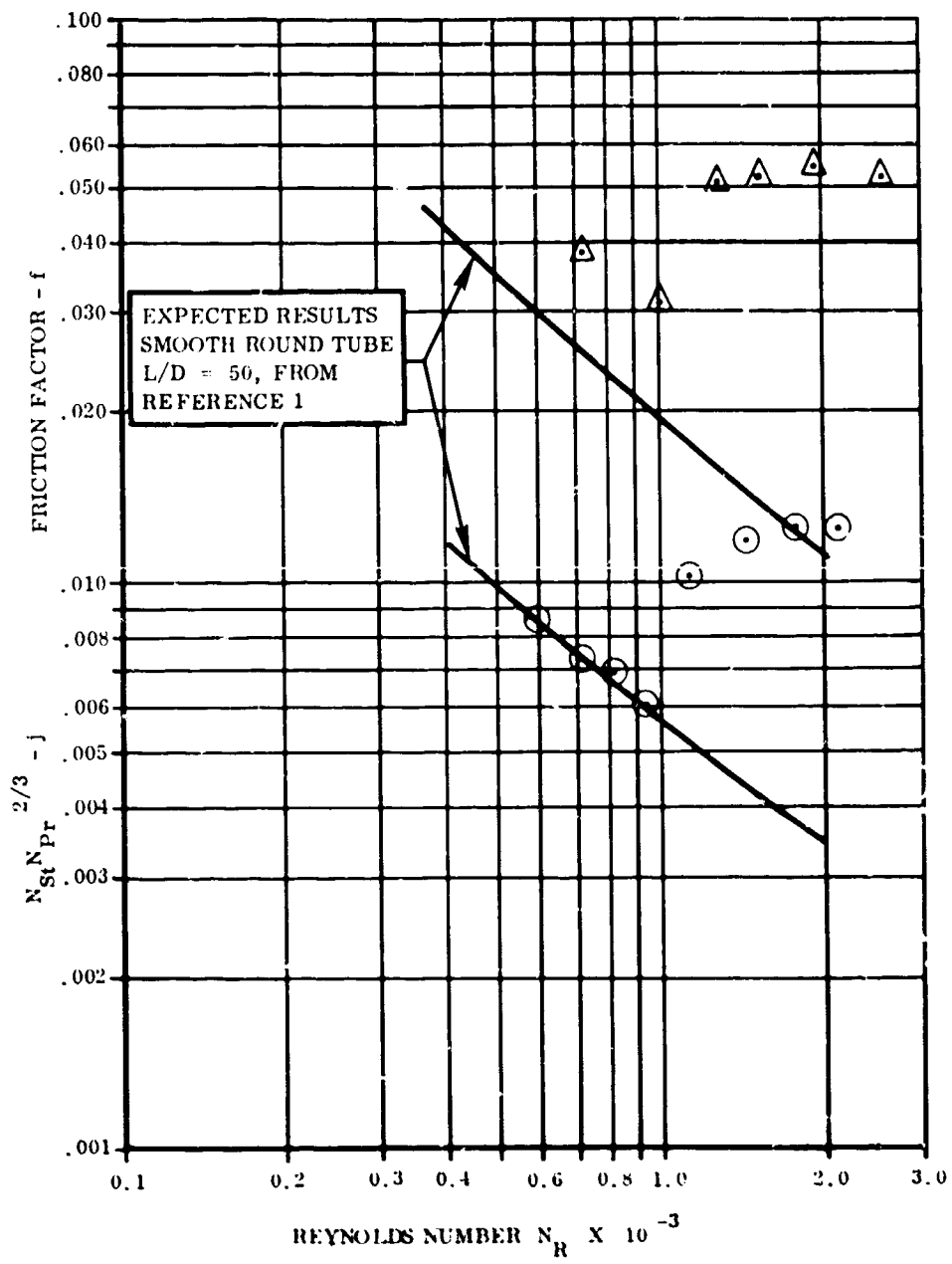
Figure 121. Heat Transfer and Pressure Drop Characteristics, Ring-Dimpled Tube.
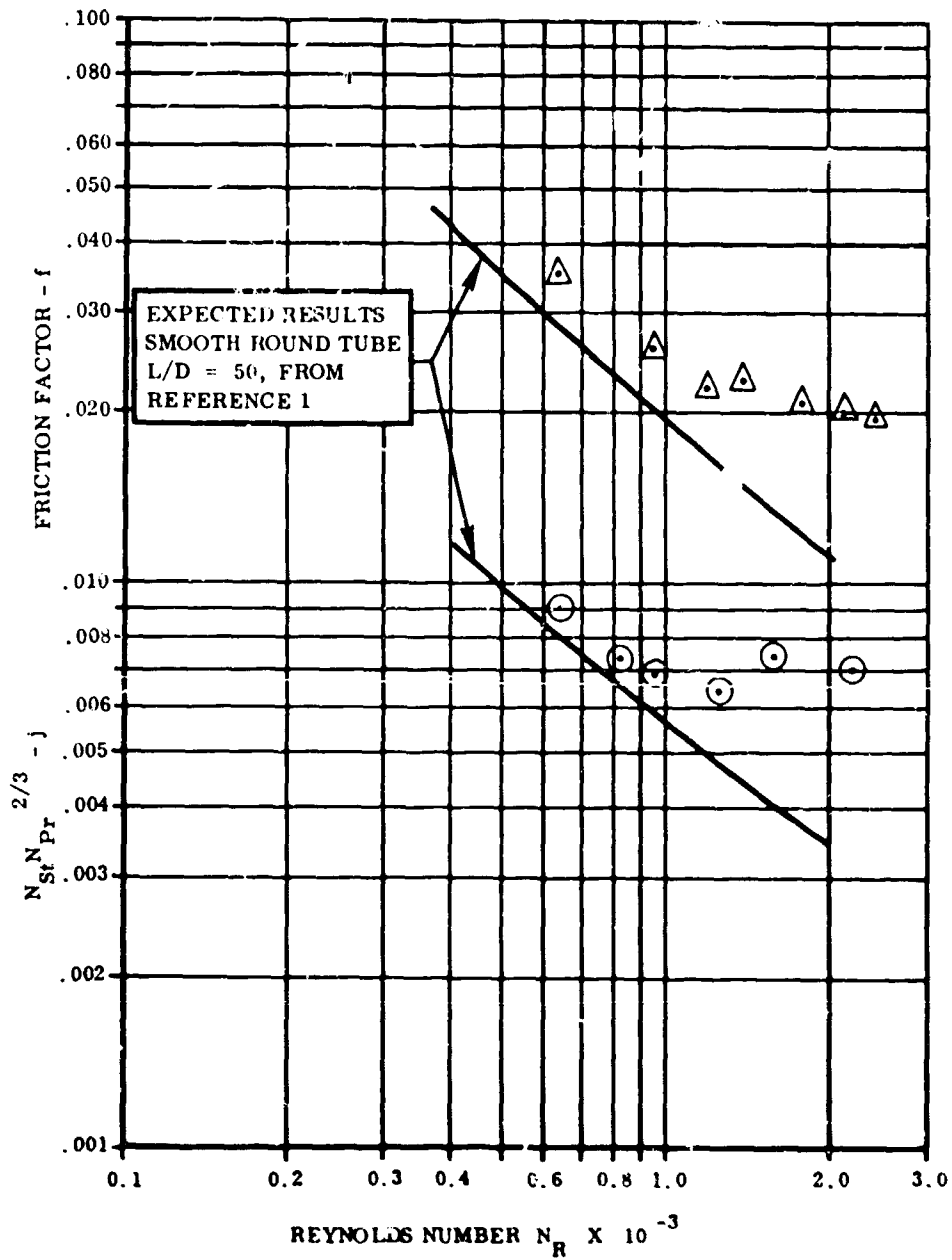
Figure 122. Heat Transfer and Pressure Drop Characteristics, Spiral-Dimpled Tube.

184
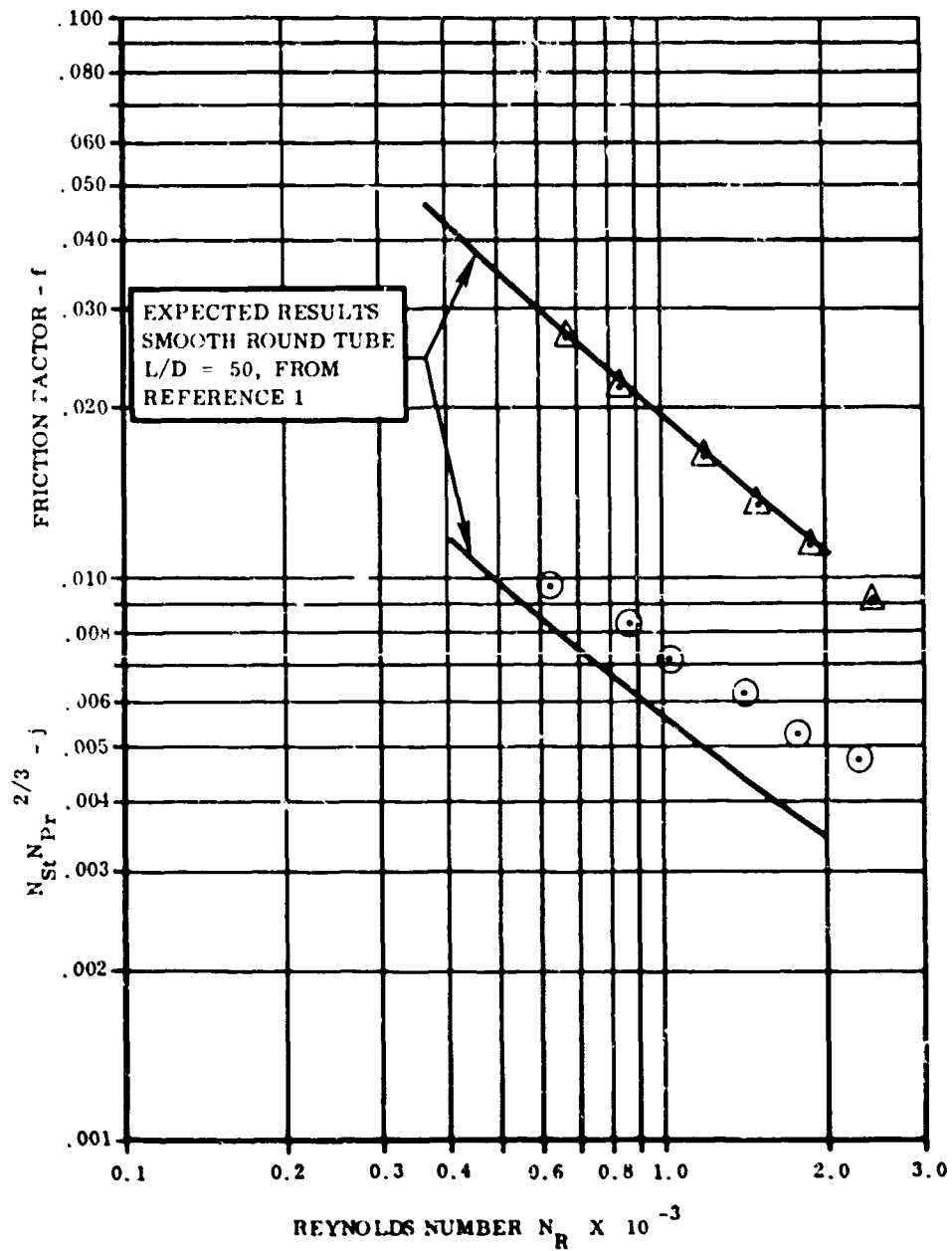
Figure 123. Heat Transfer and Pressure Drop Characteristics, 1/2-Cycle Wavy Tube.

185
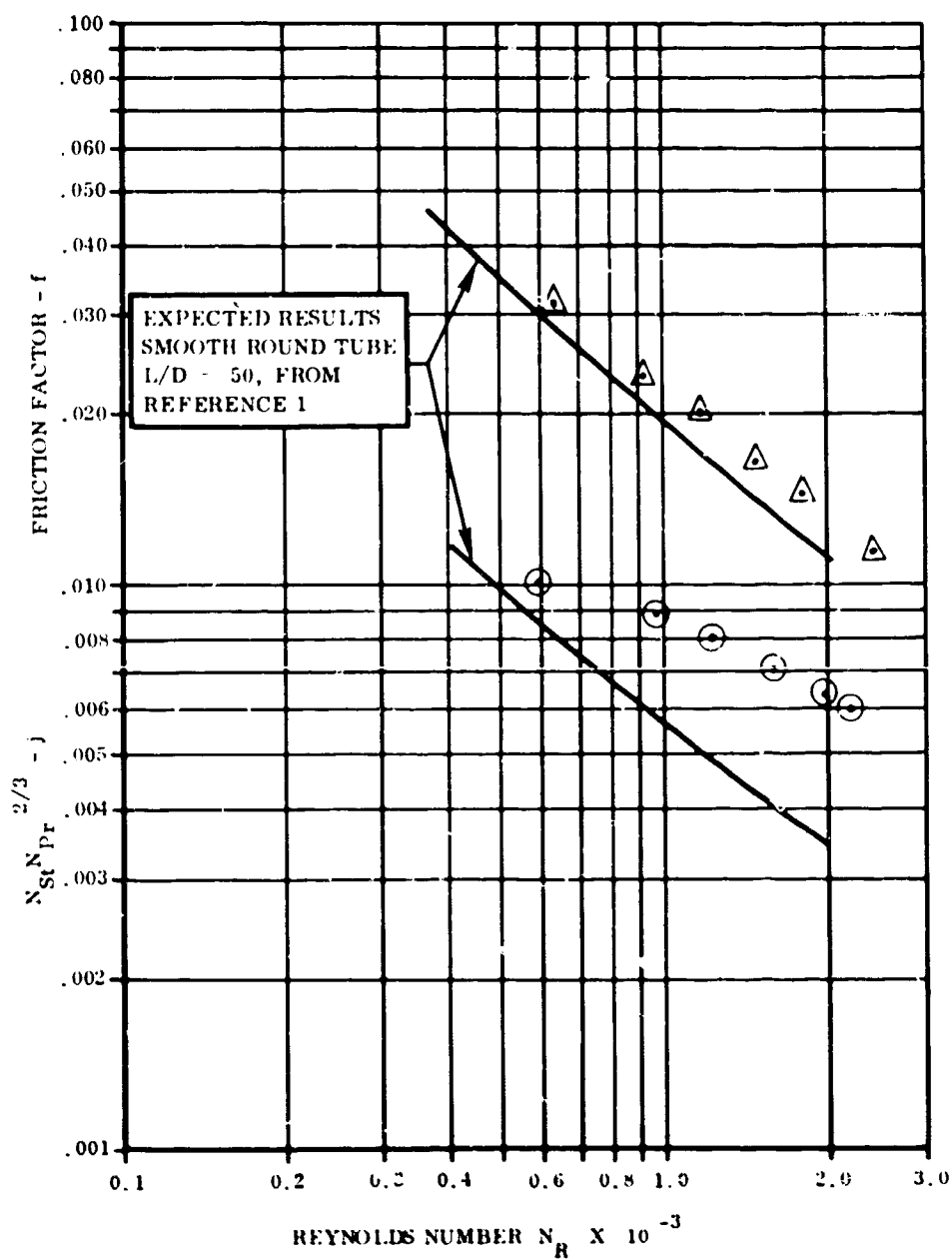
Figure 124. Heat Transfer and Pressure Drop Characteristics, 1-Cycle Wavy Tube.

136
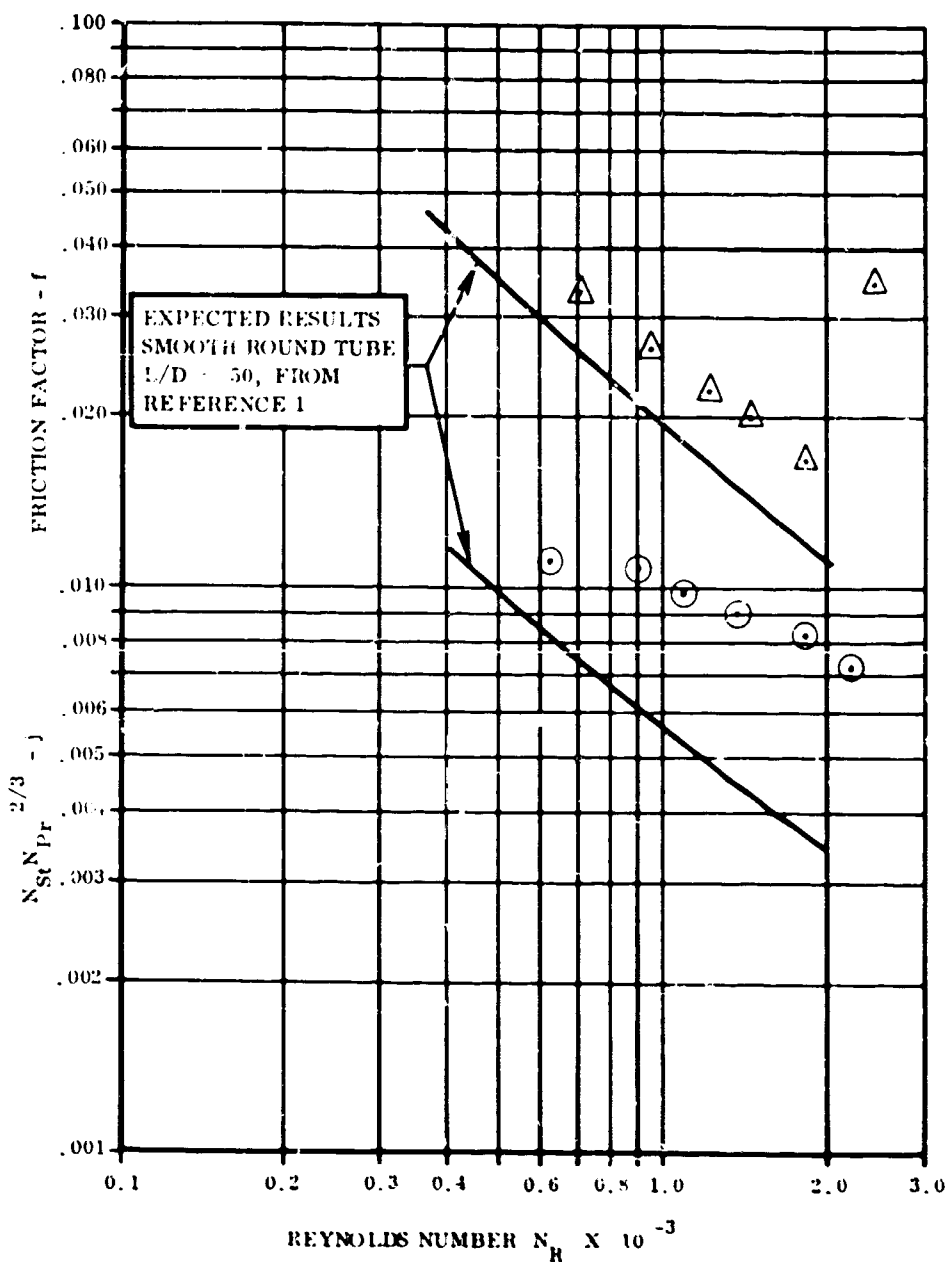
Figure 125. Hea⁺ Transfer and Pressure Drop Characteristics, 1-1/2-Cycle Wavy Tube.

187
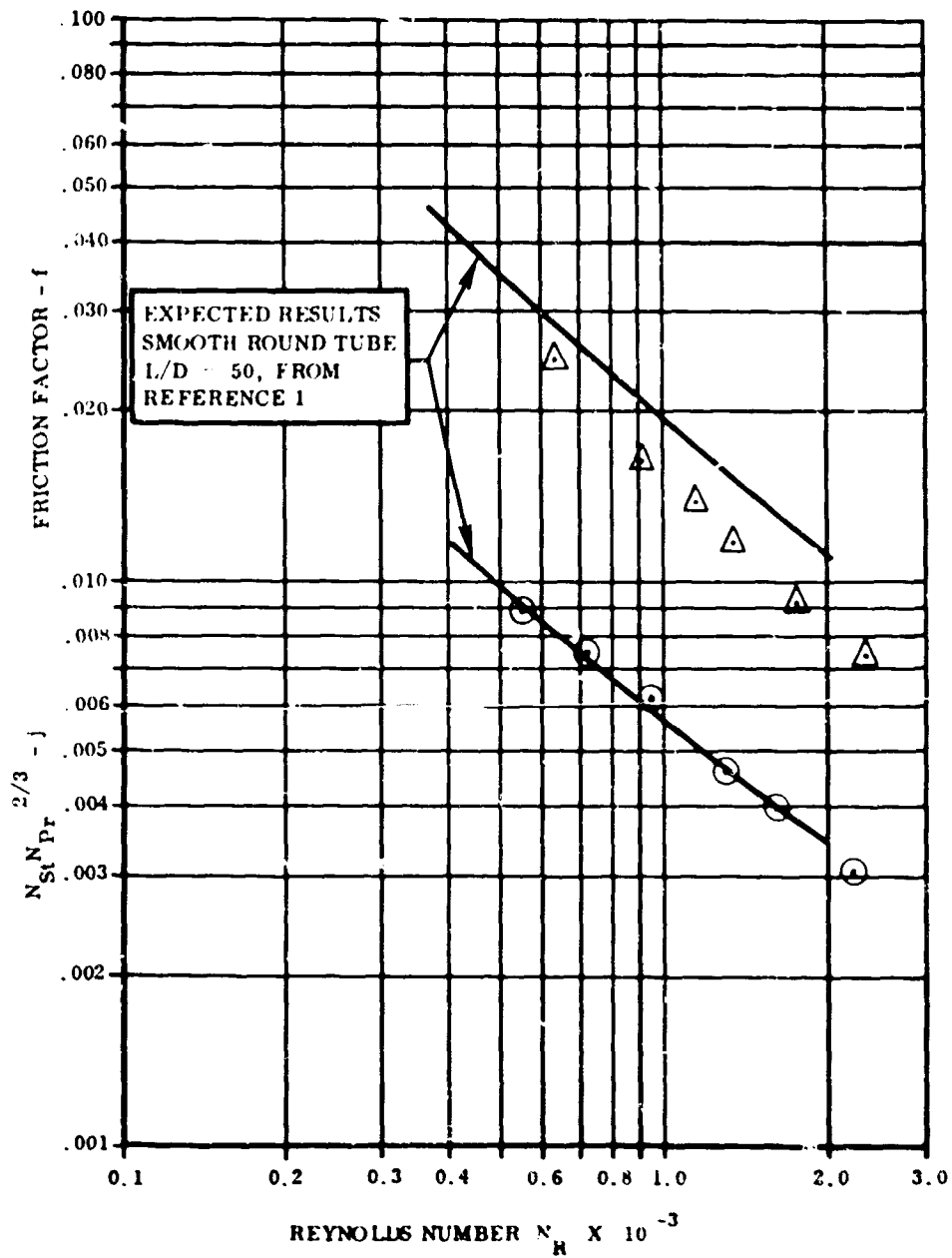
Figure 126. Heat Transfer and Pressure Drop Characteristics, Ring Expanded Tube.

188
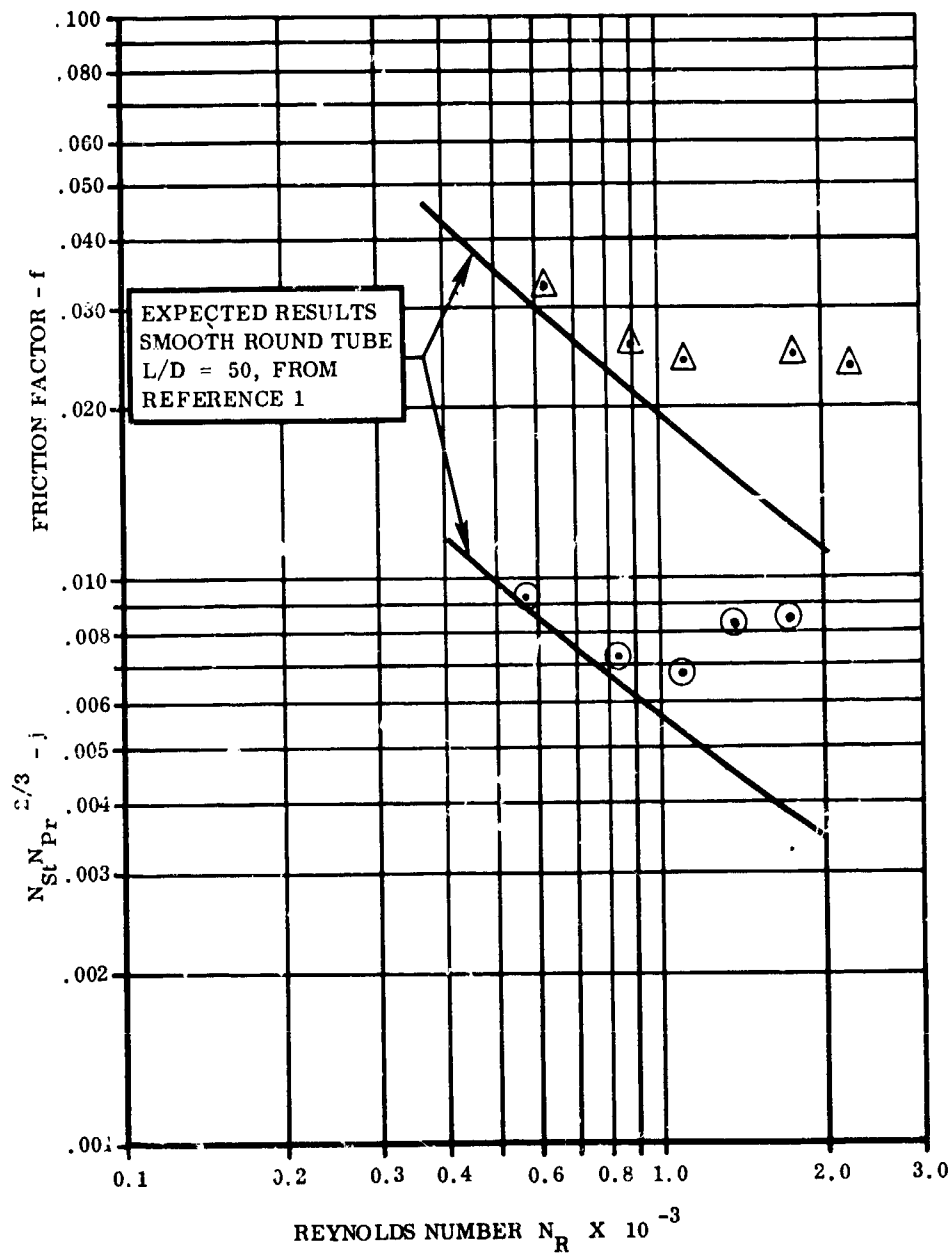
Figure 127. Heat Transfer and Pressure Drop Characteristics,
Surface Roughened Tube, 0.042-Diameter
Particles in 0.210 ID Tube.

189
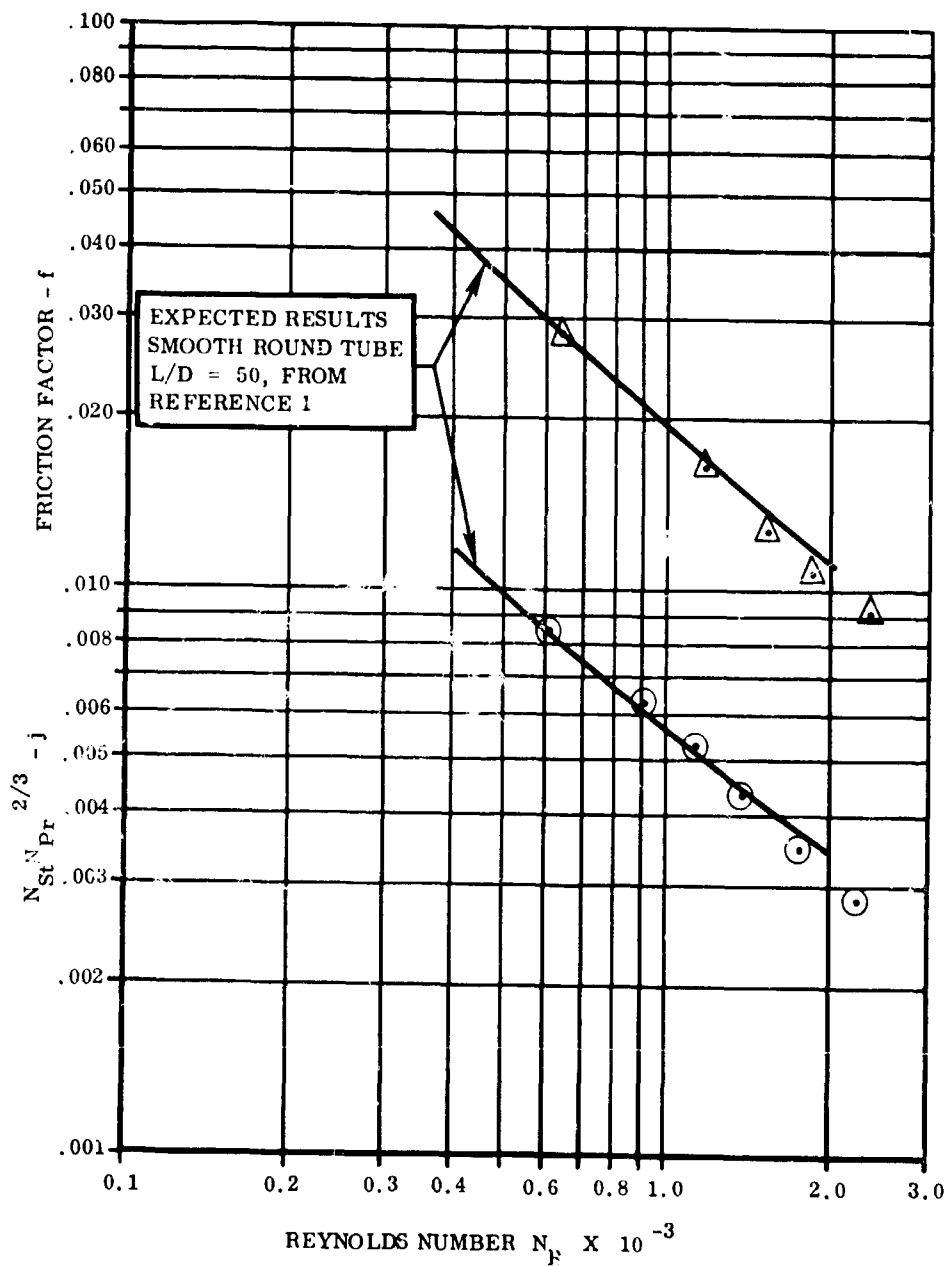
Figure 128. Heat Transfer and Pressure Drop Characteristics, Surface Roughened Tube, 0.021-Diameter Particles in 0.210 ID Tube.

190
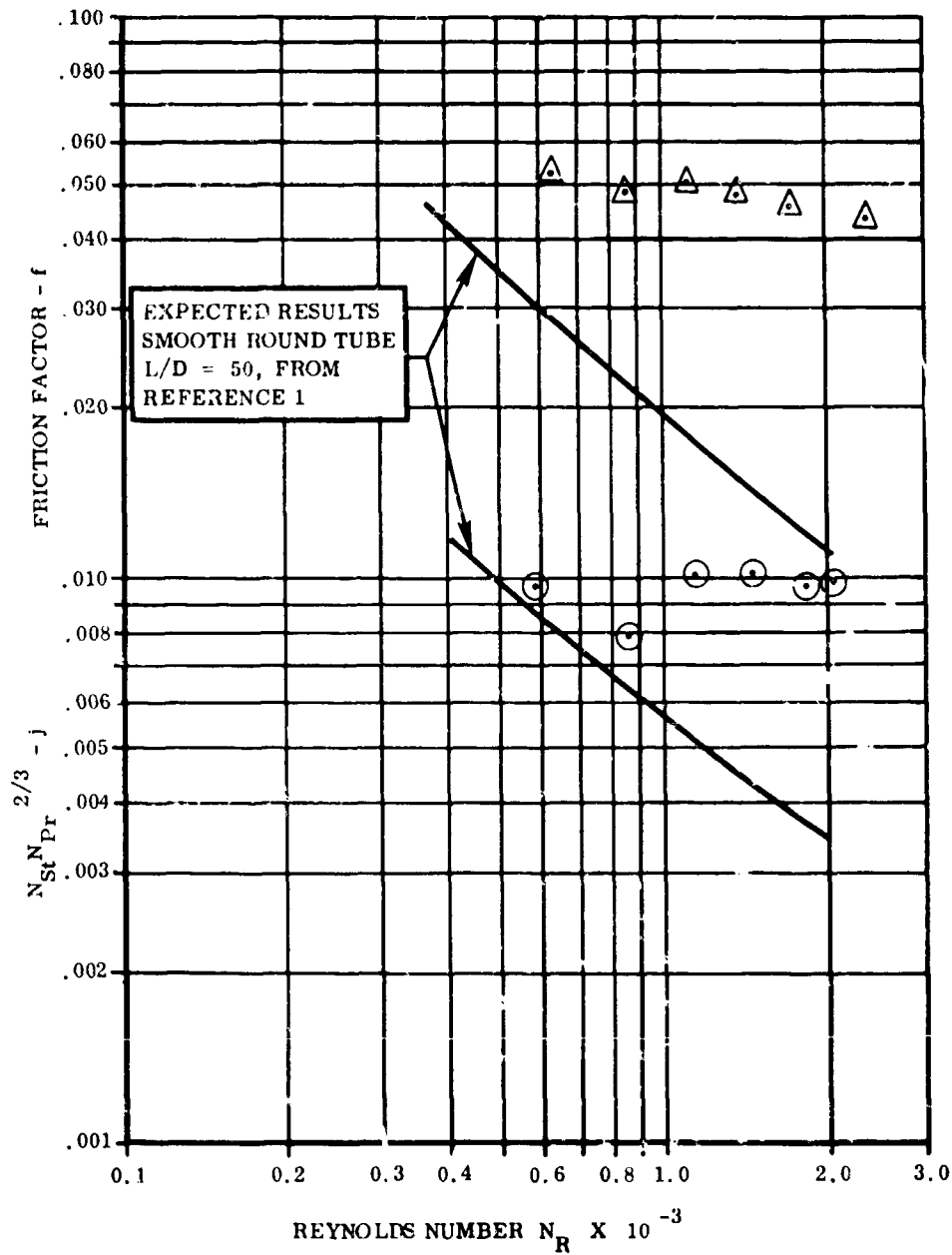
Figure 129. Heat Transfer and Pressure Drop Characteristics,
Surface Roughened Tube. Mixed Sand Grains From
0.016 to 0.046 Diameter ir 0.210 ID Tube.

191

TABLE XV
RESULTS OF BRAZED FOIL TESTS AT VARIOUS BRAZING TEMPERATURES

Palniro 1 foil

	347	316L
2075-2100° F	Clean	Clean
	No erosion	No erosion
	Some flow	Some flow
2100-2125° F	Clean	Clean
	No erosion	No erosion
	Some flow	Some flow
2125-2150° F	Clean	Clean
	No erosion	No erosion
	Some flow	Some flow
2150-2175° F	Clean	Clean
	Eroded through	Incipient erosion
	Some flow	Some flow

Palniro 7 foil

	347	316L
1950-1975° F	Clean	Clean
	No erosion	No erosion
	Some flow	Some flow
1975-2000° F	Clean	Clean
	No erosion	No erosion
	Some flow	Some flow
2000-2025° F	Clean	Clean
	No erosion	No erosion
	Flow	Flow
2025-2050° F	Clean	Clean
	Erosion	No erosion
	Flow	Flow

Palniro 7 powder

	347	316L
1950-1975° F	Clean	Clean
	No erosion	No erosion
	Flow	Flow
1975-2000° F	Clean	Clean
	Erosion	No erosion
	Flow	Flow
2000-2025° F	Clean	Clean
	Erosion	Erosion
	Flow	Flow
2025-2050° F	Clean	Clean
	Erosion	Erosion
	Good flow	Good flow

Engelhard 440 foil

	347	316L
2075-2100° F	Very slight contamination	Very slight contamination
	No erosion	No erosion
	Some flow	Some flow
2100-2125° F	Clean	Clean
	No erosion	No erosion
	Flow	Flow
2125-2150° F	Slight contamination	Slight contamination
	No erosion	No erosion
	Flow	Flow
2150-2175° F	Slight contamination	Slight contamination
	No erosion	No erosion
	Flow	Flow

Engelhard 135 powder

	347	316L
2050-2075° F	Slight Grey contamination	Slight grey contamination
	No erosion	No erosion
	Some flow	Some flow
2100-2125° F	Some grey contamination	Some grey contamination
	No erosion	No erosion
	Some flow	Some flow
2125-2150° F	Some grey contamination	Some grey contamination
	No erosion	No erosion
	Some flow	Some flow

All specimens brazed 15/20 minutes in argon atmosphere. Type 347 stainless steel, 0.003 in. thick, AMB 5512 & MIL-S-6721B annealed.

Type 316L stainless steel, 0.004 in. thick, MIL-S-5059A, annealed

Specimens were cleaned 15 minutes in hot phosphosilicate solution, pickled 15 minutes in HF/HNO$_3$, cleaned in methyl ethyl ketone

TABLE XV (Continued)

Coast Metals 52 foil

	347	316L
1950-1975° F	Clean	Bluish contamination
	No erosion	No erosion
	Flow	Flow
1975-2000° F	Clean	Bluish contamination
	No erosion	No erosion
	Flow	Flow
2000-2025° F	Slight contamination	Bluish contamination
	No erosion	No erosion
	Good flow	Good flow
2025-2050° F	Slight contamination	Slight contamination
	No erosion	No erosion
	Good flow	Good flow

Coast Metals 62 powder

	347	316L
1950-1975° F	Slight contamination	Bluish contamination
	No erosion	No erosion
	Some flow	Some flow
1975-2000° F	Contamination at edge of alloy	Bluish contamination overall
	No erosion	No erosion
	Flow	Flow
2000-2025° F	Contamination at edge of alloy	Bluish contamination overall
	No erosion	No erosion
	Flow	Flow
2025-2050° F	Contamination edge of alloy	Bluish contamination
	No erosion	No erosion
	Good flow	Good flow

Nicrobraz 200 powder

	347	316L
2000-2025° F	Clean	Clean
	Erosion	Erosion
	Little flow	Little flow
2025-2050° F	Clean	Clean
	Erosion	Incipient erosion
	Little flow	Little flow
2050-2075° F	Clean	Clean
	Erosion	Incipient
	Little flow	Some flow
2050-2100° F	Clean	Clean
	Erosion	Erosion
	Some flow	Some flow

General Electric 8102 powder

	347	316L
2200-2225° F	Clean	Clean
	No erosion	No erosion
	Some flow	Some flow
2225-2250° F	Clean	Clean
	Incipient erosion	No erosion
	Some flow	Some flow

Coast Metals 52 + Co

	347	316L
2100-2125° F	Some contamination	Some contamination
	Erosion	Erosion
	Good flow	Good flow
2125-2150° F	Some contamination	Some contamination
	Erosion	Erosion
	Good flow	Good flow
2150-2175° F	Some contamination	Some contamination
	Erosion	Erosion
	Good flow	Good flow

APPENDIX VI

BRAZING INVESTIGATIONS

Investigations of various brazing alloys, temperature ranges, and erosion-strength characteristics were made to determine the best brazing alloy for module fabrication. Results of the specific tests conducted have been put in table form: numbers XII through XV in this appendix. The following provides a brief description of each test.

TEST DESCRIPTION	TABLE
1) Determination of temperature variation upon the erosion and flow characteristics of brazed foil specimens using eight various brazing alloys.	XV
2) Determination of erosion of tube clusters brazed with the five most promising alloys.	XVI
3) Determination of braze strength and quality of five brazing alloys.	XVII
4) Determination of braze shear strength at room and elevated temperatures for four brazing alloys.	XVIII

TABLE XVI
BRAZED TUBE CLUSTERS

Alloy	Results
Palniro 1	Sound joint, no evident erosion, general penetration - close to 100 Pct in TEE section.
E-440	No erosion, penetration about 10 Pct.
E-135	Evidence of erosion, general penetration - 100 Pct in TEE section.
Palniro 7	100 Pct erosion at TEE section, general 40-60 Pct erosion.
CM-62	Voids in joint, slight erosion, some penetration up to 100 Pct in some areas.

TABLE XVII
BRAZE STRENGTH TEST
(Pillow Tests)

Alloy	Brazing Temp. (°F)	Brazing Atmosphere	Braze Quality	Burst Pressure (Psi)	Remarks
Palniro 7	2000-25	Argon	Smooth, clean small fillets	2650-2850	Failed in parent material adjacent to braze
	2000-25	Hydrogen	Smooth, clean	3500-3900	Failed in parent material adjacent to braze.
Palniro 1	2125-50	Argon	Smooth, clean	3650-4150	Failed in parent material adjacent to braze.
	2125-50	Hydrogen	Fairly smooth	3700-4200	Failed in parent material adjacent to braze.
E-440	2125-50	Argon	Rough but Clean	900-1000	Failed through braze.
	2125-50	Hydrogen	Rough but Clean	850-1000	Failed through braze.
E-135	2125-50	Argon	Gray rough surface, large amount of porosity	2150-2600	Failed in braze.
	2125-50	Hydrogen	Clean, slightly rough	2700-2850	Failed in braze.
CM-62	2025-50	Argon	Voids, poor fillets	1200-1300	Failed through braze.
	2025-50	Hydrogen	Uneven braze	1000	Failed through braze.

195

TABLE XVIII
BRAZED JOINT SHEAR TESTS ~ MILLER - PEASLEE SPECIMENS

Brazing Alloy	Specimen	Test Temp. (° F)	Ultimate Load (Lbs)	Shear Strength (Psi)	Remarks
E 440	A	Room temp.	692	29,960	Braze failure
	B	Room temp.	734	29,960	Braze failure
	C	Room temp.	718	28,160	Braze failure
	D	1,350	200	8,260	Braze failure
	E	1,350	190	8,300	Braze failure
	F	1,350	230	9,540	Braze failure
	G	1,600	108	4,469	Braze failure
	H	1,600	115	4,670	Braze failure
	I	1,600	86	3,480	Braze failure
Palniro 1	A	Room temp.	1,320	53,010	Base metal failure
	B	Room temp.	1,650	61,809	Base metal failure
	C	1,350	572	23,060	Base metal failure
	D	1,600	300	11,490	Braze failure
Palniro 7	A	Room temp.	1,390	54,090	Base metal failure
	B	Room temp.	1,590	62,110	Base metal failure
	C	1,350	348	14,320*	Braze failure
	D	1,600	205	7,770*	Braze failure
Coast Metals 62	A	Room temp.	1,220	48,220	Braze failure
	B	Room temp.	1,230	47,670	Braze failure
	C	1,350	506	20,160	Braze failure
	D	1,600	262	10,270	Braze failure

*Porous brazed joint

196

APPENDIX VII

WAVY-TUBE FORMING MACHINE

The wavy tubes are formed from precut tube lengths in a fully automatic machine, shown in Figure 130. The cut tubes are picked up, fed into the die, formed, and returned to the chute by a series of sequenced movements. The sequence of movements is controlled by a cam-timer, operating pneumatic valves.

FORMING STEPS

Figure 131 shows the machine with the dies partially disassembled. The pneumatic timer ⑥ is visible in the upper right hand corner. The loading chutes ① are filled with precut straight tubes at ⑧. A trip lever ⑩ at the feeding end of the loading chute is actuated by a lever attached to the loading finger mechanism ②. The trip lever allows a single tube from each chute to drop into position for picking by the loading fingers. Two tubes at a time are picked by the loading finger mechanism ②, and the finger mechanism rotates downward until the tubes contact one side of the wave-form die ③.

The other half of the wave-form die closes and forms the wave in the tube. The loading finger ② allows the exposed ends of the tubes to slip horizontally and to seek a neutral position while the wave form is set. The die ③ remains closed while the loading fingers ② proceed downward to a position that leaves both ends of the tubes in the clear. The pneumatic cylinders ⑦ move the header die assemblies ④ in toward the exposed tube ends. The split die ⑤ encloses the tube ends by cam action; as the cylinder continues inward, the pilots on the two top punches ⑪ enter the tubes. A cone shape behind the pilot tip of the punches upsets the tube end to thicken the material and shorten the tube ends. The punches continue in until the tube passes over the cone shape onto the final size diameter of the punches. Speed of the header cylinder action ⑦ is controlled by an orifice located at each cylinder. The punch holders are spring loaded ⑫ to provide enough force against the cylinder action to coordinate the position of the two headers and hold the header dies ⑤ against the wave dies ③ during closure. This also equalizes the force at each end to prevent the tubes from slipping along the axis of the tube in the wave die ③.

The header assemblies ④ retract by reverse action of the cylinders ⑦. A cam bar (not shown) below the headers is actuated by a cylinder-operated
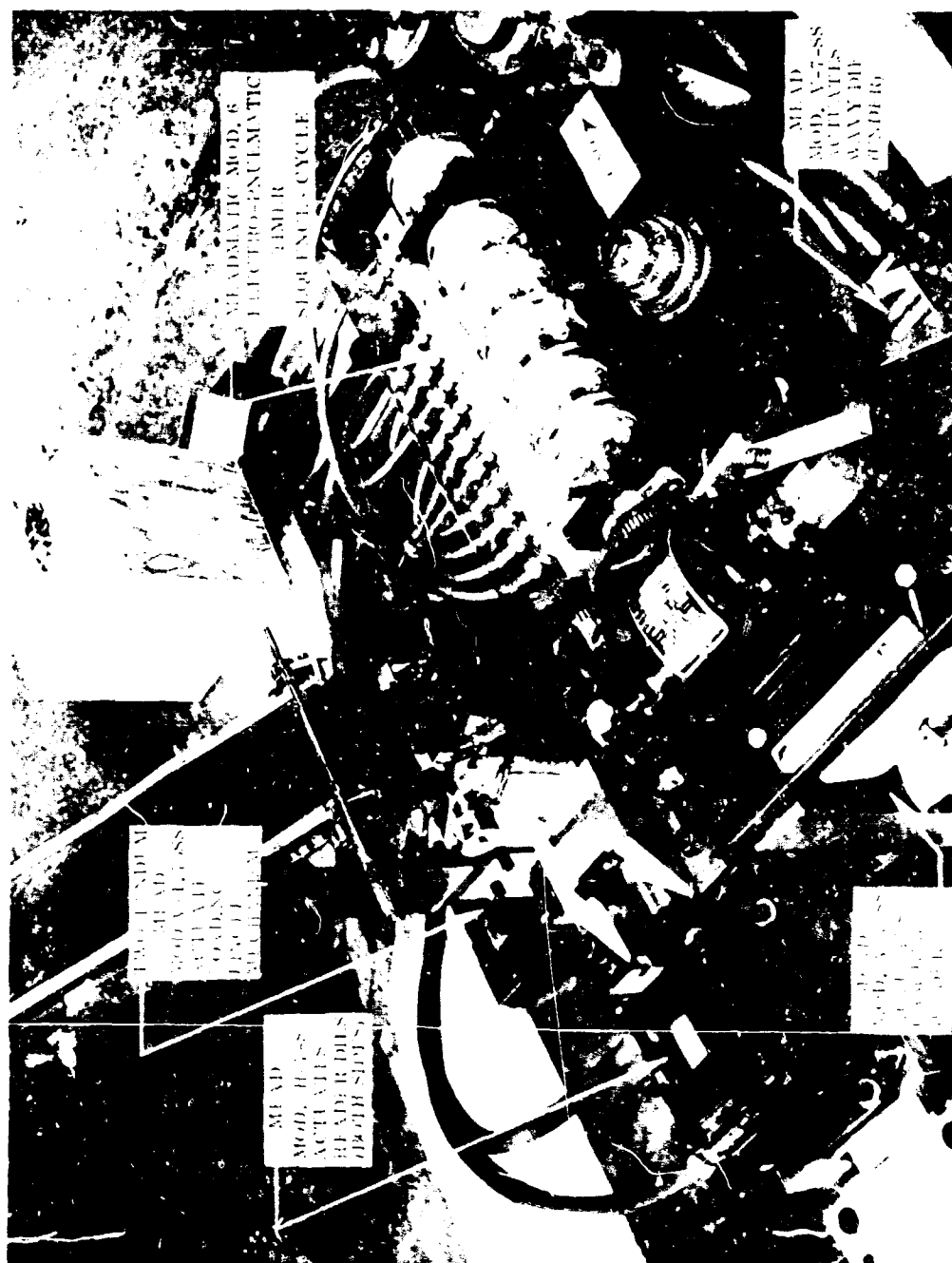
Figure 130. Wavy-Tube Former Machine.
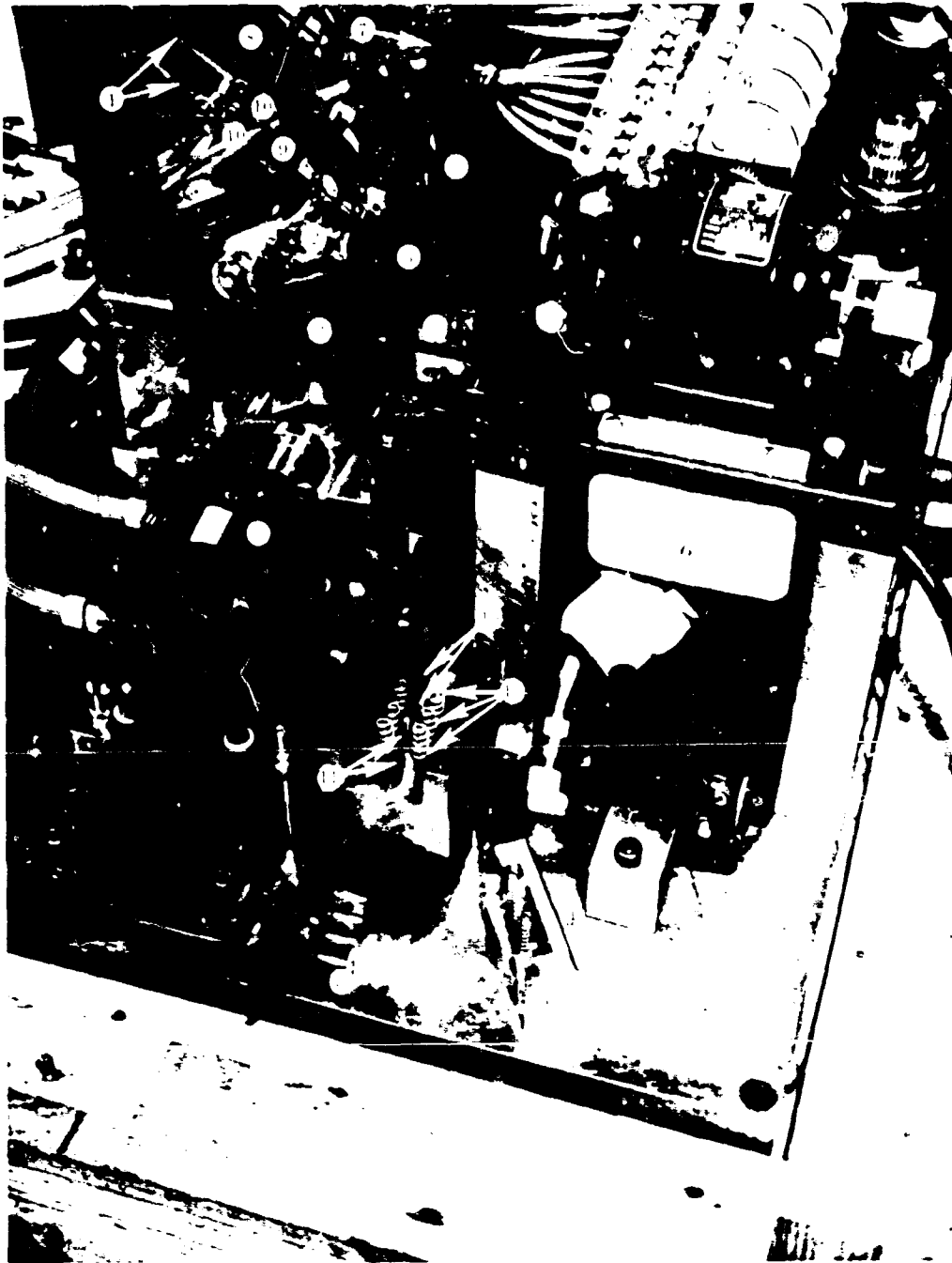
Figure 131. Wavy-Tube Forming Machine.

199

lever and raises the punch assembly ⑤ up to position the two lower punches ⑬ of each header. The headers ④ again move in, and the lower punches and dies ⑤ engage the tubes to form the final rectangular tube ends. The headers ④ are again retracted by the cylinders ⑦, and the cam bar below returns to the original position.

The loading finger mechanism ② rotates back up, engaging the formed tubes; and the wavy die ③ opens, allowing the finger mechanism to proceed upward. When the finger mechanism reaches a point above the discharge chute ⑨, a tripper releases the tubes to drop into the discharge chute. The loading finger returns ② and the cycle is repeated. Figure 132 shows the shape of the die to allow for springback.
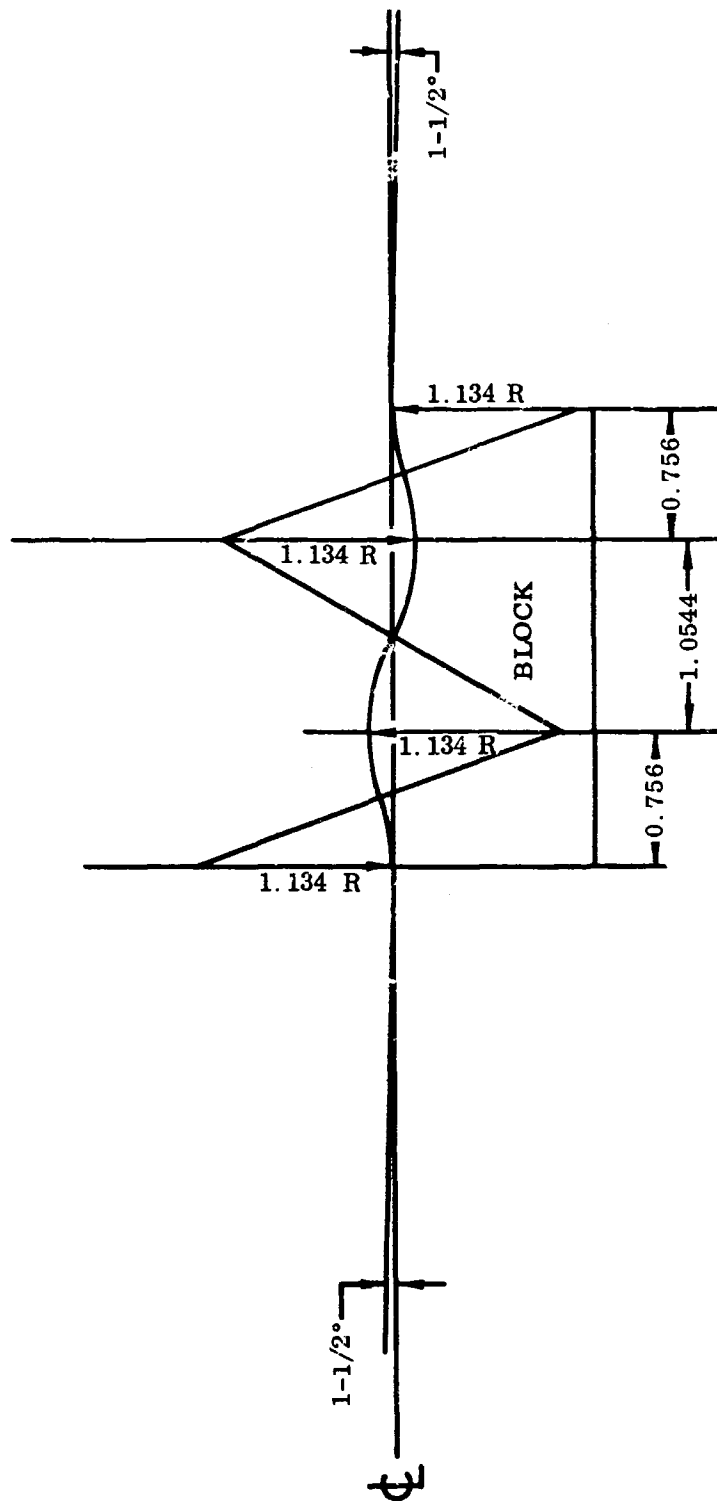
Figure 132. Wavy-Tube Die Block.

201

APPENDIX VIII

THERMAL SHOCK RIG SAMPLE DATA SHEETS
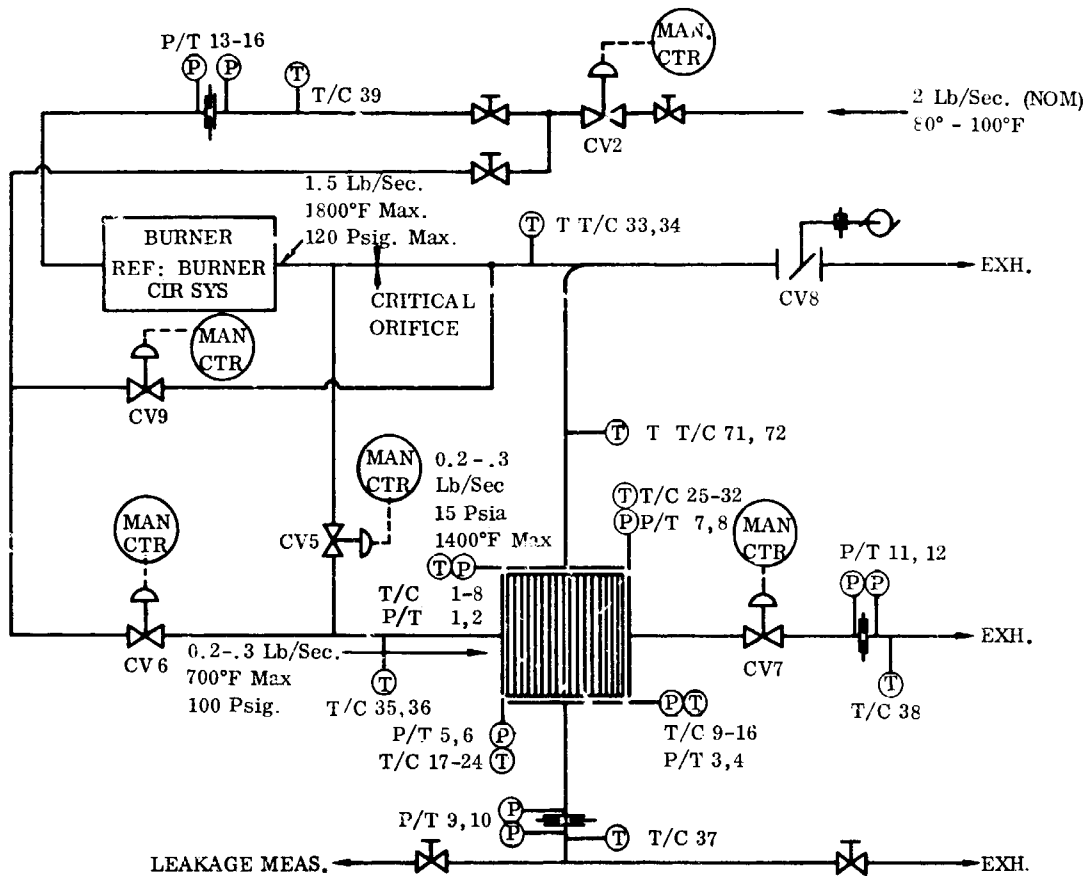
Figure 133. Thermal Shock Rig Instrumentation Locations.

TABLE XIX
THERMAL SHOCK RIG DATA SHEETS

	Run No.	Date (1965)	Time	Test Time	Baro	Mainline Temp T/C 39
			Hr–Min	Hr	In HG	°F
	6.45	6/24	11:30	1-1/2	30.01	78
	6.45	6/24	1:30	3-1/2		80
	6.45	6/24	2:30	4-1/2	29.99	81
8:50 AM 120 PSI	6.45	6/24	3:30	5-1/2	29.98	84
	6.45	Initiated at 8:50 AM				
	6.45	6/28	9:15	5-3/4	30.23	69
	6.45	6/28	10:15	6-3/4	30.22	76
	6.45	6/28	11:15	7-3/4	30.21	79
	6.45	Shutdown at 11:30 AM 6/28/5 8 Hr Completion				
8:30 AM 120 PSI	6.46	6/30	9:00	0	29.98	87
	6.46	6/30	10:00	1	--	--
	6.46	6/30	11:00	2	29.97	90
	6.46	6/30	1:00	4	29.95	102
	6.46	6/30	2:00	5	29.93	104
	6.46	6/30	3:00	6	29.92	106
	6.46	6/30	4:00	7	29.91	106
	6.46	6/30	5:00	8	29.89	108
8:20 AM 120 PSI	6.47	7/1	9:00	0	30.06	82
	6.47	7/1	10:00	1	30.08	88
	6.47	7/1	11:00	2	30.08	88
	6.47	7/1	1:00	4	30.07	95
	6.47	7/1	2:00	5	30.06	98
	6.47	7/1	3:00	6	30.05	100
	6.47	7/1	4:00	7	30.04	103
	6.47	7/1	5:00	8	30.04	103

*Approx 20 sec of elevated temp (1650-1700°) on G/S Control T/C No. 33.

	AIR SIDE								ORIFIC
Amb Temp	VALVE SETTING			MODULE				Inlet Pres	ΔP$_G$
	No. 5	No. 6	No. 7	Inlet Pres P5	Control Temp T/C 35, 36	ΔP P7-P5 ÷.965	ΔP P7-P5 2.965	P11	P11-P12
°F	PSI	PSI	PSI	PSIG	°F	2.965	2.965	In HG	In H$_2$0
60	3.9	9.7	10.1	55	423	47.5	--	.61	--
None taken because of consultation on pillow problem with T. Wheeler and Cell 9 control with Earl Reid									
72	4.0	9.5	10.0	54	426	63.1	--	.60	--
71	4.0	9.5	10.0	55	430	67.2	--	.61	--
62	4.0	9.2	10.1	55.1	433	43.6	--	.59	--
63	3.9	9.2	10.1	56.2	434	54.0	--	.60	--
66	3.9	9.2	10.0	55.2	438	61.5	--	.61	--
63	4.8	10.6	10.2	86.0	580	31.8	--	1.05	--
--	4.8	11.2	10.1	84.3	587	37.9	--	1.29	--
69	4.9	11.1	10.1	85.0	580	38.2	--	1.29	--
74	4.9	11.1	10.1	85.0	580	36.8	--	1.28	--
77	4.9	11.2	10.1	84.8	580	38.7	--	1.28	--
79	4.9	11.2	10.1	85.2	580	39.2	--	1.30	--
82	4.9	11.2	10.1	84.6	590	39.0	--	1.28	--
83	4.9	11.2	10.1	83.9	588	38.1	--	1.25	--
62	5.9	12.6	9.9	100.2	675	43.0	--	2.12	--
62	5.9	12.5	9.9	99.4	686	43.1	--	2.12	--
64	5.9	12.5	9.9	100.4	680	43.2	--	2.14	--
72	5.9	12.5	9.9	99.2	683	43.2	--	2.11	--
76	5.9	12.5	9.9	100.2	680	42.9	--	2.12	--
79	6.0	12.6	9.9	100.3	680	42.9	--	2.13	--
87	6.0	12.5	9.8	100.6	690	43.2	--	2.15	--
84	6.0	12.6	9.8	100.7	685	42.6	--	2.14	--

			GAS SIDE						
		VALVE SETTING		MODULE				ORIFICE	
E ΔP_B P11-P12 In H$_2$0	Temp T/C 38 °F	No. 8 MA	No. 9 PSI	Inlet Pres P1 In HG	Control T/C 33, 34 °F	Temp T/C 71, 72 °F	ΔP P1-P3 In H$_2$0	Inlet Pres P9 In HG	ΔP_G P9-P10 In H$_2$0
16.5	505	.55	0	2.3	880	818	8.6	1.27	--
16.2	507	.55	0	2.45	875	820	10.6	1.28	--
16.4	510	.55	0	2.50	885	824	11.3	1.28	--
16.0	513	.55	0	2.50	890	827	11.3	1.27	--
16.2	521	.55	0	2.70	886	836	13.1	1.32	--
16.5	520	.55	0	2.70	884	825	14.1	1.27	--
26.8	728	.56	0	3.80	1225	1137	12.5	2.14	--
34.9	734	.54	0	3.95	1225	1145	12.8	2.21	--
33.4	719	.55	0	3.95	1192	1116	12.8	2.21	--
33.3	725	.58	0	4.00	1198	1130	12.9	2.21	--
33.3	717	.56	0	3.95	1185	1110	12.9	2.20	--
33.7	716	.53	0	3.95	1200	1118	13.0	2.20	--
33.2	719	.55	0	3.95	1202	1119	13.1	2.20	--
32.8	720	.53	0	4.00	1202	1124	13.15	2.21	--
55.4	895	.47	0	6.40	1475	1390	18.7	3.76	--
55.3	902	.46	0	6.45	1482	1398	18.65	3.78	--
55.2	887	.46	0	6.55	1450	1370	18.5	3.75	--
55.2	892	.46	0	6.45	1450	1375	18.5	3.81	--
55.1	891	.46	0	6.50	1452	1378	18.5	3.81	--
55.1	892	.46	0	6.50	1454	1379	18.6	3.82	--
55.1	895	.44	0	6.50	1445	1373	18.6	3.83	--
55.1	895	.43	0	6.50	1450	1376	18.6	3.83	--

3

	ORIFICE			BURNER	
let res ?9 HG	ΔP_G P9–P10 In H_2O	ΔP_B P9–P10 In H_2O	Temp T/C 37 °F	Nozzle Pres Gage PSI	Valve No. 2 PSI
.27	--	19.1	553	265	15.0
.28	--	19.2	561	268	15.0
.28	--	19.2	570	265	15.0
.27	--	19.2	561	283	13.0
.32	--	19.5	582	283	15.0
.27	--	19.2	566	279	15.0
.14	--	33.8	765	367	13.9
.21	--	35.4	760	369	13.9
.21	--	35.4	752	362	13.9
.21	--	35.4	755	369	13.9
.20	--	35.1	746	352	13.9
.20	--	35.1	747	360	13.9
.20	--	35.2	753	358	13.9
.21	--	35.3	757	354	13.9
.76	--	60.0	928	480	15.0
.78	--	60.4	935	482	15.0
.75	--	60.3	924	474	15.0
.81	--	60.1	929	470	15.0
.81	--	60.3	927	472	15.0
.82	--	60.4	930	468	15.0
.83	--	60.6	929	468	15.0
.83	--	60.5	931	470	15.0

3   4

TABLE XIX (Continued)

Run No.	Date (1965)	Time Hr-Min	Test Time Hr	17 °F	18 °F	19 °F	20 °F	2 °]
6.45	6/24	11:30	1-1/2	397	394	325	390	39
6.45	6/24	1:30	3-1/2	390	385	333	377	38
6.45	6/24	2:30	4-1/2	403	402	341	394	39
6.45	6/24	3:30	5-1/2	405	400	345	394	39
6.45	6/28	9:30	5-3/4	406	402	326	396	39
6.45	6/28	10:30	6-3/4	405	401	352	396	39
6.45	6/28	11:30	7-3/4	412	407	352	402	40
6.46	6/30	9:00	0	555	545	480	535	53
6.46	6/30	10:00	1	558	549	549	541	54
6.46	6/30	11:00	2	555	546	500	540	54
6.46	6/30	1:00	4	555	545	498	545	55
6.46	6/30	2:00	5	557	552	496	545	55
6.46	6/30	3:00	6	550	544	491	540	54
6.46	6/30	4:00	7	562	553	496	549	55
6.46	6/30	5:00	8	565	560	502	549	55
6.47	7/1	9:00	0	651	640	595	634	64
6.47	7/1	10:00	1	658	648	606	640	64
6.47	7/1	11:00	2	653	645	605	638	64
6.47	7/1	1:00	4	660	651	605	640	64
6.47	7/1	2:00	5	657	648	607	640	64
6.47	7/1	3:00	6	655	644	605	640	64
6.47	7/1	4:00	7	645	636	625	635	64
6.47	7/1	5:00	8	657	650	610	645	64

				AIR-SIDE TEMPERATURES							
IN					OUT						
21	22	23	24	$\bar{T}_{A_1}$	25	26	27	28	29	30	31
°F	°F	°F	°F	°F	°F	°F	°F	°F	°F	°F	°F
392	387	316	395	392.3	561	636	484	628	602	623	425
380	377	324	385	382.2	585	695	481	621	581	607	461
395	394	330	401	398.1	585	690	480	638	581	607	465
395	395	336	399	398.0	595	691	476	645	590	612	468
397	394	310	402	393.3	605	690	441	691	583	551	430
396	394	390	400	398.4	600	725	465	670	602	585	461
403	401	337	406	405.1	596	691	462	650	601	585	463
538	542	460	553	544.4	810	945	660	662	835	801	613
545	548	480	555	549.2	830	948	681	NG	900	839	628
542	547	476	558	548.0	817	932	682	---	855	825	624
554	556	482	563	553.0	828	942	700	---	890	831	640
550	545	475	551	550.0	804	940	693	---	890	822	631
544	543	475	555	546.1	813	925	694	---	870	815	635
550	551	480	562	---	---	928	690	---	872	818	634
553	553	483	556	557.1	819	920	698	NG	875	823	637
640	645	569	650	643.3	1151	1191	885	NG	1158	1021	781
644	646	571	659	648.2	1155	1130	902	---	1174	1031	790
640	640	572	653	644.8	1140	1130	893	---	1151	1055	789
645	644	573	660	650.0	1146	1165	897	---	1161	1060	794
645	648	575	664	653.2	1141	1165	895	---	1150	1045	790
648	643	572	660	647.0	1142	1172	895	---	1155	1040	790
641	645	569	652	642.3	1144	1180	898	---	1161	1035	790
648	655	575	660	652.5	1147	1180	900	---	1156	1035	793

| 32 °F | $\bar{T}_{A_2}$ °F | IN | | | | | | | | $\bar{T}_{G_1}$ |
		1 °F	2 °F	3 °F	4 °F	5 °F	6 °F	7 °F	8 °F	°F
573	630.8	770	NG	505	736	758	761	480	772	759,
552	668.2	771	NG	522	745	760	761	497	770	761,
558	609.8	765	NG	523	735	754	755	495	760	753,
562	615.5	765	NG	521	740	760	760	495	755	756,
631	625.1	762	NG	519	762	761	759	478	NG	561,
635	636.1	765	NG	542	770	770	766	513	NG	767,
625	624.4	763	NG	536	760	765	765	505	NG	762,
870	820.5	1069	1055	766	1010	1040	1053	748	1055	1047,
897	882.4	1078	1070	783	1050	1065	1085	770	1085	1072,
884	862.3	1060	1095	768	1015	1041	1060	755	1066	1056,
896	877.2	1070	1055	772	--	1052	1067	761	1073	1063,
890	869.1	1060	1045	765	--	1050	1061	755	1065	1046,
891	862.4	1058	1045	760	--	1042	1060	751	1060	1053,
891	---	1055	1095	757	--	1038	1055	750	1060	1049,
891	865.6	1057	1045	765	--	1041	1058	756	1055	1051,
1085	1121.2	1318	1298	965	--	1300	1328	969	1330	1314,
1090	1110.6	1330	1310	974	--	1317	1344	982	1347	1329,
1083	1111.8	1306	1285	961	--	1288	1315	972	1319	1302,
1092	1124.8	1310	1288	964	--	1294	1323	973	1325	1308,
1090	1118.1	1305	1282	960	--	1287	1318	970	1320	1302,
1090	1119.4	1310	1285	960	--	1290	1320	969	1325	1306,
1092	1122.4	1311	1286	962	--	1293	1323	973	1325	1307,
1091	1121.8	1310	1288	962	--	1294	1323	975	1325	1308,

3

TEMPERATURES

l	OUT								$\overline{T}_{G_2}$
	9	10	11	12	13	14	15	16	
	°F	°F	°F	°F	°F	°F	°F	°F	°F
.2	502	603	649	285	606	511	490	320	560.4
.0	502	605	644	301	605	506	491	343	558.5
.4	506	605	640	308	603	501	499	349	559.0
.0	510	616	645	310	610	506	505	354	565.1
.0	506	601	648	293	590	502	490	286	556.1
.3	514	610	655	321	599	508	497	324	551.3
.1	509	603	641	321	590	504	495	320	556.0
.0	690	800	878	450	837	680	660	450	757.3
.1	700	820	901	465	855	692	676	475	774.0
.1	694	811	886	462	844	683	670	470	764.4
.2	698	821	898	472	855	700	680	475	775.2
.1	690	810	893	470	844	691	670	466	766.2
.0	691	814	900	471	846	690	665	466	767.4
.8	693	810	891	470	845	697	672	448	768.0
.0	690	811	893	476	845	697	670	465	767.6
.8	855	1010	1101	577	1049	862	823	522	950.0
.6	875	1020	1120	595	1064	875	840	542	966.4
.3	863	1010	1101	591	1048	862	835	545	953.2
.0	870	1015	1110	595	1054	868	838	550	959.2
.2	870	1012	1105	591	1049	869	839	550	957.2
.0	865	1010	1105	598	1049	865	835	552	954.5
.6	865	1010	1110	690	1055	865	835	551	958.0
.0	868	1015	1112	602	1055	870	837	556	959.5

APPENDIX IX

FORMULAE FOR EXTRAPOLATING TEST DATA TO OTHER FLUID CONDITIONS AND CORE DIMENSIONS

Because performance testing was done at fluid conditions and with geometries different from those that would match the model engine cycle of 2300°F and 10:1 pressure ratio, it became necessary to derive a set of suitable correction formulae. These formulae, simplified from standard fluid mechanics and heat transfer equations, give suitably accurate results for the extrapolations used. T is the subscript used to denote test conditions, and X denotes extrapolated conditions.

AIR-SIDE PRESSURE DROP

$$\left(\frac{\Delta P}{P}\right)_{A,X} = \left(\frac{\Delta P}{P}\right)_{A,T} \left(\frac{N_X}{N_T}\right) \left(\frac{L_{A,X}}{L_{A,T}}\right) \left(\frac{L_{G,T}}{L_{G,X}}\right)^{1.82} \left(\frac{L_{NF,T}}{L_{NF,X}}\right)^{1.82}$$

$$\left(\frac{P_{1,T}}{P_{1,X}}\right)^2 \left(\frac{T_{1,X}}{T_{1,T}}\right) \left(\frac{\mu_X}{\mu_T}\right)^{.18}$$

GAS-SIDE PRESSURE DROP

$$\left(\frac{\Delta P}{P}\right)_{G,X} = \left(\frac{\Delta P}{P}\right)_{G,T} \left(\frac{N_X}{N_T}\right) \left(\frac{L_{A,T}}{L_{A,X}}\right)^2 \left(\frac{L_{G,X}}{L}\right) \left(\frac{L_{NF,T}}{L_{NF,X}}\right)^2 \left(\frac{P_{1,T}}{P_{1,X}}\right)^2$$

$$\left(\frac{T_{1,X}}{T_{1,T}}\right) \left(\frac{f_X}{f_T}\right)$$

f_X and f_T are the friction factors based on the Reynolds numbers and L/D's at extrapolated and test conditions.

The Reynolds number is evaluated from

$$N_R = \frac{D_{HG}}{L_A L_{NF} \sigma_G \mu_G}$$

EFFECTIVENESS

Reduction of test data gives the effectiveness at test conditions. From Figure 134 (taken from Reference 1, page 52) the number of transfer units, Ntu, can be determined. The Ntu can be extrapolated by

$$Ntu_X = Ntu_T \left(\frac{N_X}{N_T}\right) \left(\frac{L_{A,X}}{L_{A,T}}\right)^{.86} \left(\frac{L_{G,X}}{L_{G,T}}\right)^{.91} \left(\frac{L_{NF,X}}{L_{NF,T}}\right)^{.77}$$

$$\left(\frac{T_{A1,T}}{T_{A1,X}}\right)^{.1} \left(\frac{T_{G1,X}}{T_{G1,T}}\right)^{.61}$$

The extrapolated effectiveness can be found at the calculated Ntu_X in Figure 134.

NUMERICAL EXAMPLE

	TEST DATA (2nd Straight-Tube Module)	EXTRAPOLATED CONDITIONS
No-Flow Length	15.85 IN/LB/SEC	20 IN/LB/SEC
Gas-Flow Length	2.85 IN/(2.625 IN ON AIRSIDE)	1.70 IN
Airflow Length	3.96 IN	4.9 IN
T Gas In	1347 °F (1807°R)	1316 °F (1776°R)
T Air In	654 °F	654 °F
P Gas In	16.8 psia	15.2 psia
P Air In	114.7 psia	147.0 psia
Number Passes	1	2
Effectiveness	56.0%	See
Gas-Side Pressure Drop	2.84%	Following
Air-Side Pressure Drop	1.46%	Calculations
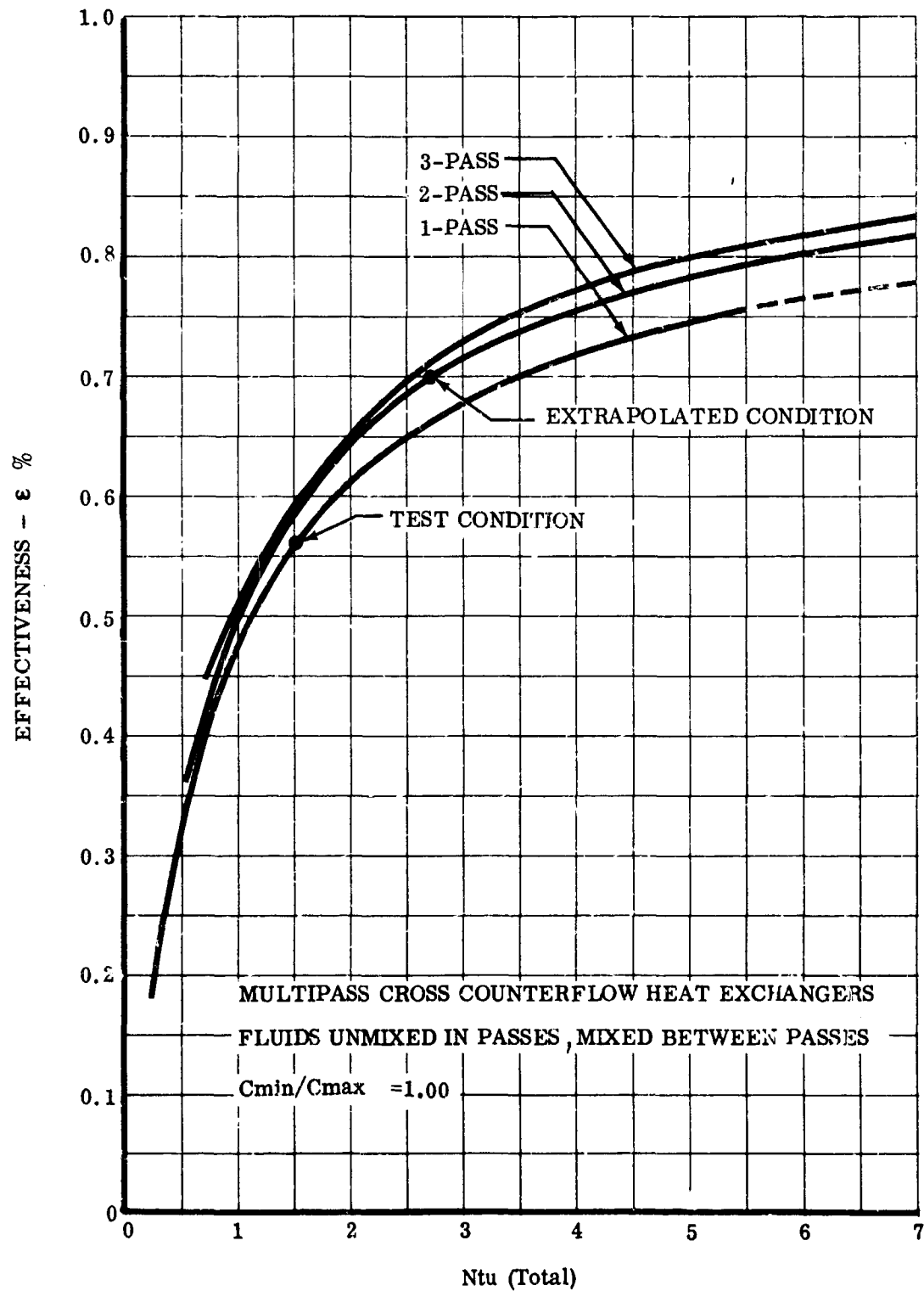
Figure 134. Effectiveness Versus Ntu.

209

AIR-SIDE PRESSURE DROP

$$\left(\frac{\Delta P}{P}\right)_{A,X} = 1.46 \left(\frac{2.0}{1.0}\right) \left(\frac{4.9}{4.5}\right) \left(\frac{2.625}{1.70}\right)^{1.82} \left(\frac{15.85}{20}\right)^{1.82} \left(\frac{114.7}{147.0}\right)^{2}$$

$$\left(\frac{1110}{1114}\right) \left(\frac{.075}{.075}\right)^{.18}$$

$$\left(\frac{\Delta P}{P}\right)_{A,X} = 2.8\%$$

GAS-SIDE PRESSURE DROP

$$N_{RG,T} = \frac{WD_H}{A_c \mu} = \frac{1\frac{Lb}{Sec}\ 0.054\ In.\ 3600\frac{Sec}{Hr}\ 12\frac{In}{Ft}}{4.5\ 15.85\ .429\ In^2 \cdot 1\frac{Lb}{Hr} - ft}$$

$$N_{RGT} = 765. \qquad f_T = .025$$

$$(L/D)_T = 53.$$

$$N_{RG,X} = 555. \qquad f_X = .035$$

$$(L/D)_X = 31.5$$

$$\left(\frac{\Delta P}{P}\right)_{G,X} = 2.84 \left(\frac{2}{1}\right) \left(\frac{4.5}{4.9}\right)^{2} \left(\frac{1.63}{2.85}\right) \left(\frac{15.85}{20}\right) \left(\frac{16.8}{15.2}\right)^{2} \left(\frac{1776}{1807}\right) \left(\frac{.035}{.025}\right)$$

$$\left(\frac{\Delta P}{P}\right)_{G,X} = 3.1\%$$

$$\left(\frac{\Delta P}{P}\right)_{Total,\ X} = 5.9\%$$

<u>EFFECTIVENESS</u>

$$Ntu_T = 1.5$$

$$Ntu_X = 1.5 \left(\frac{2}{1}\right) \left(\frac{4.9}{4.5}\right)^{.86} \left(\frac{1.7}{2.625}\right)^{.91} \left(\frac{20}{15.85}\right)^{.77} \left(\frac{1110.}{1114.}\right)^{.1} \left(\frac{1776}{1807}\right)^{.61}$$

$$Ntu_X = 2.66$$

$$\epsilon_X = 70\%$$

DISTRIBUTION

US Army Materiel Command	5
US Army Aviation Materiel Command	6
United States Army, Pacific	1
US Army Forces Southern Command	1
Chief of R&D, DA	2
US Army R&D Group (Europe)	2
US Army Aviation Materiel Laboratories	19
US Army Engineer R&D Laboratories	1
US Army Ballistic Research Laboratories	2
Army Aeronautical Research Laboratory, Ames Research Center	1
US Army Research Office-Durham	1
US Army Test and Evaluation Command	1
US Army Combat Developments Command, Fort Belvoir	2
US Army Combat Developments Command Transportation Agency	1
US Army Aviation School	1
US Army Tank-Automotive Center	2
US Army Aviation Test Board	2
US Army Materials Research Agency	1
US Army Aviation Test Activity, Edwards AFB	2
Air Force Flight Test Center, Edwards AFB	2
US Army Field Office, AFSC, Andrews AFB	1
Air Force Aero Propulsion Laboratory, Wright-Patterson AFB	1
Systems Engineering Group, Wright-Patterson AFB	4
Naval Air Systems Command, DN	15
Office of Naval Research	2
Commandant of the Marine Corps	1
Marine Corps Liaison Officer, US Army Transportation School	1
Lewis Research Center, NASA	1
NASA Scientific and Technical Information Facility	2
NAFEC Library (FAA)	2
US Army Board for Aviation Accident Research	1
Bureau of Safety, Civil Aeronautics Board	2
US Naval Aviation Safety Center, Norfolk	1
Federal Aviation Agency, Washington, D. C.	2
US Government Printing Office	1
Defense Documentation Center	20

212

DOCUMENT CONTROL DATA - R&D

(Security classification of title, body of abstract and indexing annotation must be entered when the overall report is classified)

1. ORIGINATING ACTIVITY (Corporate author)	2a. REPORT SECURITY CLASSIFICATION
THE BOEING COMPANY, Turbine Division P.O. Box 3955 Seattle, Washington 98124	For Official Use Only
	2b. GROUP

3. REPORT TITLE

Small Gas Turbine Engine Component Technology -
Regenerator Research

4. DESCRIPTIVE NOTES *(Type of report and inclusive dates)*

Final

5. AUTHOR(S) *(Last name, first name, initial)*

Acurio, John   Klein, Vernon J.
Dolf, Hans R.   Wheeler, Anthony J.

6. REPORT DATE	7a. TOTAL NO. OF PAGES	7b. NO. OF REFS
January 1967	232	10

8a. CONTRACT OR GRANT NO.	9a. ORIGINATOR'S REPORT NUMBER(S)
DA 44-177-AMC-173(T)	
b. PROJECT NO.	USAAVLABS Technical Report 66-90
c. Task Number 1M121401D14413	9b. OTHER REPORT NO(S) (Any other numbers that may be assigned this report)
d.	D4-3371

10. AVAILABILITY/LIMITATION NOTICES

Each transmittal of this document outside the Department of Defense must have
prior approval of US Army Aviation Materiel Laboratories, Fort Eustis, Va.

11. SUPPLEMENTARY NOTES	12. SPONSORING MILITARY ACTIVITY
N/A	Commanding Officer U. S. Army Aviation Materiel Laboratories Fort Eustis, Virginia

13. ABSTRACT

This report finalizes the research conducted on the regenerator section of
Contract DA 44-177-AMC-173(T) - Advancement of Small Gas Turbine Engine Component
Technology. The program was authorized by Task 1M121401D14413. Work conducted
by The Boeing Company under this task also included research on high-temperature
turbine materials and high-pressure-ratio centrifugal compressors.

The regenerator program covered by this report was started in May, 1964, and
included (a) analytical studies of the heat transfer and pressure drop
characteristics associated with small diameter, thin-walled tubes, (b) design
of full-size modules for regenerators, and (c) development of these modules
by testing.

DD FORM **1473**

14.		LINK A		LINK B		LINK C	
KEY WORDS		ROLE	WT	ROLE	WT	ROLE	WT
Regeneration, Regenerator, Regenerated Engine Effectiveness, Heat Transfer Pressure Drop, Pressure Loss Core Weight, Core Volume Small Diameter, Thin-Walled Tubing Braze, Brazed, Brazing Straight Tubes, Wavy Tubes, Tubular Gas-Flow Length, Air-Flow Length, No-Flow Length Specific Fuel Consumption, Specific Power, Part Power Simple Cycle, Regenerated Cycle Reynolds Number, Stanton Number, Prandtl Number, Colburn Factor Module Steady State, Transient, Thermal Shock							

INSTRUCTIONS

1. **ORIGINATING ACTIVITY:** Enter the name and address of the contractor, subcontractor, grantee, Department of Defense activity or other organization *(corporate author)* issuing the report.

2a. **REPORT SECURITY CLASSIFICATION:** Enter the overall security classification of the report. Indicate whether "Restricted Data" is included. Marking is to be in accordance with appropriate security regulations.

2b. **GROUP:** Automatic downgrading is specified in DoD Directive 5200.10 and Armed Forces Industrial Manual. Enter the group number. Also, when applicable, show that optional markings have been used for Group 3 and Group 4 as authorized.

3. **REPORT TITLE:** Enter the complete report title in all capital letters. Titles in all cases should be unclassified. If a meaningful title cannot be selected without classification, show title classification in all capitals in parenthesis immediately following the title.

4. **DESCRIPTIVE NOTES:** If appropriate, enter the type of report, e.g., interim, progress, summary, annual, or final. Give the inclusive dates when a specific reporting period is covered.

5. **AUTHOR(S):** Enter the name(s) of author(s) as shown on or in the report. Enter last name, first name, middle initial. If military, show rank and branch of service. The name of the principal author is an absolute minimum requirement.

6. **REPORT DATE:** Enter the date of the report as day, month, year; or month, year. If more than one date appears on the report, use date of publication.

7a. **TOTAL NUMBER OF PAGES:** The total page count should follow normal pagination procedures, i.e., enter the number of pages containing information.

7b. **NUMBER OF REFERENCES:** Enter the total number of references cited in the report.

8a. **CONTRACT OR GRANT NUMBER:** If appropriate, enter the applicable number of the contract or grant under which the report was written.

8b, 8c, & 8d. **PROJECT NUMBER:** Enter the appropriate military department identification, such as project number, subproject number, system numbers, task number, etc.

9a. **ORIGINATOR'S REPORT NUMBER(S):** Enter the official report number by which the document will be identified and controlled by the originating activity. This number must be unique to this report.

9b. **OTHER REPORT NUMBER(S):** If the report has been assigned any other report numbers *(either by the originator or by the sponsor),* also enter this number(s).

10. **AVAILABILITY/LIMITATION NOTICES:** Enter any limitations on further dissemination of the report, other than those imposed by security classification, using standard statements such as:

   (1) "Qualified requesters may obtain copies of this report from DDC."

   (2) "Foreign announcement and dissemination of this report by DDC is not authorized."

   (3) "U. S. Government agencies may obtain copies of this report directly from DDC. Other qualified DDC users shall request through

         _____ ."

   (4) "U. S. military agencies may obtain copies of this report directly from DDC. Other qualified users shall request through

         _____ ."

   (5) "All distribution of this report is controlled. Qualified DDC users shall request through

         _____ ."

If the report has been furnished to the Office of Technical Services, Department of Commerce, for sale to the public, indicate this fact and enter the price, if known.

11. **SUPPLEMENTARY NOTES:** Use for additional explanatory notes.

12. **SPONSORING MILITARY ACTIVITY:** Enter the name of the departmental project office or laboratory sponsoring *(paying for)* the research and development. Include address.

13. **ABSTRACT:** Enter an abstract giving a brief and factual summary of the document indicative of the report, even though it may also appear elsewhere in the body of the technical report. If additional space is required, a continuation sheet shall be attached.

It is highly desirable that the abstract of classified reports be unclassified. Each paragraph of the abstract shall end with an indication of the military security classification of the information in the paragraph, represented as *(TS), (S), (C),* or *(U).*

There is no limitation on the length of the abstract. However, the suggested length is from 150 to 225 words.

14. **KEY WORDS:** Key words are technically meaningful terms or short phrases that characterize a report and may be used as index entries for cataloging the report. Key words must be selected so that no security classification is required. Identifiers, such as equipment model designation, trade name, military project code name, geographic location, may be used as key words but will be followed by an indication of technical context. The assignment of links, rules, and weights is optional.

SUPPLEMENTARY

INFORMATION

	FILE	DATE
REQUEST FOR OR NOTIFICATION OF REGRADING ACTION (AR 380-5)	SAVFE-SOS	16 June 1969

NOTE: Read instructions on reverse side before completing this form.

TO:

Administrator
Defense Documentation Center
Cameron Station
Alexandria, VA   22314

FROM: Commanding Officer, US Army Aviation Materiel Laboratories
Fort Eustis, VA   23604

XX☐ THE DOCUMENT(S) DESCRIBED BELOW HAS/HAVE BEEN REVIEWED FOR REGRADING AND ACTION HAS BEEN TAKEN AS INDICATED. APPROPRIATE ACTION SHOULD BE TAKEN TO MARK YOUR COPIES AND NOTIFY ALL RECIPIENTS TO WHOM ADDITIONAL DISTRIBUTION WAS FURNISHED IN ACCORDANCE WITH AR 380-5. DOCUMENTS CONCERNING THIS SAME SUBJECT SHOULD BE REVIEWED FOR POSSIBLE REGRADING.

☐ REQUEST DOCUMENT(S) DESCRIBED BELOW BE REVIEWED TO DETERMINE WHETHER THEY CAN BE DOWNGRADED OR DECLASSIFIED AT THIS TIME. (Include justification in the Remarks Section of this form.)

☐ REQUEST APPROPRIATE GROUP MARKINGS FOR DOCUMENTS DESCRIBED BELOW.

☐ DOCUMENT(S) DESCRIBED BELOW HAS/HAVE BEEN PLACED IN A DIFFERENT GROUP AND WILL BE RE-MARKED IN ACCORDANCE WITH AR 380-5 AND AR 380-6.

CONTROL NUMBER a	DOCUMENTS (Type, Headquarters of Origin, Date, Subject or Short Title) b	CLAS OF SUBJ c	INCL d	CLAS AND GP NO. e	RE-GRADED TO CLAS & GP NO. f
	USAAVLABS Technical Report 66-90, Small Gas Turbine Engine Component Technology Regenerator Research, January 1967. Contract DA 44-177-AMC-173(T). (Boeing Company, Turbine Division Report D4-3371). NOTE: DELETE DDC STATEMENT: Each transmittal of this document outside the Department of Defense must have prior approval of the US Army Aviation Materiel Laboratories, Fort Eustis, VA. INSERT DDC STATEMENT: This document has been approved for public release; its distribution is unlimited.			OFLUSE	U

AUTHORITY OR COMMAND LINE (When applicable)

ELSIE E. GILLIAM, Security Officer

PRINTED OR TYPED NAME AND TITLE OF OFFICER

SIGNATURE

DA FORM 1575   REPLACES EDITION OF 1 AUG 61 WHICH IS OBSOLETE.

SUPPLEMENTARY

INFORMATION

NOTICES OF CHANGES IN CLASSIFICATION, DISTRIBUTION AND AVAILABILITY

69-17   **1 SEPTEMBER 1969**

AD-809 557L Boeing Co., Seattle, Wash. Turbine Div. Final rept. Rept. no. D4-3371, USAAVLABS TR-66-90 Jan 67 Contract DA-44-177- AMC-173(T)	DoD only: others to Army Aviation Materiel Labs., Fort Eustis, Va.	No limitation	USAAML notice, 16 Jun 69